SOUND FIELD RECONSTRUCTION FOR AN UNDER-DETERMINED SYSTEM AND ITS APPLICATION

A Dissertation

Submitted to the Faculty

of

Purdue University

by

Tongyang Shi

In Partial Fulfillment of the

Requirements for the Degree

of

Doctor of Philosophy

May 2019

Purdue University

West Lafayette, Indiana

THE PURDUE UNIVERSITY GRADUATE SCHOOL
STATEMENT OF DISSERTATION APPROVAL

Dr. J. Stuart Bolton, Chair

School of Mechanical Engineering

Dr. Charles M. Krousgrill

School of Mechanical Engineering

Dr. Jeffery F. Rhoads

School of Mechanical Engineering

Dr. Patricia Davies

School of Mechanical Engineering

Dr. Robert L. Nowack

Department of Earth, Atmospheric, and Planetary Sciences

Approved by:

Dr. Jay P. Gore

Head of the School Graduate Program

ACKNOWLEDGMENTS

First and foremost, I would like to express my sincere gratitude to my advisor Prof. Bolton. I really appreciate all your patience, motivation, and support of my Ph.D study and related research. Your guidance and immense knowledge helped me in all the time of research and writing of this thesis. I could not have imagined having a better advisor and mentor for my Ph.D study. Your inspiration to me is not only in my Ph.D period but also to my whole life. It is my honor to work with you.

Besides my advisor, I would like to thank the rest of my thesis committee: Prof. Davies, Prof. Rhoads, Prof. Nowack and Prof. Krousgrill. Thank you for give me good comments and advises which give me various perspectives to widen my research.

I also would like to thank to all the professors and staff in Ray W. Herrick Laboratories. Donna and Cindy, thank you for help me arrange all the event. Charles and Ryan, thank you for all the work and advises in experiment design.

My sincere thanks also goes to Frank Eberhardt, who is my project mentor, and my manager during my intern at Walesboro Noise and Vibration Laboratories, Cummins Inc. Thank you for arrange the experiment at Cummins, and always take care of me during my intern.

I thank my fellow labmates for their support and love during the past five years: Rui Cao, Daniel Carr, Jillian Joffe, Nicholas Kim, Seungkyu Lee, Yangfan Liu, Jiawei Liu, Anna Loehr, Yuan Peng, Jelena Paripovic, Hyunjun Shin, Weonchan Sung, Weimin Thor, Yiming Wang, and Yutong Xue. Yanfang, thank you for teach me all the mathematics when I began my study in Purdue. Yiming and Rui, thank you all in for the stimulating discussions, for the sleepless nights we were working together before deadlines. Weonchan and Yutong, thank you for all the fun we have had in the last five years. Thor, thank you for make the intensity measurement possible and conduct the experiments for my thesis.

Last but not the least, I would like to thank my family for all their love and encouragement. For my parents who raised me with love and support me from China to France, and from France to United State. For my girlfriend Sylvia, thank you for your presence and love in my life and all the support during my Ph.D study.

TABLE OF CONTENTS

Page

LIST OF FIGURES

Figure Page

Figure Page

Figure Page

Figure Page

Figure Page

Figure Page

Figure Page

ABBREVIATIONS

NAH	Near-field Acoustical Holography
ESM	Equivalent Source Method
WBH	Wideband Acoustical Holography
TSVD	Truncated Singular Value Decomposition
SONAH	Statistically Optimized Near-field Acoustical Holography
IBEM	Inverse Boundary Element Method
IRM	Inverse Radiation Mode
SVD	Singular Value Decomposition
GCV	Generalized Cross-Validation
NCP	Normalized Cumulative Periodogram
MDP	Morozov's Discrepancy Principle
PFD	Partial Field Decomposition
NVH	Noise Vibration Harshness
B&K	Bruel & Kjaer

ABSTRACT

Shi, Tngyang PhD, Purdue University, May 2019. Sound Field Reconstruction for an Under-Determined System and its Application. Major Professor: J. Stuart Bolton, School of Mechanical Engineering.

Near-Field Acoustical Holography (NAH) is an inverse process in which sound pressure measurements made in the near-field of an unknown sound source can be used to reconstruct the sound field so that source locations can be identified. Usually a large number of measurements is required for the usual NAH methods since a large number of parameters in the source or field model need to be determined. However, a large-scale microphone measurement is costly and hard to perform, so the use of NAH is limited by practical experimental conditions. In the present work, with the motivation of decreasing the number of microphone measurements required, and thus facilitating the measurement process, two sparse Equivalent Source Method (ESM) algorithms were studied: i.e., Wideband Acoustical Holography (WBH) and l_1-norm minimization. Based on these two algorithms, a new hybrid NAH procedure was proposed and demonstrated. To study and verify the above mentioned algorithms, simulations of different sources were conducted and then experiments were conducted on different sources: i.e., a loudspeaker cabinet and a diesel engine.

1. INTRODUCTION

1.1 Noise Source Identification

Noise reduction is an attractive topic in industry since nowadays customers have higher requirements on the product noise level for their concerns related to both the municipal environment and to occupational health and safety. Therefore to characterize the noise source of products is an important step in the product development process. In order to control the noise source level, a precise knowledge of the major noise source locations is needed to guide the efficient application of noise control resources. In some cases the noise source locations may be obvious and the locations can be found directly. But in most cases the noise source is complex, and a noise source identification tool is needed to find the noise source location. The examples of such tools are, e,g., intensity probe, accelerometer, beamforming, and Near-Field Acoustical Holography (NAH).

The intensity probe measures the true sound intensity at a single point, so an intensity probe measurement scan over the sound source region can help us get an idea of the acoustic energy distribution of the source. Taking a measurement at one point at one time makes the intensity probe most useful when measuring a stationary sound field. The limitation is when the source cannot be measured from a close distance: i.e., the inlet and outlet pipes around the diesel engine make a close measurement impossible. In that case, the intensity probe cannot be used to get near-field sound field information. Scanning measurements can also be very time consuming.

An accelerometer measures the displacement, velocity and acceleration directly from the source surface. Since the signal from different accelerometers can be acquired simultaneously, so this approach can be used to measure non-stationary vibrations. The limitation of using accelerometers is when mounting them on the source surface,

they affect the vibration pattern if the source is light, and when the surface is porous it is hard to attach them on the surface. In addition, there may also be problems when attaching accelerometers to a very hot surface: e.g., an engine.

Beamforming and NAH are sound source identification methods based on microphone array measurements. Beamforming is an efficient method to identify the major noise source location [1]. The phase of the signal received by the microphones are shifted forward by the time needed for the sound wave to propagate from the source to the microphones, so the sound source location can be found by accumulating the phase difference and identifying the local maximum which corresponds to the sound source position. When using beamforming methods, a far-field measurement is desired in order to cover the whole measurement region. It is noted that beamforming is a convenient tool for sound source identification but not for sound field reconstruction. And certain convolution techniques are needed to decrease the side-lobes in the beam pattern in order to get a clear source position image. NAH is a technique that can be used to construct a model to describe the acoustic field generated by the source based on near-field microphone array measurements [2–4]. Identifying the noise source with NAH involves two steps: 1. constructing the source model from measurements, 2. reconstruct a detailed image of the sound field sound pressure, particle velocity and sound intensity distribution on the source surface or at any desired location in space. The NAH procedure requires different mathematical models depending on different NAH methods, and some of the methods are computationally expensive. From the measurement point-of-view, depends on the size of the source, usually NAH requires a large number of microphone measurements (i.e., hundreds of measurement), so it is also economically costly.

1.2 Motivation and Objective

From all the sound source identification tools mentioned in the previous section, NAH is the preferred tool to identify noise source locations. With NAH, acoustical

field information can be obtained on the source surface without affecting the sound field itself. The general procedure in NAH is to measure the sound pressure with the microphones in the near-field of the source (see Figure 1.1), and reconstruct the sound field on the source surface. It is also possible to reconstruct the sound field at other locations: e.g., it is possible to reconstruct the sound field at other measurement locations to verify the reconstruction accuracy. However, the need for a large number of microphone measurements not only makes NAH economically costly, but also increases the measurement difficulty. If the number of microphone measurements could be decreased, then NAH could be applied to more noise source identification scenarios.

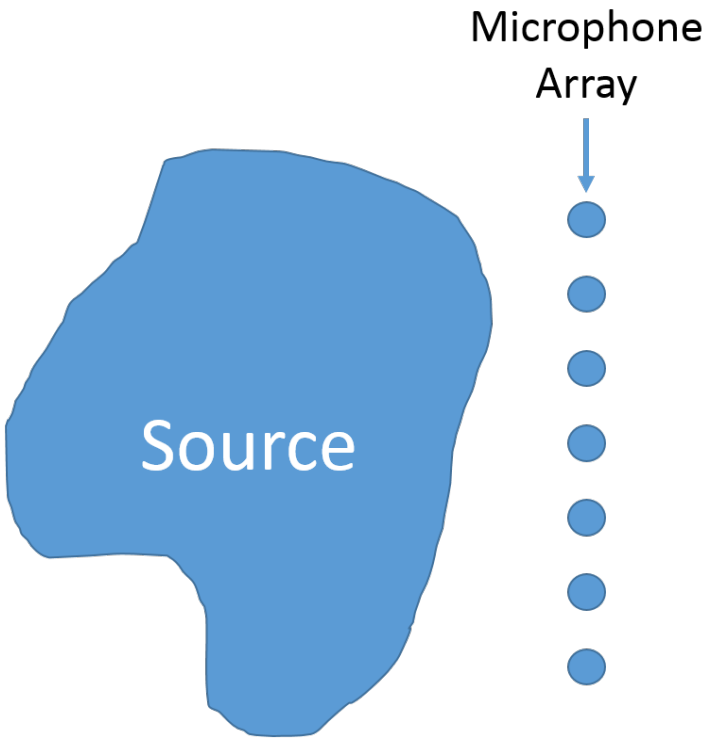

Figure 1.1. Two-dimensional sketch of a microphone array in the near-field of an acoustics source.

The objective of the work described in this dissertation is to study the characteristic of different sparse NAH algorithms that use a relative small number of microphone

measurements. To achieve the objective of the present work, different NAH methods were investigated. Based on the characteristics of different NAH methods, the monopole-based Equivalent Source Method (ESM) was chosen as the NAH method in this project because of the clear relation between the mathematical expressions and the physical meaning. Another difficulty is in the process of estimating the parameters, i.e., the source strength of each monopole in the model, in order to cover the whole sound source region; usually the number of measurements is smaller than the number of monopoles, thus the problem is under-determined and usually ill-posed, so certain regularization processes are needed to solve this inverse problem. However, traditional regularization methods like Tikhonov regularization were proven not suitable for solving an under-determine system. In the present work, three sparse ESM algorithms were studied to solve the inverse problem: i.e., WBH, l_1-norm minimization and a hybrid of these two algorithms. All the algorithms are based on the assumption that the solution for the inverse problem is sparse, which means the sound sources are concentrated, and both algorithms try to find the best solution by balancing the solution accuracy and sparsity. WBH solves the inverse problem with a steepest descent method embedded within an iterative process to eliminate monopoles with small source strength thus controlling solution sparsity. The second studied algorithm is l_1-norm minimization. In that algorithm, the objective function, which consists of the sum of the first norm of all the monopole source strengths and the second norm residue between the measurement and reconstruction at microphone positions is minimized. In this function, the first norm of source strength controls the solution sparsity and the second norm residue guarantees the solution accuracy. Finally, based on the characteristic of these two algorithms, a hybrid process of these two methods is proposed to further improve the reconstruction result.

1.3 The Structure of the Thesis

The thesis is organized in seven chapters to explain the choice of NAH method, different sparse ESM algorithms and the experimental results.

In Chapter 2, different NAH methods will be presented, the theory behind each method will be introduced, and the limitation of each method will be commented upon. Then an important step in solving the NAH inverse problem called regularization will be introduced, and classical regularization methods will be reviewed: i.e, Truncated Singular Value Decomposition (TSVD), Tikhonov regularization, etc. Finally the reason for choosing the ESM as the NAH method in the present work for an under-determined system will be explained.

In Chapter 3, two sparse ESM algorithms will be introduced: Wideband Acoustical Holography and l_1-norm minimization. Both methods balance the solution sparsity and accuracy, and in this section, the details of both methods will be explained: e.g., the different strategies to ensure solution sparsity.

In Chapter 4, different types of sound sources were simulated: i.e., monopoles and baffled plate vibration. To reconstruct the simulated sound source, a distributions of hundreds of monopoles will be used as the equivalent source model. With only dozens of measurements, a strongly under-determined system will be solved by WBH and l_1-norm minimization to reconstruct the sound sources. From the reconstruction result, the ability of WBH and l_1-norm minimization in an under-determined system will be illustrated, and their characteristics will be commented upon.

In Chapter 5, based on the study of WBH and l_1-norm minimization, a combination of these two methods is proposed. Based on the simulation result in chapter 4, it was found that WBH method cannot separate closely positioned sound sources, and l_1-norm minimization could cause a ghost source problem if the objective function was not formulated correctly. A hybrid method was proposed to mitigate the weakness of both methods, and the reconstruction results of WBH, l_1-norm minimization and the hybrid method will be compared in this chapter.

In Chapter 6, sound field reconstruction results with different types of real sound source will be presented. In these experiments, there is simple sound source like loudspeaker, and complex sound sources like a diesel engine. In these experiments the measurements were conducted with dozens of microphones, and there are hundreds of parameters that need to be estimated. The sound field reconstruction results of these experiments will be presented. The ability of WBH, l_1-norm minimization and the hybrid method in practice will be discussed.

In Chapter 7, the work presented in this document is summarized, then motivations and preliminary ideas for future works will be mentioned.

2. REVIEW OF NEAR-FIELD ACOUSTICAL HOLOGRAPHY METHODS

2.1 Introduction

In the previous chapter, it has been illustrated that the NAH is a powerful sound field reconstruction tool, and the motivation of the present work is to reduce the number of microphone measurements required in the NAH process. In this chapter, five NAH methods will be reviewed: the Fourier-based method, Statistically Optimized Near-Field Acoustical Holography (SONAH), the Inverse Boundary Element Method (IBEM), the Equivalent Source Method (ESM) and the Inverse Radiation Mode method (IRM). The theory behind each method will be explained, then the characteristics of each method will be commented upon. Based on the characteristic of different methods, the reason why ESM is finally chosen as the method applied in an under-determined system will be explained. In the present work, all the reconstruction is in free-space, which means the Sommerfeld boundary condition is satisfied in the far-field.

2.2 The Fourier-based Method

The Fourier-based method was based on computing the wavenumber spectrum of the measured data by performing spatial Fourier transforms, then multiplying that by a spectral propagator, so that finally the sound field can be reconstructed through the inverse transform from the wavenumber domain to the spatial domain. Thus, the sound field in the whole space can be reconstructed [5, 6]. In this section the derivation process of this method is shortly reviewed.

Originally the sound field solutions in different coordinates were derived separately, but they can all be derived from the Helmholtz equation [7,8]. The Helmholtz equation at a fixed frequency in a source free region is:

$$\nabla^2 p(\vec{X},\omega) + k^2 p(\vec{X},\omega) = 0, \tag{2.1}$$

where $p(\vec{X},\omega)$ is the sound pressure at the frequency ω and location $\vec{X}$, and $k = \omega/c$ is the wavenumber. Separation of variables is a common way to solve this second order partial differential equation, and with the Sommerfeld boundary condition, the general solution in Cartesian coordinate can be written as:

$$p(x,y,z,\omega) = A(\omega)e^{j(k_x x + k_y y + k_z z)}, \tag{2.2}$$

with $A(\omega)$ is the signal amplitude for different frequencies and where $k^2 = k_x^2 + k_y^2 + k_z^2$, where k_x, k_y, k_z are the wavenumbers in $x-, y-$ and $z-$directions. With this relation, when the wavenumbers in any two directions is known, then the wavenumber at the third direction can be determined, i.e., $k_z = \pm\sqrt{k^2 - k_x^2 - k_y^2}$. Then the total sound field can be written as a summation over k_x and k_y with the substitution of $A(\omega)$ to $P(k_x, k_y)$: i.e.,

$$p(x,y,z) = \sum_{k_x=-\infty}^{\infty} \sum_{k_y=-\infty}^{\infty} P(k_x,k_y)e^{j(k_x x + k_y y + k_z z)}. \tag{2.3}$$

Now transform this discrete summation to a continuous integration, and multiply it by a constant $1/4\pi^2$:

$$p(x,y,z) = \frac{1}{4\pi^2}\int_{-\infty}^{+\infty}\int_{-\infty}^{+\infty} P(k_x,k_y)e^{j(k_x x + k_y y + k_z z)}dk_x dk_y. \tag{2.4}$$

This expression connects the sound pressure in the spatial domain and the wavenumber domain by a two-dimensional inverse Fourier transform:

$$p(x,y,z) = \mathcal{F}_x^{-1}\mathcal{F}_y^{-1}[P(k_x,k_y,z)]. \tag{2.5}$$

And the sound pressure in the wavenumber domain can also be calculated through the forward Fourier transform:

$$\mathcal{F}_x\mathcal{F}_y[p(x,y,z)] = P(k_x,k_y,z) = P(k_x,k_y)e^{jk_z z}. \tag{2.6}$$

From this expression it can be seen that the plane wave amplitude has a phase change from one plane to another in the $z-$direction for k_z real. This general expression allows one to extrapolate the sound pressure from one plane $z = z_h$ to another plane $z = z_s$ once $P(k_x, k_y)$ is known: i.e.,

$$P(k_x, k_y, z_s) = P(k_x, k_y, z_h)e^{jk_z(z_s - z_h)}. \tag{2.7}$$

By combining equations (2.5), (2.6) and (2.7), the Fourier-based method can be organized into a four-step process: first, measure the sound pressure at the hologram plane z_h: $p(x, y, z_h)$. Secondly, perform a two-dimensional Fourier transform to compute wavenumber spectrum: $P(k_x, k_y, z_h)$. Thirdly, multiply the wavenumber spectrum by the inverse propagator $G(k_x, k_y, z_s - z_h) = e^{jk_z(z_s - z_h)}$, to obtain the wavenumber spectrum at plane z_s. Finally, transfer the wavenumber spectrum to the spatial sound pressure $p(x, y, z_s)$ at z_s by performing a two-dimensional inverse Fourier transform.

Similarly, if the measurement is chosen in a cylindrical form, then the solution can be expressed in cylindrical coordinates:

$$P(r, \theta, z) = \sum_{n=-\infty}^{\infty} e^{jn\theta} \frac{1}{2\pi} \int_{-\infty}^{+\infty} A_n(k_z) e^{jk_z z} H_n^{(1)}(k_r r) dk_z, \tag{2.8}$$

where $H_n^{(1)}$ is the Hankel function of the first kind [9], and $k^2 = k_r^2 + k_z^2$. The inverse propagator is defined as $G(\vec{X}_H, \vec{X}) = H_n^{(1)}(k_r r)/H_n^{(1)}(k_r r_H)$, where $\vec{X}_H$ is the location of measurement, and $\vec{X}$ is the location to reconstruct the sound field. Then in spherical coordinates, the final solution is written as a sum of spherical waves:

$$P(r, \theta, \phi) = \sum_{n=-\infty}^{\infty} \sum_{n=-\infty}^{\infty} C_{mn} h_n^{(1)}(kr) Y_n^m(\theta, \phi), \tag{2.9}$$

where $h_n^{(1)}$ is the spherical Hankel function of the first kind and Y_n^m is spherical harmonic. The inverse propagator is defined as $G(\vec{X}_H, \vec{X}) = h_n^{(1)}(k_r r)/h_n^{(1)}(k_r r_H)$.

In this section, the theory of the Fourier-based method was discussed: i.e., perform the two-dimensional inverse Fourier transform with the measurement data under different coordinates, multiply by the inverse propagator in the wavenumber domain, then reconstruct the sound field with the two-dimensional inverse Fourier transform.

From the theory of this method, in order to perform the Fourier transform, the distance between each measurement is usually required to be the same, so a regular microphone array measurement is required. In the Fourier-based method, there are two errors that need to be considered. First is the ill-conditioning due to the evanescent wave components in the wavenumber domain; the application of a low-pass k-space filter is a general method to avoid this ill-conditioning. Secondly, the finite measurement aperture effects need to be considered; this requires the size of the microphone array to be big enough to cover the whole source region to avoid windowing errors, i.e., the sound pressure must fall to a low level by the edge of the aperture. And in order to obtain a high spatial resolution, the spacing between microphones need to be smaller than a half wavelength at the reconstruction frequency. Thus to avoid aliasing, usually a large number of measurements is required in the Fourier-based method, which is costly and the time to process the data is long. Different efforts to improve the measurement condition have been made [10] [11] [12] [13], and in the next section an improved method: Statistically Optimized Near-Field Acoustical Holography (SONAH) will be reviewed.

2.3 Statistically Optimized Near-Field Acoustical Holography (SONAH)

The SONAH method was originally proposed by Steiner and Hald in 2001 [14], and was made into a well-developed NAH method in the following years; the advantage of this method is that it overcomes the measurement limitations and errors caused by the use of spatial Fourier transform in NAH. Instead of using the spatial Discrete Fourier Transform (DFT), the SONAH method describes the sound field in a source-free region Ω occupied by homogeneous fluid by using elementary wave functions, Φ_n, $n = 1...N$, which satisfy the homogeneous wave equation in Ω. These elementary wave functions can be plane, cylindrical, or spherical waves [15]. A specific sound field can be described by these elementary wave functions with different weighting functions [16]. The idea of SONAH is to express the sound field by these elementary

wave functions and then to describe the sound field by the measurements, then these functions can be used to reconstruct the sound field at other positions: i.e., on the source surface [17].

With different elementary functions, the measured sound pressure at $\vec{r}_i$ can be expressed as:

$$p(\vec{r}_i) = \sum_{n=1}^{N} a_n \psi_n(\vec{r}_i), \qquad i = 1, ..., I, \tag{2.10}$$

where a_n is the complex expansion coefficients. Further, multiple sound pressure measurements at different positions, $\vec{p}$, can be represented in matrix form: i.e.,

$$\vec{p} = \mathbf{B}\vec{a}, \tag{2.11}$$

with $\vec{a}$ is the weighting coefficients for corresponding function, and $\mathbf{B}$ is the wave function matrix at the measurement positions. Then with Elementary Wave Method (EWM), the sound pressure can be predicted at position $\vec{r}$ in space Ω by using the same $\vec{a}$: i.e.,

$$p(\vec{r}) = \sum_{n=1}^{N} a_n \psi_n(\vec{r}) = \vec{a}^{\mathrm{T}} \vec{\alpha}(\vec{r}). \tag{2.12}$$

There are two possible issues with the EWM: first, the coefficients a_n are estimated at the measurement positions $\vec{r}_i$, and these coefficients may not be able to well represent the sound field at $\vec{r}$. Secondly, it would be ideal if i could go to infinity to include all elementary functions to accurately represent the sound field; however, this is impossible in the numerical calculation, so a truncation error needs to be considered. In order to overcome these errors, in the SONAH method, the sound pressure at $\vec{r}$ is calculated as a linear combination of the measured sound pressures $\vec{p}$:

$$p(\vec{r}) = \vec{p}^{\mathrm{T}} \vec{c}(\vec{r}), \tag{2.13}$$

where the vector $\vec{c}(\vec{r})$ is the complex estimation weights which need to be determined in the SONAH method. With the use of equations (2.12) and (2.13), it is found that $\vec{c}(\vec{r})$ can be determined from the linear equation:

$$\mathbf{B}^{\mathrm{T}} \vec{c}(\vec{r}) = \vec{\alpha}(\vec{r}). \tag{2.14}$$

By using Tikhonov regularization, $\vec{c}(\vec{r})$ can be solved for as:

$$\vec{c}(\vec{r}) = (\mathbf{A}^{\mathrm{H}}\mathbf{A} + \epsilon\mathbf{I})^{-1}\mathbf{A}^{\mathrm{H}}\vec{\alpha}(\vec{r}), \tag{2.15}$$

where the matrix $\mathbf{A}$ is the transpose of $\mathbf{B}$ and ϵ is the Tikhonov regularization parameter, which could be chosen by General Cross Validation (GCV) or the L-curve method. To avoid the wavenumber wrap-round error, it is desired that the number of elementary wave functions should tend to infinity. In this case, the elements in $\vec{\alpha}(\vec{r})$ cannot be calculated explicitly, but the product of $\mathbf{A}^{\mathrm{H}}\mathbf{A}$ and $\mathbf{A}^{\mathrm{H}}\alpha(\mathbf{r})$ have a finite size, so the elements in these products can be expressed as:

$$[\mathbf{A}^{\mathrm{H}}\mathbf{A}]_{ii'} = \sum_{n=1}^{\infty} \psi_n^*(r_i)\psi_n(r_{i'}), \tag{2.16}$$

and

$$[\mathbf{A}^{\mathrm{H}}\alpha]_i = \sum_{n=1}^{\infty} \psi_n^*(r_i)\psi_n(r), \tag{2.17}$$

where ψ_n denote wave functions in $\mathbf{A}$, $*$ is the complex conjugate, $r_i = (x_i, y_i, z_i)$ and $r_{i'} = (x_{i'}, y_{i'}, z_{i'})$ are microphone positions, and $r = (x, y, z)$ is a reconstruction point. The equations (2.16) and (2.17) can be calculated with numerical truncation errors since the wave functions are known. If the wave function is chosen as plane wave, then these two equations can be transformed into the integration of two plane waves in the $x-$ and $y-$direction. Then, transfer the Cartesian coordinates to polar coordinates and the two-dimensional integral can be reduced to a one-dimensional integral, and the polar angle integration can be worked out analytically. This process will help reduce the numerical truncation errors. Then with equation (2.13), the sound field reconstruction result is obtained at $\vec{r}$. And then, with Euler's equation, the particle velocity can be estimated:

$$\vec{u}_z(\vec{r}) = \frac{-1}{j\omega\rho_0}\frac{\partial p(\vec{r})}{\partial z}, \tag{2.18}$$

where z is the direction of vibration.

In comparison with the Fourier-based method, instead of performing a large scale two-dimensional inverse Fourier transform, the SONAH method is mathematically

more straightforward and computationally more efficient. From the measurement point-of-view, the spacing between two sample points does not have to be same, which gives more flexibility on the measurement condition: i.e., an irregular microphone array could be used with this method. But a large number of measurements is still desired to avoid an under-determined system: i.e., where the number of measurements is less than the number of reconstruction points. Finally, as discussed in this section, regularization is necessary to avoid an ill-posed problem. In Hald's original paper, the planar SONAH method was developed, then cylindrical SONAH was also developed by Cho, Bolton and Hald [15].

2.4 The Inverse Boundary Element Method (IBEM)

Acoustical holography performed with the IBEM is an integral equation-based method [18]. With the integral equation, the acoustic field on a closed integrable surface can be related to any point exterior or interior to this surface. In the present work only the exterior problem will be considered. This means that the interior contains all the sources, and the exterior region is a source-free and homogeneous medium. Figure (2.1) defines the interior region Ω_{in} and exterior region Ω_{ex}.

There are two types of IBEM: direct IBEM and indirect IBEM. The difference is these two methods use different integration functions. The direct IBEM uses the Helmholtz integral equation [19]:

$$c(\vec{r})p(\vec{r}) = \oint_S (p(\vec{r}_s)\frac{\partial G(\vec{r},\vec{r}_s)}{\partial \mathbf{n}(\vec{r}_s)} + j\omega\rho_0 v_n(\vec{r}_s)G(\vec{r},\vec{r}_s))dS, \tag{2.19}$$

where v_n is the particle velocity in the normal direction on the surface, $\vec{r}_s$ is a point on the boundary S, $c(\vec{r})$ is the solid angle with $c(\vec{r}) = 1$ if $\vec{r}$ is in the exterior region and $c(\vec{r}) = \frac{1}{2}$ if $\vec{r}$ is on a smooth surface. For non-smooth surfaces we have [20]:

$$c(\vec{r}) = 1 + \oint_S (\frac{\partial}{\partial \mathbf{n}(\vec{r}_s)}(\frac{1}{4\pi|\vec{r}-\vec{r}_s|}))dS(\vec{r}_s). \tag{2.20}$$

The free space Green's function, G is defined as:

$$G(\vec{r},\vec{r}_s) = \frac{e^{-jk|\vec{r}-\vec{r}_s|}}{4\pi|\vec{r}-\vec{r}_s|}. \tag{2.21}$$

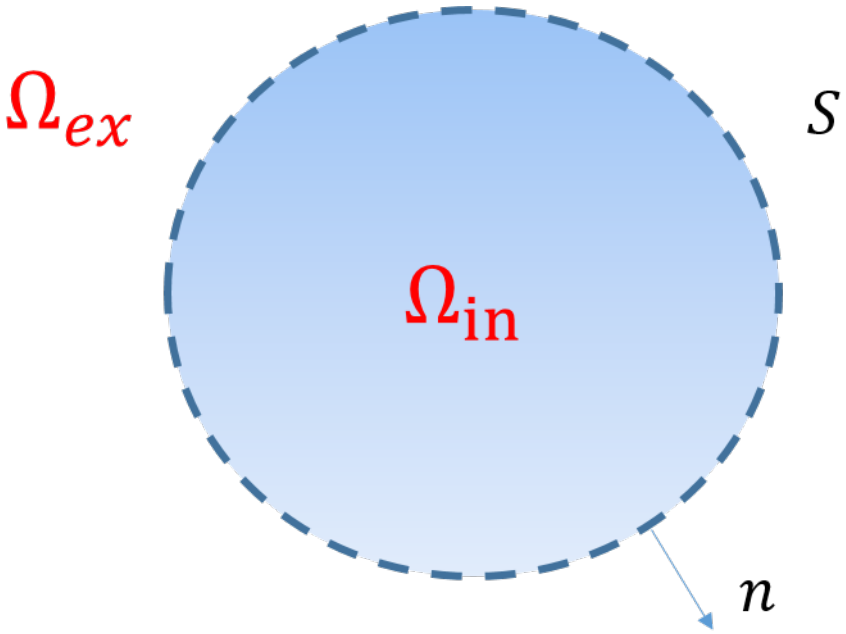

Figure 2.1. IBEM exterior problem. All sources are in the volume Ω_{in} bounded by the surface S, the exterior region Ω_{ex} is a homogeneous and source-free medium. The normal vector $\mathbf{n}$ points from the interior region to exterior region.

The sound field at the microphone locations can be interpolated by shape functions on nodes of the elements, so the integral equation (2.19) can be discretized along the boundary and integrated numerically. The pressure at the microphone location can be written as:

$$\vec{p} = \mathbf{A}_m \vec{p}_s + \mathbf{B}_m \vec{v}_s, \tag{2.22}$$

where the subscript m denotes the measurement locations. The solid angles $c(\vec{r})$ are unity, since the microphone locations are exterior to the source, that is why they disappear in the equation (2.22).

The sound pressure and velocity at a field point can be expressed by the linear relation at the nodes:

$$\mathbf{c}\vec{p}_s = \mathbf{A}_s \vec{p}_s + \mathbf{B}_s \vec{v}_s, \tag{2.23}$$

where $\mathbf{c}$ is a diagonal matrix with solid angles at nodes positions. Isolating $\vec{p}_s$ in equation (2.23), and combining with equation (2.22) yields:

$$\vec{p} = \mathbf{H}\vec{v}_s, \tag{2.24}$$

where $\mathbf{H} = \mathbf{A}_f(\mathbf{C} - \mathbf{A}_S)^{-1}\mathbf{B}_s + \mathbf{B}_f$. This equation is the forward process of BEM, in which the sound pressure is described as the product of the transfer matrix $\mathbf{H}$ and the normal velocity at the nodes. In the IBEM, the pressure is measured at microphone locations and the normal velocity is unknown, so this is also an inverse process which requires regularization.

The other type of IBEM is the indirect IBEM. The indirect formulations uses layer potentials to describe the sound pressure. The simplest version of the indirect IBEM formulation is a single layer integral representation which can be seen as a monopole distribution on the surface S [21, 22], while another version of the indirect IBEM formulation is a double layer representation which can be seen as dipoles distribution [23]. There is also a mixed layer formulation version which is based on the combination of single and double layer formulations. In the present work only the single layer formulation will be discussed as an example. The single layer formulation can express the sound field in the exterior region Ω_{ex} as:

$$p(\vec{r}) = \int_S a(\vec{r}_s)G(\vec{r}, \vec{r}_s)dS(\vec{r}_S), \tag{2.25}$$

where $a(\vec{r}_s)$ represents the source strengths for each monopole, and G is the Green's function for the monopole. Equation (2.25) can be discretized in the same way as the direct method, by using shape functions to solve the numerical integration, and the pressure at the nodes can be described by a product between the transfer function and the source strengths. Finally both direct and indirect formulations will encounter singularities at critical frequencies which causes mathematical problems. So a certain regularization process is also needed for IBEM to deal with the ill-posed problem.

The IBEM does not require a certain measurement shape at the boundary, thus it gives flexibility on the measurement. Since IBEM is based on Boundary Element

Method (BEM) so it also requires large number of measurement to obtain an accurate mesh to match the sound source geometry [24] .

2.5 Equivalent Source Method (ESM)

The equivalent source method (ESM) here refers to a parametric acoustical holography procedure which is based on the idea that a number of equivalent sources with appropriate source strengths are located in a certain region that generate the same sound field as the physical source. A number of ESMs have been developed and have shown promising results. The equivalent source models used in this type of procedure can generally be classified into two categories: one in which a large number of lower order (i.e., monopole) sources are distributed at fixed locations [25] [26] [27] and one in which a single higher order (i.e., multipole) source is located at a certain location determined by an optimization procedure based on the measurement of the sound field [28]. In this section, different models will be reviewed and compared.

The first model comprises a mesh of monopole point sources fixed at certain locations in a plane which is referred as the equivalent source plane. Then the equivalent source plane is placed behind the reconstruction plane, on which the sound field will be reconstructed. The third plane is called the measurement plane: this plane is where the measurements are taken. The position of these three planes is shown in Figure (2.2).

The expression for the sound pressure at position $\vec{X}$ generated by a monopole with unit source strength located at $\vec{X}_i$ at frequency ω is:

$$P_0(\vec{X}|\vec{X}_i,\omega) = \frac{e^{-jk||\vec{X}-\vec{X}_i||}}{4\pi||\vec{X}-\vec{X}_i||}. \tag{2.26}$$

With equation (2.26), the sound pressure p_m at measurement position $\vec{X}_m$ can be written as a linear combination of all monopoles with different source strength:

$$p_m = \sum_{i=1}^{I} A_{mi} q_i, \tag{2.27}$$

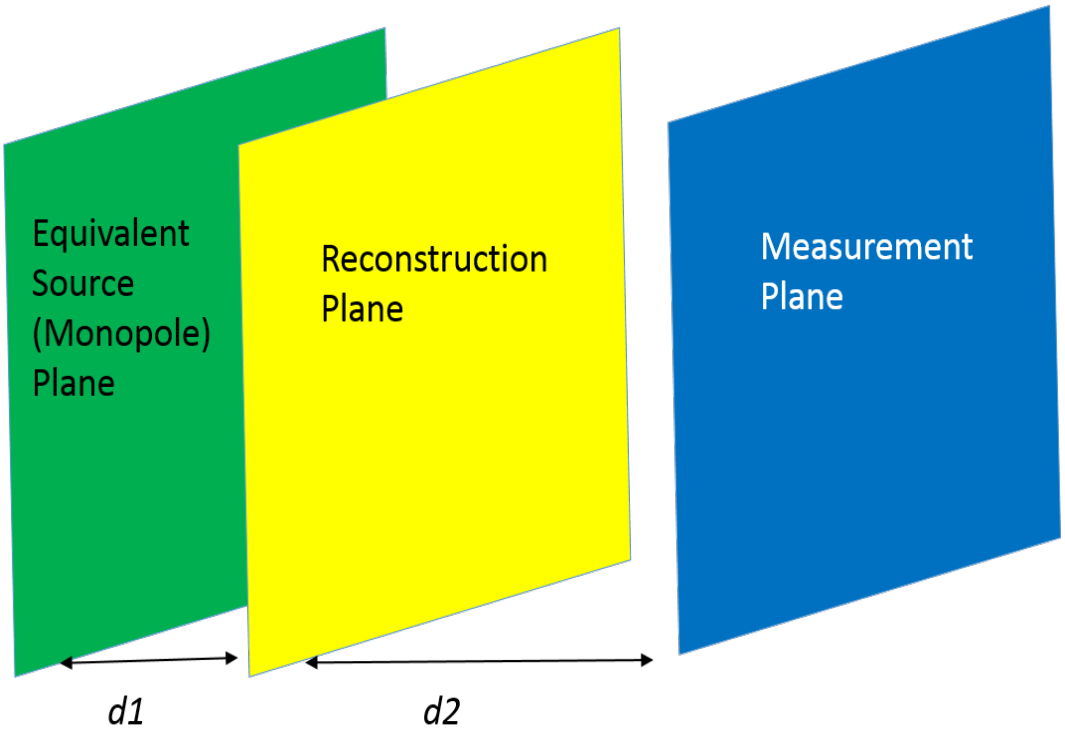

Figure 2.2. Sketch of the relative positions of equivalent source plane, reconstruction plane and measurement plane. $d1$ is the distance between equivalent source plane, reconstruction plane and $d2$ is the distance between reconstruction plane and measurement plane.

where i is the index of monopoles, q_i are the complex amplitudes for corresponding monopoles, and $A_{mi} = \exp(-jk||\vec{X}_m - \vec{X}_0||)/4\pi||\vec{X}_m - \vec{X}_0||$. Then equation (2.27) can be written in matrix-vector form as:

$$\vec{p} = \mathbf{A}\vec{q}, \tag{2.28}$$

where $\mathbf{A}$ is an $M \times I$ matrix with members A_{mi} and $\vec{q}$ is the source strength vector containing all the $q_i's$. Since the distance between the monopoles and the microphones are constants, and since the monopole locations are fixed and the measurement positions are known, so the only parameters that need to estimated in equation (2.28) is the source strength vector $\vec{q}$, which is a vector of complex numbers containing the

source strength and phase information. Once $\vec{q}$ is decided, the sound field in space can be predicted.

The general process to estimate the $\vec{q}$ is to minimize the second norm between microphone measurement and reconstruction i.e.,: $\min||\vec{p} - \mathbf{A}\vec{q}||^2$. The solution of this minimization is similar to equation (2.15), and regularization still needed in order to avoid ill-posed problem. In this model, a large number of monopole will be used in order to cover the whole sound source region. So usually the number of monopoles will be larger than the number of microphones, which increases the difficulty to solve the minimization problem.

The second model consists of only one series of non-collocated, higher-order multipoles at unfixed locations [29,30]. The model typically comprises monopoles, dipoles, quadrupoles and octupoles. Then the equivalent source locations are determined by a non-linear optimization process. This unfixed, non-collocated model, compared with a model with a fixed, single source location, allows greater flexibility in model structure, thus, this model may be able to approximate a sound field using a smaller number of sources.

To construct the model, the sound field expression of each individual source should be derived in the first place. The terminology used in the present work to describe the multipole sequence is as follows: the monopole is referred to as a source of order zero, the dipole as a first order source, etc. The expression of a monopole with unit source strength is defined by equation (2.26). Based on this definition, a source of order n ($n > 0$) can be constructed as a vector sum of two closely-placed $(n-1)$st order sources with the same strength but opposite sign, and aligned in the direction $\vec{u}_n$, where $||\vec{u}_n|| = 1$. So the sound field of an nth order source can be written as:

$$P_{S_n}(\vec{X}|\vec{X}_i,\omega) = d_n \quad _{\vec{u_n}} P_{S_{n-1}}(\vec{X}|\vec{X}_i,\omega) = S_{n-1}d_n \quad (P_{n-1}) \cdot \vec{u}_n, \tag{2.29}$$

where d_n (a small number) is the distance between the two lower order sources. Also, P_{n-1} denotes the sound field of the $(n-1)$st order source with unit strength, and is the del operator. It is also defined here that the strength of the nth order source

is $S_n = dS_{n-1}$. Then the explicit expression for a general nth order source can be written in tensor form as:

$$\mathbf{P}_{\mathbf{S}_n} = \mathbf{S_n}\mathbf{P_n} = \mathbf{S_n}\mathbf{R_n}(\mathbf{P}_0) \cdot \vec{u}_1 \cdot \vec{u}_2 ... \cdot \vec{u}_n, \mathbf{R_n} = \quad ^{\bigotimes \mathbf{n}}, \tag{2.30}$$

where the strength $\mathbf{S}_n = \mathbf{S}_0 \cdot \mathbf{d}_1 \cdot \mathbf{d}_2 ... \mathbf{d}_n$, $\bigotimes$ denotes the tensor outer product, $^{\bigotimes \mathbf{n}}$ indicates performing the outer product on the del operator n times, and $(\cdot)$ denotes the tensor inner product. It can be seen that the tensor, $\mathbf{R}_n$, has a rank of n and has 3^n components in total.

Here it is assumed that measurements of the sound field are obtained at different locations, ξ_1, ξ_2,...ξ_W, and that the equivalent sources consist of M_0 monopoles, M_1 dipoles, etc., up to M_N sources of order N. By arranging the equivalent sources into a vector with a global index, instead of two indices, representing the number of sources for each order, the relationship between the measured sound pressures and the equivalent sources can be written as:

$$\begin{bmatrix} \hat{P}_1(\vec{\xi}_1, \omega) \\ \hat{P}_2(\vec{\xi}_2, \omega) \\ ... \\ \hat{P}_M(\vec{\xi}_M, \omega) \end{bmatrix} = \begin{bmatrix} g_1(\vec{\xi}_1|\vec{X}_1, \omega) & g_2(\vec{\xi}_1|\vec{X}_2, \omega) & ... & g_W(\vec{\xi}_1|\vec{X}_W, \omega) \\ g_1(\vec{\xi}_2|\vec{X}_1, \omega) & g_2(\vec{\xi}_2|\vec{X}_2, \omega) & ... & g_W(\vec{\xi}_2|\vec{X}_W, \omega) \\ ... & ... & ... & ... \\ g_1(\vec{\xi}_M|\vec{X}_1, \omega) & g_2(\vec{\xi}_M|\vec{X}_2, \omega) & ... & g_W(\vec{\xi}_M|\vec{X}_W, \omega) \end{bmatrix} \begin{bmatrix} Q_1(\omega) \\ Q_2(\omega) \\ ... \\ Q_W(\omega) \end{bmatrix} \tag{2.31}$$

where $\hat{P}_i$ is the measured sound field at the ith location, g_j denotes the unit strength sound field of the jth source in terms of the global index, and Q_j is the strength of the jth source. In the above equation, the measurement locations $\vec{\xi}_i$ are known from the design of the measurement, and the source locations $\vec{X}_j$ and the corresponding strengths $\vec{Q}_j$ are the parameters to be estimated.

Equation (2.30) is in the form of $\vec{\hat{P}} = \mathbf{A}(\vec{X})\vec{Q}$; thus the parameters, $\vec{X}$ and $\vec{Q}$, can be determined by solving the following optimization problem: $\min||\vec{\hat{P}} - \mathbf{A}(\vec{X})\vec{Q}||^2$. The latter is a non-linear optimization problem, since the matrix $\mathbf{A}$ is not constant but depends on $\vec{X}$. However, if the source locations are known, the estimation of the source strength is a linear least-squares problem. Based on this observation, the

parameter estimation process is based on a non-linear optimization algorithm that updates the source locations only, and the source strengths are subsequently determined by a linear process with each update. As a part of the non-linear optimization that updates the source locations, the Trust Region Reflective Method is used chosen due to its quadratic convergence rate and the ability to handle relatively large number of parameters [31]. This method will help to reach a balance between flexibility of the model and the capability and speed of the optimization algorithm.

The ESM is a relatively new NAH method, in which instead of using complex governing equation to describe the sound field like other methods, the ESM uses a mathematical model to represent the sound source and adding the contribution of each equivalent source to construct the sound field, so mathematically it is more straight-forward. The other advantage of ESM is it does not have special requirement on the measurement array, or measurement position, which offers more flexibility on the measurements.

2.6 Inverse Radiation Mode Method (IRM)

The Inverse Radiation Mode method (IRM) is a recently developed NAH method. In this method, the sound field is represented by different acoustic radiation modes which only depend on the shape of the sound source [32, 33]. The advantage of this method is that the radiation modes are a set of velocity distributions which radiate sound power independently, so this method can estimate the contribution to the total radiated sound power of different radiation modes at particular locations. Thus this method can give a direction on the NVH design process to decrease sound power radiation.

Assume the elements on a planar vibrating surface have the same size and has their own normal velocity and sound pressure, $\hat{v}_{eN}$, and $\hat{p}_{eN}$, respectively. Then each element has the radiating sound power:

$$P_{eN} = 0.5 A_{eN} \mathrm{Re}(\hat{v}^*_{eN} \hat{p}_{eN}), \tag{2.32}$$

where A_{eN} is the area of the Nth element. Summing all the elements on the vibrating surface, the total radiating sound power can be expressed as:

$$P = \frac{S}{2M}\mathrm{Re}(\vec{v}_e^{\mathrm{H}}\vec{p}_e) \tag{2.33}$$

where S is the total area and M is the total number of elements. The discretized Rayleigh Integral then gives the result:

$$\hat{p}_{ei} = \frac{j\rho_0\omega A_e e^{-jkr_{ij}}}{2\pi r_{ij}}\hat{v}_{ej}, \tag{2.34}$$

where r_{ij} is the distance between the ith and jth elements. Then the relation between sound pressure and velocity can be express in vector form:

$$\vec{p}_e = \mathbf{Z}\vec{v}_e, \tag{2.35}$$

where $\mathbf{Z}$ is composed of $Z_{ij} = \frac{j\rho_0\omega A_e e^{-jkr_{ij}}}{2\pi r_{ij}}$. Then substitution of equation (2.35) into equation (2.33) yields:

$$P = \frac{S}{2M}\mathrm{Re}(\vec{v}_e^{\mathrm{H}}\mathbf{Z}\vec{v}_e) = \vec{v}_e^{\mathrm{H}}(\frac{S}{2M}\mathrm{Re}(\mathbf{Z}))\vec{v}_e, \tag{2.36}$$

From equation (2.36) one can define the radiation resistance matrix:

$$\mathbf{R} = \frac{S}{2M}Re(\mathbf{Z}). \tag{2.37}$$

Next, perform a singular value decomposition on the radiation resistance matrix, which gives $\mathbf{R} = \mathbf{Q}^{\mathrm{T}}\lambda\mathbf{Q}$, where λ is a diagonal matrix and $\mathbf{Q}$ is a matrix consisting of orthogonal vectors. Substituting this expression into equation (2.36) gives:

$$\mathbf{P} = \vec{v}_e^{\mathrm{H}}\mathbf{Q}^{\mathrm{T}}\lambda\mathbf{Q}\vec{v}_e, \tag{2.38}$$

It is noted here that the acoustic radiation modes are row vectors of $\mathbf{Q}$, and each mode is an independent contributor to the overall radiating sound power. Then the measured pressure at point i outside the sound source can be described as:

$$p_{m_i} = c_j\hat{p}_{ij}, \tag{2.39}$$

where p_{m_i} denotes the measured sound pressure at point i, $\hat{p}_{ij}$ is the pressure at point i caused by the jth radiation mode, which is called the modal pressure, and c_j is the source strength function which needs to be estimated.

With this method not only the noise source location can be identified, but also the contribution of different radiation modes can be calculated at the noise source location, so this method can provide guidance for NVH design. The IRM method is still a young method for NAH, and more study is needed to develop the potential of this method.

2.7 Regularization Process

In the previous sections, it was mentioned that to solve the inverse problem, in the NAH inverse process, the major difficulty is the ill-posed nature of the system. This is because the propagation matrix normally includes both propagating wave components and wave components that decay exponentially in the propagation direction: i.e., evanescent waves. Due to the decay of the evanescent wave components, their contribution to the sound field will decrease when the measurement plane moves away from the source [19]. This means that the contribution of these evanescent wave components could be small, but they have important influence on the reconstruction surface, so the noise components at the evanescent wavenumbers will be treated as evanescent waves and will be amplified in the reconstruction surface. At these evanescent wavenumbers, small perturbations in the measurement may cause a huge influence on the solution, hence this system is said to be ill-posed. The mathematical description of the ill-posed problem will be explained with Singular Value Decomposition (SVD) in this section. To overcome this problem, different regularization techniques have been developed to limit the influence of measurement noise at evanescent wavenumbers. The idea of regularization is to balance the norm of solution and the norm of residue between the reconstructed and measured sound pressure at the microphone positions to limit the influence of measurement noise.

The forward problem behind NAH is the sound propagating from the sound source. This forward problem can be generalized as:

$$\vec{p} = \mathbf{A}\vec{q}, \tag{2.40}$$

where $\vec{p}$ is the measured sound pressure at the microphones, $\mathbf{A}$ is the transfer matrix to describe the sound propagation from the sound source to the microphone locations, $\vec{q}$ is the weighting coefficient for each transfer function in matrix A. In NAH, the measured sound pressure $\vec{p}$ is known, the transfer matrix A is decided by the NAH method, the only unknown in this equation is the weighting coefficient $\vec{q}$, so the NAH problem can be solved by inverting of equation (2.40): i.e.,

$$\vec{q} = \mathbf{A}^{-1}\vec{p}. \tag{2.41}$$

The SVD of the matrix A is [34]:

$$\mathbf{A} = \mathbf{U}\Sigma\mathbf{V}^{\mathrm{H}}, \tag{2.42}$$

where the columns of $\mathbf{U}$ are the orthonormal left singular vectors, Σ is a diagonal matrix with the singular values in descending order, and the columns of $\mathbf{V}$ are the orthonormal right singular vectors. After inserting equation (2.42) into equation (2.41), the inverse problem can be expressed as:

$$\vec{q} = \mathbf{V}\Sigma^{-1}\mathbf{U}^{\mathrm{H}}\vec{p} = \sum_{i=1}^{n} \frac{\vec{u}_i^{\mathrm{H}}\vec{p}}{\sigma_i}\vec{v}_i, \tag{2.43}$$

where $\vec{u}_i$ are the left singular vectors, $\vec{v}_i$ are the right singular vectors and σ_i are the singular values. The singular values will decrease as the index i increases, so the singular values stand for the evanescent wave components with high index, since the contribution of the evanescent wave components is small. In the experiment, the measured data from the sound source is influenced by noise, that is, $\vec{p} = \tilde{p} + e$, where $\tilde{p}$ is the true sound pressure generated by the sound source, e is the noise, so equation (2.43) can be written as:

$$\vec{q} = \sum_{i=1}^{n} \frac{\vec{u}_i^{\mathrm{H}}\tilde{p}}{\sigma_i}\vec{v}_i + \sum_{i=1}^{n} \frac{\vec{u}_i^{\mathrm{H}}e}{\sigma_i}\vec{v}_i. \tag{2.44}$$

In equation (2.44) $\vec{u}_i^{\mathrm{H}}\tilde{p}$ expresses the basis vector of the measured sound field generated by the sound source; this term will decrease as the index i increases since the singular values with high index stand for the evanescent waves. At a certain singular value with high index, the noise term in equation (2.45) can be dominant in the solution. This will cause a large error in the sound field reconstruction, so to prevent this unwanted noise amplification, regularization is needed.

Since the small singular values cause the ill-posed problem, so the most intuitive idea is to drop these small singular values. This can be done by introducing a low-pass filter to keep the singular values with low index and eliminate the singular values with high index. After passing this filter, the equation (2.43) becomes:

$$\vec{q}_{reg} = \sum_{i=1}^{n} f_i \frac{\vec{u}_i^{\mathrm{H}}\vec{p}}{\sigma_i}\vec{v}_i, \tag{2.45}$$

where f_i stand for the low-pass filter. A simple way to define this low-pass filter is to introduce a truncation parameter I: i.e., let $f_i = 1$ for $i <= I$ and $f_i = 0$ for $i > I$, so the truncation parameter I will determine how much the solution is regularized. This regularization technique is referred to as Truncated Singular Value Decomposition (TSVD) [35]. The truncation parameter I is important for TSVD; if I is chosen too low, the propagating wave component may be eliminated from the final sound field and the reconstructed sound field will not be accurate. If I is chosen too high, then the amplified noise will distort the reconstruction sound field. The optimal choice for the truncation parameter in practice is unknown, but there are different algorithms for the selection of the truncation parameter. Another well-known method is Tikhonov regularization [36]. The idea behind this regularization method is that for the ill-posed problem if too many high index singular values are kept in the inverse problem the norm of the final solution will be large because of the amplification of noise, while if too many singular values are eliminated from the ill-posed problem the residue norm will be large. So finding a balance between these two norms will offer a well regularized solution: i.e.,

$$\min \quad ||\mathbf{A}\vec{q}_\lambda||_2^2 \quad + \quad \lambda^2||\vec{q}_\lambda||_2^2, \tag{2.46}$$

where λ is the regularization parameter. The effect is to minimize the residual second norm subject to a penalty on the solution second norm. It can be proven that the solution of equation (2.46) can be written as:

$$\vec{q}_\lambda = (\mathbf{A}^{\mathrm{H}}\mathbf{A} + \lambda^2\mathbf{I})^{-1}\mathbf{A}^{\mathrm{H}}\vec{p}, \tag{2.47}$$

where I is the identity matrix in this equation. With the SVD of matrix $\mathbf{A}$ the solution can be written as:

$$\vec{q}_\lambda = \sum_{i=1}^{n} \frac{\sigma_i}{\sigma_i^2 + \lambda^2} \frac{\vec{u}_i^{\mathrm{H}}\vec{p}}{\sigma_i}\vec{v}_i, \tag{2.48}$$

where the $\sigma_i/(\sigma_i^2 + \lambda^2)$ are the filter factors. As the regularization parameter λ increases, only the components with lower index will be included in the inverse problem. Notice here that the truncation parameter in TSVD is a step function, while the Tikhonov regularization parameter caused a smoother transition from small index to the higher ones. However the optimal regularization parameter for Tikhonov method is also unknown.

Different parameter choice techniques have been developed based on different criteria. It is noted here that the performance of different techniques depends on the specific problem: i.e., there does not exist a universal technique for all problems. In this paragraph four parameter choosing techniques are introduced: Generalized Cross-Validation (GCV) [37], L-curve criterion [38], Normalized Cumulative Periodogram (NCP) [39], and Morozov's Discrepancy Principle (MDP) [40]. Consider first the GCV, where the idea of GCV is to remove one of the measurements from the measurement vector, then predict the missing data with the remaining measurements. The optimal regularization parameter is obtained at the point when the average error between the measurement and the reconstruction is minimized. The second method is the L-curve criterion, and this method is based on plotting the relation between the norms of residual and solution at different regularization parameter values: i.e., norms of the residual as a function of norms of solution. Plotting out the two norms against each other in a log-log scale, it is found that the figure usually is a L-shape

curve. The optimal choice of regularization parameter is the one corresponding to the corner point on the curve, which is found at the point with maximum curvature. It is believed that this point gives the best balance between the least square and the least norm solution. Third is NCP, which is a relatively new method. The idea of this method is to find the regularization parameter which makes the residual vector close to white noise. This is done by computing the Fourier transform of the residual, $\tilde{r} = fft(\vec{p} - \mathbf{K}\vec{x}_{reg})$, and the normalized cumulative periodogram is calculated as $\mathbf{c} = \sum_{i=2}^{k} |\tilde{r}_i|^2 / \sum_{i=2}^{M-1} |\tilde{r}_i|^2$. The most white noise is considered to be when $\mathbf{c}$ is a straight line when plotted out against the its indices. Finally the last method is MDP, in this method the optimal regularization parameter is assumed to be at the point where the norm of residual is closest to the ambient noise level.

2.8 Summary and Method Selection

Five methods of NAH were reviewed and commented upon in this chapter: the Fourier-based method, Statistically Optimized Near-Field Acoustical Holography, the Inverse Boundary Element Method, the Equivalent Source Method and the Inverse Radiation Mode method. Then different regularization methods were presented to avoid ill-posed problem during the inverse process. Based on this knowledge, in this section the monopole-based ESM was chosen in the present work to reconstruct the sound field in an under-determined system, i.e., when the number of measurements is less than the number of parameters that need to be determined. The reason for choosing this method is explained as follows.

First, the other methods have their limitations when the number of microphone measurements is relatively small. The Fourier-based method requires a large regular array for sound field measurement, which does not fit the small number measurement requirement of the present work. The SONAH method does not have a strict requirement on the shape or microphone number of array, however, in SONAH method the sound field is composed with a linear combination of elementary functions, so the

solution, i.e., the weighting coefficient for each function, is not necessarily sparse. In fact, the more function components that are included in the model, the more accurate the reconstruction result. So the sparse condition is not satisfied by the SONAH method. The IBEM is an attractive method due to the reconstruction accuracy and does not have the limitation on the sound source geometry. However, due to the large number of mesh grids required in order to capture the precise geometry of the sound source, the number of measurements is also very large, so IBEM is also not preferred for an under-determined system. The IRM method will not be discussed in the present work since this method is still under development.

Besides the disadvantages of other methods, there are advantages for using the ESM method to reconstruct the sound field with an under-determined system. First, the equivalent sources used in the ESM have strongly associated physical meaning: i.e., the monopole describes the volume contraction and expansion, the dipole acts like an oscillating force, the lateral quadrupole can be used to express a rotational torque or vortex, etc. Then the model used in the NAH is closer to the physical sound source, and so the fewer parameters need to be estimated in the inverse process. Secondly, compared with calculating the two-dimensional inverse Fourier transform or numerical integration to reconstruct the sound field, the ESM involve simply summing the contributions of equivalent sources, which is mathematically more straightforward and computationally more efficient. From the measurement point-of-view, the ESM does not have strict limitations on the requirement of the microphone array: i.e., the spacing between the microphone or shape of the array. Finally, the sparsity condition in ESM means using as few monopoles as possible to reconstruct the sound field, which could give a clear indication on sound source location, so sparsity is itself a useful condition when solving an under-determined system, so sparsity is also a desired property for ESM solutions.

3. SPARSE EQUIVALENT SOURCE METHOD FOR NEAR-FIELD ACOUSTICAL HOLOGRAPHY

3.1 Introduction

In the previous chapter, monopole-based ESM method was adopted as the NAH method in the present study due to its advantages in both theoretical computation and measurement process. However, it is still hard to obtain a stable solution from the inversion of an under-determined system for two reasons: first, the ill-posed nature due to the evanescent components in sound field, secondly, since the system is under-determined, the number of equations is smaller than the number of unknowns, so there are a large number of possible solutions to this system, which is why the regularization methods discussed in the previous chapter cannot guarantee a stable solution. For example, ghost sources, that is small source strength terms, are created at locations where there are no sources simply to satisfy the system, which could mislead as to the sound source location. So the desired solution should not only guarantee the model accuracy, but also guarantee the sparsity of the system at the same time, so that the source location is pin-pointed. In this chapter, based on the sparse solution assumption, two algorithms were proposed to solve the inverse problem. The first method considered was Wideband Acoustical Holography (WBH), as developed by Hald, and further studied by different researcher [41–44]. In this method, the under-determined system is solved by the steepest descent method and the model sound sources having small strengths are progressively removed in an iterative process. The second method considered is l_1-norm minimization, as previously considered by several researchers [45–48]. In that approach, the sound source localization problem is formulated as a convex function, which can then be solved, for example, by using the open source program, CVX [49].

3.2 Wideband Acoustical Holography (WBH)

In 2014, Hald developed a procedure named Wideband Acoustical Holography (WBH) [41]; this algorithm was proposed specifically to balance the model accuracy and the sparsity of the system, so that the solution of an under-determined system could be optimized to focus on the major noise source and offer accurate sound source locations. The major process of WBH is to remove the confusing ghost sources associated with the real sources in an iterative process. This process is introduced with a large number of lower order sources distributed at fixed locations as the ESM model.

The inverse process still can be described with equation (2.41), with vector $\vec{q}$ including the source strengths of all the monopoles which need to be estimated, the terms in the transfer matrix $\mathbf{A}$ can be expressed by equation (2.26), and $\vec{p}$ is the vector of measured sound pressure. First define the residual vector $\vec{r}$ as:

$$\vec{r}(\vec{q}) = \vec{p} - \mathbf{A}\vec{q}, \tag{3.1}$$

and the quadratic residual function F to be minimized as:

$$F(\vec{q}) = \frac{1}{2}||\vec{r}(\vec{q})||_2^2. \tag{3.2}$$

Now, define $\vec{q}_k$ to be the solution at the kth iteration step, and then compute the step $\delta\vec{q}_k$ that minimizes the residual function F in the steepest descent direction: i.e.,

$$\Delta\vec{q}_k = s_k \quad F. \tag{3.3}$$

Here, $\quad F$ is the gradient vector:

$$F = -\mathbf{A}^{\mathrm{H}}\vec{r}(\vec{q}_k) = -\mathbf{A}^{\mathrm{H}}(\vec{p} - \mathbf{A}\vec{q}_k), \tag{3.4}$$

and s_k is the step-length in that direction,

$$s_k = \frac{\vec{g}_k^{\mathrm{H}}\vec{r}(\vec{q}_k)}{\vec{g}_k^{\mathrm{H}}\vec{g}_k}, \tag{3.5}$$

where the vector $\vec{g}_k$ is defined as:

$$\vec{g}_k = \mathbf{A} \quad F. \tag{3.6}$$

The next candidate solution vector is then

$$\tilde{\vec{q}}_{k+1} = \vec{q}_k + \alpha \Delta \vec{q}_k, \tag{3.7}$$

where α is a relaxation factor: Hald suggested that the value of α should lie between 0.5 and 1.0 [41], and in the present work, it was chosen to be 1.

Note, however, that the solution derived from equation (3.7) will spread the excitation over all point sources of the source model and will cause ghost source problems as mentioned above. Therefore we need to remove the ghost sources by setting a threshold, T_k, below which the components in $\tilde{\vec{q}}_{k+1}$ will be set to zero. That threshold, T_k, is computed as:

$$T_k = 10^{\frac{-D_k}{20}} |\tilde{\vec{q}}_{k+1,max}|, \tag{3.8}$$

where D_k is a positive number of decibels below the amplitude $\tilde{\vec{q}}_{k+1,max}$ of the largest element in $\tilde{\vec{q}}$. So the elements $q_{k+1,i}$ of the next solution estimate $\vec{q}_{k+1}$ are:

$$\vec{q}_{k+1,i} = \begin{cases} \tilde{\vec{q}}_{k+1,i}, & \text{if } |\tilde{\vec{q}}_{k+1,i}| \geq T_k. \\ 0, & \text{otherwise.} \end{cases} \tag{3.9}$$

The dynamic range D_k is increased during each iteration, so more sources will be added to the model as the iteration process continues: i.e.,

$$D_{k+1} = D_k + \Delta D. \tag{3.10}$$

In Hald s paper [41], the conditions to stop the iteration are given as:

$$D_{k+1} > D_{max} \quad or \quad ||\nabla F||_2 < \varepsilon ||\nabla F_0||_2, \tag{3.11}$$

where D_{max} is an upper limit on D_k and ε is a small number. So the former stop condition represents the sparsity of the system and the latter condition represents the model accuracy, which means that the iteration will stop and give the solution when

either we reach the lowest desired source strength, beyond which, if the iteration continued, a ghost source problem would result, or the accuracy of source model cannot be further improved. In the present work the sparsity stop condition, $D_{k+1} > D_{max}$, was adopted as given, but for the model accuracy condition, it was assumed that the microphone measurement could capture the major sound source region, and so the averaged relative error, e, between the source model prediction and the measured data at each microphone position was applied directly: i.e.,

$$e = \text{avg}\left(\frac{|\vec{p} - \vec{p}_r|}{|\vec{p}|}\right), \tag{3.12}$$

where $\vec{p}$ is the vector of measured pressures at the microphone positions, and $\vec{p}_r$ is the reconstructed sound pressure at the microphone positions. This iterative process is illustrated in Figure (3.1), and the following parameter values were used in the

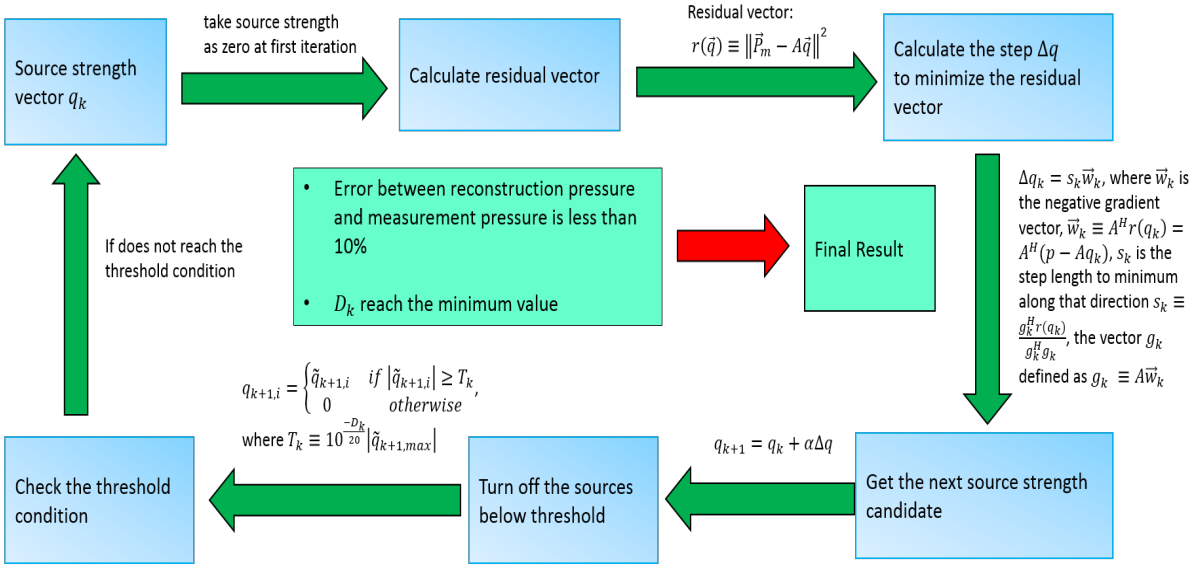

Figure 3.1. Wideband Acoustical Holography (WBH) process.

present work:

$$\vec{q}_0 = \vec{0}; \quad \alpha = 1; \quad D_0 = 0.1\,\text{dB}; \quad \Delta D = 1.0\,\text{dB}; \quad D_{max} = 60\,\text{dB}; \quad e = 0.05. \tag{3.13}$$

Then based on the knowledge of source strength, the sound pressure $\vec{p}_r$ at the reconstruction position $\vec{X}_r$ can be calculated by equation (2.28), further the particle velocity in the normal direction, e.g., z-direction can be calculated as:

$$V_z = \sum_{i=i}^{I} \frac{q_i}{4\pi j \rho_0 \omega} \frac{e^{-jk||\vec{X}_r - \vec{X}_i||}(z_r - z_i)(jk||\vec{X}_r - \vec{X}_i|| + 1)}{||\vec{X}_r - \vec{X}_i||^3}, \tag{3.14}$$

where q_i is the source strength of the ith monopole at $\vec{X}_i$, and z_i and z_r are the coordinates of i^{th} monopole and r^{th} reconstruction point, respectively (here the z-coordinate is considered to be normal to the reconstruction surface). Then the sound intensity in the z-direction, I_z, can be calculated as:

$$I_z = \frac{1}{2}\text{Re}(\text{P}V_z{}^*). \tag{3.15}$$

3.3 The l_1-Norm Minimization

The second proposed sparse NAH algorithm is l_1-norm minimization. In a previous study, it was shown that l_1-norm minimization can encourage solution sparsity [45]. Thus in this section the monopole source strength estimation has been formulated using an objective function consisting of the solution l_1-norm combined with the residual l_2-norm. The minimization of this objective function balances source sparsity and reconstruction accuracy in a systematic way and, at least in ideal circumstances, guarantees an optimal solution. Since both the l_1-norm and l_2-norm are convex functions, so the sum of them is still a convex function, and thus this minimization problem can be solved with an open source Convex Optimization solver CVX [49]. Convex optimization, also known as convex minimization, is a subfield of optimization in which the problem of minimizing convex functions over convex sets is studied [50]. The convexity makes optimization easier than the general case since a local minimum must also be a global minimum, and first-order conditions are sufficient for optimality [51]. Convex optimization has applications in a wide range of disciplines, such as automatic control systems, estimation and signal processing, etc [52, 53]. In this section the necessary definitions for convex optimization will be presented,

then the NAH problem will be modeled as an array of monopoles, and the source strength parameter estimation and regularization problem will be formulated as a convex function.

A function $f : \mathbf{R}^n \rightarrow \mathbf{R}$ is convex if $\mathbf{dom}f$ is a convex set and if for all $x, y \in \mathbf{dom}f$, and θ with $0 \leq \theta \leq 1$, we have:

$$f(\theta x + (1-\theta)y) \leq \theta f(x) + (1-\theta)f(y). \tag{3.16}$$

From the geometry point-of-view, this inequality can be visualized by Figure (3.2). There the line segment between $(x, f(x))$ and $(y, f(y))$ lies above the graph of f. A function f is strictly convex if the strict inequality holds in equation (3.16) whenever $x \neq y$ and $0 < \theta < 1$. A function is convex if and only if it is convex when restricted to any line that intersects its domain $\mathbf{dom}f$, which is a convex set. A convex set is defined as follows: a set C is convex if the line segment between any two points in C lies in C: i.e., if for any $x_1, x_2 \in C$ and any θ with $0 \leq \theta \leq 1$, we have:

$$\theta x_1 + (1-\theta)x_2 \in C. \tag{3.17}$$

A convex optimization problem is one of the form:

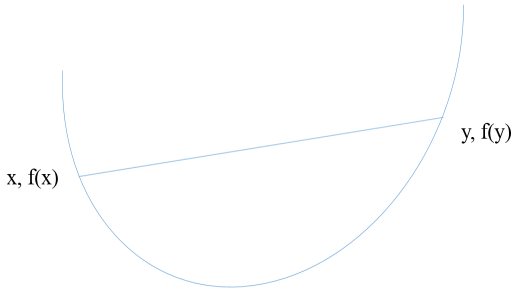

Figure 3.2. Graph of a convex function. The line segment between any two points on the graph lies above the graph.

$$\begin{aligned} \text{minimize} \quad & f_0(x) \\ \text{subject to} \quad & f_i(x) \leq 0, \quad i = 1, \ldots, m \\ & h_i(x) = 0, \quad i = 1, \ldots, m, \end{aligned} \tag{3.18}$$

where $x \in \mathbf{R}^n$ is called the optimization variable and the convex functions $f_0 : \mathbf{R}^n \to \mathbf{R}$ is called the objective function. The inequalities $f_i(x) \leq 0$ are called inequality constraints, and the corresponding convex functions $f_i : \mathbf{R}^n \to \mathbf{R}$ are called inequality constraint functions. The equations $h_i(x) = 0$ are called the equality constraints, and the function $h_i : \mathbf{R}^n \to \mathbf{R}$ are the equality constraint functions, which are affine. If there are no constraints, then the problem is unconstrained.

Different methods to solve optimization problems have been proposed, and those methods are classified into two categories: methods to solve unconstrained minimization and methods to solve equality constrained problem (the inequality constraints can be transformed to equality constrains). These methods will be briefly reviewed in this section.

The descent methods with different descent direction searching and step size choosing strategies are widely used to solve the unconstrained minimization problem. The general descent method can be described as a three step iterative process, with a starting point $x \in \mathbf{dom} f$: first, determine a descent direction Δx, then, secondly, choose a step size $t > 0$ with a line search, i.e., exact line search or backtracking line search, and then finally update the value of x: $x = x + t\Delta x$. This iteration will stop when the criterion is satisfied. Different techniques can be used to choose the descent direction, i.e., a gradient descent method:

$$\Delta x = - \bigtriangledown f(x), \tag{3.19}$$

or a steepest descent method:

$$\Delta x_{sd} = || - \bigtriangledown f(x)||_2 \Delta x_{nsd}, \tag{3.20}$$

where

$$\Delta x_{nsd} = \text{argmin}\{- \bigtriangledown f(x)^T v \mid ||v|| \leq 1\}, \tag{3.21}$$

or Newton's method:

$$\Delta x_{nt} = - \bigtriangledown^2 f(x)^{-1} \bigtriangledown f(x). \tag{3.22}$$

The idea to solve the equality constrained minimization problem is to create a dual problem from the original problem. Then solve the dual problem using an unconstrained minimization method, and then recover the solution of the equality constrained problem from the dual solution. The constrained problem described in equation (3.18) can be transformed to an unconstrained minimization problem with Lagrangian L associated with the constrained problem: i.e.,

$$\text{minimize } L(x, \lambda, \nu) = f_0(x) + \sum_{i=1}^{m} \lambda_i f_i(x) + \sum_{i=1}^{p} \nu_i h_i(x), \tag{3.23}$$

where $\mathbf{dom}L = D \times \mathbf{R}^m \times \mathbf{R}^p$, λ_i is the Lagrange multiplier associated with ith inequality constraint $f(x)_i \leq 0$, ν_i as the Lagrange multiplier associated with the ith equality constraint $h(x)_i = 0$. The vectors λ and ν are called dual variables or Lagrange multiplier vectors associated with the equation (3.18). The idea in the Lagrangian duality is to take the constraints in equation (3.18) into account by augmenting the objective function with a weighted sum of the constraint functions. Then this unconstrained minimization problem can be solved by the unconstrained methods.

With a basic knowledge of how convex optimization solves the minimization problem, now the objective function to balance the model sparsity and accuracy in NAH is introduced. The monopole source strength estimation is formulated as an unconstrained convex optimization problem: i.e.,

$$\text{minimize } ||\vec{q}||_1 + \lambda_w ||\mathbf{A}\vec{q} - \vec{p}||_2, \tag{3.24}$$

where $\vec{q}$ is the source strength vector, $\mathbf{A}$ is the transfer matrix between the monopoles and the microphones, $\vec{p}$ is the measured data from the microphones, and λ_w is the weighting factor specifying the allowed error between reconstruction and measurement. A similar formulation was previously proposed by Chardon et al. [45]. Note also that a similar formulation has recently been considered by Hald.

In equation (3.24), $||\dots||_1$ is the l_1-norm operator, defined as:

$$||\vec{q}||_1 = \sum_{i=1}^{m} |q_i|, \tag{3.25}$$

and $||\dots||_2$ is the l_2-norm operator, defined as:

$$||\vec{q}||_2 = \sqrt{q_1^2 + q_2^2 + \cdots + q_n^2}. \tag{3.26}$$

In equation. (3.24), the first term represents the total source strength reconstructed in the model, and by using the l_1-norm, the model sparsity is ensured. The second term measures the relative error between the reconstruction and measurement, which acts as a penalty term. The l_1-norm is used in the first term since the l_1-norm approximate solution tends to feature more zero and very small residuals compared with the l_2-norm approximate solution, with the result that the l_1-norm solution is sparser than the l_2-norm solution. The reason for using the l_2-norm in the second term follows a similar logic: since a small error at all microphone positions is desired, the l_2-norm will tend to allow relatively fewer large residuals.

A simple example is offered here to illustrate why the l_1-norm solution can result in greater sparsity than the l_2-norm solution in an under-determined system. When it is assumed that there are two monopoles with source strength $\vec{q} = [q_1, q_2]$, and that the sound pressure p is measured by one microphone, then at the microphone location, the measured pressure can be described by the linear equation:

$$p = a_1 q_1 + a_2 q_2, \tag{3.27}$$

where a_1 and a_2 are the transfer functions between the monopoles and the microphones. Figure (3.3) gives a geometric view of the l_1-norm and l_2-norm solutions. From equations (3.25) and (3.26), the geometrical l_1-norm solution forms a square with its edges lying on the axes, in contrast the l_2-norm solution is a circle centered at the origin. The linear equation is a line in the same coordinates. To find the solution, the square or circle expand until they intersect with the line, and the intersection point is then the solution of the system. From Figure (3.3), it is seen that when

using the l_1-norm, the solution is always found on the edges of the square, which corresponds to one of the values q_1 or q_2 being zero. In contrast the solution from the l_2-norm cannot guarantee that the intersection point lies on the axis when the circle touches the line: thus for the same linear system, the l_1-norm solution is generally sparser than that of the l_2-norm.

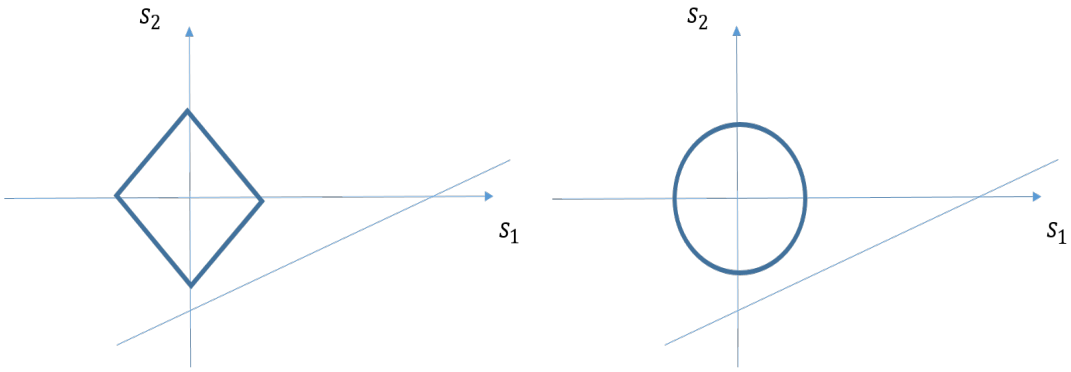

(a) (b)

Figure 3.3. Geometric explanation and comparison between l_1-norm and l_2-norm solution: (a) geometric explanation for l_1-norm solution (b) geometric explanation for l_2-norm solution.

3.4 Summary

In this chapter, two sparse monopole-based ESM algorithms were introduced to solve the under-determined system: WBH and l_1-norm minimization. Both methods balance solution sparsity and accuracy, so that the solution should avoid the ghost source problem and clearly indicate sound source locations. WBH is an algorithm that solves the inverse problem by a steepest descent method embedded in an iterative process. The solution sparsity is controlled by the number of monopoles in the solution: i.e., monopole with small source strength will be removed by a dynamic threshold condition in an iterative process. And the relative error between measurement and reconstruction is the threshold condition to guarantee solution accuracy. If

one of the threshold conditions is satisfied then the final solution is obtained. The second algorithm is l_1-norm minimization, the inverse problem is formulated as the sum of solution first norm and the residual second norm. This objective function balances the solution sparsity by the first norm and accuracy by the second norm. In the next chapter, the capability of both algorithm will be tested by using a computer simulated sources reconstruction experiment.

4. SIMULATION EXPERIMENTS

4.1 Introduction

Several different acoustic field reconstruction methods and regularization techniques that can be used to obtain stable solutions have been reviewed in Chapter 2, then two sparse ESM algorithms for NAH that allow for a relatively small number of microphone measurements were presented in Chapter 3: i.e., WBH and l_1-norm minimization. The latter two methods are the major research interest in the present work. In this chapter, in order to further study the potential and characteristics of these sparse ESM algorithms, different types of sound sources were simulated as an input to the sparse ESM algorithms in particular: a concentrated sound source, i.e., a monopole with unite source strength; a pair of closely-spaced sound sources, i.e., two monopoles placed 0.2 m apart; and a distributed sound source, i.e., the vibration of a baffled plate driven at a point. The equivalent source model used in these simulations is a large number of monopoles distributed on the equivalent source plane, where the simulated sound sources were placed. The equivalent source plane was placed 2 cm behind the reconstruction plane, where the sound pressure and sound intensity distribution was visualized. There were imagined to be 18 virtual microphones composing an irregular microphone array, and the positions of these microphones are the same as the microphones on the Bruel and Kjaer 18 channels irregular array (type 8608). Figure (4.1) illustrates this microphone array. The virtual microphone array was placed 5 cm away from the reconstruction plane, and the "measurement" data at the virtual microphone locations was calculated by using equation (2.28). The relative position of these three planes is demonstrated in Figure (4.2).

The reconstruction results of WBH and l_1-norm minimization will be compared and commented upon. In addition, in order to compare the reconstruction result of

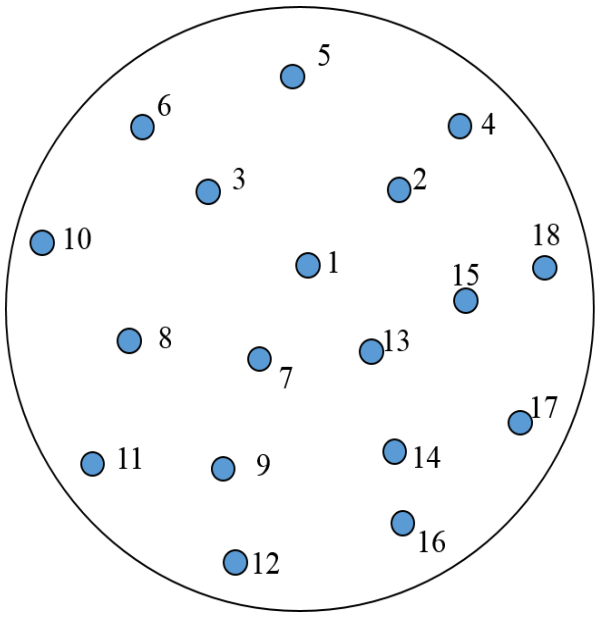

Figure 4.1. Microphone locations on 18 channels irregular array.

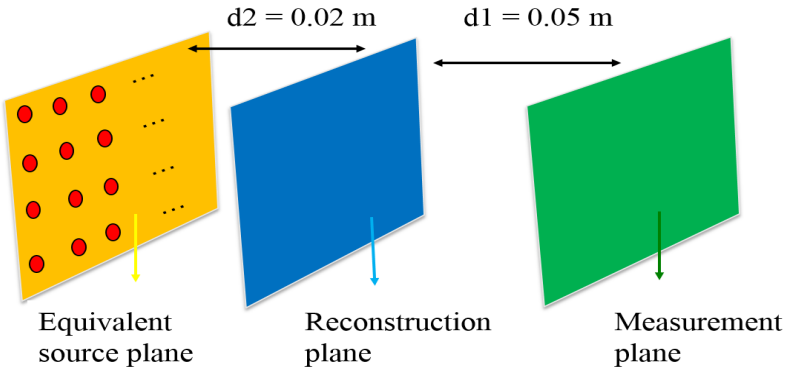

Figure 4.2. Sketch of the simulated experiment setup, simulated monopole source on the equivalent source plane.

the sparse ESM algorithms with another NAH method, SONAH will also be used to reconstruct the simulated sound sources with the same measurement data set. The SONAH results could be compared with WBH and l_1-norm minimization. Since SONAH is also an algorithm that does not place too many restrictions on the measurement array. Based on this comparison, the characteristics of sparse ESM will be further demonstrated.

4.2 Sound Source Localization and Sound Field Visualization with Simulated One Monopole

In this section a single monopole was the simulated sound source, located at (0.2 m, 0.2 m) in the center of the equivalent source plane covering an area of 0.4 m by 0.4 m. The virtual measurement was taken with the 18 channel irregular array described in the previous section. To reconstruct the sound field generated by this monopole, 1681 monopoles were included in the equivalent source model and the equivalent source mesh had 41 rows and 41 columns with a 1 cm spacing. That is, 1681 parameters needed to be estimated, with only 18 channels of measurements, so this is a strongly under-determined system. In this simulation, as described in the previous section, the equivalent sources plane was placed 0.07 m from the measurement position, that is, 0.02 m behind the reconstruction plane. In order to study the sound field reconstruction ability across the frequency range, the sound field was reconstructed at 300 Hz and 2000 Hz corresponding to a low and high frequency case.

SONAH, WBH and l_1-norm minimization were used to reconstruct the sound pressure and intensity field generated by the monopole on the reconstruction plane. To reconstruct the sound field with the SONAH method, the virtual source plane, which plays a role in scaling the elementary wave functions, in that case was placed 0.07 m behind the reconstruction plane, and the regularization parameter, , was calculated by using the L-curve method. The monopole equivalent source model described in the previous paragraph was used for both the sparse ESM algorithms. With the WBH

method, the parameters used in the WBH process were presented in equation (3.13). And for the l_1-norm minimization procedure, the weighting parameter, λ_w, was chosen to be 10 based on multiple trials. The sound pressure and intensity field reconstruction results obtained using all three methods were compared with the simulated sound field. The equations for the sound pressure P and velocity $\vec{V}$ for the different methods at the reconstruction positions have been presented in previous chapters, and the sound intensity was calculated as:

$$\vec{I} = \frac{1}{2}\mathrm{Re}(P\vec{V}^*), \tag{4.1}$$

where $*$ means complex conjugate. Then the total radiated sound power, $\mathbf{P}$, on the reconstruction plane can be calculate by integrate the sound intensity over the reconstruction plane:

$$\mathbf{P} = \int_S \vec{I}\, dS, \tag{4.2}$$

The reconstruction results for the sound pressure and intensity distribution at 300 Hz on the reconstruction plane are shown in Figures (4.3) and (4.4), respectively. Note that 300 Hz is a very low frequency in this context, the wave length is about 1.14 m, which is much larger than the dimension of the microphone array or the equivalent source plane. From the sound pressure reconstruction results, it can be seen that all three methods found the correct monopole location. However, the source reconstructed by the SONAH method was more spread out than the true source and the WBH method seems to underestimate the source strength, while l_1-norm minimization seems to deliver the best reconstruction result among these three methods. The sound intensity reconstruction results are similar to the pressure reconstruction results, and the true radiated sound power generated on the reconstruction plane was 76.5 dB; SONAH recovers 75.0 dB, WBH recovers 60.3 dB, and l_1-norm minimization recovers 75.1 dB. So WBH did substantially, underestimate the source strength at 300 Hz. Once again, the SONAH reconstruction of the intensity is substantially spread out compared with the other results.

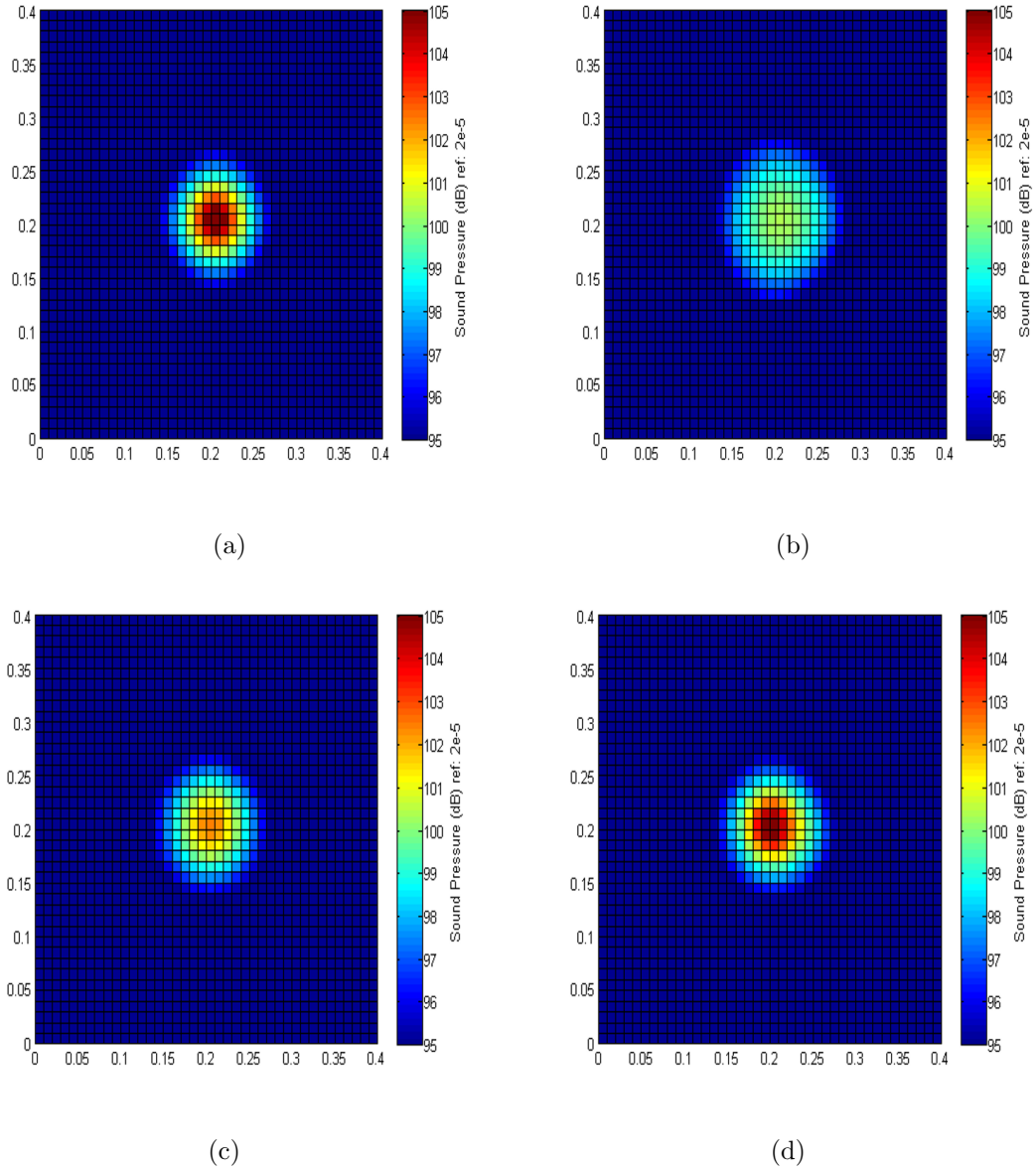

Figure 4.3. Comparison between true sound pressure distribution and reconstructed sound pressure distribution by different methods on the reconstruction plane at 300 Hz, one monopole case: (a) true sound pressure distribution (b) reconstructed sound pressure by SONAH (c) reconstructed sound pressure by WBH and (d) reconstructed sound pressure by l_1-norm minimization.

The reconstruction results for the sound pressure and intensity distributions at 2000 Hz on the reconstruction plane are shown in Figures (4.5) and (4.6) respectively.

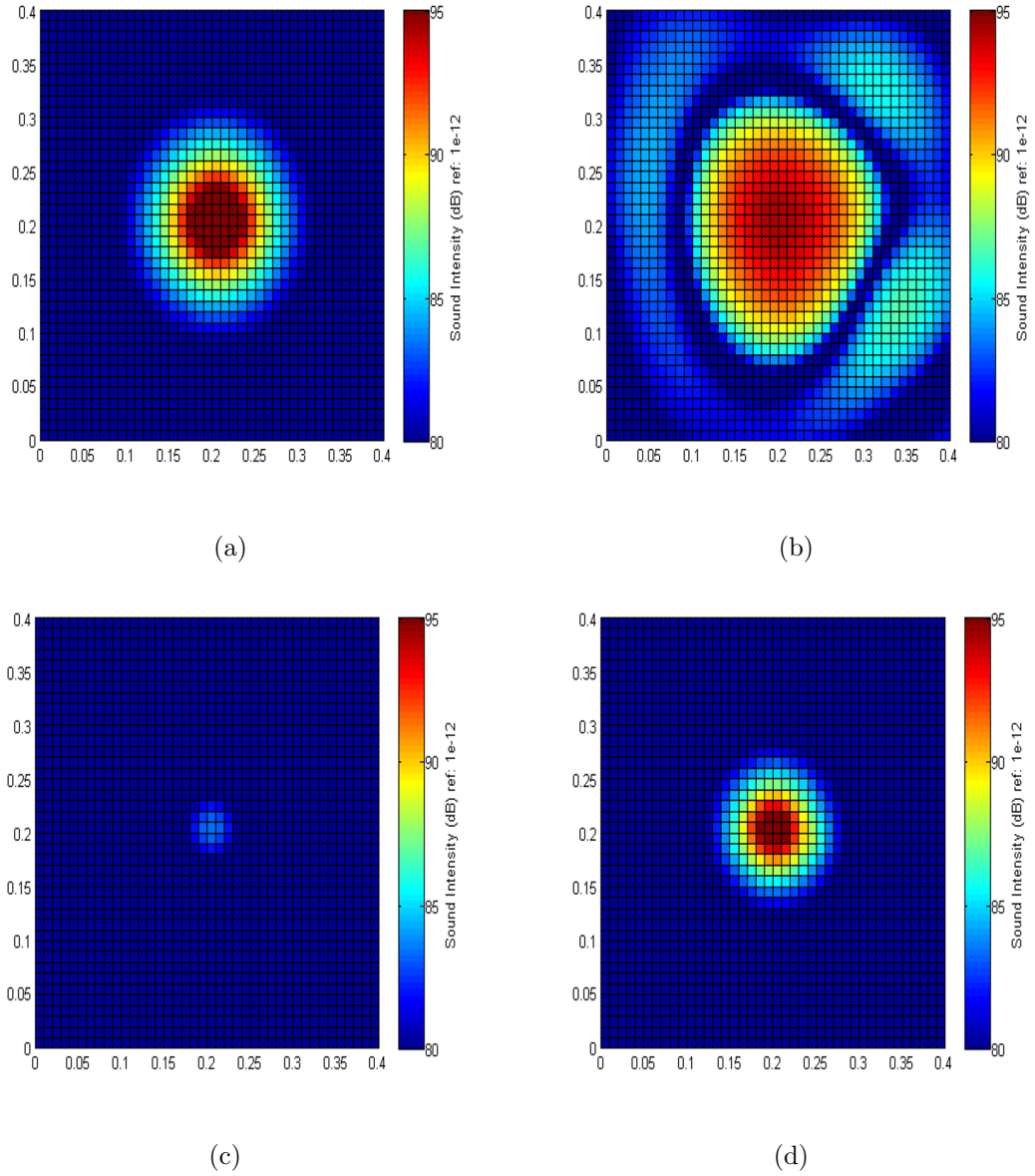

Figure 4.4. Comparison between true sound intensity distribution and reconstructed sound intensity distribution by different methods on the reconstruction plane at 300 Hz, one monopole case: (a) true sound intensity distribution, (b) reconstructed sound intensity by SONAH (c) reconstructed sound intensity by WBH, and (d) reconstructed sound intensity by l_1-norm minimization.

At 2000 Hz, the wavelength decreases to about 0.17 m. From the sound pressure reconstruction result, all three methods successfully reconstructed the sound field and

identified the monopole position. From the sound intensity reconstruction results, the sound intensity distribution reconstructed by SONAH and l_1-norm minimization are very close to the true sound intensity field, but WBH identified a smaller region compared with the other two methods. The true sound power on the reconstruction plane was 76.5 dB, SONAH recovered 74.4 dB, while WBH recovered 69.0 dB and l_1-norm minimization recovered 76.2 dB. So WBH were able to indicate indicate a clearer position of monopole, but the trade off is underestimate the total sound power.

4.3 Sound Source Localization and Sound Field Visualization with Simulated Two Closed-Positioned Monopoles

In this section, instead of one single monopole, two closely-positioned monopoles were simulated as the sound source to test the ability of the methods to distinguish closely-spaced sources. The two monopoles were placed 20 cm apart from each other on the equivalent source plane, i.e., one monopole at (0.2 m, 0.1 m), and another monopole at (0.2 m, 0.3 m). The experimental setup is the same as described in the previous section: i.e., for the relative positions of the equivalent source plane, reconstruction plane, and measurement plane, number of monopoles, and number of measurements. SONAH, WBH and l_1-norm minimization were used to reconstruct the sound pressure and intensity fields. And the parameters used in each methods were also kept the same, i.e., the same virtual source plane position for SONAH, the same WBH parameters and the same weighting parameter in l_1-norm minimization.

The reconstruction results for the sound pressure and intensity distributions at 300 Hz on the reconstruction plane are shown in Figures (4.7) and (4.8) respectively. From the sound pressure reconstruction results, it can be seen that the SONAH method correctly identified that there were two sound sources, but the reconstructed source region is larger than the true sound source region. The WBH algorithm failed to separated the two monopoles:, i.e., it identified a hot spot location in between the two true monopole positions. The explanation for this reconstruction result is that

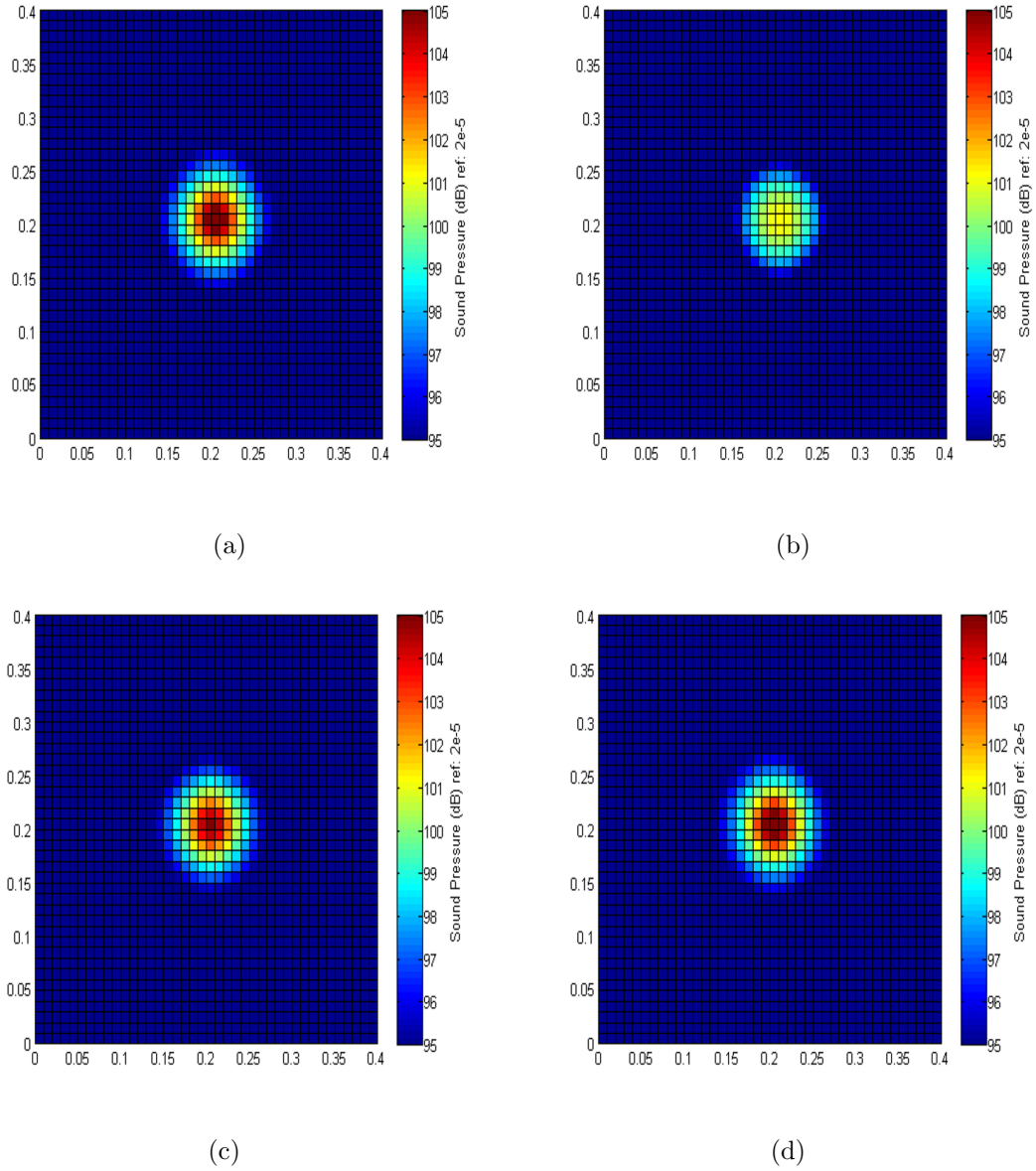

Figure 4.5. Comparison between true sound pressure distribution and reconstructed sound pressure distribution by different methods on the reconstruction plane at 2000 Hz, one monopole case: (a) true sound pressure distribution, (b) reconstructed sound pressure by SONAH, (c) reconstructed sound pressure by WBH, and (d) reconstructed sound pressure by l_1-norm minimization.

at 300 Hz, the wavelength was about 1.14 m, which is much larger than the distance between two monopoles and the virtual microphone array dimension. So the phase

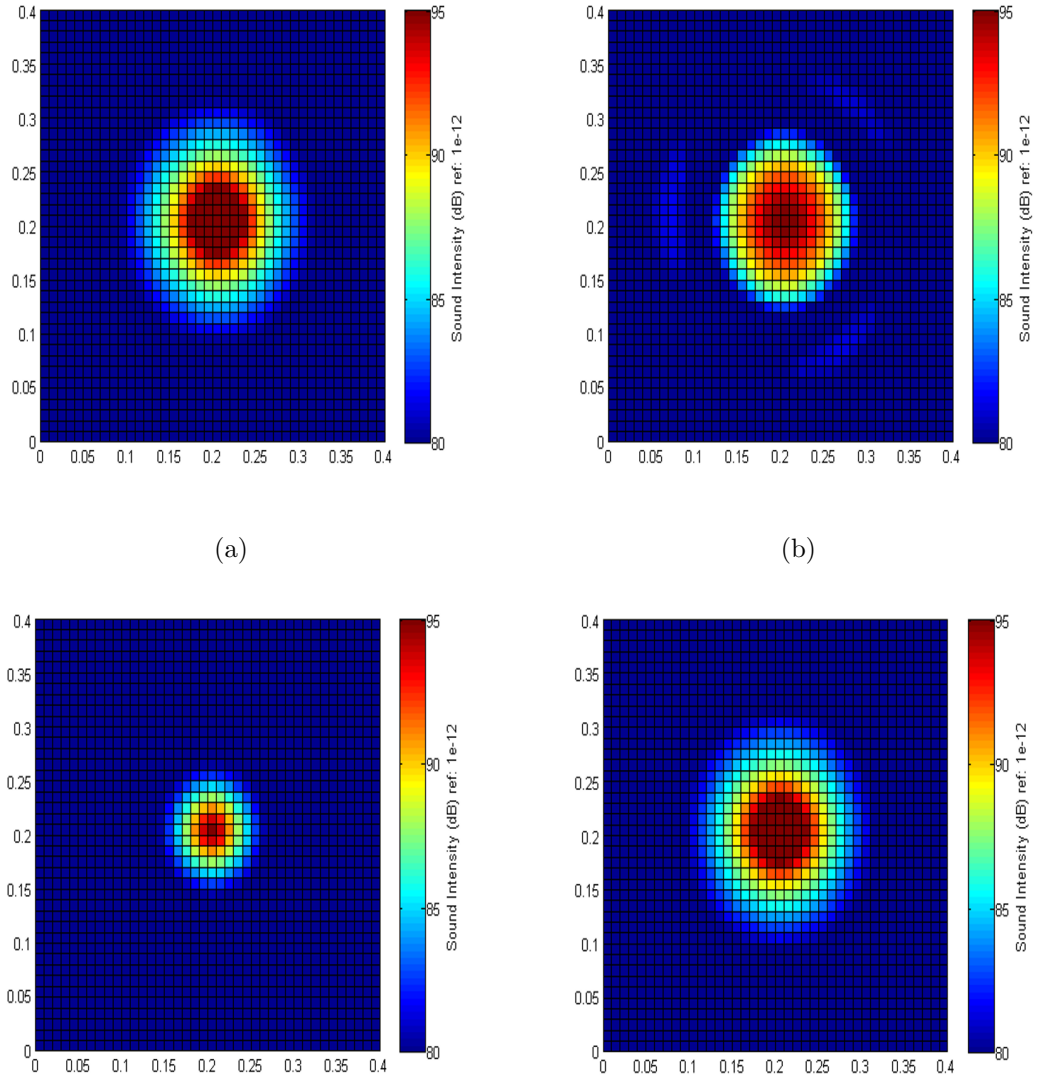

Figure 4.6. Comparison between true sound intensity distribution and reconstructed sound intensity distribution by different methods on the reconstruction plane at 2000 Hz, one monopole case: (a) true sound intensity distribution, (b) reconstructed sound intensity by SONAH, (c) reconstructed sound intensity by WBH, and (d) reconstructed sound intensity by l_1-norm minimization.

difference between the two monopoles at microphone positions is small, which causes the algorithm to identify one source located in between two monopoles instead of

two separate sources. This is also due to the nature of the under-determined system; there exists a large number of combination solutions to this system. The l_1-norm minimization successfully identified the two monopoles with the most accurate sound field reconstruction result. The sound intensity reconstruction result shows the same conclusion as the sound pressure reconstruction result: i.e., SONAH reconstructed two sound sources with an apparently large source region, WBH identified one source in between the two true sound positions, and l_1-norm minimization gives the most accurate result. The true sound power on reconstruction plane was 79.4 dB; SONAH recovered 80.6 dB which overestimated the sound power, WBH underestimated the sound power recovered as 63.7 dB, and l_1-norm minimization recovered 76.1 dB, which is also smaller than the true sound power, but was still relatively close.

At 2000 Hz, the reconstruction results for the sound pressure and intensity distributions on the reconstruction plane are shown in Figures (4.9) and (4.10), respectively. From the sound pressure comparison between the true simulated sound field and the reconstruction results, it can be seen that all three methods successfully identified the two monopole positions. But from the sound intensity reconstruction results, SONAH and l_1-norm minimization can both identify the two monopoles most clearly. However, although WBH identified two sound source positions, WBH didn't recovered the correct weight for the two sound sources: i.e., the upper source is stronger than the lower one. This could be caused by the monopole elimination process that controls the solution sparsity, i.e., the algorithm finds one monopole with a strong source strength and eliminated the monopole with weaker source strength, then developeed the solution around the strong one. At 2000 Hz, the true sound power on reconstruction plane was 79.4 dB; SONAH recovered 77.2 dB, WBH recovered as 70.6 dB, and l_1-norm minimization recovered 78.5 dB.

It was noted that at low frequency, WBH identified one monopole located in between true monopoles, but can identify monopole positions more accurate at higher frequencies. Based on this observation, it seems that for the WBH algorithm, the ability to separate different sound source is related to the wavelength and distance

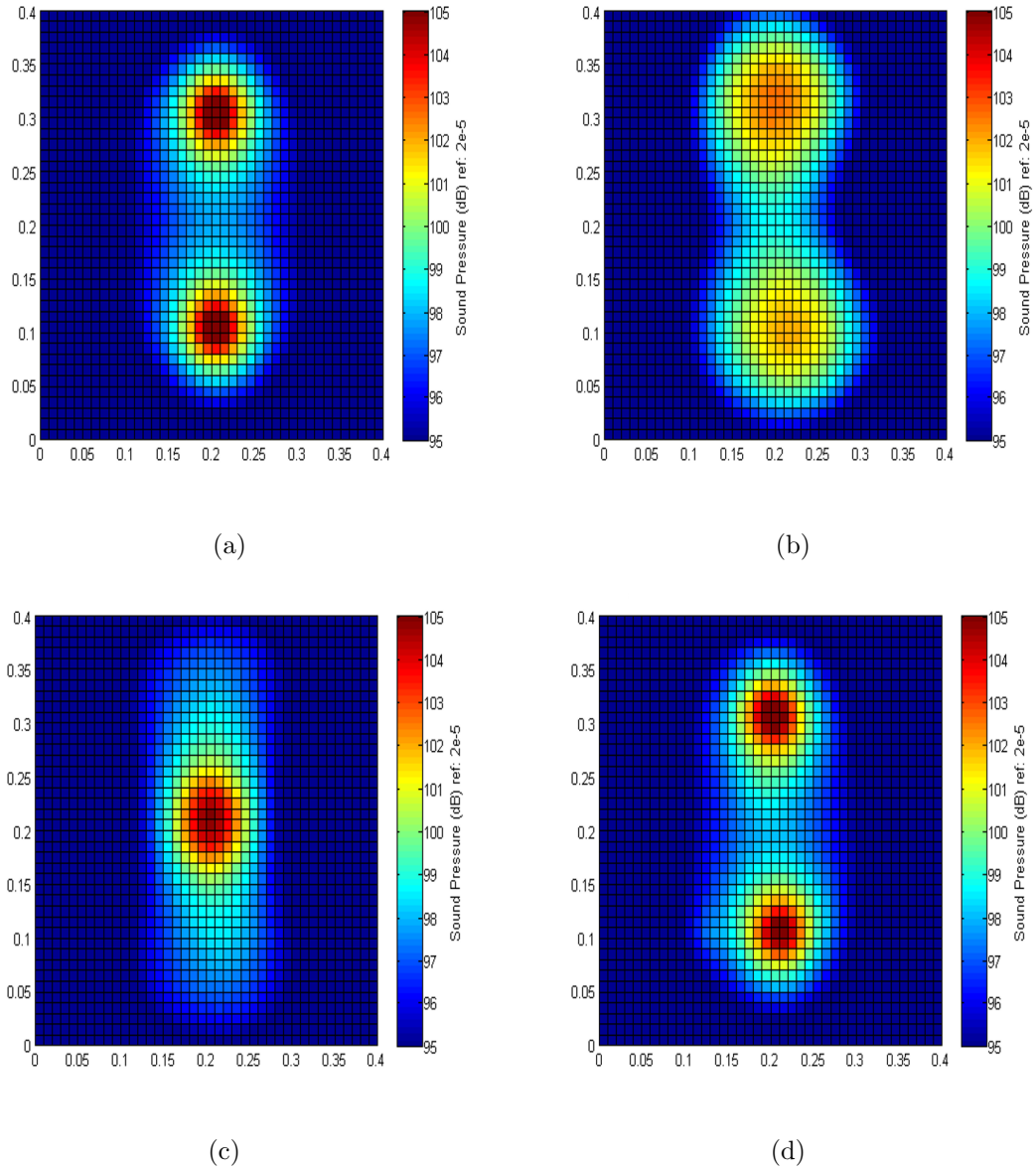

Figure 4.7. Comparison between true sound pressure distribution and reconstructed sound pressure distribution by different methods on the reconstruction plane at 300 Hz, two monopoles case: (a) true sound pressure distribution, (b) reconstructed sound pressure by SONAH, (c) reconstructed sound pressure by WBH, and (d) reconstructed sound pressure by l_1-norm minimization.

between the two sound sources. Thus, a dimensionless quantity r_d, i.e., the ratio between the sound sources separation distance and wavelength, is proposed here, so as

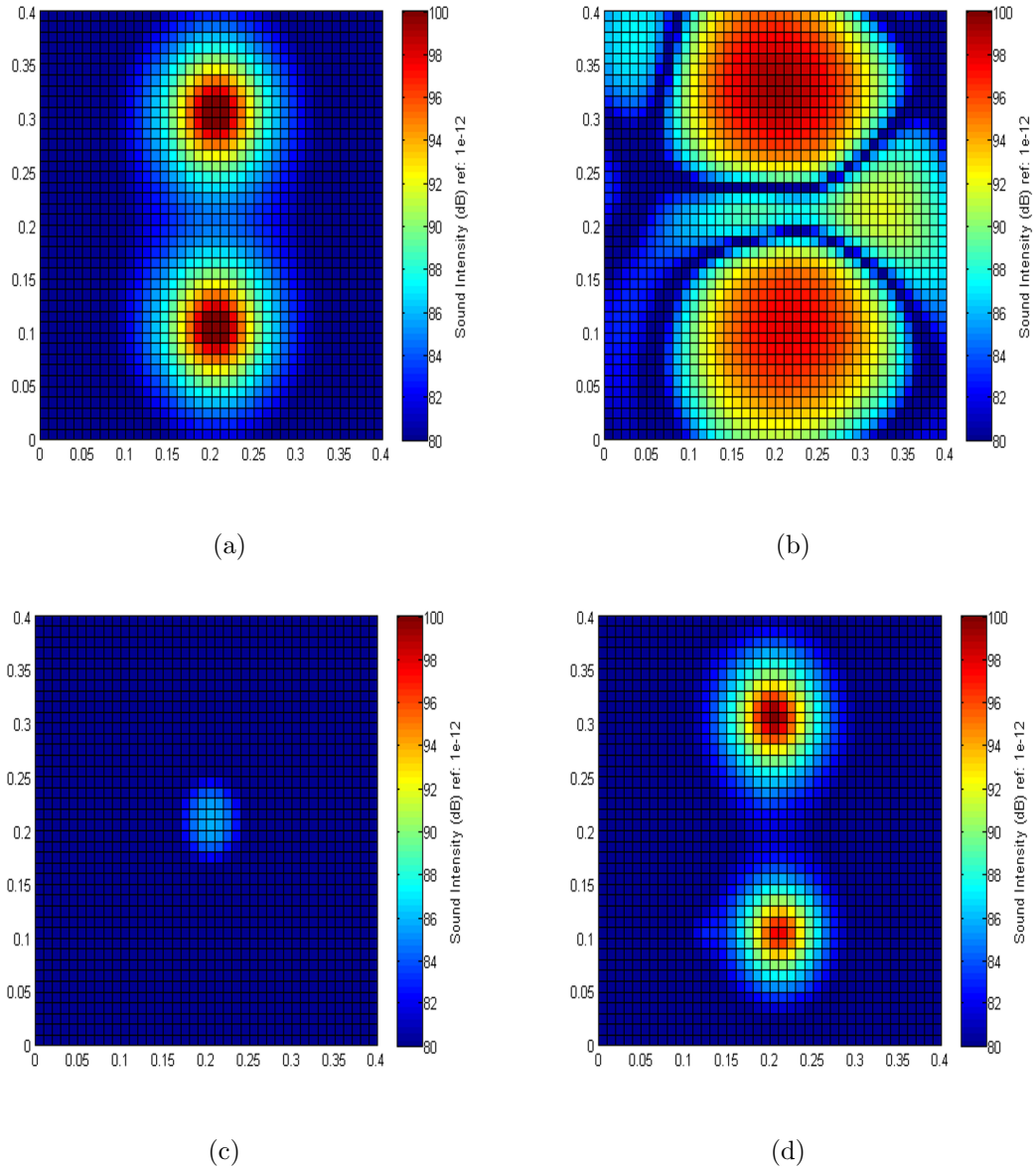

Figure 4.8. Comparison between true sound intensity distribution and reconstructed sound intensity distribution by different methods on the reconstruction plane at 300 Hz, two monopoles case: (a) true sound intensity distribution, (b) reconstructed sound intensity by SONAH, (c) reconstructed sound intensity by WBH, and (d) reconstructed sound intensity by l_1-norm minimization.

the value of r_d increases, the frequency increases and the wavelength becomes smaller. In order to find when the WBH algorithm can separate two sound sources, the follow-

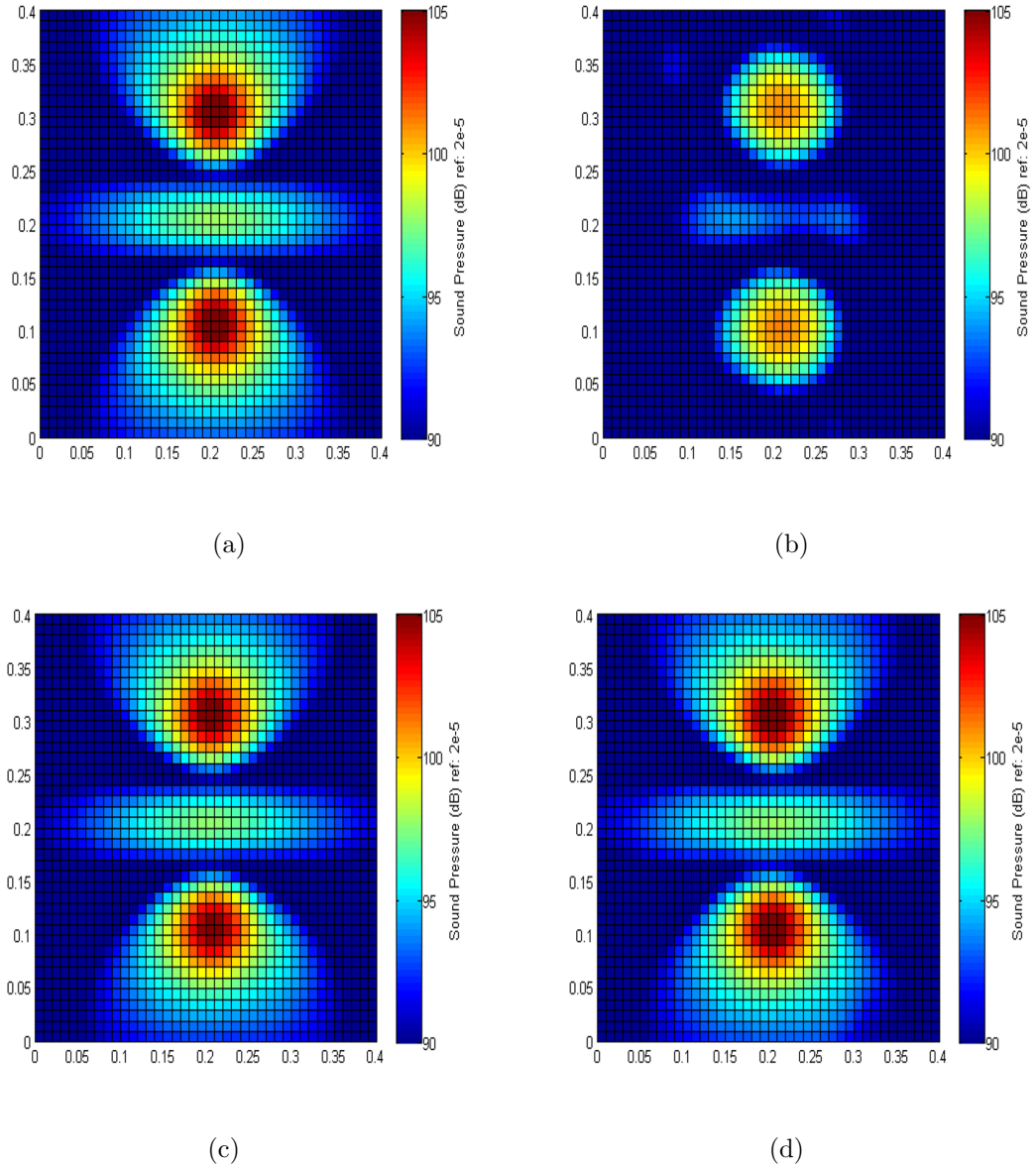

Figure 4.9. Comparison between true sound pressure distribution and reconstructed sound pressure distribution by different methods on the reconstruction plane at 2000 Hz, two monopoles case: (a) true sound pressure distribution, (b) reconstructed sound pressure by SONAH, (c) reconstructed sound pressure by WBH, and (d) reconstructed sound pressure by l_1-norm minimization.

ing simulation experiment was conducted: the sound intensity field was generated by two monopoles at (0.2 m, 0.1 m) and (0.2 m, 0.3 m), then the calculation frequency

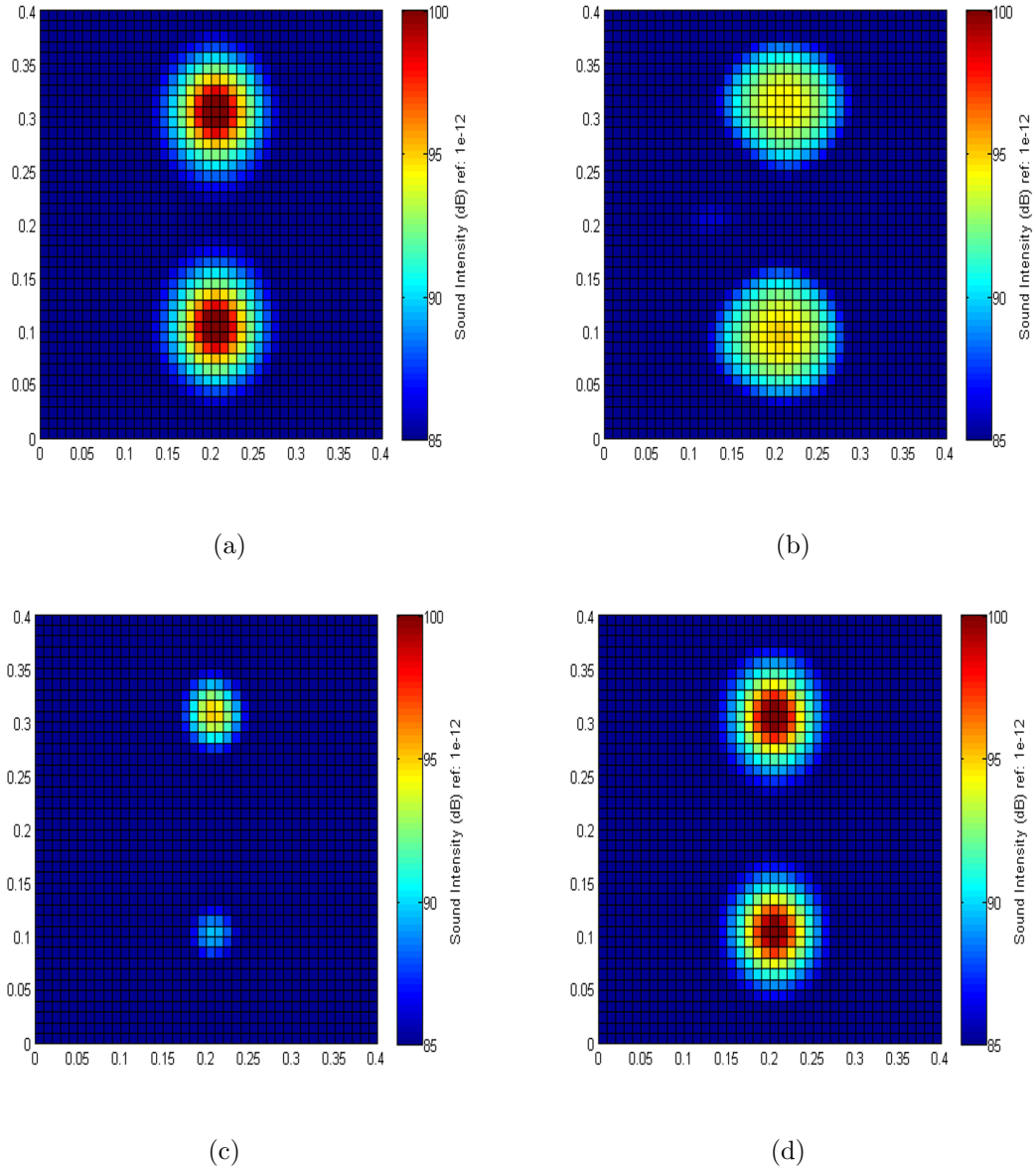

Figure 4.10. Comparison between true sound intensity distribution and reconstructed sound intensity distribution by different methods on the reconstruction plane at 2000 Hz, two monopoles case: (a) true sound intensity distribution, (b) reconstructed sound intensity by SONAH, (c) reconstructed sound intensity by WBH and (d) reconstructed sound intensity by l_1-norm minimization.

was increased from 300 Hz to 2000 Hz in 100 Hz steps. The sound field on the reconstruction plane was reconstructed with SONAH, WBH and l_1-norm minimization at

all frequencies. Note, based on the previous experiment, both SONAH and l_1-norm minimization are able to separate different monopoles at 300 Hz, so this experiment was tried to find out the threshold of the WBH algorithm's ability to separate the monopoles.

The figures below were selected to demonstrate the sound intensity reconstruction results when r_d is small, the r_d when WBH algorithm can separate two monopoles, and a large r_d. Figure (4.11) shows the WBH algorithm sound intensity reconstruction results as r_d increases, it was found that when r_d is small the WBH algorithm cannot separate the monopoles, when r_d equals or larger than 0.765, the WBH algorithm was able to separate the two sound sources. Figure (4.12) shows the SONAH reconstruction results with different r_d, and even with a very small value of r_d, e.g., 0.471, the SONAH algorithm can still separate the two sources with a relative large region. And as r_d increases, the reconstruction result gives better indication on sound source locations, i.e., the hot spot region indicate sound source location gets smaller. Finally, Figure (4.13) shows the sound intensity reconstruction results with l_1-norm minimization algorithm are accurate for all the r_ds.

However, this does not means that the absolute error between the true sound intensity field and the reconstructed intensity field will decrease as r_d increases: see Figure (4.14). The absolute error is defined here as the absolute different between true intensity and reconstructed intensity: i.e.,

$$e_{abs} = \sum |\vec{I}_{true} - \vec{I}_{reconstruct}|. \tag{4.3}$$

It was found that as r_d increases, the absolute error between true intensity field and WBH reconstruction result does not dramatically decrease, even though the algorithm does not successfully reconstruct the two sound sources when r_d is smaller than 0.765. For SONAH, the reconstruction result approaches true sound field as r_d increases, it is because as r_d increases the reconstruction result is more concentrated and more close to the true intensity distribution. Finally, l_1-norm minimization always give the most accurate reconstruction result across frequencies and always correctly

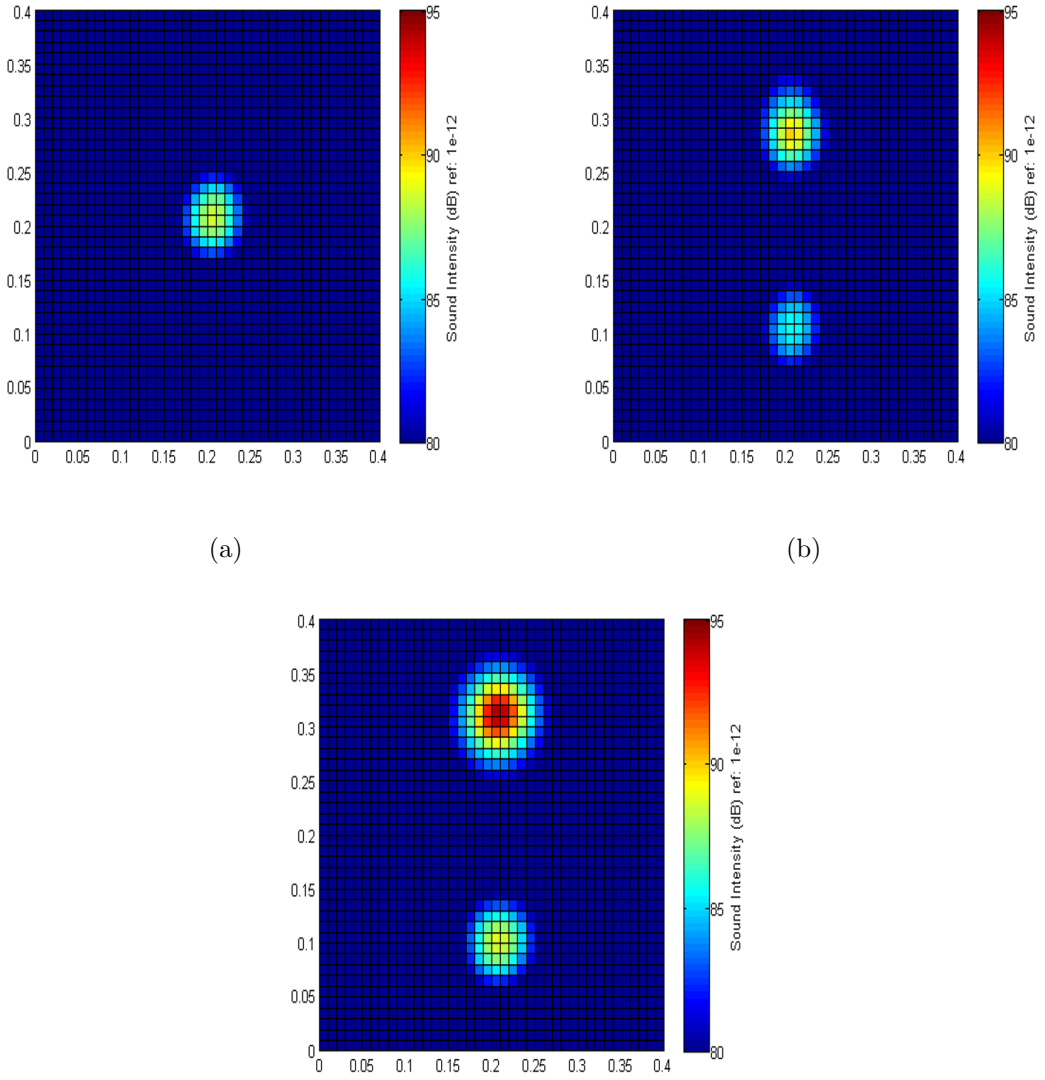

(a) (b)

(c)

Figure 4.11. Sound intensity reconstruction results with WBH algorithm with different value of r_d: (a) reconstructed sound intensity field when $r_d = 0.471$, (b) reconstructed sound intensity field when $r_d = 0.765$, and (c) reconstructed sound intensity field when $r_d = 1.059$.

identified the monopole positions. However, it is note that the l_1-norm minimization results is based on multiple trial to select the best weight parameter, in practical

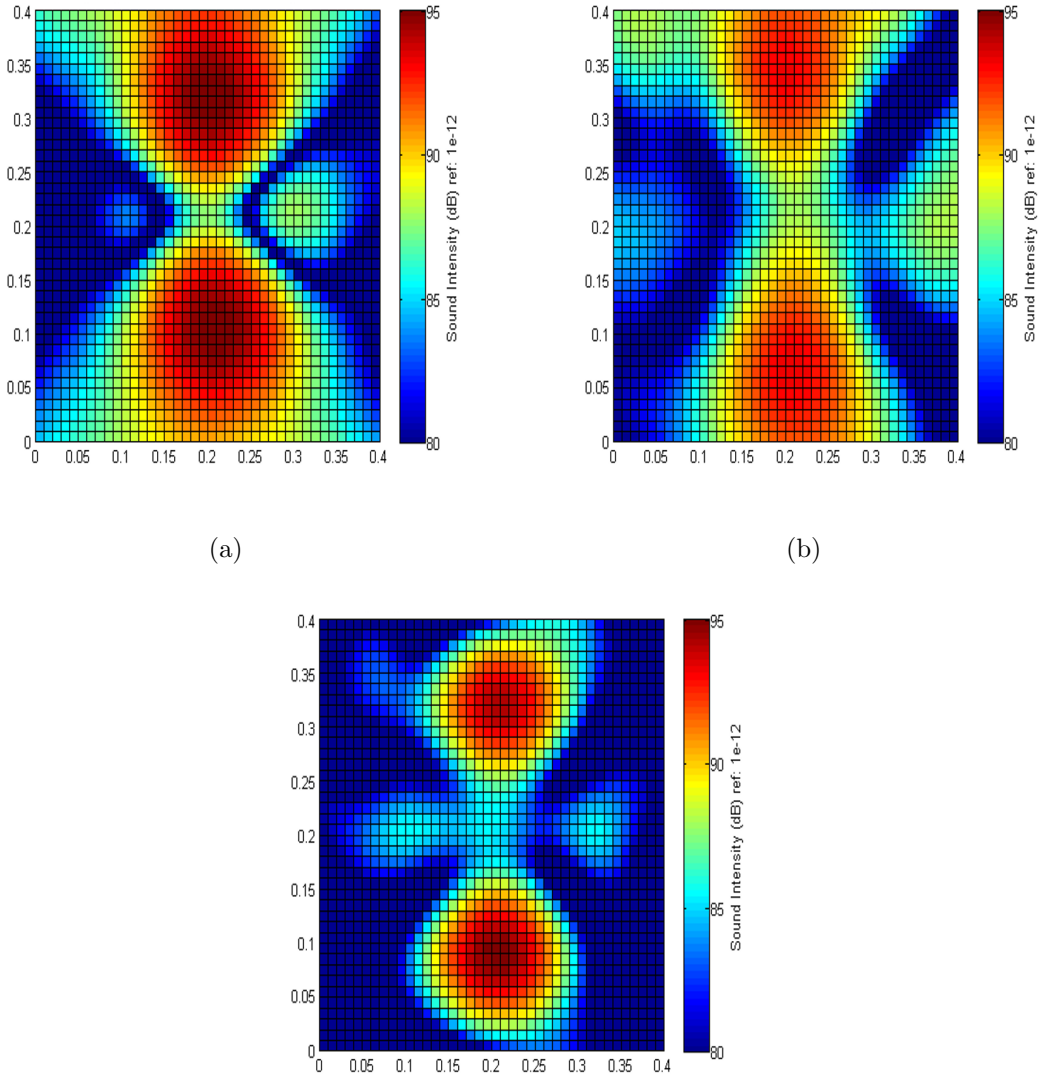

(a)

(b)

(c)

Figure 4.12. Sound intensity reconstruction results with SONAH algorithm with different value of r_d: (a) reconstructed sound intensity field when $r_d = 0.471$, (b) reconstructed sound intensity field when $r_d = 0.765$, and (c) reconstructed sound intensity field when $r_d = 1.059$.

to obtain this result could be harder. From this experiment, it was found that a smaller difference between the true and reconstructed sound field does not mean the reconstruction result is accurately indicates the correct sound source location,

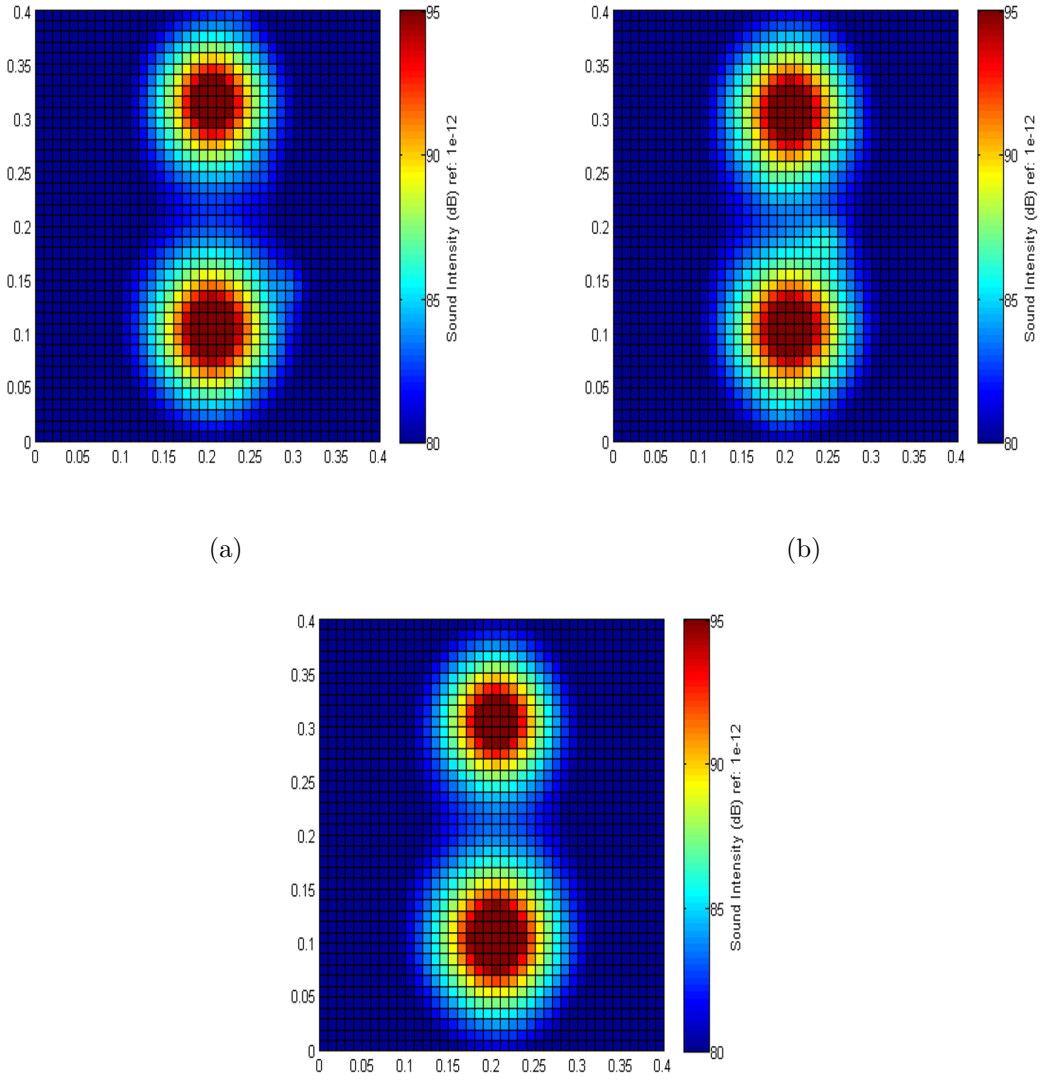

(a) (b)

(c)

Figure 4.13. Sound intensity reconstruction results with CVX algorithm with different value of r_d: (a) reconstructed sound intensity field when $r_d = 0.471$, (b) reconstructed sound intensity field when $r_d = 0.765$, and (c) reconstructed sound intensity field when $r_d = 1.059$.

since in the under-determined case similar sound fields can be generated by different sound source distributions. It is also note that this simulation result is based on the

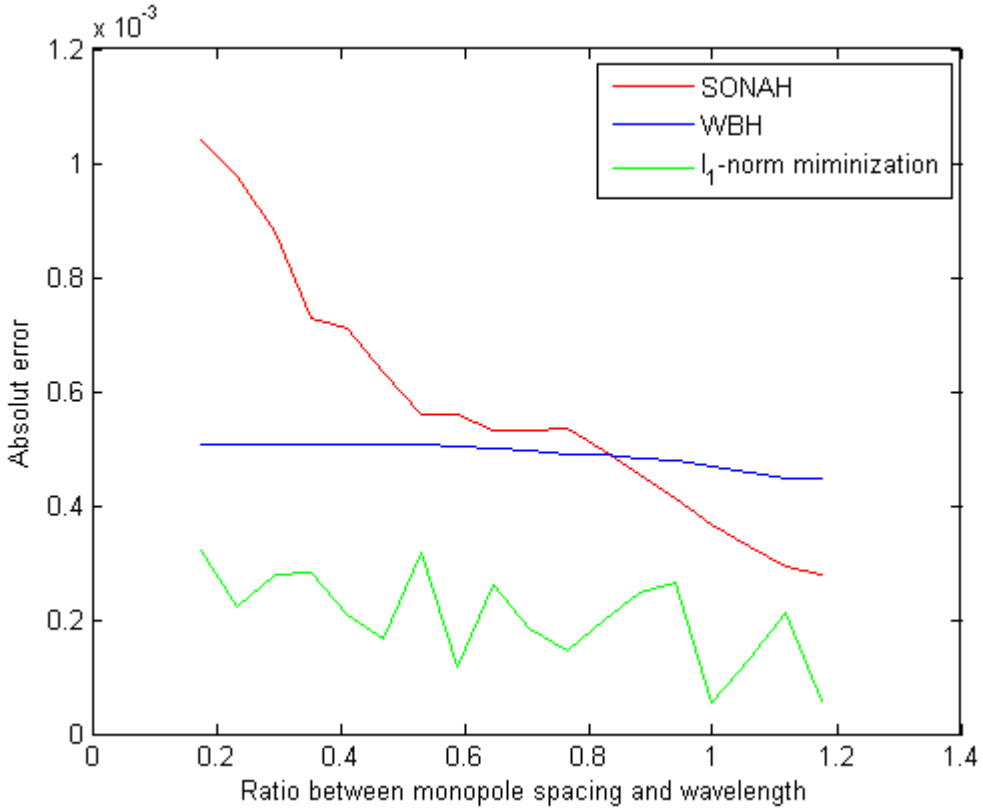

Figure 4.14. Reconstructed intensity absolute error at different source-spacing-to-wavelength-ratio.

measurement with the 18 channels array, with a different microphone array different result should be expected for the same r_d value.

4.4 Sound Source Localization and Sound Field Visualization with Baffled Plate Vibration

In previous sections, concentrated sound sources, i.e., monopoles, were used as simulated sound sources to study the WBH and l_1 minimization algorithms' ability to identify sound source location. And a dimensionless quantity was introduced to quantify the algorithms' ability to spatially separate different sound sources. In the work this section, a spatially-extended sound source was simulated, i.e., baffled plate

vibration. The sound source in this simulation was a baffled aluminum plate with a size of 0.4 m by 0.4 m. A point force was applied at position (0.2 m, 0.2 m), which is at the center of the plate. This plate was placed in the same position as the equivalent source plane in previous sections. The sound field generated by this plate was visualized on the reconstruction plane. The experimental setup is the same as described in the previous section: i.e., the relative positions of the equivalent source plane, reconstruction plane, and measurement plane, number of monopoles, and number of measurements. SONAH, WBH and l_1-norm minimization was used to reconstruct the sound pressure and intensity fields. And the parameters used in each methods were also kept the same: i.e., the same virtual source plane position for SONAH, same WBH parameters and same weighting parameter in l_1-norm minimization.

The reconstruction results for the sound pressure and intensity distributions at 300 Hz on the reconstruction plane are shown in Figures (4.15) and (4.16), respectively. From the sound pressure and sound intensity reconstruction results, SONAH successfully reconstructed some details of the sound field, while WBH and l_1-norm minimization seemed to reconstructed the field as several point sources instead of an extended sound source. This is expected since the spatially-extended source does not satisfy the sparsity condition, so that the two sparse ESM algorithms cannot recover all the sound field details. The total sound power on the reconstruction plane generated by the vibrating plate was 103.0 dB: SONAH recovered 98.2 dB, WBH reconstructed 80.0 dB and l_1-norm minimization recovered 98.2 dB.

The reconstruction results for the sound pressure and intensity distributions at 2000 Hz on the reconstruction plane are shown in Figures (4.17) and (4.18), respectively. At this frequency, the total radiated sound power on the reconstruction plane was 70.8 dB: SONAH recovered 67.9 dB, WBH recovered 61.2 dB and CVX recovered 67.1 dB. At 2000 Hz, all the methods failed to reconstruct the exact sound field details, even though all three methods identified the driven-point. There are two factor that could cause these results: first, the number of virtual measurement is too small to capture all the sound field details, e.g., vibrations at corners, since the vibration

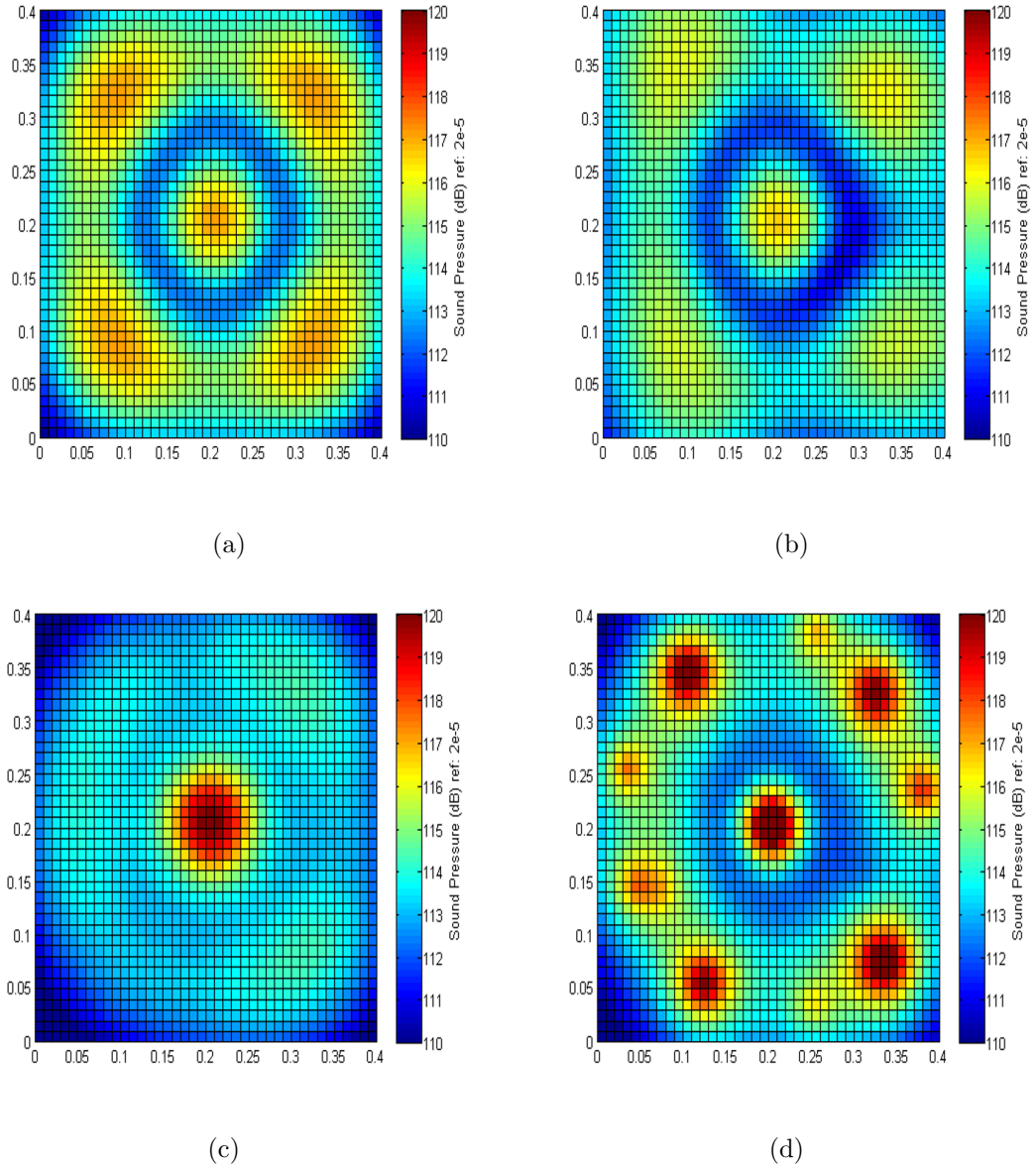

Figure 4.15. Comparison between true sound pressure distribution and reconstructed sound pressure distribution by different methods on the reconstruction plane at 300 Hz, baffled plate case: (a) true sound pressure distribution, (b) reconstructed sound pressure by SONAH, (c) reconstructed sound pressure by WBH, and (d) reconstructed sound pressure by l_1-norm minimization.

patten at 2000 Hz was much more complicated than at 300 Hz. Secondly, since at 2000 Hz the wavelength is smaller than that at 300 Hz, the plate vibration begins

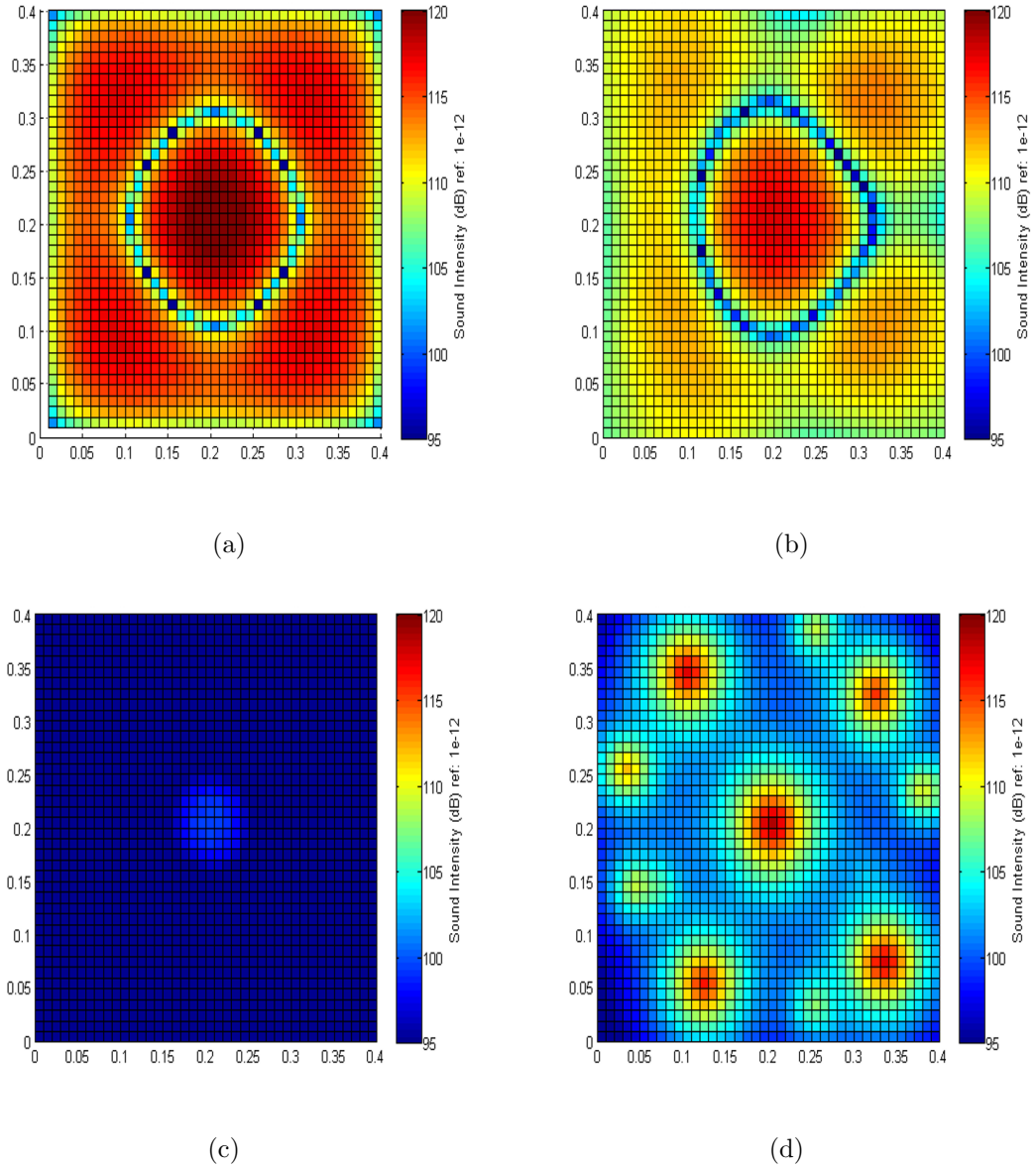

Figure 4.16. Comparison between true sound intensity distribution and reconstructed sound intensity distribution by different methods on the reconstruction plane at 300 Hz, baffled plate case: (a) true sound intensity distribution, (b) reconstructed sound intensity by SONAH, (c) reconstructed sound intensity by WBH, and (d) reconstructed sound intensity by l_1-norm minimization.

to act like a collection of elementary radiators. So the algorithms only identified the strongest position, the driven-point.

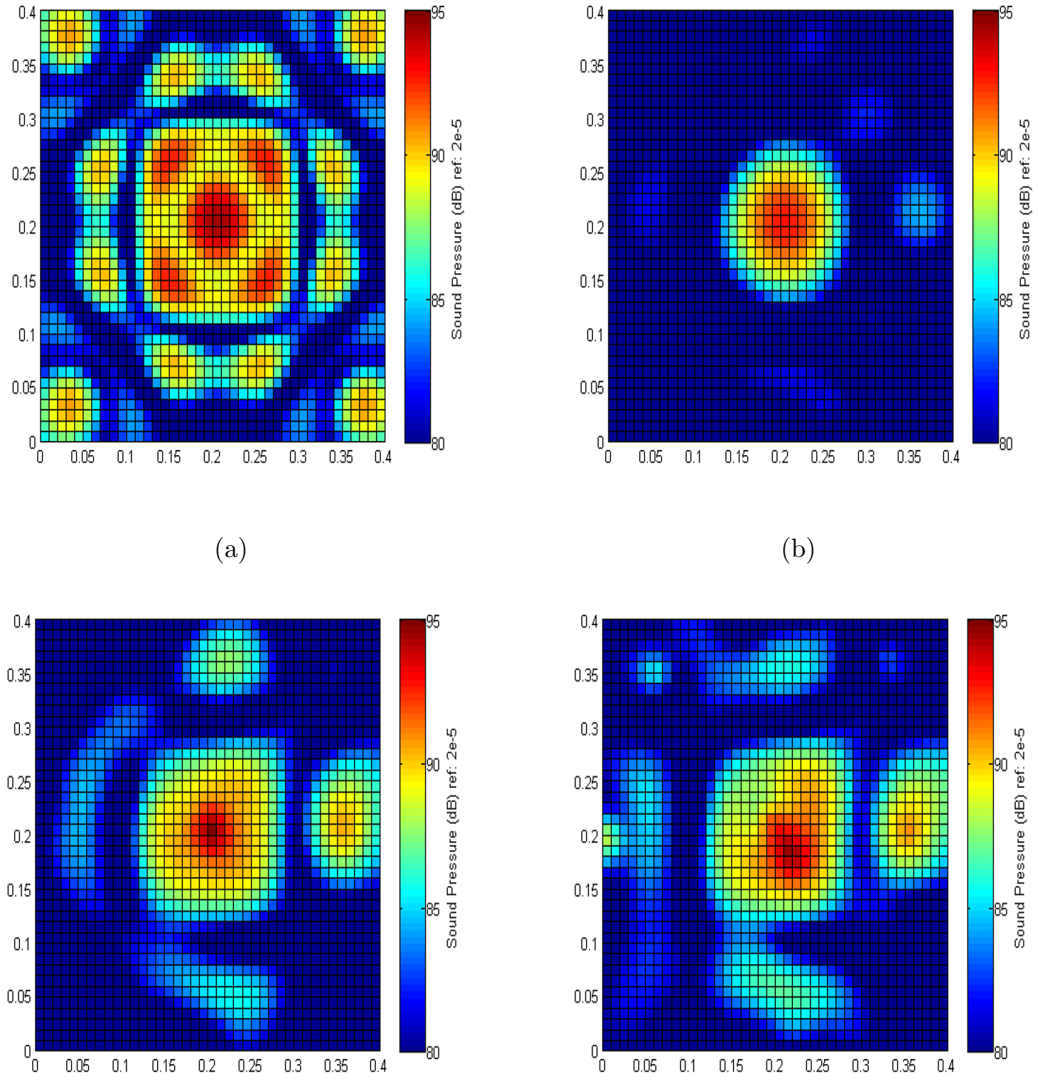

Figure 4.17. Comparison between true sound pressure distribution and reconstructed sound pressure distribution by different methods on the reconstruction plane at 300 Hz, baffled plate case: (a) true sound pressure distribution, (b) reconstructed sound pressure by SONAH, (c) reconstructed sound pressure by WBH, and (d) reconstructed sound pressure by l_1-norm minimization.

4.5 Summary

In this chapter, three different simulated sound source reconstruction experiments were conducted, and the reconstruction results obtained by using different NAH meth-

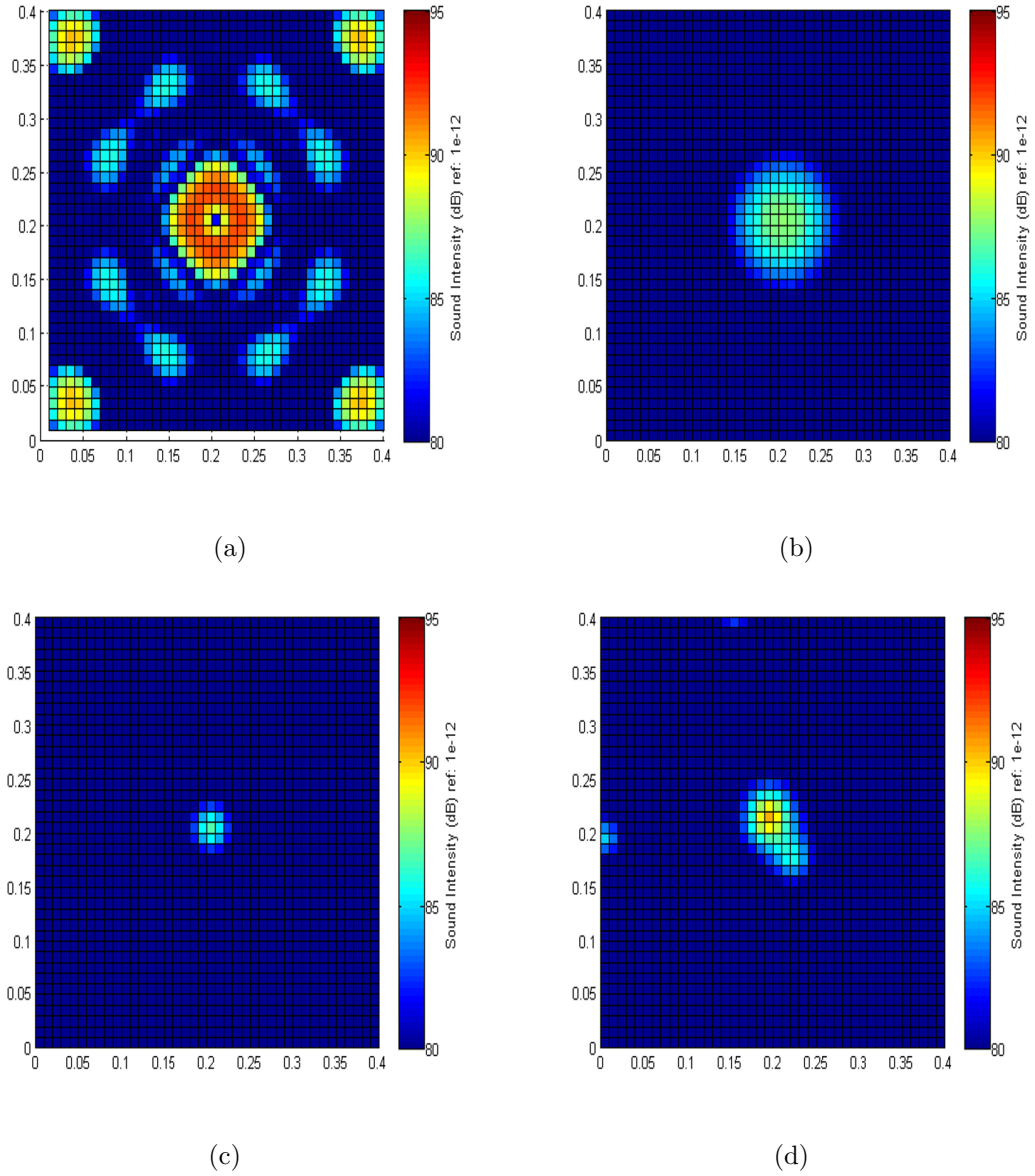

Figure 4.18. Comparison between true sound intensity distribution and reconstructed sound intensity distribution by different methods on the reconstruction plane at 2000 Hz, baffled plate case: (a) true sound intensity distribution, (b) reconstructed sound intensity by SONAH, (c) reconstructed sound intensity by WBH, and (d) reconstructed sound intensity by l_1-norm minimization.

ods were compared and commented upon. In all simulation experiments, only 18 channels of virtual measurements were used to reconstruct the sound field. Based

on the simulation result, for a single concentrated source, i.e., a monopole, all three methods can identify the sound source location, with WBH and l_1-norm minimization yielding better concentration at the source position compared with SONAH at both low and high frequencies. In the second simulation experiment, two closely-positioned monopoles were simulated as sound sources. It was found that WBH cannot separate the two monopoles and identified them as one single source located in between the true monopole positions at low frequency, e.g., 300 Hz, which correspond to the conclusion found in Hald's original WBH paper [41]. In contrast, at high frequency, WBH can find the two monopole positions but were assigned incorrect weighting for the two monopoles, while SONAH and l_1-norm minimization could reconstruct the sound field correctly at low and high frequencies. In order to further study the WBH algorithm, a dimensionless quantity r_d was proposed, where r_d is the ratio between the monopole spacing and the wavelength. It was found that when r_d is larger than 0.765, the WBH algorithm was able to separate the two monopoles. Then the absolute error between the true intensity field and the reconstructed intensity field at different frequencies was calculated, and the absolute error between the different methods was examined. It was found that for the WBH algorithm, it could not identify correct monopole positions at low frequency, but the absolute error was still not large compare with the SONAH method. However, the SONAH method was able to separate the monopoles at low frequencies. So identification sound source positions and sound field reconstruction accuracy do not always more in the same direction. Thais, it is necessary to check both in order to make sure a good result. For spatially-extended sources, such as baffled plate vibration, it was found that all three methods were able to identify the point of excitation, but the SONAH method recovered the most spatial detail about the sound field at low frequency. So for different types of sound sources, with a relatively small number of microphone measurement, all three methods can find the major sound source positions. But, depending on the sound source type, it is crucial to choose the appropriate NAH method to ensure accurate sound field reconstruction.

5. HYBRID COMPRESSIVE SENSING METHOD

5.1 Introduction

In the previous chapters, WBH and l_1-norm minimization were applied to reconstruct simulated sound fields and to identify sound source locations when the number of measurements was substantially smaller than the number of unknown parameters in the model. The reconstruction results from both methods were shown and commented upon, and from those results, the characteristics of the two methods could be identified. In this chapter, the study begins with trying to improve the WBH algorithm reconstruction result by changing $\vec{q}_0$, which is the initial solution from which the WBH iteration process begins. Based on the simulations shown in this chapter, it was found that the initial value of $\vec{q}_0$, which was set to zero in Chapter 3, based on Hald's previous work, plays an important role in determining the accuracy of WBH.In the previous chapter, it was shown that the l_1-norm minimization could obtain ideal reconstruction results with an appropriate choice of the weighting parameter λ_w. In this chapter it will be shown that a bad choice of λ_w could cause ghost sources to appear in the reconstruction solutions. Based on these observations, in order to improve the sound source localization results, a hybrid method is proposed in this section, and then the simulation results are compared with the previous WBH and l_1-norm minimization results.

5.2 The Influence of Initial Sound Field Guess on the Final Sound Field Reconstruction Result with WBH

Previously, it was seen that the WBH method could identify the major sound source locations, but that the results were not always accurate, especially at low frequencies. In the WBH algorithm, the initial solution, $\vec{q}_0$, was always chosen as zero in

Chapter 3, which means that no assumptions are made based on some foreknowledge of the sound source distribution, to begin the solution search. But, if the approximate sound source location is known, it should be possible to improve the WBH algorithm result by beginning the iteration process with a non-zero initial guess. However, there is the possibility that the foreknowledge of the sound source distribution is not very accurate or that unanticipated sound sources could exist. The following simulations were motivated by the wish to determine whether the WBH algorithm can still identify a relatively accurate solution when the initial solution is not accurate or even completely wrong.

The same two closely-positioned monopoles simulated in the previous chapter were also considered here. The set up of the measurement plane, equivalent source plane and reconstruction plane, and the parameters in the WBH algorithm were exactly the same as described previously in Chapter 3, except in this simulation, the $\vec{q}_0$ was not zero. Then white, Gaussian random noise was added to the virtual measurements with a signal-to-noise ratio of 30 dB. Recall that the true sound source comprised two monopoles, and in this simulation, it is assumed that the location and source strength of the monopole on the top was known, but that the strength and location of the monopole at the bottom was unknown, then the WBH iteration process began with that assumption. In this experiment, the reconstructed monopole distribution, which is the solution of the inverse problem, was directly compared with the simulated monopole distribution which is the true solution, since the monopole location is directly related to the sound source position. The true sound source distribution, the initial guess source distribution and the final sound source reconstruction results are shown in Figures (5.1) and (5.2) for 300 Hz and 2000 Hz, respectively.

In these simulations, the total source strength was recovered relatively accurately: e.g., at 300 Hz the true source strength was 2 and the reconstructed source strength was 1.89 (monopoles with small values barely invisible are widely distributed around bottom monopole position), and at 2000 Hz the true source strength was 2 and the algorithm recovered 1.96. However, at both frequencies, the WBH algorithm failed to

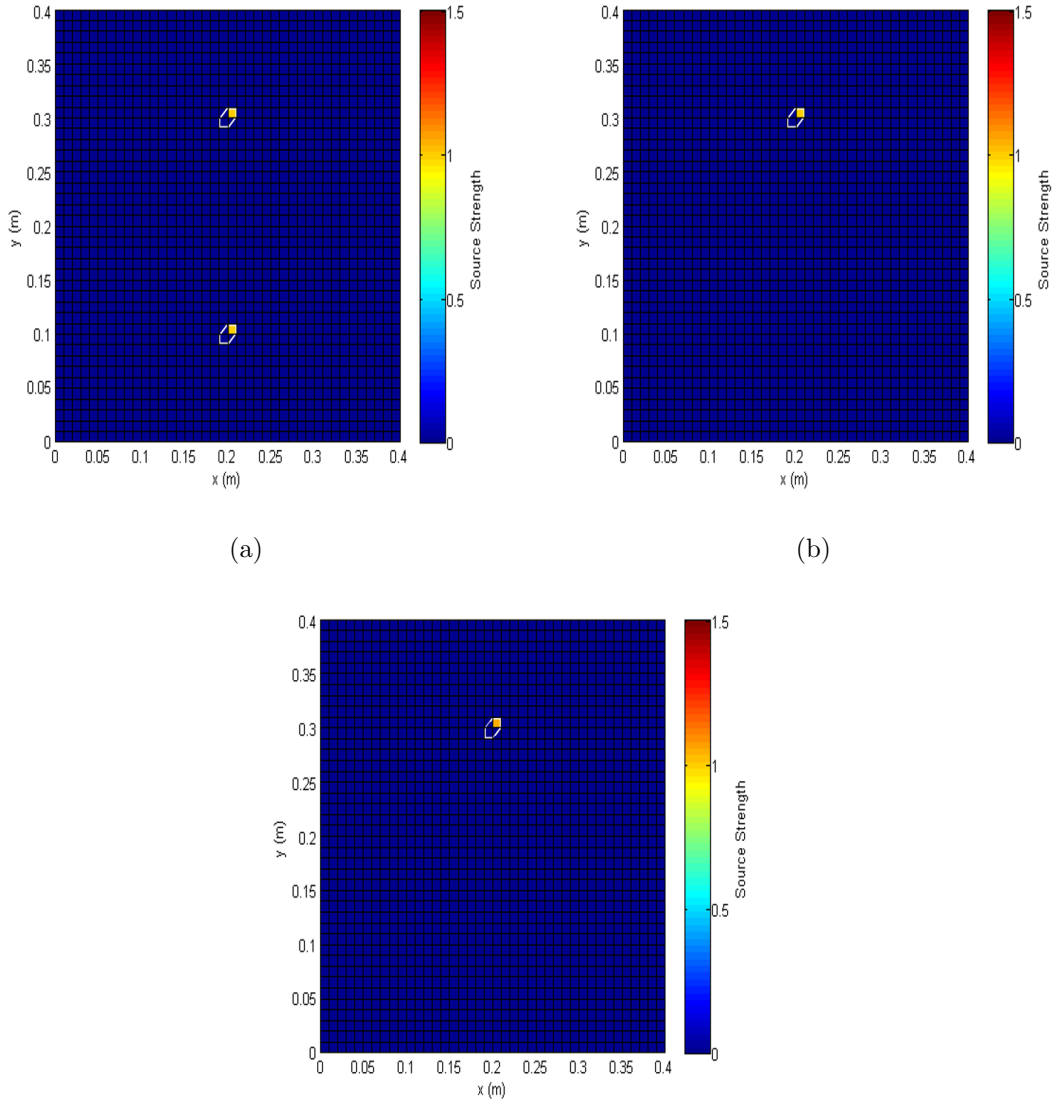

(a) (b)

(c)

Figure 5.1. WBH reconstruction result with inaccurate initial solution at 300 Hz: (a) simulated sound source, (b) initial solution $\vec{q}_0$, and (c) reconstruction result with initial solution.

identify the sound source at the bottom correctly, especially at 300 Hz. At 2000 Hz the algorithm did find the visible source at bottom, but its strength is much smaller than that of the top source. This result is due to the fact that the linear system is under-determined, so there exist a large number of solution combinations that satisfy

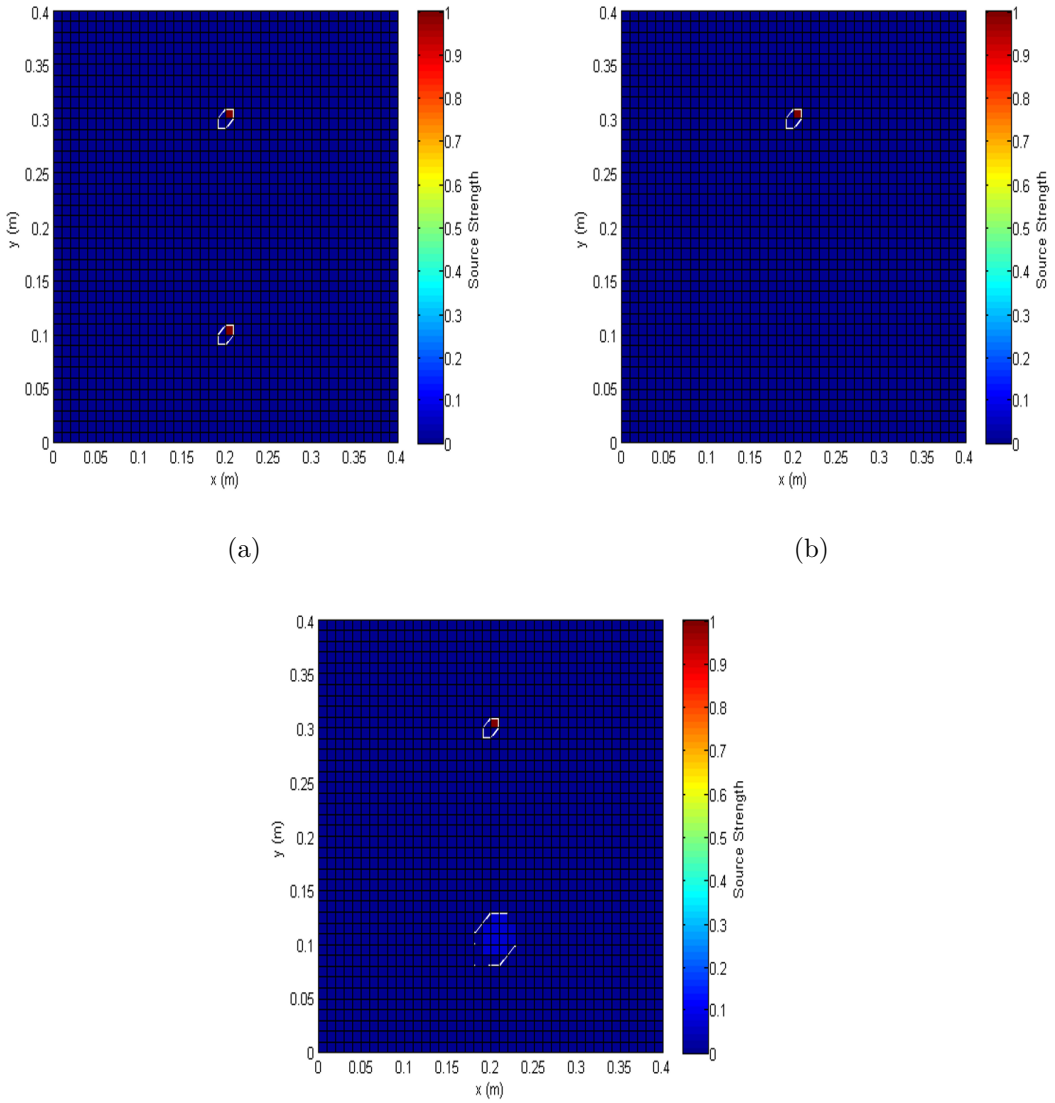

Figure 5.2. WBH reconstruction result with inaccurate initial solution at 2000 Hz: (a) simulated sound source, (b) initial solution $\vec{q}_0$, and (c) reconstruction result with initial solution.

the equations. So, once an initial solution is set, the algorithm develops the final result around it. This set of simulations shows that the initial solution strongly influence the final result in the WBH algorithm.

5.3 The Influence of Weighting Parameter in l_1-Norm Minimization

In the previous chapter it was found that l_1-norm minimization is an effective algorithm to identify concentrated sound sources. The algorithm is able to separate closely-positioned sound sources even at very low frequencies. However, the results in previous chapter were based on performing multiple trials to choose the appropriate weighting parameter, λ_w, which is crucial in the objective function, since it governs how much noise is tolerated in the solution. In this section, in order to study how λ_w influences the final solution, the closely-position monopoles described in the previous chapter were simulated. The set up of the measurement plane, equivalent source plane and reconstruction plane were exactly the same as described in Chapter 3. White Gaussian random noise was added to the virtual measurement with a signal-to-noise ratio of 30 dB. In this simulation the sound source distribution reconstruction results with λ_w equaling either to 1 or 100 were compared, instead of a value of 10 as used in the previous chapter.

Figure (5.3) shows the sound source reconstruction results and the comparison between the virtual measured sound pressure and the reconstructed sound pressure with different value of λ_w. When λ_w was chosen to be a large value, e.g., 100 in this experiment, the reconstructed sound pressure will be very close to the measured sound pressure, since more weighting was assigned to minimize the second norm residual. In this simulation the reconstructed sound pressure is exactly the same as the measured sound pressure at measurement position, as shown in Figure (5.3.c). However, this also means that too much noise was included in the solution, so that ghost sources were also included in the reconstructed solution, as shown in Figure (5.3.a) outlined with white lines. Another case is when λ_w equals to 1, which is a relatively small value. In that case, the reconstructed sound pressure at the measurement position is not exactly the same as the measured sound pressure in Figure (5.3.d), but the sound source distribution gives a clear indication of the sound source location, as shown in

Figure (5.3.b). The same conclusions can also be drawn at 2000 Hz, with different value of λ_w, as seen in Figure (5.4).

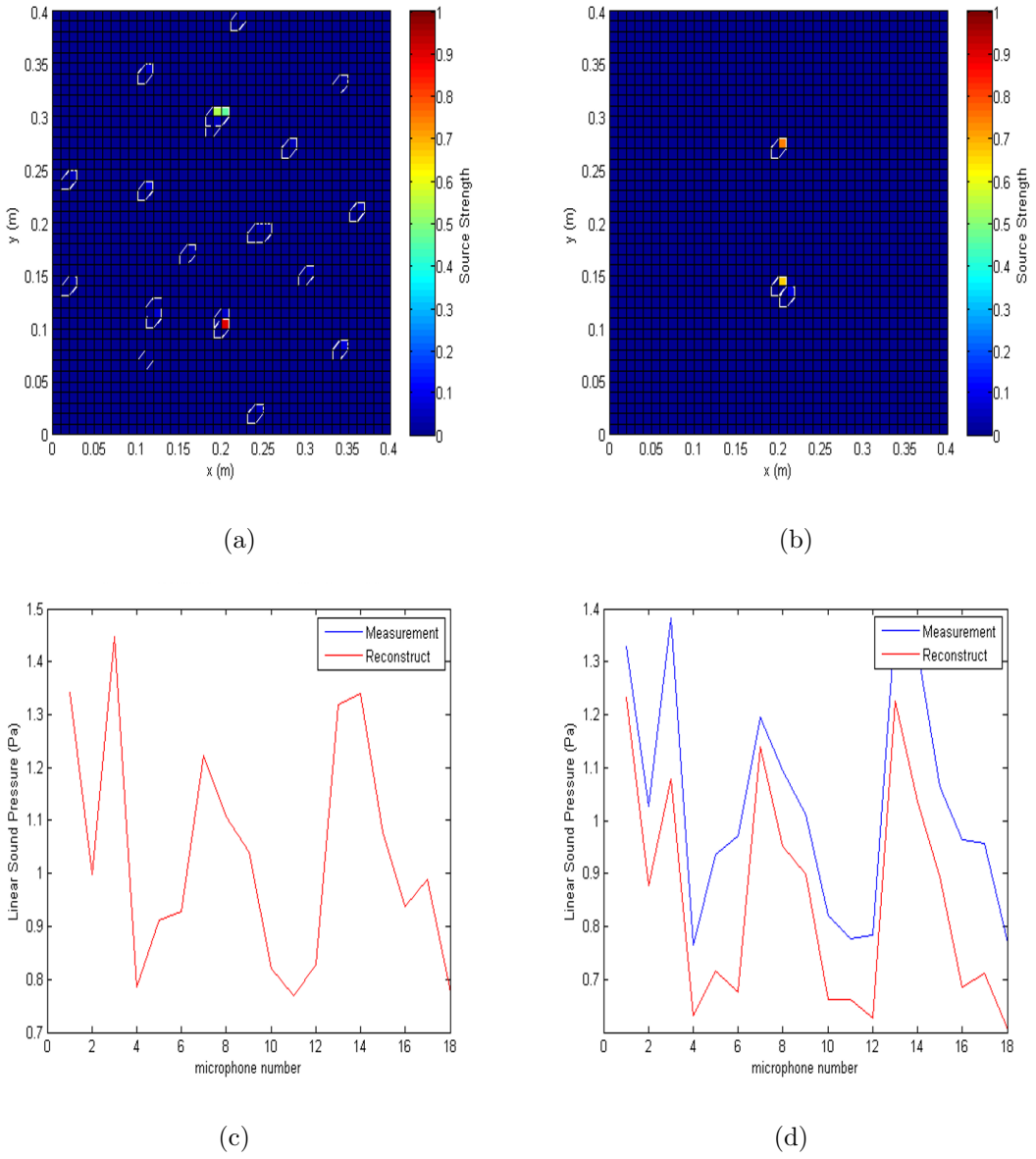

Figure 5.3. Final sound source reconstruction and reconstructed sound pressure with different λ_w at 300 Hz: (a) reconstructed sound source distribution with $\lambda_w = 100$, (b) reconstructed sound source distribution with $\lambda_w = 1$, (c) reconstructed sound pressure and virtual measurement comparison with $\lambda_w = 100$, and (d) reconstructed sound pressure and virtual measurement comparison with $\lambda_w = 1$.

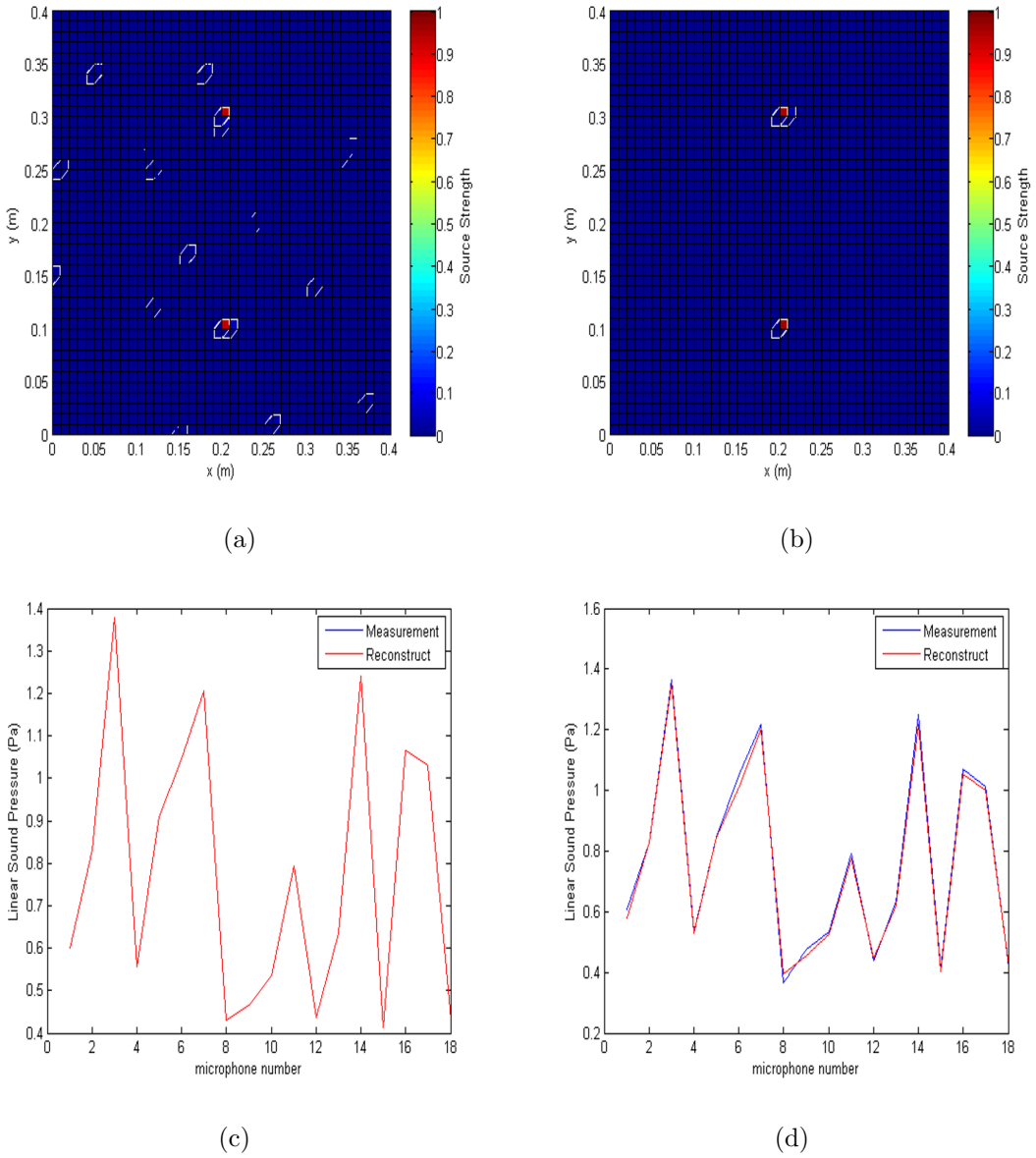

Figure 5.4. Final sound source reconstruction and reconstructed sound pressure with different λ_w at 2000 Hz: (a) reconstructed sound source distribution with $\lambda_w = 100$, (b) reconstructed sound source distribution with $\lambda_w = 1$, (c) comparison between reconstructed sound pressure and virtual measurement with $\lambda_w = 100$, and (d) comparison between reconstructed sound pressure and virtual measurement with $\lambda_w = 1$.

Based on these observations, it can be concluded that even though the l_1-norm minimization is a powerful tool in reconstructing sound fields and identifying sound source positions, but the weighting parameter λ_w has a strong influence on the final solution. If the value of λ_w is chosen to be too small, it is possible to obtain a clear image of the major sound source location, but it is also possible that the solution will miss minor sound sources since the solution probably is not accurate enough. On the other hand, if λ_w is chosen to be too large, then probably too much noise will be included in the solution which could cause a ghost source problem, as shown in the simulation. It is noted that in this section, the simulation experiment was very simple and the signal-to-noise ratio was large, so the ghost sources were not that obvious compared with the true sound sources. In practice, when the sound source is more complicated, the choice of an appropriate λ_w could be difficult.

5.4 Hybrid Method Compressive Sensing Method

Based on the observations of the WBH and l_1-norm minimization algorithms' characteristics, a hybrid method is proposed here. When using l_1-norm minimization, the reconstructed source locations were generally more accurate than when using WBH, but the appearance of ghost sources could mislead the observer as to the true sound source locations. So it seems promising to use l_1-norm minimization to find the initial solution from which the WBH algorithm can begin. This combined approach should allow accurate location of sound sources and, at the same time, the elimination of ghost sources. Under this motivation, and to improve the reconstruction results, a combination of these two methods is proposed. That is, the inverse problem is first solved by convex optimization, then instead of beginning the WBH iteration with zero source strengths, the source strength distribution resulting from the convex optimization is used as the initial solution for the WBH process. In this way, the WBH algorithm begins to search for the solution starting from a relatively accurate guess rather than from a zero source strength guess. Then, in the iterative WBH

process, the ghost sources created in the l_1-norm minimization solution are removed by enforcing the cardinality threshold in the WBH algorithm, with the result that the solution is concentrated at the correct source locations.

To test the proposed hybrid method, the same simulation experiment with two monopoles was conducted. The set up of the simulation is exactly the same as in Chapter 3: two closely-positioned monopoles with unit source strengths, and which were placed 0.2 m apart. The equivalent source plane was placed 2 cm behind the sound pressure reconstruction plane, and the virtual measurements were taken 0.05 m from the equivalent source plane at the same 18 virtual microphone locations as described in Chapter 3. Gaussian random white noise was added to the virtual measurements, with a signal-to-noise ratio of 30 dB. The first step of this hybrid process begins with l_1-norm minimization, and the weighting parameter in equation (3.24) was chosen to be $\lambda_w = 100$, to encourage an initial solution with ghost sources. Then the solution of the l_1-norm minimization procedure was used as the initial solution for WBH. The parameters in WBH were chosen to be the same as described in equation (3.13), but the value of D_0 was chosen to be 4. The reason to choose a larger D_0 is to avoid eliminating too many sources in the first iteration, which would cause inaccurate result: i.e., missing minor sources. The true sound source distribution, initial solution solved with l_1-norm minimization, reconstructed sound source distribution, and comparison between measurement and reconstruction at the virtual measurement position is shown in Figures (5.5) and (5.6) for 300 Hz and 2000 Hz, respectively. Based on these result, it can be seen that at both frequencies, the hybrid method did eliminate the ghost sources with a clearly accurate solution that indicates the correct sound source locations, and which adds more weighting to the correct sound sources to well represent the total sound field. The total source strength at both frequencies was 2, and at 300 Hz the hybrid method reconstructed the solution with total source strength of 2.03, and at 2000 Hz the reconstructed total source strength was 1.92. It is noted that the small over-estimation of the source strength at 300 Hz comes from the slightly inaccuracies of the sound source reconstruction

position: i.e., the true monopoles was located at (0.2 m, 0.1 m) and (0.2 m, 0.3 m), and the hybrid algorithm reconstructed them at (0.21 m, 0.1 m) and (0.19 m, 0.3 m). In order to compensate for the phase difference from the different sound source location, the algorithm over-estimated the total source strength.

It is noted that there are two important parameters in the hybrid process: the weighting parameter, λ_w in l_1-norm minimization, and D_0 in WBH. In this simulation, λ_w was chosen to be a large value in order to demonstrate the ghost sources elimination step in WBH, but in practice this value should be chosen based on the background noise level in order to obtain a good initial solution for the WBH process. Secondly, D_0 is the threshold that determines the smallest source strength to be considered as a true sound source in the first iteration, which was also chosen manually in this simulation. If a sound source is turned off in the first iteration, then it cannot be correctly recovered in the following iterations. So this value should be chosen based on the expectation of the true sound source strength in practice.

5.5 Summary

In this chapter, based on the motivation to improve the two sparse ESM algorithms, a hybrid of the WBH and l_1-norm minimization compressive sensing method was proposed. The search began with the motivation of improving the WBH algorithm reconstruction result, so the influence of the initial solution that begins the WBH algorithm iteration was studied. Instead of beginning the iteration with zero source strength, as described in the previous chapter, the iteration was began with an inaccurate initial solution in this chapter: i.e., only part of the initial solution was correct. It was found that the final solution obtained through the WBH algorithm is strongly influenced by the initial solution, so the reconstruction result could be improved if the initial solution for WBH algorithm is very close to the true sound field. Then the influence of different values of λ_w in the l_1-norm minimization was studied. Instead of using the optimal value in the previous chapter, in this chapter

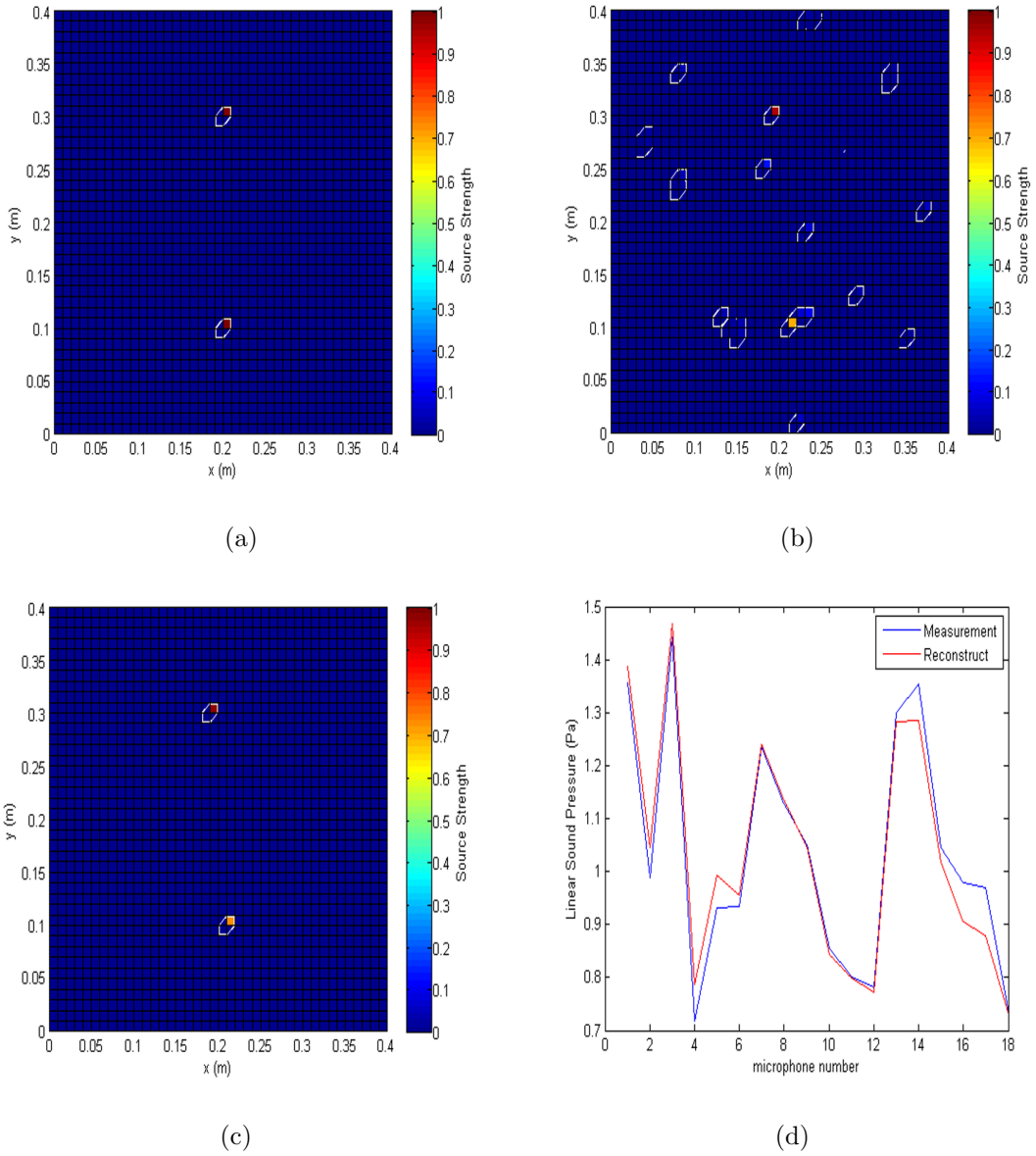

Figure 5.5. Comparison of location and strength between true sound source, initial solution solved with l_1-norm minimization and the hybrid method reconstructed sound source at 300 Hz: (a) simulated sound source, (b) initial solution $\vec{q}_0$ obtained with l_1-norm minimization, (c) reconstruction result with initial solution, and (d) reconstructed sound pressure and virtual measurement comparison.

the λ_w was intentionally chosen very small and very large. With a small λ_w, the solution could give a clear indication on sound source location, however, there is pos-

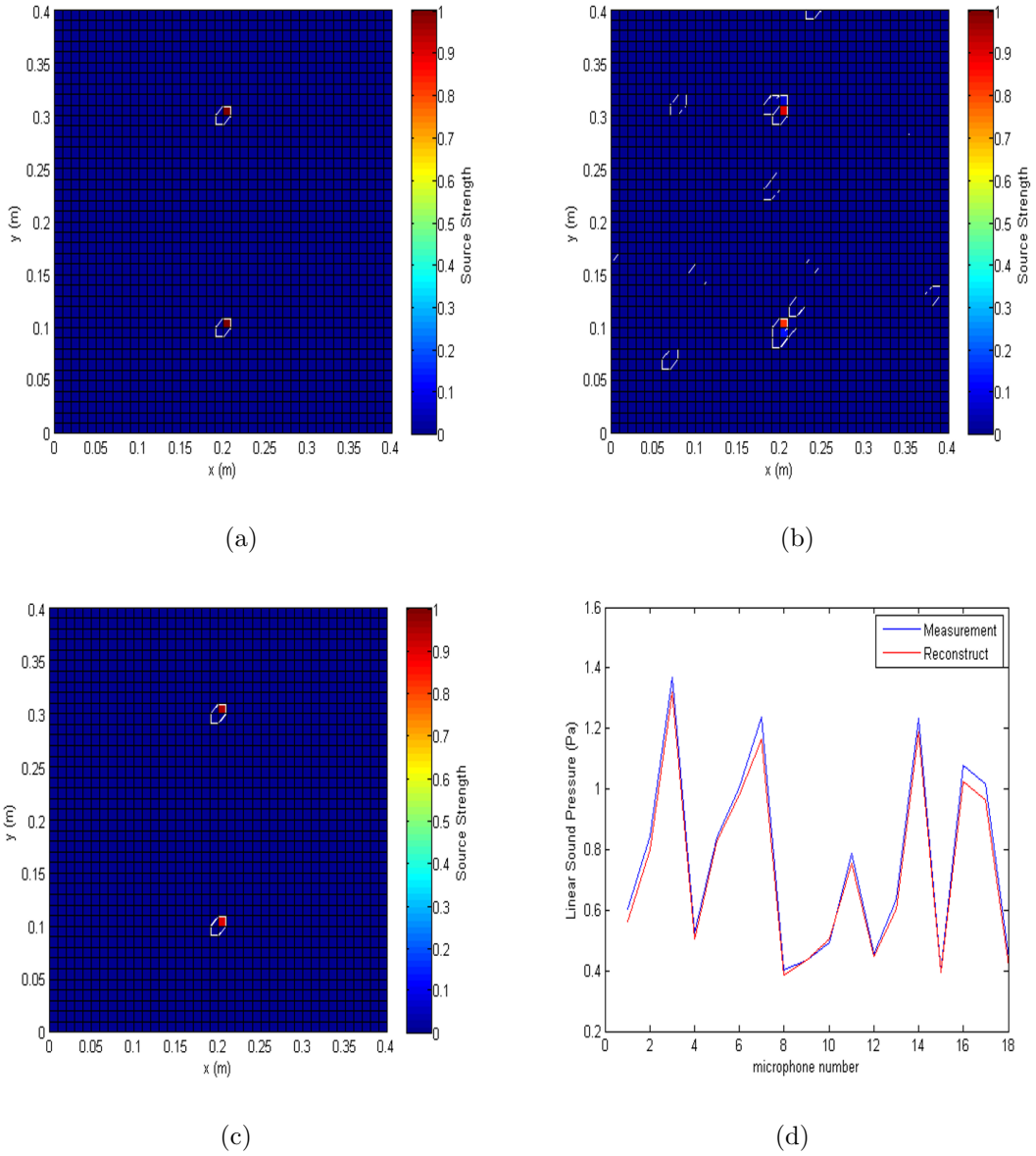

Figure 5.6. Comparison of location and strength between true sound source, initial solution solved with l_1-norm minimization and the hybrid method reconstructed sound source at 2000 Hz: (a) simulated sound source, (b) initial solution $\vec{q}_0$ obtained with l_1-norm minimization, (c) reconstruction result with initial solution, and (d) reconstructed sound pressure and virtual measurement comparison.

sibility that the solution cannot well represent the sound field. And if the λ_w was chosen to be a large value, then it is possible that the solution includes too much

noise in the solution, and causes ghost sources, which could mislead as to the true sound source location. Based on these observation, the hybrid method combining these two algorithm was proposed. From the simulation result, it could be seen that the hybrid method combined the advantages of these two methods: i.e., the major sound source locations were accurately determined and ghost sources were removed by controlling the cardinality of the solution. In the hybrid method, two parameter are particularly important: the first is the weighting parameter, λ_w, since it controls how much noise is included in the initial solution, which serves as the starting point of the WBH procedure. Here, this parameter was chosen manually based on multiple experiments and comparisons of the reconstruction result and the expected result. The application of certain parameter selection strategies will be studied in future work, and might involve the use of the L-curve method, for example. The second important parameter is D_0, which appears in the WBH process, since this parameter determines how many sources will be turned off in the first iteration. This parameter was also chosen manually in the present work as discussed above.

6. EXPERIMENT WITH DIFFERENT SOUND SOURCES

6.1 Introduction

In the previous chapters, two sparse ESM algorithms, WBH and l_1-norm minimization, were studied through simulation experiments. Then based on the characteristics of those two algorithms, a hybrid compressive sensing process combining these two algorithms was proposed and studied through simulation experiments. Through the simulation experiments, it was proven that the proposed hybrid compressive sensing methods can be used to identify the major sound sources when using only dozens of measurements, even when the sound sources are closely-positioned. In this chapter, several experimental test results will be presented. The first experiment is the reconstruction of the sound field generated by one loudspeaker, which is a relatively simple source to test the capability of the sparse ESM algorithms. Then following the same logic as the simulation experiment, in the second experiment two loudspeakers were used as sound sources and placed side by side to test the capability of the sparse ESM algorithm to separate the sound sources. In these experiments, the three sparse ESM algorithms were used to reconstruct the sound field. In order to verify the sound field reconstruction result, a sound intensity measurement with an intensity probe scan was conducted and that measurement result was used to compare with the sound field reconstruction results. The third experiment was a test on a diesel engine.

Diesel engine noise is a concern in both municipal environments and in an occupational health and safety context due to the use of diesel engines in heavy industry and transportation. In order to reduce engine noise levels, a precise knowledge of the primary noise source locations is required to guide the efficient application of noise control resources. As a complex sound source (i.e., combustion noise, mechanical noise, etc.) [54, 55], a large array of measurements must be conducted to identify the

noise source locations when using conventional holography approaches, in order simultaneously to ensure good spatial resolution while avoiding spatial aliasing. Thus, it would be useful if the solutions proposed here can offer accurate noise source locations with a relatively small number of spatial measurements. In the diesel engine experiment the Partial Field Decomposition (PFD) is proposed to separate uncorrelated sound sources. PFD is based on the use of SVD to decompose the total sound field into different partial fields which are generated by uncorrelated sound sources, then these partial field can be reconstructed independently [56–58]. With this method the sound source location and the sound field can be reconstructed more accurately, and the uncorrelated sound sources can also be quantified separately. Based on these experimental tests, the capability to apply these algorithms in practice was commented upon.

6.2 One Loudspeaker Sound Field Reconstruction

The first experiment was a one loudspeaker test which was conducted in the Herrick Laboratories anechoic chamber. The loudspeaker used in this experiment was an Infinity Primus P163 as shown in Figure (6.1). This loudspeaker generates low frequency noise, i.e., below 2000 Hz, from the diaphragm, which is located in the center of the loudspeaker. High frequency noise is generated by the tweeter, which located at the top of the loudspeaker. The frequencies between 2 kHz and 3 kHz cover the transition frequencies, in which range the diaphragm and the tweeter act together.

In order to compare the the reconstruction results with the true sound field, it is desired to use the same input signal for both an intensity scan measurement and the microphone array measurement. In the experiment, the sound intensity was measured with a Bruel and Kjaer sound intensity probe type 3654 and 3599, which is composed of two microphones. Since the sound intensity was calculated with two-microphones

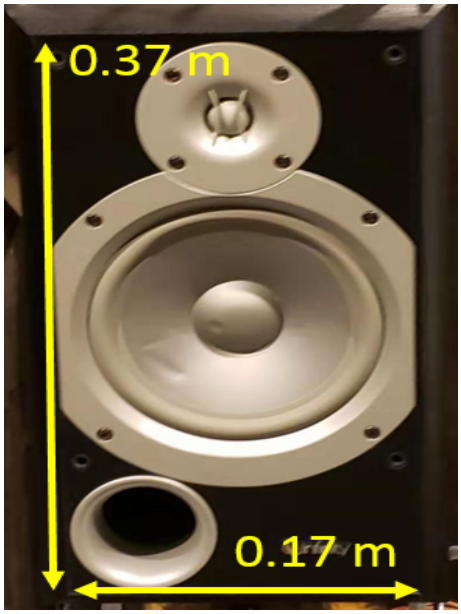

Figure 6.1. Loudspeaker (Infinity Primus P163) used in experiment.

cross-spectral approach, based on the sound pressure measured at two microphones, the sound intensity at the middle point between the two microphones is:

$$I = \frac{1}{2}\frac{1}{\omega\rho_0\Delta}\mathrm{Im}(P_1P_2^*), \tag{6.1}$$

where ω is the angular frequency, ρ_0 is the density of air, Δ is the distance between the two microphones, P_1 and P_2 are the measured sound pressure spectra at microphones 1 and 2, respectively, and $*$ stand for complex conjugate. So it is possible to extract the sound pressure data at the intensity measurement position and calculate the sound pressure transfer functions between each measurement point and the input signal to the loudspeaker with Welch s averaged periodogram method [59]. Then with the patched measurement principle, an effectively simultaneously measured sound pressure data set at all the measurement points can be constructed by multiplying all the transfer functions by the input signal to the loudspeaker, which is equivalent to a microphone array measurement. In the present work, sound reconstruction results are shown for different measurement conditions: i.e., near-field measurements, and far-field measurements.

6.2.1 Reconstruction with Near-field Measurement

The intensity was measured 0.055 m in front of the loudspeaker, the measurement covered an area of 0.27 m by 0.45 m, which is slightly larger than the surface of the loudspeaker front face. In order to visualize the sound field up to 4000 Hz, the spacing between the intensity measurement was chosen to be 0.03 m, which is less than half of the wavelength at 4000 Hz, in both x and y directions; so there were 160 measurements in total, which comprised an equivalent regular rectangular microphone array measurement after the patched measurement calculation. During the measurement, the input signal to the loudspeaker was Gaussian white noise of 25.6 kHz bandwidth generated by PULSE software through a computer. At each measurement point, the intensity probe recorded 10 seconds of time data at a sampling frequency of 25.6 kHz. The measured time history data was transformed to the frequency domain by PULSE too; the parameters in the Fourier transform were set up as: the Hann window with 6400 points, overlap between each window was 50%, and 100 averages in total. The monopoles were located on an equivalent source plane which was placed 0.02 m behind the loudspeaker front face. The monopole source mesh with a 0.01 m spacing in both directions covered an area of 0.27 m by 0.45 m area, which was the same as the measurement area. That is, 1288 parameters needed to be estimated based on 160 measurements, thereby forming an under-determined system. Figure (6.2) shows the relative positions between the equivalent source plane, the measurement plane and the loudspeaker position. It is noted that in this experiment, the reconstruction plane was coincident with the measurement plane to allow a direct comparison of the measured and reconstructed intensities.

SONAH, WBH, l_1-norm minimization and the hybrid method were used to reconstruct the sound pressure and intensity field generated by the loudspeaker on the reconstruction plane, and the reconstruction results were compared with the intensity probe measurement. To reconstruct the sound field with the SONAH method, the virtual source plane was placed 0.03 m behind the reconstruction plane, and the

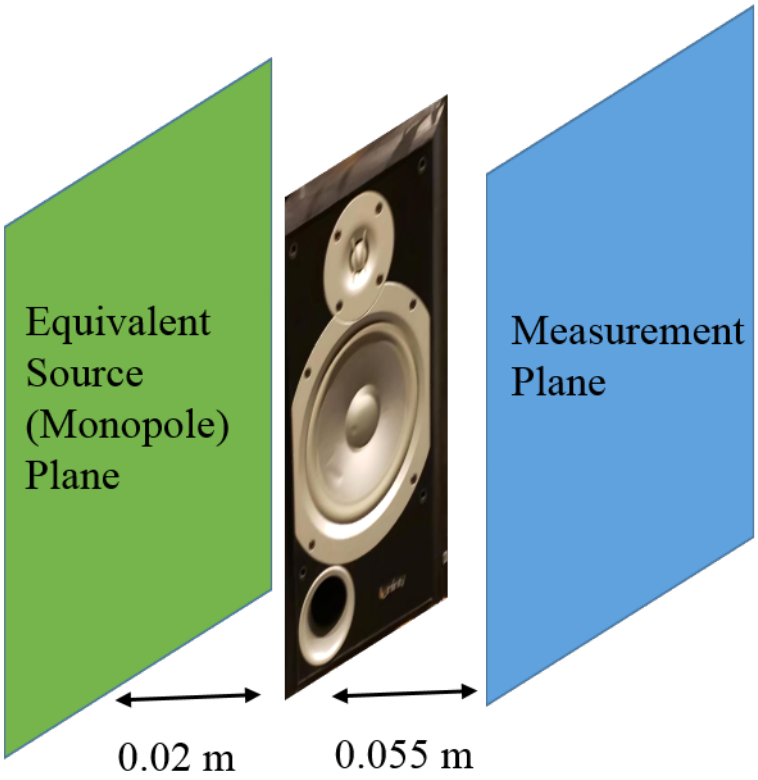

Figure 6.2. Relative position for near-field measurement set up.

regularization parameter, , was calculated by using the L-curve method. With the WBH method, the parameters used in the WBH process were presented in equation (3.13). And for the l_1-norm minimization procedure, the weighting parameter, λ_w, was chosen to be 10. For the hybrid method, the weighting parameter in the l_1-norm minimization procedure was chosen to be 100, and the parameters in the WBH method were kept the same as in equation (3.13), except for $D_0 = 10.1$ in order to keep the secondary source in the first iteration. The equations for the sound pressure, P, and velocity, $\vec{V}$, for the different methods at the reconstruction positions have been presented in previous chapters, and the sound intensity was calculated with equation (4.1). Then the total sound power over the measurement plane was calculated with equation (4.2).

Figure (6.3) shows the sound intensity distribution measured by the intensity probe at 0.8, 2.4 and 4 kHz. In this and the following figures, the black box indicates the region of the loudspeaker front face, the small circle at the top of the loudspeaker is the tweeter position, the big circle in the middle is the area of the membrane, and the small circle at the lower left corner is the loudspeaker port. Based on the measurement result, the sound source locations were as expected: i.e., at 0.8 kHz the membrane generated the low frequency sound, at 2.4 kHz the sound was generated from both tweeter and membrane, and at 4 kHz the sound radiates from the tweeter.

Figures (6.4) (6.5) and (6.6) show the contour plots of the reconstructed sound intensity distributions 0.055 m from the loudspeaker front face, where the intensity measurement was conducted, at 0.8, 2.4 and 4 kHz, respectively. At 0.8 kHz, the measured radiated sound power was 47.9 dB, SONAH recovered 40.8 dB, the WBH algorithm recovered 27.9 dB, l_1-norm minimization recovered 34.1 dB, the hybrid algorithm recovered 34.4 dB. At 2.4 kHz, the measured radiated sound power was 46.3 dB; SONAH recovered 47.5 dB, the WBH algorithm recovered 39.9 dB, l_1-norm minimization recovered 46.5 dB, and the hybrid algorithm recovered 46.1 dB. At 4 kHz, the measured radiated sound power was 49.5 dB; SONAH recovered 46.8 dB, the WBH algorithm recovered 43.2 dB, l_1-norm minimization recovered 43.8 dB, and the hybrid algorithm recovered 45.0 dB.

Thus, at low frequency, SONAH recovered the most energy while the other sparse ESM algorithms strongly under-estimated the sound power. As frequency increases, SONAH can still give a good estimation of the total sound power, l_1-norm minimization and the hybrid method also recovered sound power close to the measurement, while WBH under-estimated the total sound power for all frequencies.

By comparing the spatial sound field reconstruction result with the intensity measurement, all the methods correctly identified the major sound source locations: i.e., the noise source location moves from the diaphragm location to the tweeter position as the frequency increases, which matches the intensity measurement. Also, SONAH re-

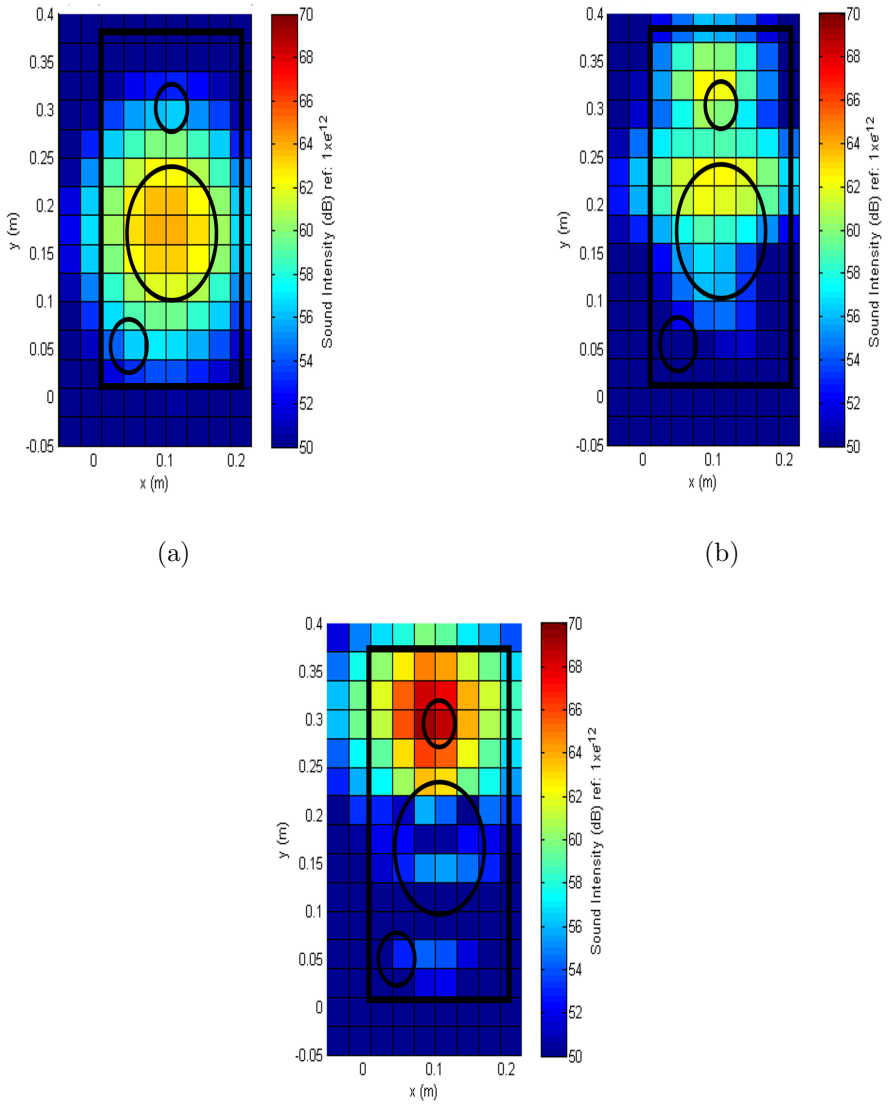

Figure 6.3. Measured sound intensity field 0.055 m from loudspeaker front face: (a) 0.8 kHz, (b) 2.4 kHz, and (c) 4 kHz.

constructed the most detail of the sound field: e.g., at 2.4 kHz it clearly separates the tweeter and membrane with the correct source strength, although it over-estimates the total sound power a little bit. The WBH algorithm identified the sound source locations at different frequencies, however, it recovered the least energy among all

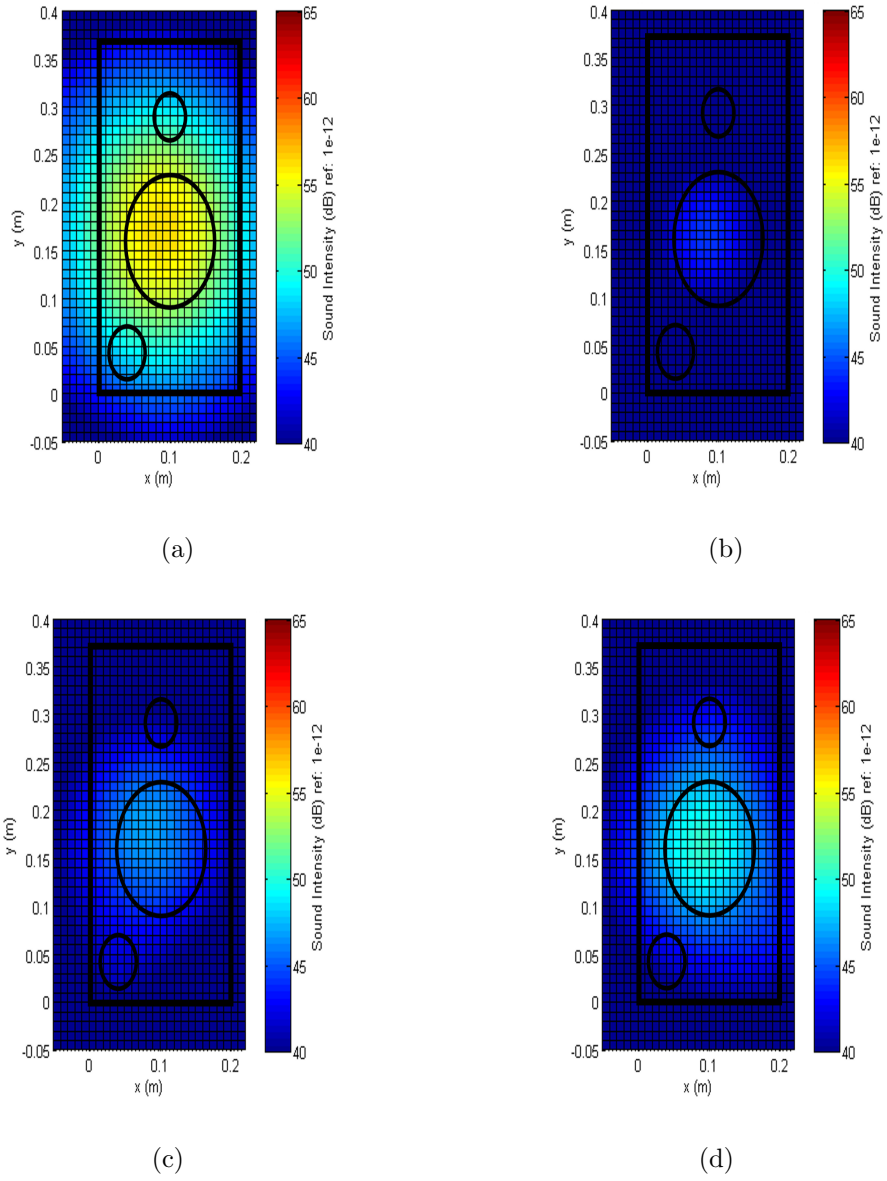

Figure 6.4. 0.055 m from loudspeaker front face sound intensity field reconstruction results with different NAH method at 0.8 kHz with 160 microphones near-field measurement: (a) SONAH method, (b) WBH method, (c) L_1-norm minimization method, and (d) hybrid method.

the methods, especially at low frequency. The l_1-norm minimization method also successfully identified sound source locations, and recovered more energy compared with the WBH algorithm, but it also didn't clearly separate the two sound source

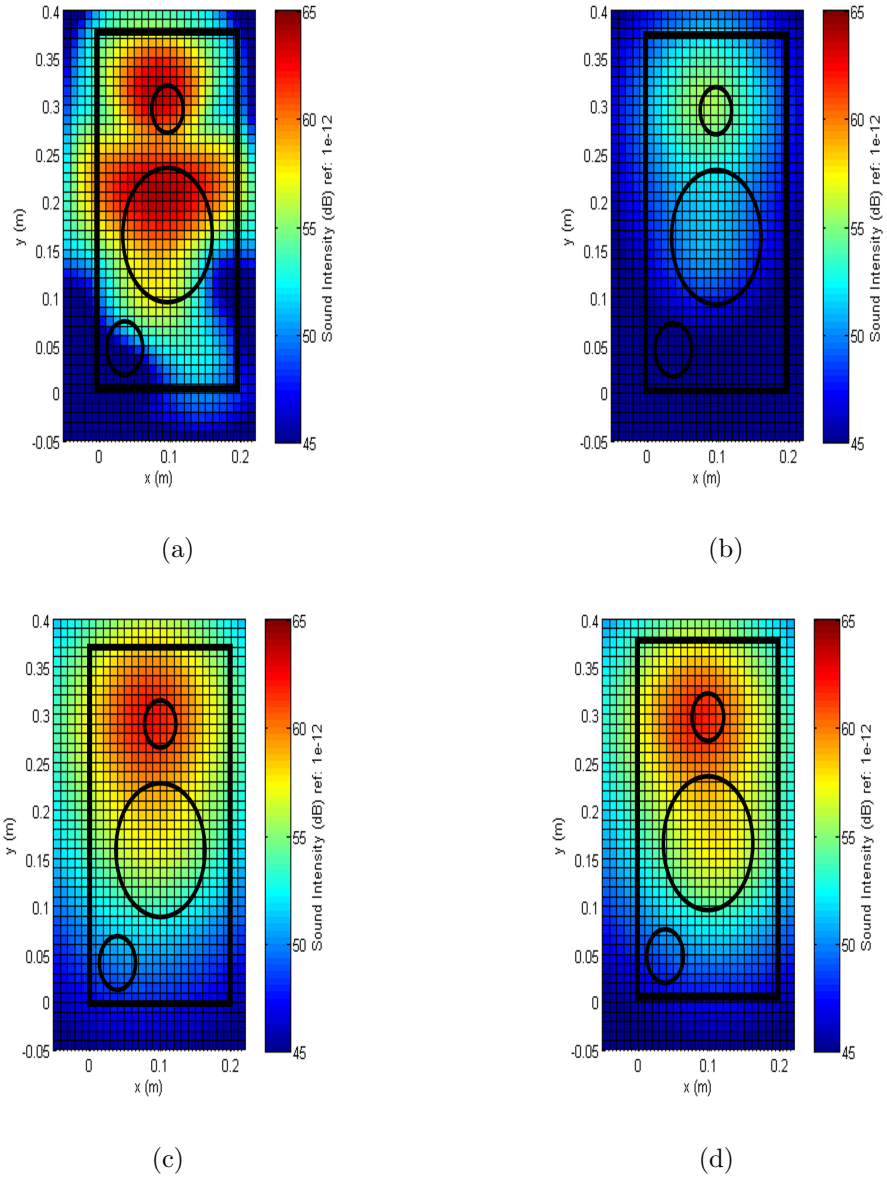

Figure 6.5. 0.055 m from loudspeaker front face sound intensity field reconstruction results with different NAH method at 2.4 kHz with 160 microphones near-field measurement: (a) SONAH method, (b) WBH method, (c) L_1-norm minimization method, and (d) hybrid method.

locations at 2.4 kHz. The hybrid method reconstructed basically the same result as l_1-norm minimization, however, at 2.4 kHz it gave a better indication of the second sound source: i.e., the membrane.

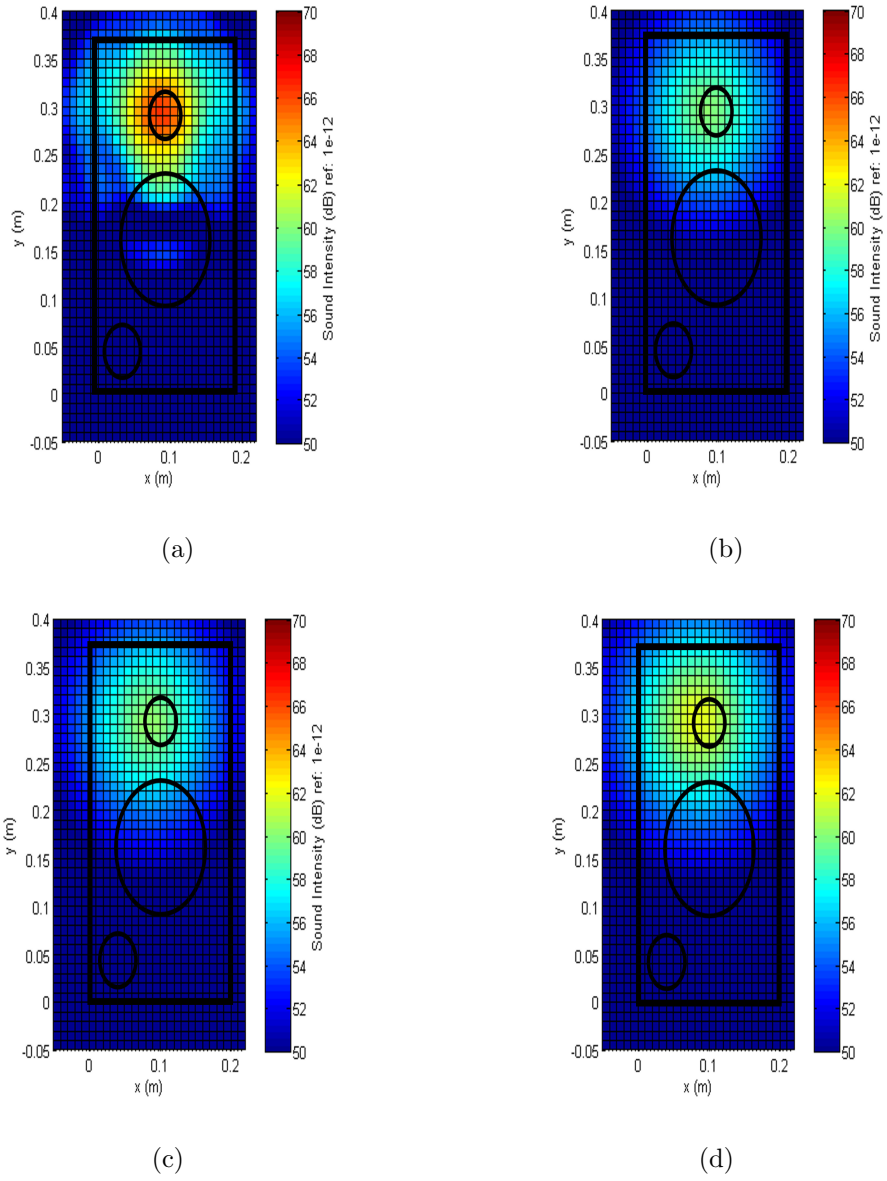

Figure 6.6. 0.055 m from loudspeaker front face sound intensity field reconstruction results with different NAH method at 4 kHz with 160 microphones near-field measurement: (a) SONAH method, (b) WBH method, (c) L_1-norm minimization method, and (d) hybrid method.

The results observed here agree with the simulations presented in previous chapters: at low frequency, the membrane is the major sound source, which can be considered as an extended sound source. So the sparse ESM algorithms identified the sound

source location but failed to well-represent the total sound field. As the frequency increases, the sound source location moves from membrane to tweeter and becomes more concentrate, so the sparse ESM algorithm reconstructed more accurate results. SONAH reconstructed the sound field accurately across all frequencies, since it includes all the elementary wave components to represent the sound field, especially evanescent waves in the near field.

In this experiment, an equivalent 160 regular rectangular microphone array was used to reconstruct the sound field with 1288 unknowns in the model, and the reconstruction results using different methods were commented upon. However, 160 is still a relatively large number of microphone measurements. In order to reduce the number of microphones but keep the same measurement area, then the spacing between the microphones was doubled in both the x and y directions, that is, to 0.06 m. Then the equivalent regular rectangular microphone array was reduced to 40 microphones, thus decreasing the spatial sampling rate and the measurement was still made 0.055 m from loudspeaker front face. The effectively simultaneously microphone array measurement was generated with the same patched measurement principle with the same data used in the 160 channels measurement, that the reconstruction results can still be compared with the direct sound intensity measurement. The set up of the equivalent source plane was kept the same: i.e., 1288 monopoles and 0.02 m behind the loudspeaker front face. The parameters in SONAH, WBH, l_1-norm minimization and the hybrid algorithm were kept the same as described in the previous experiment. The sound field reconstruction results 0.055 m away from loudspeaker front face at 0.8 kHz, 2.4 kHz and 4 kHz are shown in Figures (6.7), (6.8) and (6.9). At 0.8 kHz, the measured radiated sound power was 47.9 dB; SONAH recovered 40.7 dB, the WBH algorithm recovered 27.9 dB, l_1-norm minimization recovered 33.0 dB, the hybrid algorithm recovered 33.7 dB. At 2.4 kHz, the measured radiated sound power was 46.3 dB; SONAH recovered 47.4 dB, the WBH algorithm recovered 39.9 dB, l_1-norm minimization recovered 43.8 dB, and the hybrid algorithm recovered 44.7 dB. At 4 kHz, the measured radiated sound power was 49.5 dB; SONAH recovered

42.3 dB, the WBH algorithm recovered 42.3 dB, l_1-norm minimization recovered 43.3 dB, and the hybrid algorithm recovered 43.3 dB.

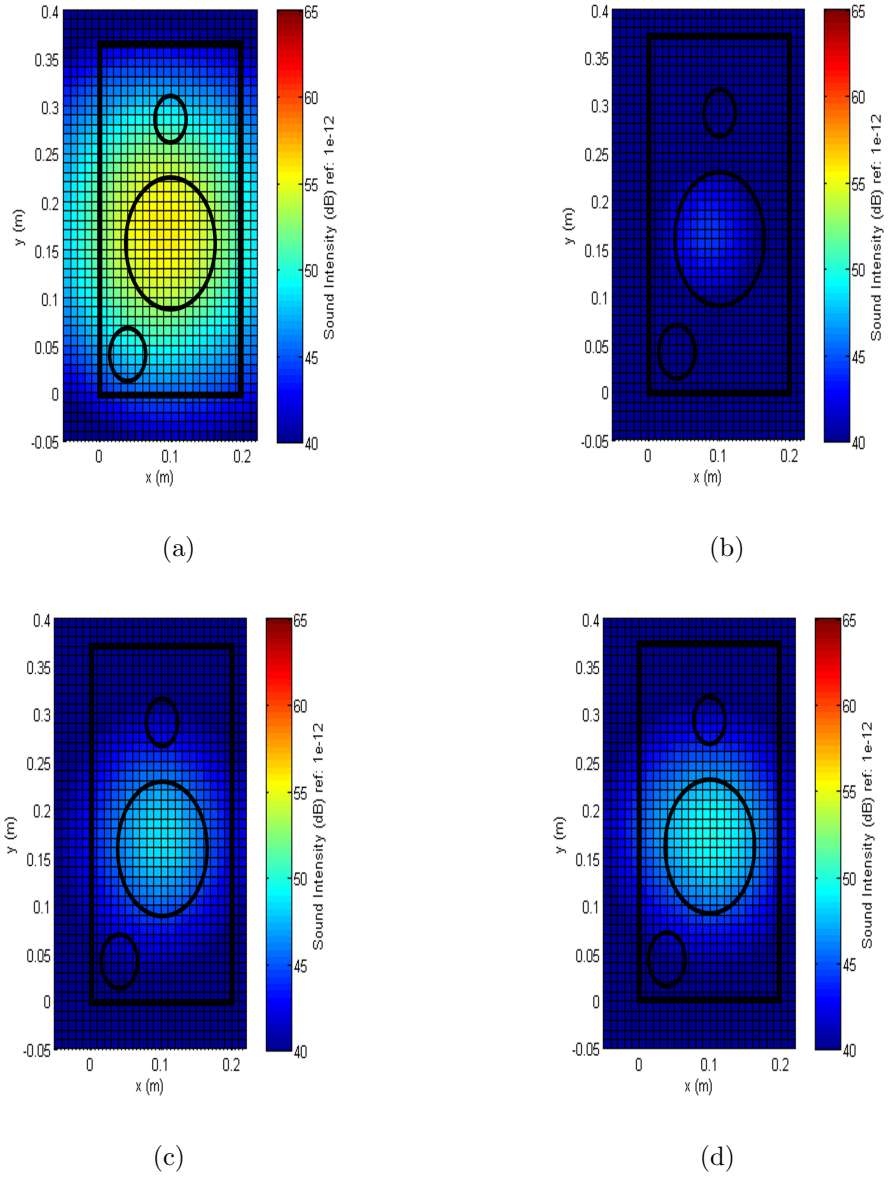

Figure 6.7. 0.055 m from loudspeaker front face sound intensity field reconstruction results with different NAH method at 0.8 kHz with 40 microphones near-field measurement: (a) SONAH method, (b) WBH method, (c) l_1-norm minimization method, and (d) hybrid method.

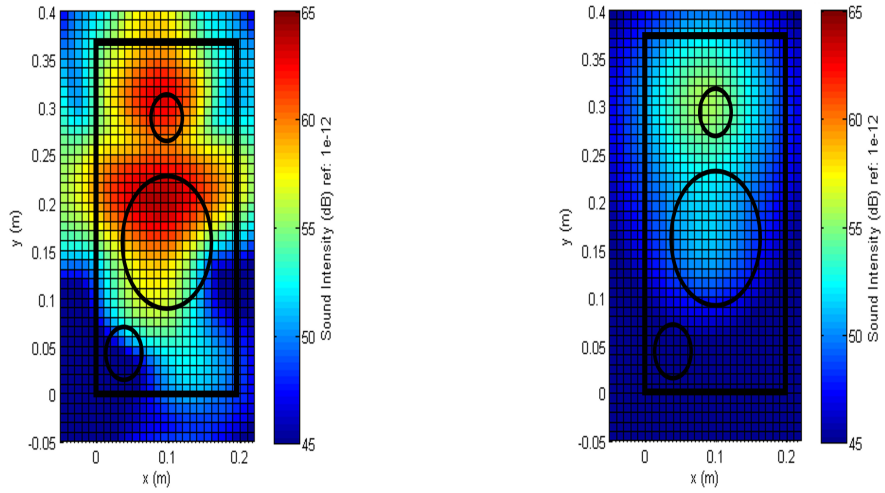

(a)

(b)

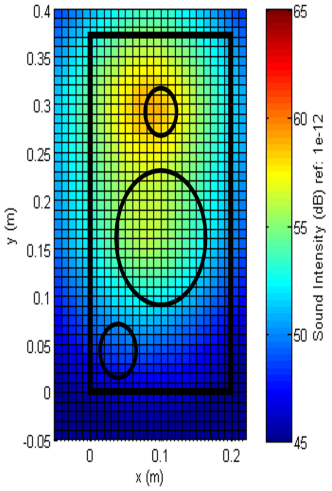

(c)

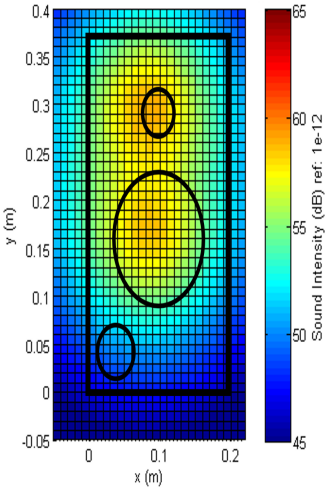

(d)

Figure 6.8. 0.055 m from loudspeaker front face sound intensity field reconstruction results with different NAH method at 2.4 kHz with 40 microphones near-field measurement: (a) SONAH method, (b) WBH method, (c) l_1-norm minimization method, and (d) hybrid method.

So the sound power reconstructed by different methods with 40 measurements are in general smaller than the sound power reconstructed with 160 measurements, especially for the SONAH method at 4 kHz. And similar conclusions can be found from

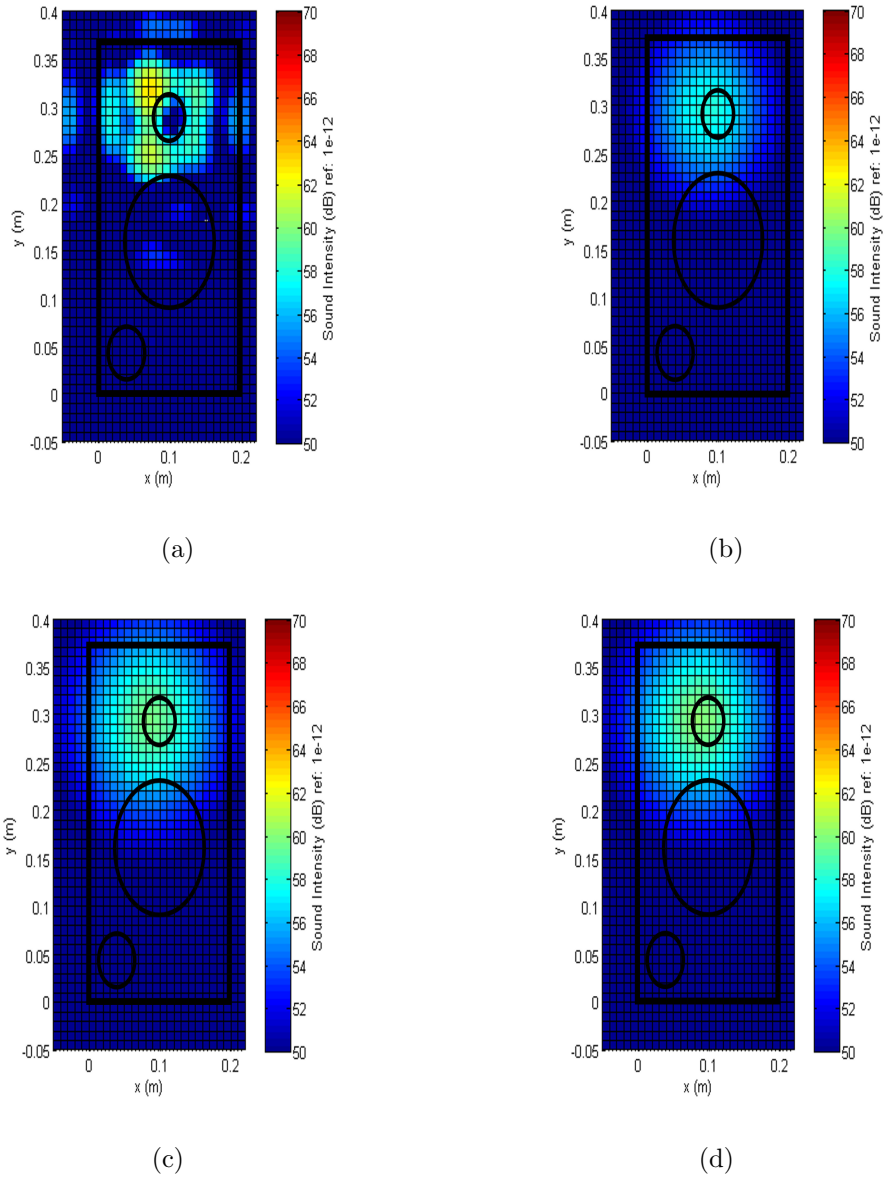

Figure 6.9. 0.055 m from loudspeaker front face sound intensity field reconstruction results with different NAH method at 4 kHz with 40 microphones near-field measurement: (a) SONAH method, (b) WBH method, (c) l_1-norm minimization method, and (d) hybrid method.

the spatial sound field reconstruction results: e.g., the SONAH method reconstructed the most detail, WBH under-estimated the total sound power, etc. But at 4000 Hz, the SONAH method cannot reconstruct an accurate sound source location compared

with the 160 channels reconstruction result. At 4000 Hz, the SONAH reconstructed two sound sources around the tweeter position, which seems like spatial aliasing due to the microphone spacing being larger than half of the wave length, which is 0.07 m at 4 kHz.

To verify if this explanation is true, the number of microphones was further reduced: the measurement area still covered the same region, but the spacing between the microphones was increased to 0.12 m in the both x and y direction. In this case, there were only 12 microphone measurements. With the same equivalent plane set up and the same parameters used in previous experiment, the sound intensity reconstruction results are shown in Figures (6.10), (6.11) and (6.12). At 0.8 kHz, the measured radiated sound power was 47.9 dB; SONAH recovered 40.8 dB, the WBH algorithm recovered 27.9 dB, l_1-norm minimization recovered 37.9 dB, and the hybrid algorithm recovered 37.8 dB. At 2.4 kHz, the measured radiated sound power was 46.3 dB; SONAH recovered 43.2 dB, the WBH algorithm recovered 38.2 dB, l_1-norm minimization recovered 45.1 dB, and the hybrid algorithm recovered 45.6 dB. At 4 kHz, the measured radiated sound power was 49.5 dB; SONAH recovered 36.8 dB, the WBH algorithm recovered 38.1 dB, l_1-norm minimization recovered 42.7 dB, and the hybrid algorithm recovered 43.6 dB.

Then, with the microphone spacing increasing to 0.12 m, aliasing is observed not only at 4 kHz but also at 2.4 kHz with the SONAH method, which confirms that the SONAH method needs to satisfy the spatial sampling law to obtain accurate reconstruction results. For the sparse ESM algorithms, even though the spatial sampling spacing is much larger than the wavelength of the frequency of interest, the major sound source locations can still be identified without aliasing in the loudspeaker test, and they recovered similar sound power compared with 40 and 160 measurements. It is noted that when the number of measurements was reduced to 12, all the reconstructed sound source locations did not exactly overlap with the true sound source location: e.g., at 4 kHz, the hot spot was not exactly inside the tweeter region.

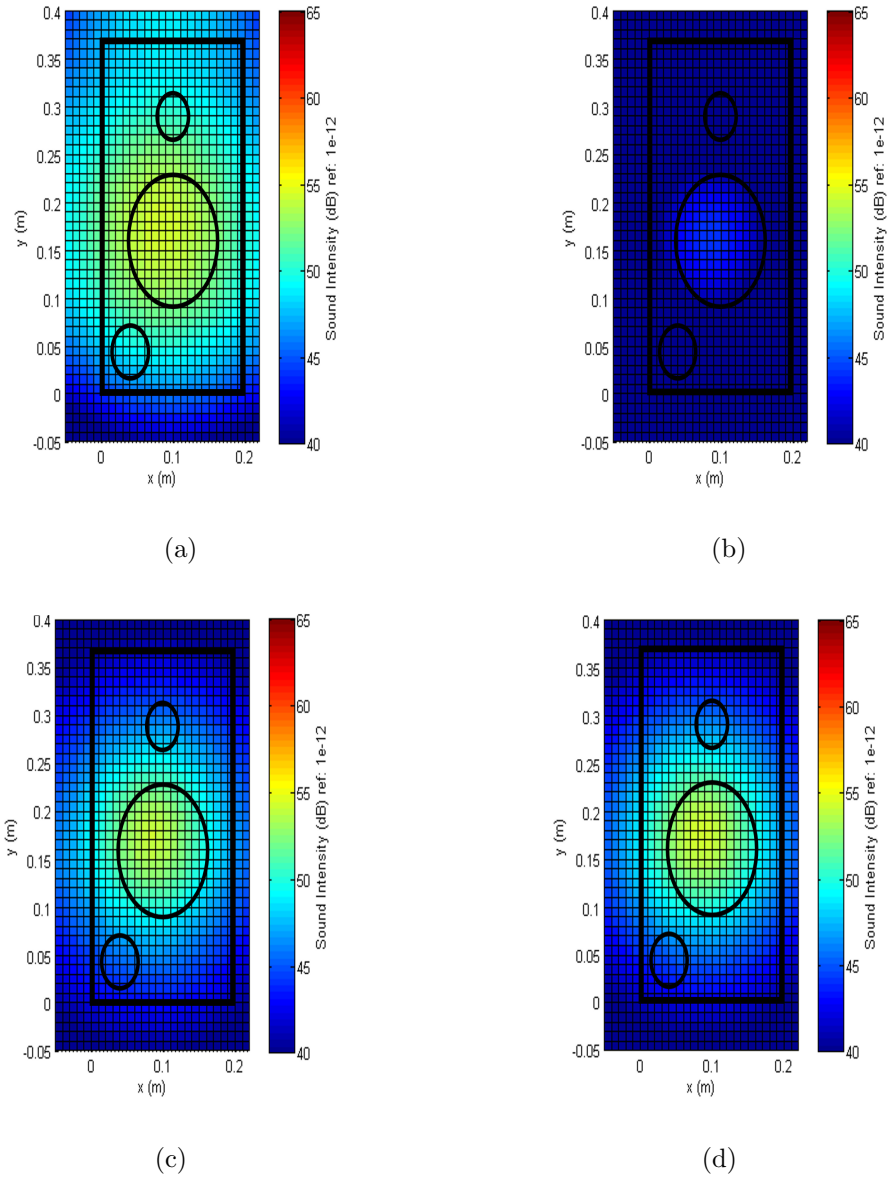

Figure 6.10. 0.05 m from loudspeaker front face sound intensity field reconstruction results with different NAH method at 0.8 kHz with 12 microphones near-field measurement: (a) SONAH method, (b) WBH method, (c) l_1-norm minimization method, and (d) hybrid method.

This observation indicates that the reconstruction result has a microphone-local effect when the number of measurements is small and taken in the near-field.

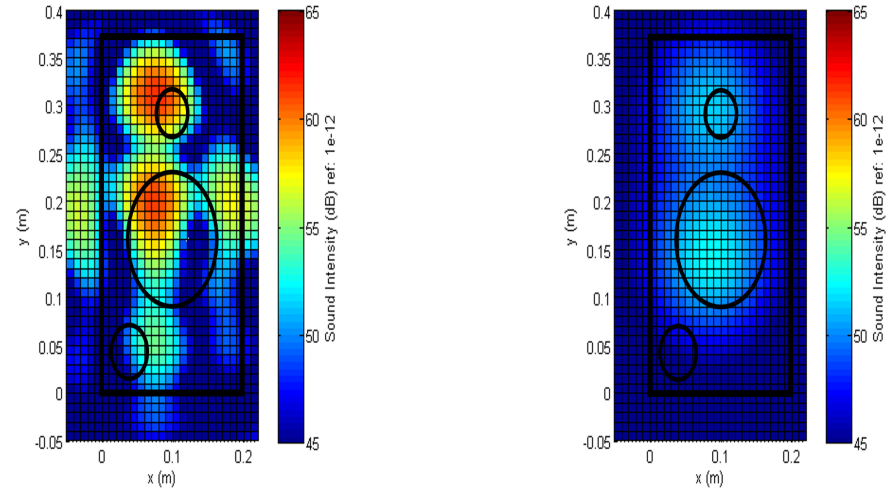

(a)

(b)

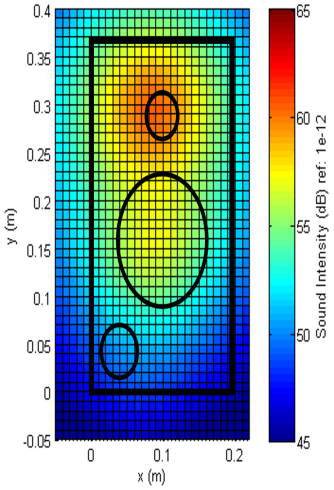

(c)

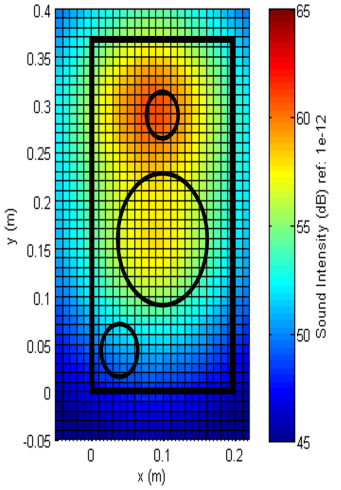

(d)

Figure 6.11. 0.05 m from loudspeaker front face sound intensity field reconstruction results with different NAH method at 2.4 kHz with 12 microphones near-field measurement: (a) SONAH method, (b) WBH method, (c) l_1-norm minimization method, and (d) hybrid method.

6.2.2 Reconstruction with Far-field Measurement

In the previous experiment, the measurement distance was 0.055 m from the loudspeaker front face, which is a very close measurement distance. However, in the

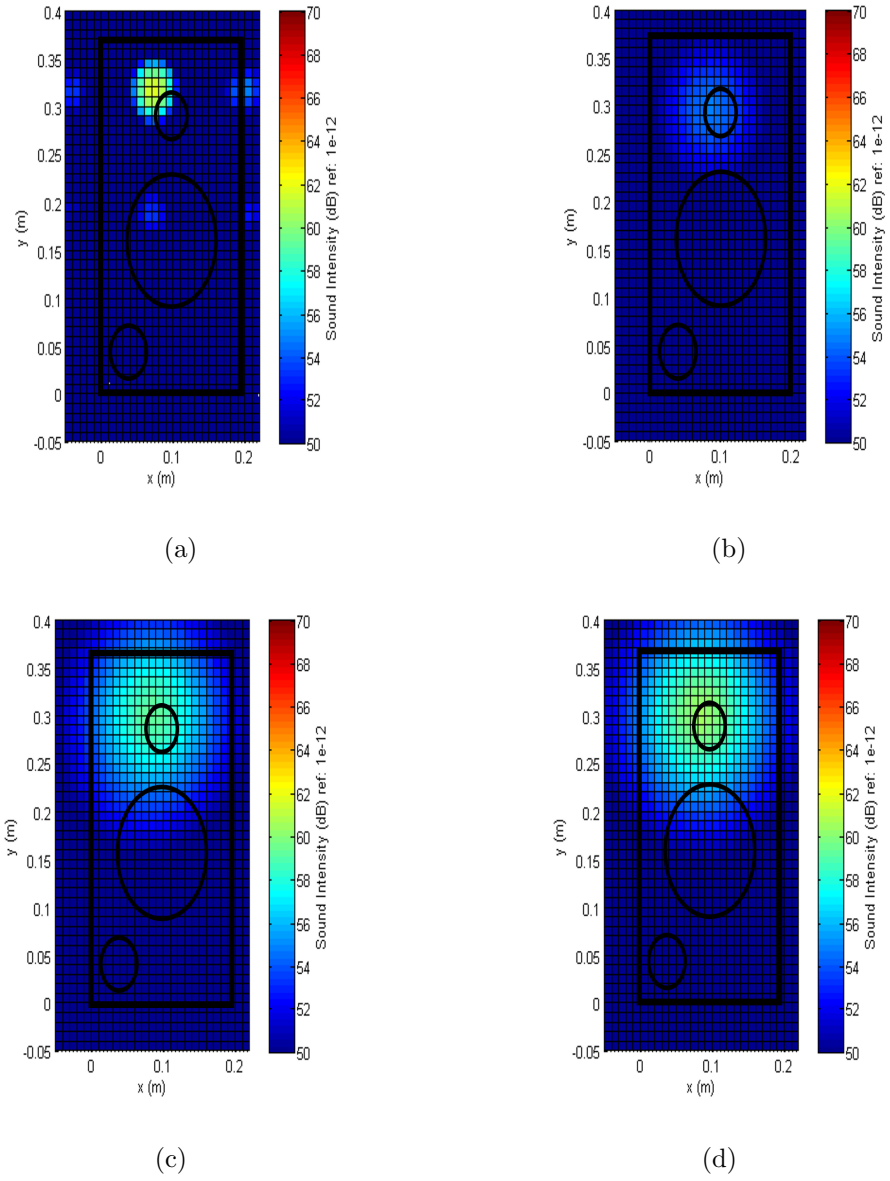

Figure 6.12. 0.05 m from loudspeaker front face sound intensity field reconstruction results with different NAH method at 4 kHz with 12 microphones near-field measurement: (a) SONAH method, (b) WBH method, (c) l_1-norm minimization method, and (d) hybrid method.

industrial experimental environment, such a close measurement distance is not always possible due to test environment: e.g., various pipes block near-field measurements in the diesel engine test. In this section, the sound source was still a single loudspeaker,

but the intensity measurement was taken 0.485 m from the loudspeaker front face. The large measurement distance will potentially increase the reconstruction difficulty due to lower signal-to-noise ratio compare with near-field measurement, especially for the evanescent wave components.

The measurement covered an area of 0.27 m by 0.45 m, and the intensity measurement spacing between neighboring measurement points was 0.03 m, in both x and y directions, thus creating 160 sound pressure measurements as described in the previous section. The input signal to the loudspeaker was Gaussian white noise of 25.6 kHz bandwidth generated by PULSE software through a computer. The time history data was processed with exactly the same parameter set up as described in the previous section. The monopoles were located on the equivalent source plane which was 0.02 m behind the loudspeaker front face. The monopole source mesh with a 0.01 m spacing in both directions covered an area of 0.27 m by 0.45 m area, which is the same as the measurement area. Figure (6.13) shows the relative positions of the equivalent source plane, the reconstruction plane, the measurement plane and the loudspeaker position.

SONAH, WBH, l_1-norm minimization and the hybrid method were used to reconstruct the sound pressure and intensity field generated by the loudspeaker on the reconstruction plane, and the reconstruction results were compared with the intensity probe measurement. All the parameters used in the different methods were exactly the same as described in the previous section. The equations for the sound pressure, P, and velocity, $\vec{V}$, for the different methods at the reconstruction positions have been presented in previous chapters, and the sound intensity was calculated with equation (4.1). Then the total sound power over measurement plane was calculated by using equation (4.2).

It is noted that in this experiment far-field measurement data was used to reconstruct the sound field at 0.055 m from the loudspeaker front face, where the near-field intensity scan measurement was conducted, as described in the previous section. Then the reconstruction result will be compared with the direct measurement result

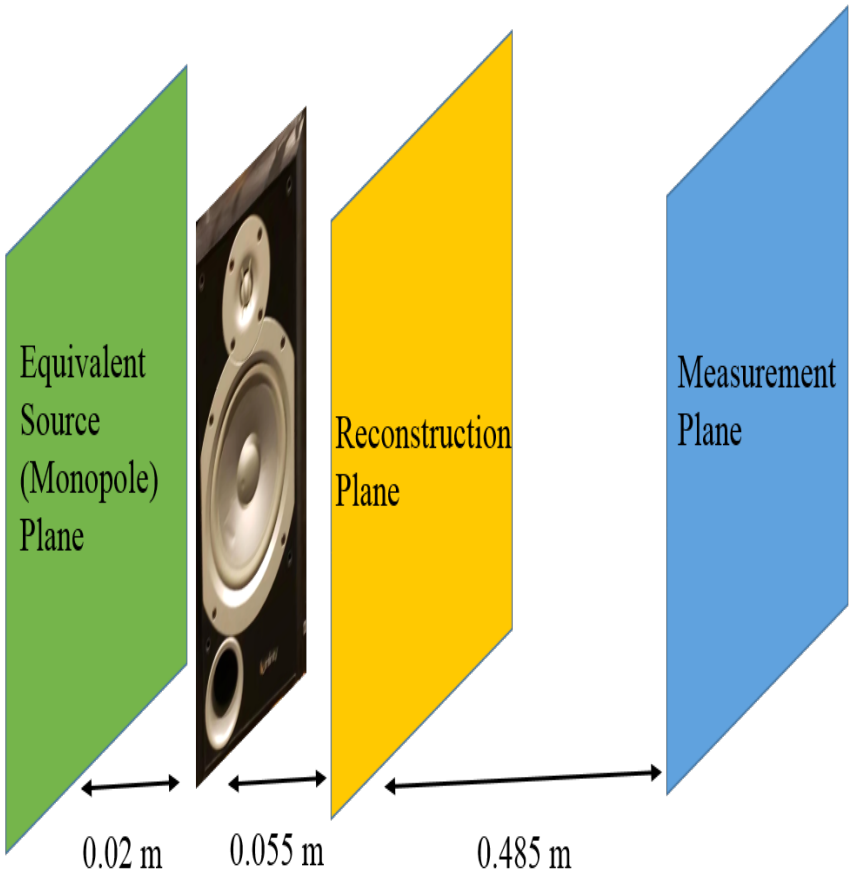

Figure 6.13. Relative position for far-field measurement set up.

presented in previous sections. Figures (6.14), (6.15) and (6.16) show the contour plots of the reconstructed sound intensity distributions 0.055 m from the loudspeaker front face, where the intensity measurement was conducted, at 0.8, 2.4 and 4 kHz, respectively.

From the spatial sound intensity reconstruction results, the SONAH method failed to reconstruct the sound field from the far-field measurements at the different frequencies. The WBH algorithm is able to identify the sound source location when there is one major sound source: e.g., at 800 Hz the loudspeaker membrane, at 4000 Hz the loudspeaker tweeter. But at 2400 Hz when the tweeter and membrane are acting together, WBH failed to separate them: a sound source located in between the

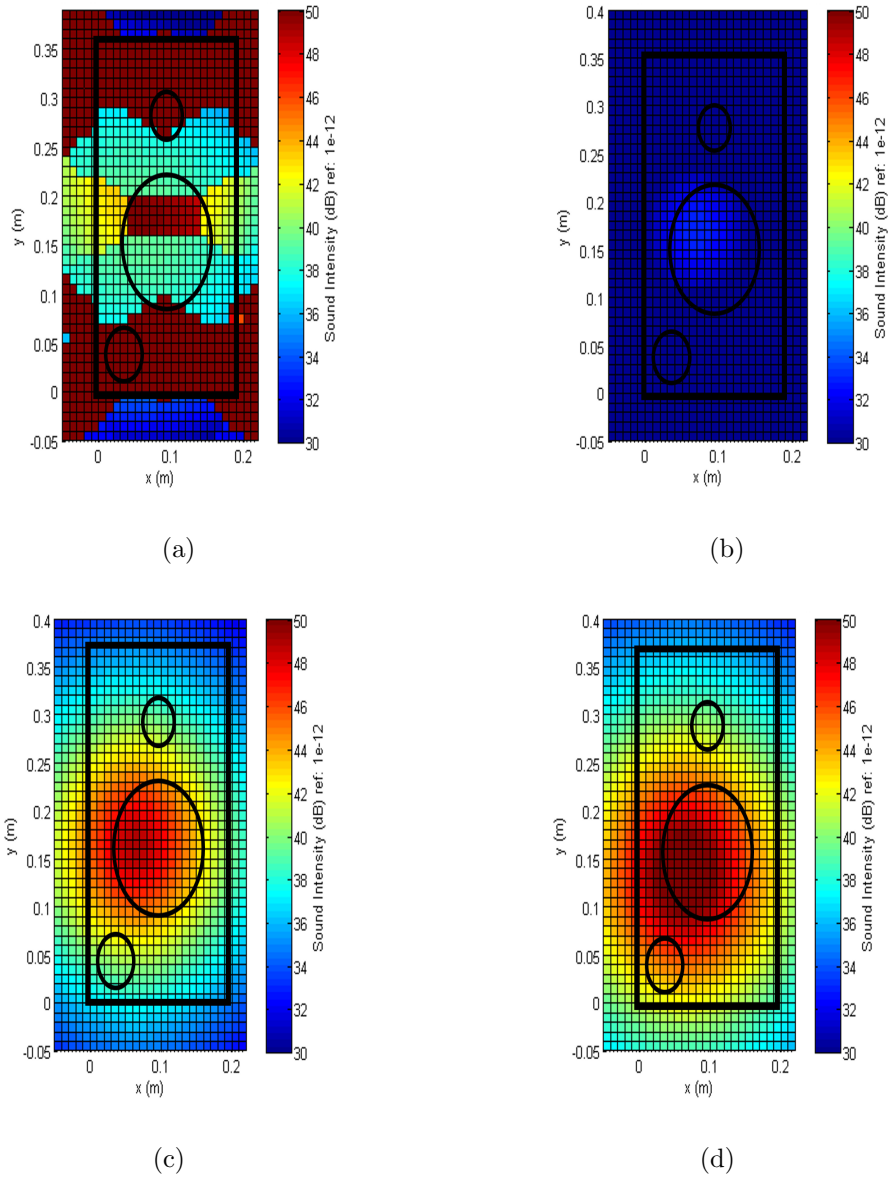

Figure 6.14. 0.05 m from loudspeaker front face sound intensity field reconstruction results with different NAH method at 0.8 kHz with 160 microphones far-field measurement: (a) SONAH method, (b) WBH method, (c) l_1-norm minimization method, and (d) hybrid method.

tweeter and membrane was reconstructed. The l_1-norm minimization and the hybrid process identified the sound source locations correctly at all three frequencies, and at 2400 Hz the algorithms are able to separate the tweeter and membrane and the result

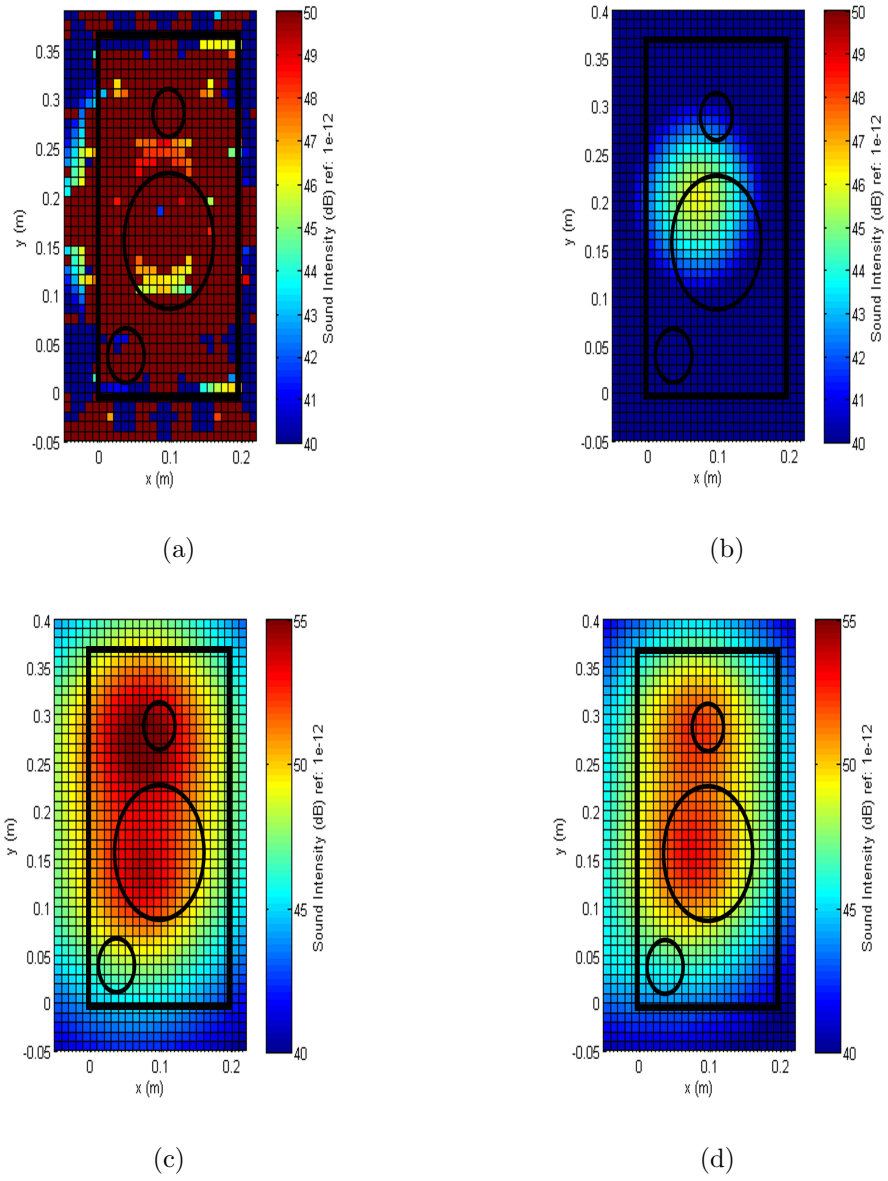

Figure 6.15. 0.05 m from loudspeaker front face sound intensity field reconstruction results with different NAH method at 2.4 kHz with 160 microphones far-field measurement: (a) SONAH method, (b) WBH method, (c) l_1-norm minimization method, and (d) hybrid method.

is better than the reconstruction result obtained from the near-field measurement. At 0.8 kHz, the WBH algorithm recovered 17.4 dB, l_1-norm minimization recovered 32.3 dB, and the hybrid algorithm recovered 34.8 dB, and recall that the near-field

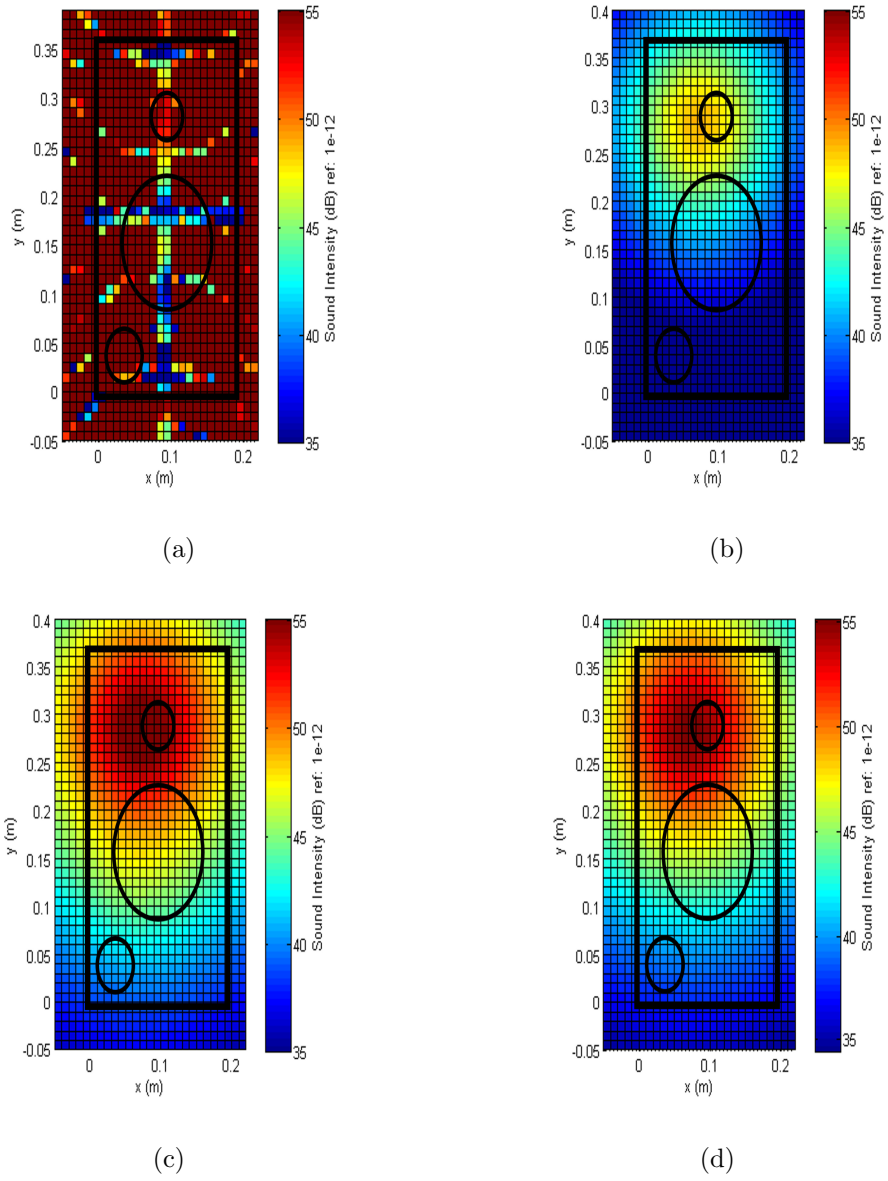

Figure 6.16. 0.05 m from loudspeaker front face sound intensity field reconstruction results with different NAH method at 4 kHz with 160 microphones far-field measurement: (a) SONAH method, (b) WBH method, (c) l_1-norm minimization method, and (d) hybrid method.

measured radiated sound power was 47.9 dB. At 2.4 kHz, the WBH algorithm recovered 29.9 dB, l_1-norm minimization recovered 40.8 dB, and the hybrid algorithm recovered 38.8 dB, while the near-field measured radiated sound power was 46.3 dB.

At 4 kHz, the WBH algorithm recovered 32.2 dB, l_1-norm minimization recovered 39.2 dB, and the hybrid algorithm recovered 38.3 dB, and the near-field measured radiated sound power was 49.5 dB. Since SONAH could not correctly identify the sound source locations, so the reconstructed sound power with SONAH was not compared with other algorithms. At 0.8 kHz, the WBH algorithm based on the far-field measurements strongly under-estimates the total sound power level, and is also 10 dB lower than the reconstructed sound power based on the near-field measurement data. While l_1-norm minimization and the hybrid process also under-estimated the total sound power, the value was close to the reconstruction result when using the near-field measurement data. At 2.4 and 4 kHz, the reconstructed sound power values were all smaller than the reconstructed sound power with the near-field measurement data. Since the near-field and far-field measurements were conducted separately, there could exist a discrepancy between the measurements that caused the difference in reconstructed sound powers. Another possibility is that the far-field measurement didn't capture the near-field components, i.e., evanescent wave components, and thus caused the sound power under-estimation in the near-field.

Then, as in the near-field measurement section, the spacing between microphones was doubled in both x and y directions and the 160 measurements were reduced to 40 measurements with the same patched measurement data. The set up of the equivalent source plane was kept the same, i.e., 1288 monopoles placed 0.02 m behind the loudspeaker front face. The parameters in the SONAH, WBH, l_1-norm minimization and hybrid algorithm were kept the same as described in the previous experiment. The sound field reconstruction results 0.055 m away from loudspeaker front face at 0.8 kHz, 2.4 kHz and 4 kHz are shown in Figures (6.17), (6.18) and (6.19).

Similar conclusions can be found from the spatial sound field reconstruction results: i.e., the SONAH method failed to reconstruct the sound field at 0.8 kHz, and arguably worked at 2.4 and 4 kHz. At 2.4 kHz, the algorithm identified a large sound source region and at 4 kHz SONAH identified a weak source at the tweeter position. Compared with the reconstruction result based on near-field measurement

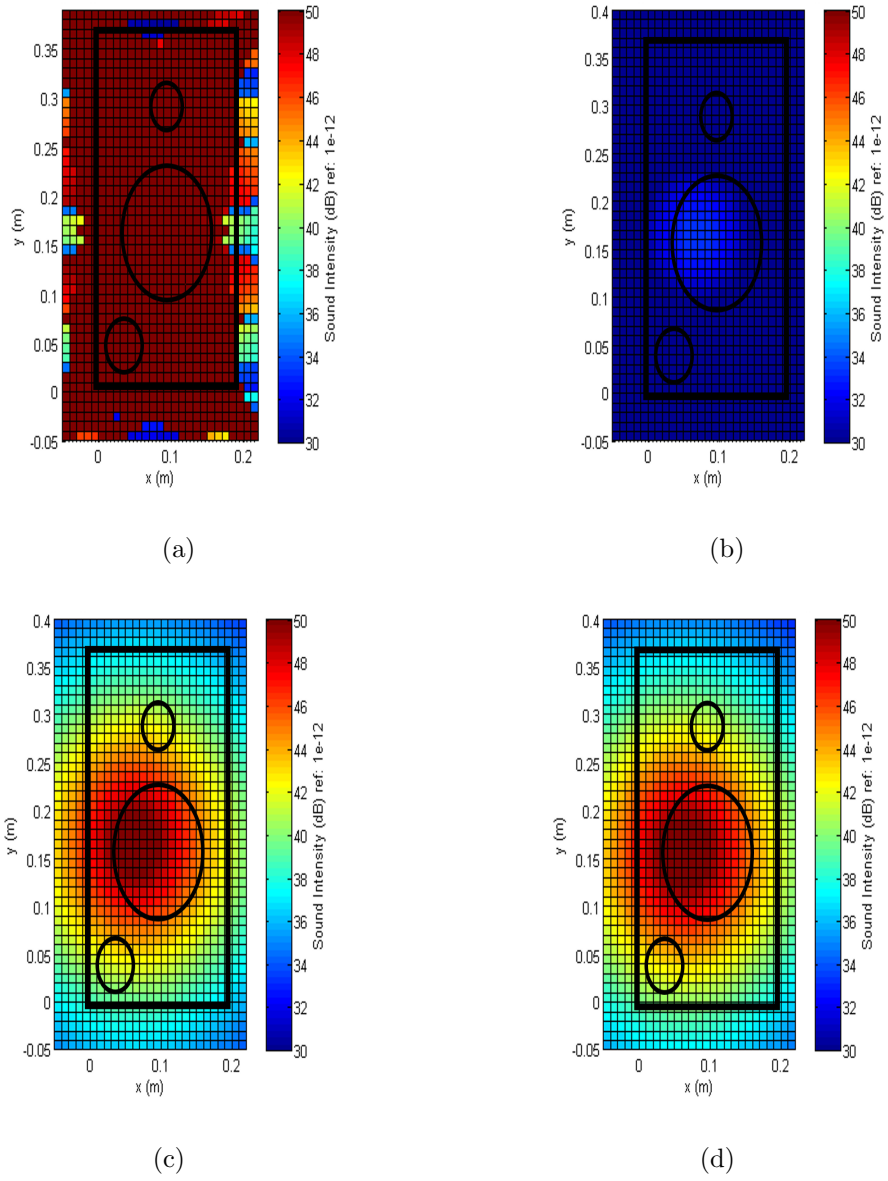

Figure 6.17. 0.05 m from loudspeaker front face sound intensity field reconstruction results with different NAH method at 0.8 kHz with 40 microphones far-field measurement: (a) SONAH method, (b) WBH method, (c) l_1-norm minimization method, and (d) hybrid method.

data, these reconstruction results didn't show the aliasing effect, but the results are not very accurate correct. The sound power reconstructed by the SONAH method was also small: i.e., 33.9 dB at 2.4 kHz and 24.6 dB at 4kHz. For the other algo-

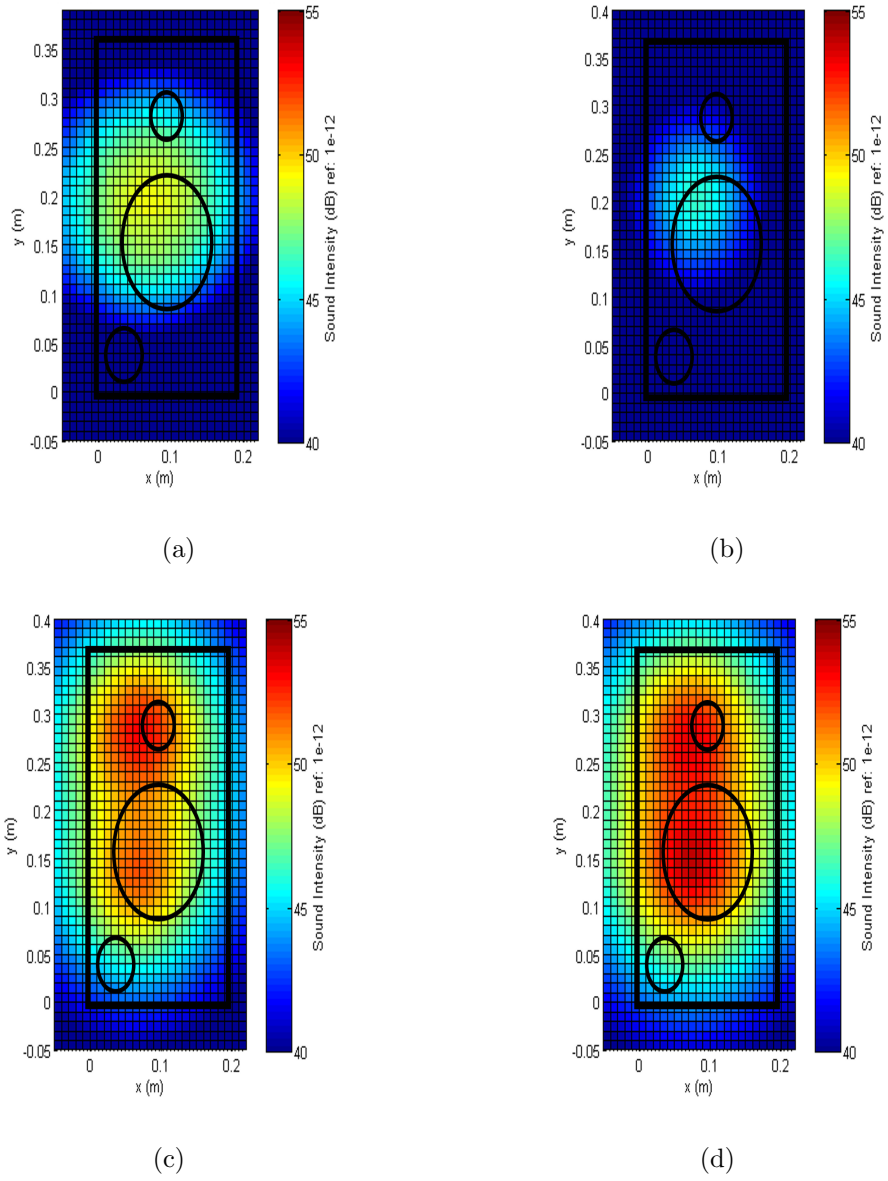

Figure 6.18. 0.05 m from loudspeaker front face sound intensity field reconstruction results with different NAH method at 2.4 kHz with 40 microphones far-field measurement: (a) SONAH method, (b) WBH method, (c) l_1-norm minimization method, and (d) hybrid method.

rithms, the conclusions are as for the reconstruction result with 160 measurements. At 0.8 kHz, the WBH algorithm recovered 17.7 dB, l_1-norm minimization recovered 34.2 dB, the hybrid algorithm recovered 34.4 dB, and the measured near-field radi-

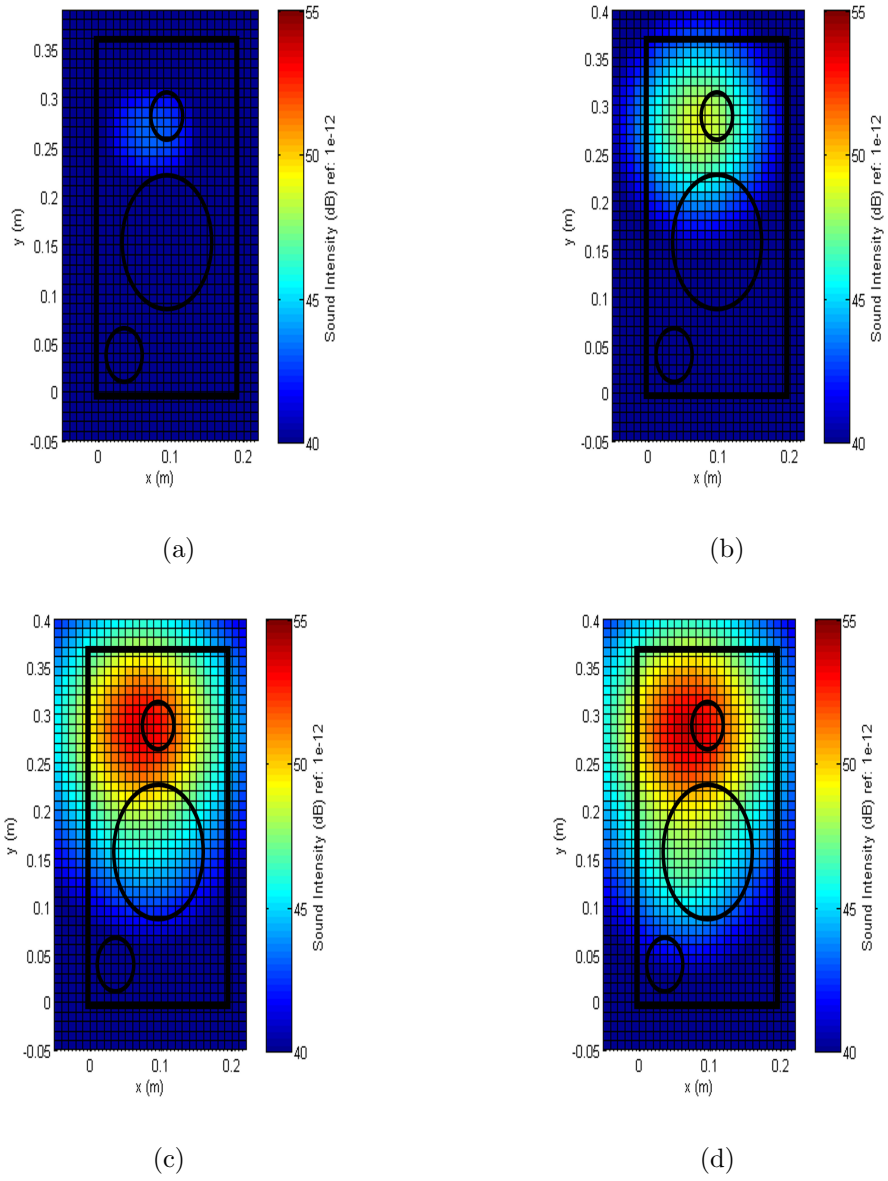

Figure 6.19. 0.05 m from loudspeaker front face sound intensity field reconstruction results with different NAH method at 4 kHz with 40 microphones far-field measurement: (a) SONAH method, (b) WBH method, (c) l_1-norm minimization method, and (d) hybrid method.

ated sound power was 47.9 dB, At 2.4 kHz, the WBH algorithm recovered 30.1 dB, l_1-norm minimization recovered 38.5 dB, and the hybrid algorithm recovered 39.5 dB, and the measured near-field radiated sound power was 46.3 dB. At 4 kHz, WBH

algorithm recovered 32.2 dB, l_1-norm minimization recovered 37.0 dB, and the hybrid algorithm recovered 37.5 dB, and the measured near-field radiated sound power was 49.5 dB. The sound power reconstructed by the different methods with 40 far-field measurements are in general similar to the sound power reconstructed with 160 far-field measurements, which are all smaller than the near-field direct measurements, for the same reasons as in the 160 measurements case.

To be consistent with the near-field measurement experiment and to study the sound field reconstruction based on a small number of microphone measurements, the spacing between microphones was increased to 0.12 m in both x and y directions. In this case, there were only 12 microphone measurements for the sound field reconstruction. With the same equivalent plane set up and same parameters are used in the previous experiment, the sound intensity reconstruction results are shown in Figures (6.20), (6.21) and (6.22).

With 12 measurements, SONAH cannot reconstruct the sound field at any frequency. For the sparse ESM algorithms, the major sound source locations can still be identified, but the closely-positioned sound sources become harder to separate as the number of microphone decreases: e.g., at 2.4 kHz, the tweeter and membrane identified as a large single sound source instead of two separate sound sources. As for the sound power, at 0.8 kHz, the WBH algorithm recovered 18.0 dB, l_1-norm minimization recovered 33.1 dB, the hybrid algorithm recovered 31.9 dB, and the measured near-field radiated sound power was 47.9 dB. At the 2.4 kHz, WBH algorithm recovered 30.8 dB, l_1-norm minimization recovered 39.6 dB, and the hybrid algorithm recovered 41.1 dB, the measured near-field radiated sound power was 46.3 dB. At 4 kHz, the WBH algorithm recovered 32.6 dB, l_1-norm minimization recovered 38.6 dB, and the hybrid algorithm recovered 39.0 dB, and the measured near-field radiated sound power was 49.5 dB. It is noted that the estimated sound power by each of the methods are consistent as the number of measurement decreased, and the identified sound source locations were the same, though the closely-positioned sources cannot be clearly separated.

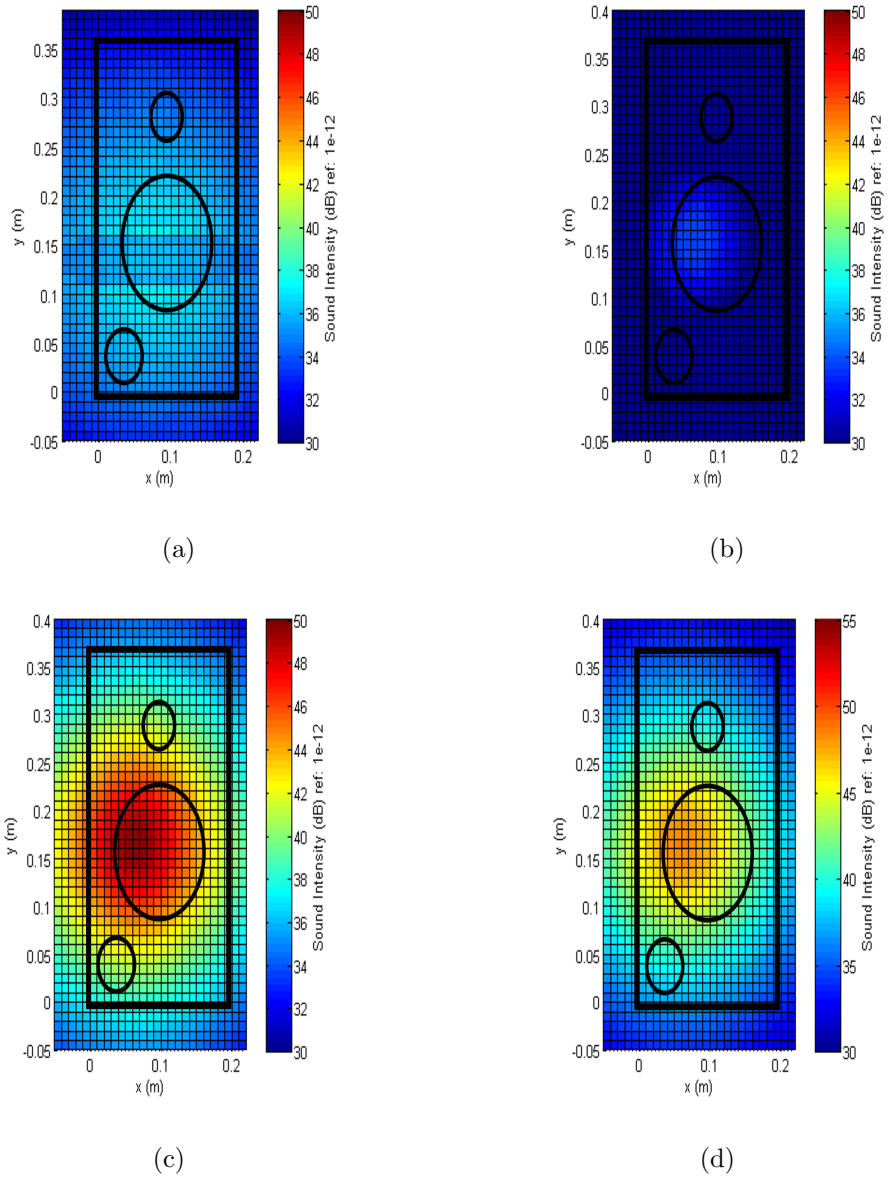

Figure 6.20. 0.05 m from loudspeaker front face sound intensity field reconstruction results with different NAH method at 0.8 kHz with 12 microphones far-field measurement: (a) SONAH method, (b) WBH method, (c) l_1-norm minimization method, and (d) hybrid method.

It is also note that for SONAH method the computation time is longer than the sparse ESM algorithms, e.g., with 160 measurements and 1288 reconstruction points, SONAH took 8 hours to finish the reconstruction, as comparison, with same 160 mea-

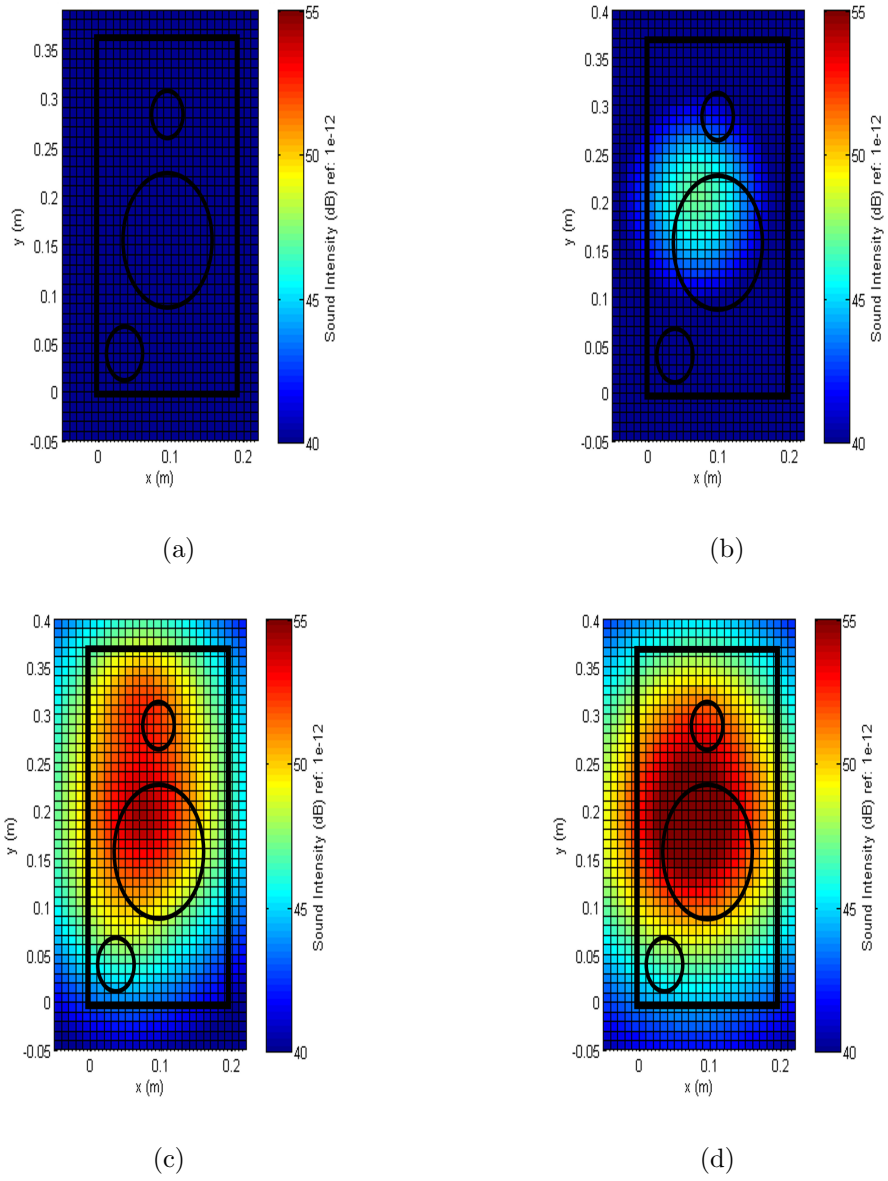

Figure 6.21. 0.05 m from loudspeaker front face sound intensity field reconstruction results with different NAH method at 2.4 kHz with 12 microphones far-field measurement: (a) SONAH method, (b) WBH method, (c) l_1-norm minimization method, and (d) hybrid method.

surements and 1288 monopoles, WBH took less than 1 minute, l_1-norm minimization and hybrid process took about 3 minutes. So the sparse ESM algorithms are able to save a lot computation time.

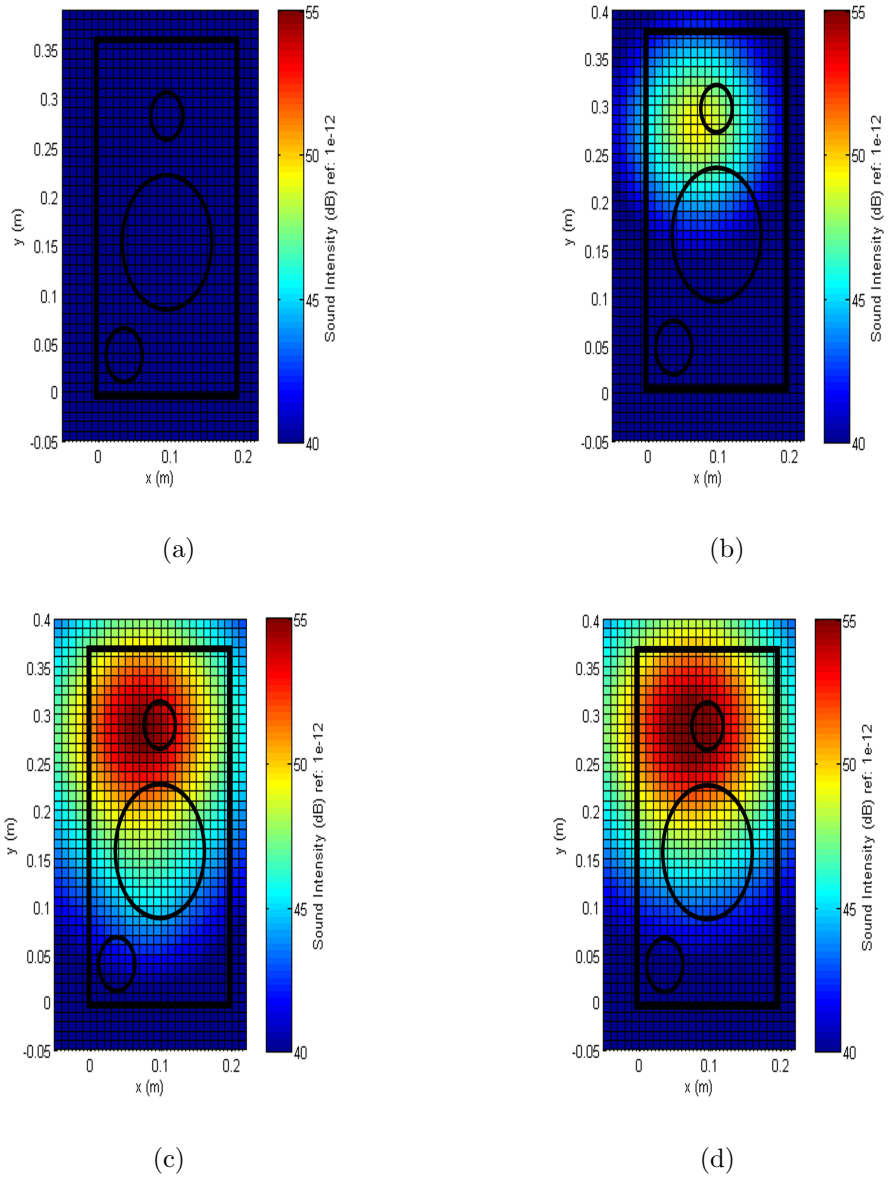

Figure 6.22. 0.05 m from loudspeaker front face sound intensity field reconstruction results with different NAH method at 4 kHz with 12 microphones far-field measurement: (a) SONAH method, (b) WBH method, (c) l_1-norm minimization method, and (d) hybrid method.

6.3 Two Loudspeakers Sound Field Reconstruction

In the previous experiment with one loudspeaker as the sound source, it was found that when the measurement was close to the sound source and satisfied sampling rule,

the SONAH method was able to accurately reconstruct the sound field. But as the spatial sampling rate decreases, aliasing appears in the reconstruction result if the spatial sampling spacing is larger than half of the wavelength. Further, the SONAH method failed to reconstruct the sound field when the measurement was token far from the sound source. As a comparison, the sparse ESM algorithms are not as accurate as SONAH when the measurement was taken close to the sound source and satisfied sampling rule, but the algorithm can still reconstruct similar result when the number of measurements is small and the measurement distance is far from the sound source. And the sparse ESM algorithms also took less computational time than the SONAH method. In this section, following the same logic as in the simulation experiment, two sound sources, i.e., loudspeakers, were set-up side by side to test the ability of different algorithms to separate closely-positioned sound sources.

6.3.1 Reconstruction with Near-field Measurement

The loudspeakers used in this experiment were the Infinity Primuis P163 as described in the previous section. The two loudspeakers were placed side by side with 0.09 m spacing between each other; the set up of the two loudspeakers is shown in Figure (6.23).

In this experiment, in order to obtain the true intensity sound field, the intensity probe scan measurement was conducted with the same patched measurement principle described in previous section, so that the effectively simultaneously measured sound pressure data could be obtained at the intensity measurement points. In the near-field measurement, the intensity was measured 0.055 m in front of the loudspeakers, the measurement covered an area of 0.48 m by 0.42 m, which is larger than the two loudspeaker front face region. The intensity measurement spacing between the measurement points was 0.03 m in both x and y directions, which is less than half of the wavelength at 4000 Hz. So there were 255 measurement points in total, which comprised an equivalent regular rectangular microphone array measurement after the

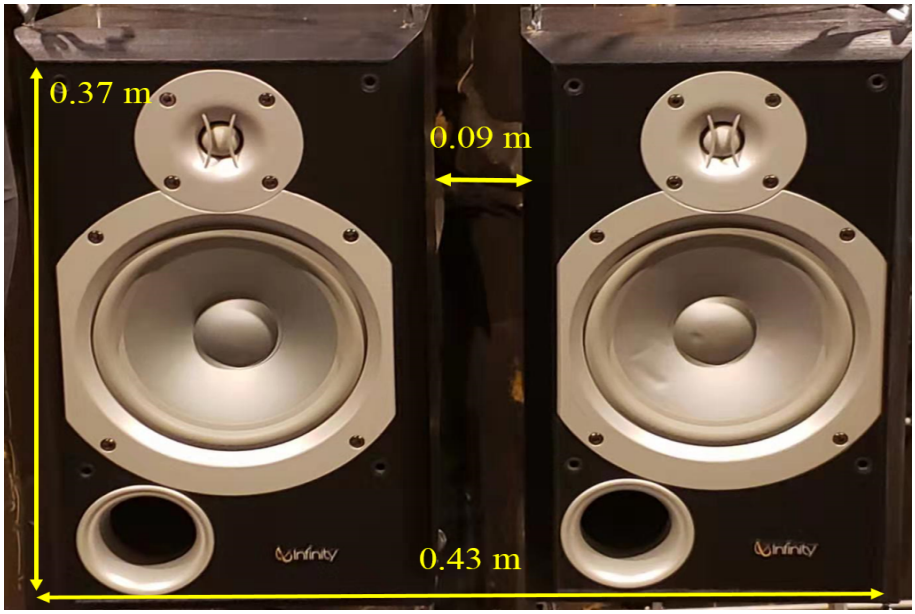

Figure 6.23. Two loudspeaker set up in experiment.

patched measurement calculation. The input signal to the loudspeakers was the same Gaussian white noise of 25.6 kHz bandwidth generated by PULSE software through the computer. At each measurement point, the intensity probe recorded 10 seconds of time data at a 25.6 kHz sampling frequency. Then the measured time history data was transformed to the frequency domain by PULSE; the parameters in the Fourier transform were set up as: Hann window with 6400 points, overlap between each window was 50%, and 100 averages in total. For the sparse ESM algorithms, the monopoles were located on the equivalent source plane which was 0.02 m behind the loudspeakers front face. The monopole source mesh covered the measurement area with 0.01 m spacing in both x and y directions, thus there were 2107 monopoles and their source strength need to be determined by using 255 measurements. Figure (6.24) shows the relative position between the equivalent source plane, the measurement plane and the loudspeaker positions, it is noted that in this experiment, the reconstruction plane is same as the measurement plane.

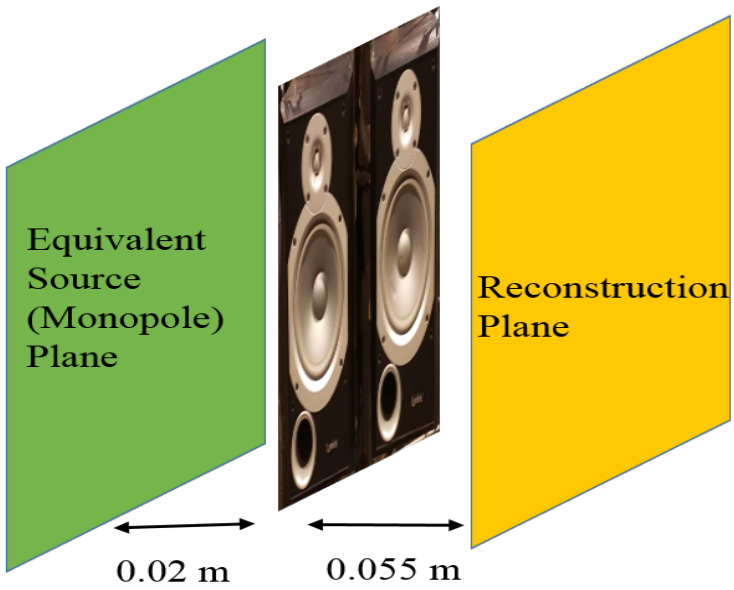

Figure 6.24. Relative position for near-field measurement set up.

As for the single loudspeaker experiment, SONAH, WBH, l_1-norm minimization and the hybrid method were used to reconstruct the sound pressure and intensity fields generated by the loudspeaker on the reconstruction plane, and the reconstruction results were compared with the intensity probe measurements. To reconstruct the sound field with the SONAH method, the virtual source plane was placed 0.03 m behind the reconstruction plane, and the regularization parameter, , was calculated by using the L-curve method. It is note that since the calculation time for SONAH method is long, the spacing on reconstruction plane was chosen to be 0.02 m instead of 0.01 m as described in the previous section. With the WBH method, the parameters used in the WBH process were presented in equation (3.13). And for the l_1-norm minimization procedure, the weighting parameter, λ_w, was chosen to be 10. For the hybrid method, the weighting parameter in the l_1-norm minimization procedure was chosen to be 100, and the parameters in the WBH method were kept the same as in equation (3.13), except for $D_0 = 10.1$ in order to keep secondary source in the first iteration. The equations for the sound pressure, P, and velocity, $\vec{V}$, for the different

methods at the reconstruction positions have been presented in previous chapters, and the sound intensity was calculated with equation (4.1). Then the total sound power over measurement plane was calculated by using equation (4.2).

Figure (6.25) shows the sound intensity distribution measured by the intensity probe at 0.8, 2.4 and 4 kHz. In this and the following figures, the black boxes indicate the region of the two loudspeaker front faces, the small circle at the top of the loudspeaker is the tweeter position, the big circle in the middle is the area of membrane, and the small circle at lower left corner is the loudspeaker port. Based on the measurement result, the sound source locations at different frequencies are as expected: i.e., at 0.8 kHz the membrane generated the low frequency sound, at 2.4 kHz the sound is generated from both tweeter and membrane, and at 4 kHz the sound radiates from the tweeter. But from the measurement result, the loudspeaker on the right hand side generated higher level sound than the loudspeaker on the left hand side. This was not exactly as expected since the input to loudspeakers was the same, but this is not crucial since the algorithms should reconstruct the same sound field as the measured sound field. And with these sound sources, it also can test the algorithm used to identify sound sources with different source strengths.

Figures (6.26) (6.27) and (6.28) show the contour plots of the reconstructed sound intensity distributions 0.055 m from the loudspeaker front face, where the intensity measurement was conducted, at 0.8, 2.4 and 4 kHz, respectively. At 0.8 kHz, the measured radiated sound power was 46.7 dB; SONAH recovered 41.5 dB, the WBH algorithm recovered 26.6 dB, l_1-norm minimization recovered 33.0 dB, and the hybrid algorithm recovered 32.4 dB. At 2.4 kHz, the measured radiated sound power was 44.0 dB; SONAH recovered 45.7 dB, the WBH algorithm recovered 37.4 dB, l_1-norm minimization recovered 41.3 dB, and the hybrid algorithm recovered 43.03 dB. At 4 kHz, the measured radiated sound power was 46.3 dB; SONAH recovered 44.2 dB, the WBH algorithm recovered 39.7 dB, l_1-norm minimization recovered 40.3 dB, and the hybrid algorithm recovered 39.9 dB.

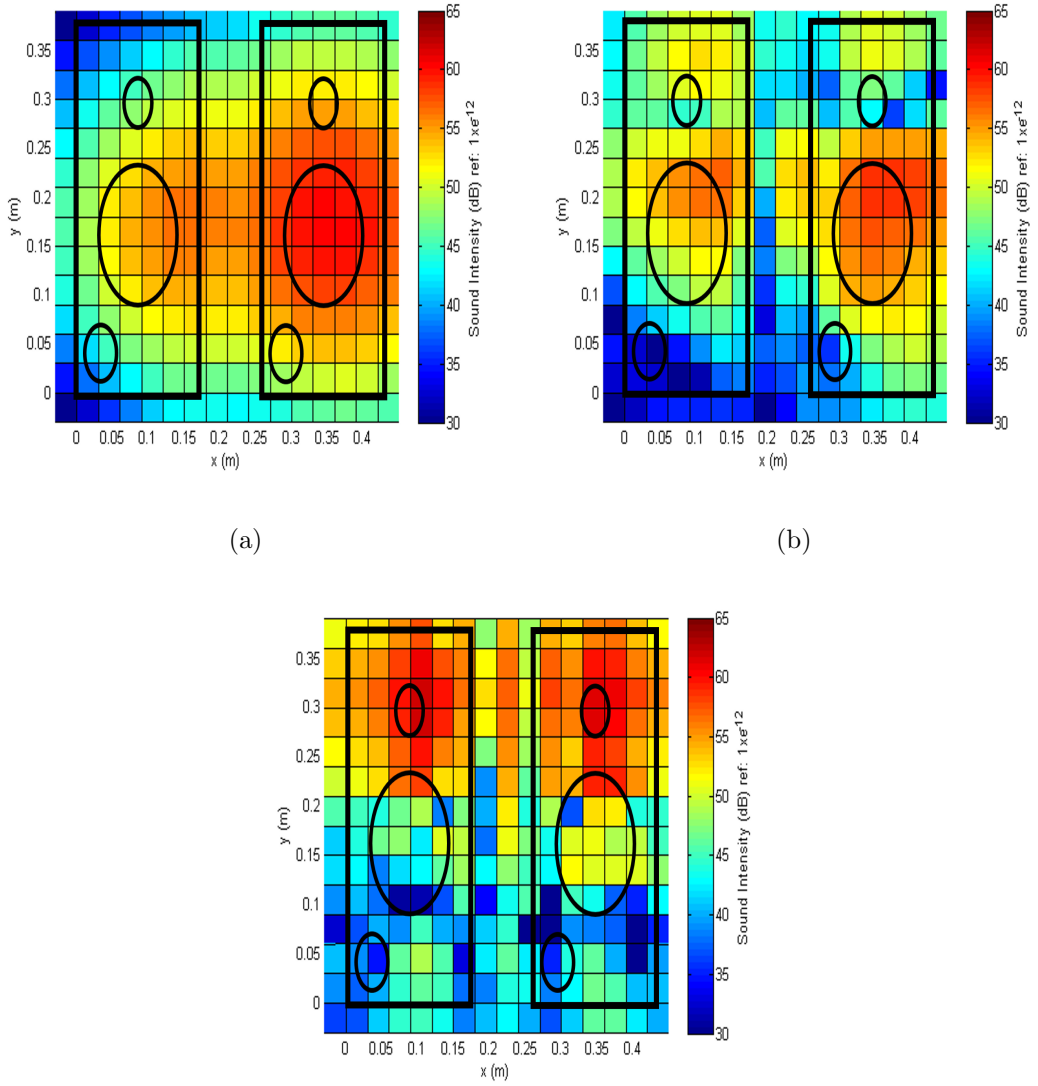

(a) (b)

(c)

Figure 6.25. Measured sound intensity field 0.055 m from loudspeaker front face: (a) 0.8 kHz, (b) 2.4 kHz, and (c) 4 kHz.

At 0.8 kHz, SONAH and WBH could not separate the two loudspeakers; the algorithms all reconstructed the sound field around the loudspeaker on the right hand side which is loudspeaker with the higher amplitude. While the l_1-norm minimization and the hybrid process reconstructed a clearer separation between the two

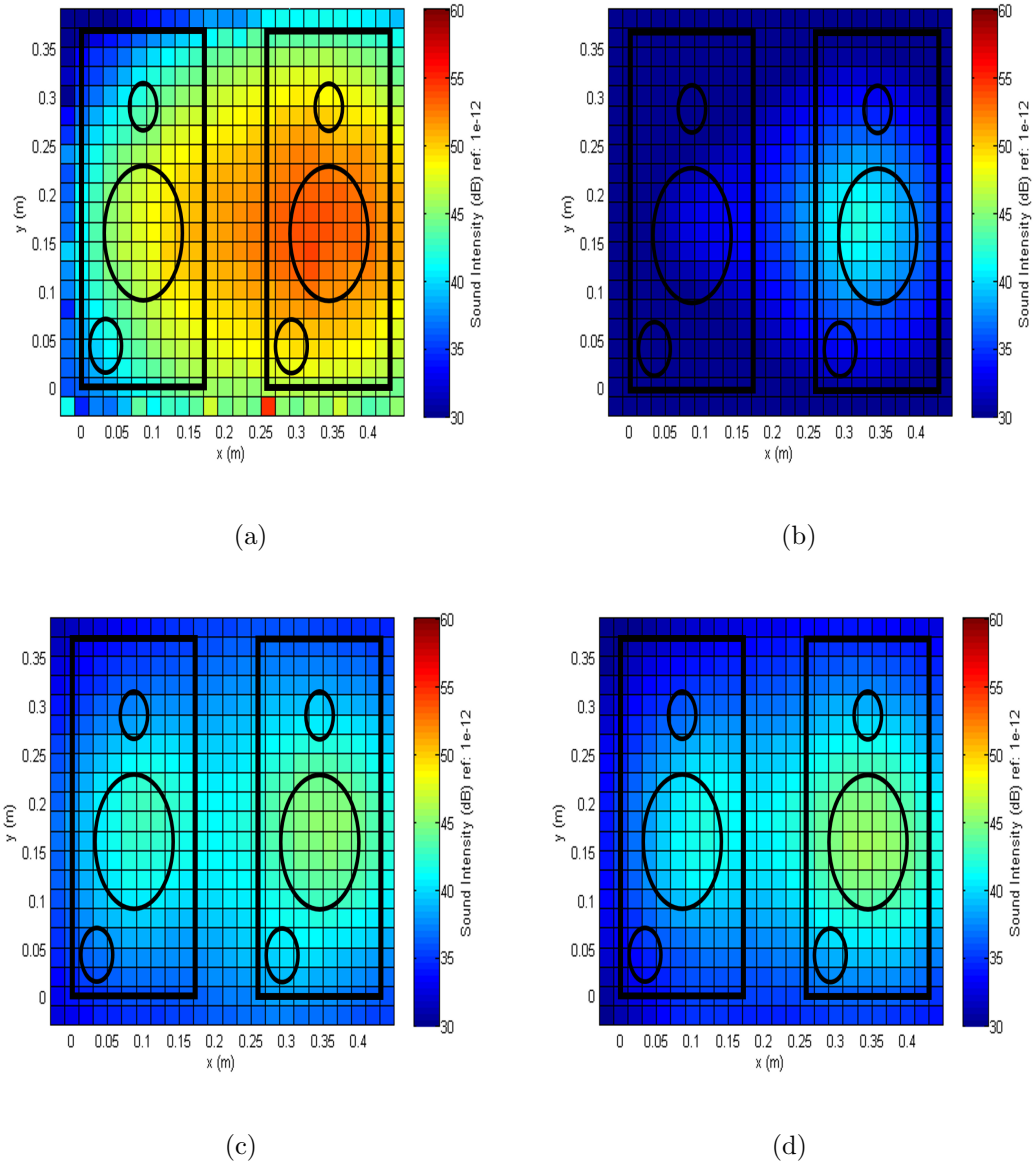

Figure 6.26. 0.05 m from loudspeaker front face sound intensity field reconstruction results with different NAH methods at 0.8 kHz with 255 microphones near-field measurement: (a) SONAH method, (b) WBH method, (c) l_1-norm minimization method, and (d) hybrid method.

loudspeaker membranes, and assigned more weighting on the loudspeaker on right hand side, SONAH recovered the most energy while the other sparse ESM algorithm under-estimated the sound power at 0.8 kHz. As the frequency increases, SONAH

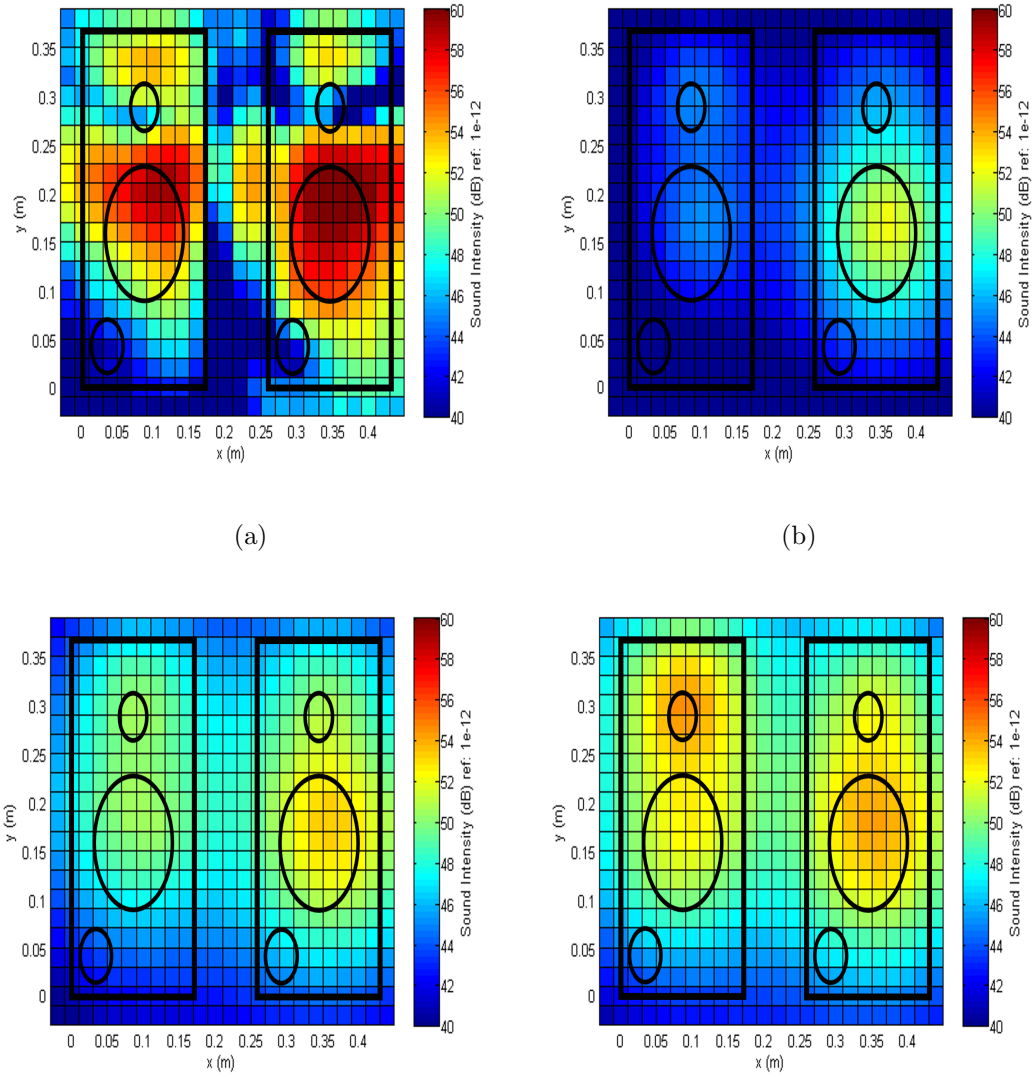

Figure 6.27. 0.05 m from loudspeaker front face sound intensity field reconstruction results with different NAH methods at 2.4 kHz with 255 microphones near-field measurement: (a) SONAH method, (b) WBH method, (c) l_1-norm minimization method, and (d) hybrid method.

reconstructed better results, e.g., at 2.4 kHz it clearly separates the two loudspeakers and indicated the loudspeaker on the right hand side is louder than the loudspeaker at the left. As a comparison, the WBH reconstructed the sound field around the

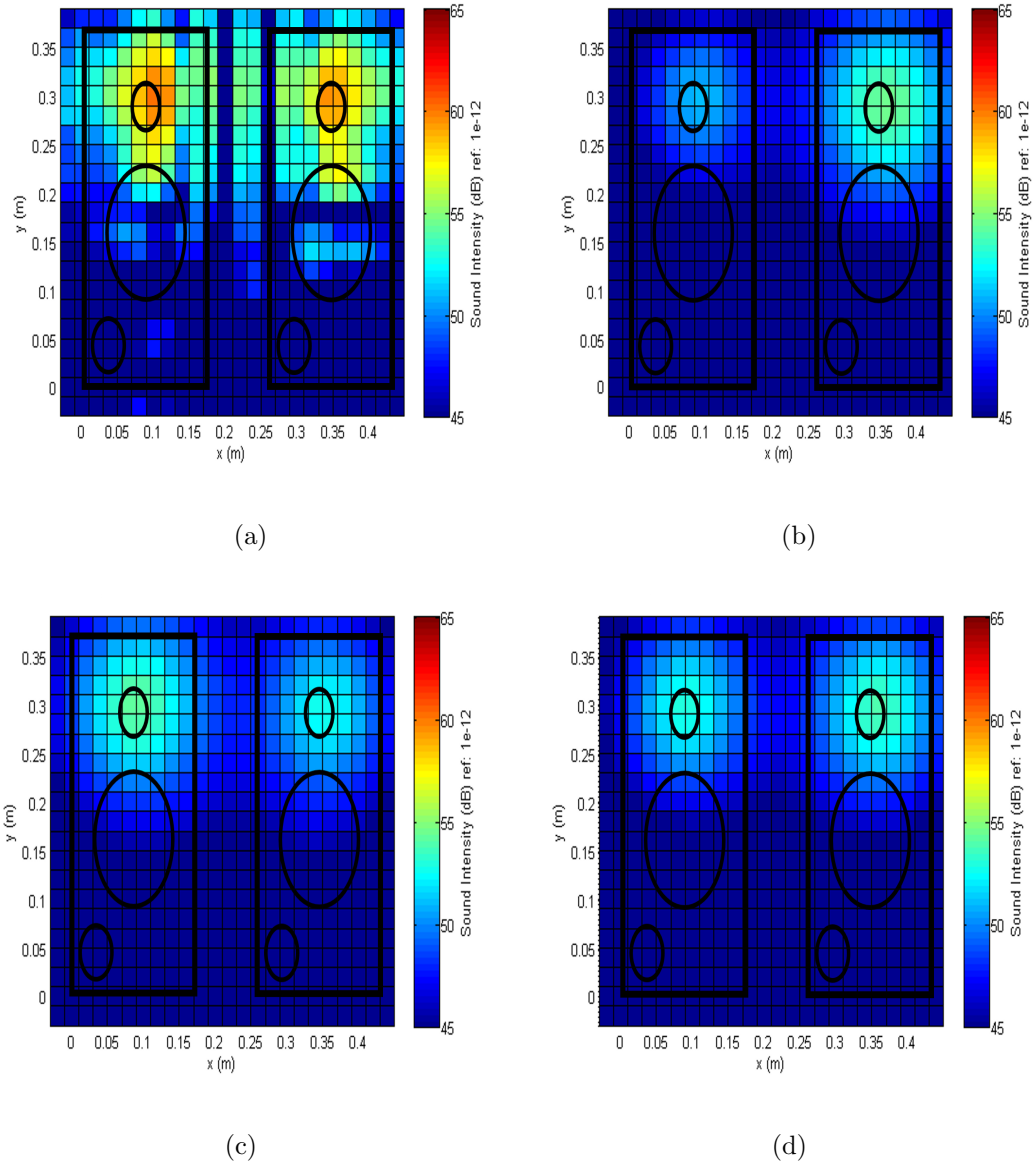

Figure 6.28. 0.05 m from loudspeaker front face sound intensity field reconstruction results with different NAH methods at 4 kHz with 255 microphones near-field measurement: (a) SONAH method, (b) WBH method, (c) l_1-norm minimization method, and (d) hybrid method.

loudspeaker on the right hand side, and assigned a very small weighting to the left hand side loudspeaker, and WBH also didn't clearly separate the tweeters and membranes. The l_1-norm minimization and the hybrid process were able to separate the

two loudspeakers and identified the membranes and tweeters separately, and the hybrid process reconstructed more detail than the l_1-norm minimization: e.g., a more balanced weighting between the loudspeakers and a clearer indication on the tweeters. At 2.4 kHz, SONAH over-estimated the total sound power by a small amount, l_1-norm minimization and the hybrid method recovered sound powers close to the measurement, while WBH under-estimated the total sound power. At 4 kHz, all algorithms successfully identified the two tweeters. SONAH reconstructed the most accurate detail and amplitude, WBH assigned unbalanced weighting to the two tweeters. The l_1-norm minimization and the hybrid process reconstructed similar results, but the hybrid method estimated a more balance weighting compared with l_1-norm minimization. When comparing the spatial sound field reconstruction result with the intensity measurement, all the methods correctly identified the major sound source locations: i.e., the noise source location moves from the diaphragm location to the tweeter position as frequency increases, which matches the intensity measurement. SONAH reconstructed the most detail of the sound field, but at low frequency, e.g., 800 Hz, it failed to separate the two loudspeaker. The WBH algorithm also has difficultly with separate closely-positioned sound sources, and it recovered the least energy among all the methods, especially at low frequency. The l_1-norm minimization method is able to successfully separate closely-positioned sound sources, and to recover more accurate estimates of sound power compared with the WBH algorithm. The hybrid method reconstructed basically the same result as l_1-norm minimization, however, it assigned a more balance weighting and gave a better indication on the second sound source than the l_1-norm minimization.

The observations of the two loudspeakers measurement is basically the same as the one loudspeaker experiment. Then the number of measurement used in the reconstruction process was reduced by doubling the spacing between microphones in both x and y directions, that is 0.06 m. Then the equivalent regular rectangular microphone array was reduced to 72 microphones and the measurement was still 0.055 m from loudspeaker front face. The effectively simultaneously microphone ar-

ray measurement was generated with the same patched measurement principle and with same data used in the 255 channels measurement. So the reconstruction results can still be compared with the direct sound intensity measurement. The set up on equivalent source plane was kept the same: i.e., 2107 monopoles and 0.02 m behind the loudspeaker front face. The parameters in SONAH, WBH, l_1-norm minimization and hybrid algorithm were kept the same as described in the previous experiments. The sound field reconstruction results 0.055 m away from loudspeaker front face at 0.8 kHz, 2.4 kHz and 4 kHz are shown in Figures (6.29), (6.30) and (6.31) At 0.8 kHz, the measured radiated sound power was 46.7 dB, SONAH recovered 41.5 dB, the WBH algorithm recovered 26.8 dB, l_1-norm minimization recovered 34.14 dB, and the hybrid algorithm recovered 33.4 dB. At 2.4 kHz, the measured radiated sound power was 44.0 dB, SONAH recovered 45.7 dB, the WBH algorithm recovered 37.8 dB, l_1-norm minimization recovered 42.1 dB, and the hybrid algorithm recovered 42.4 dB. At 4 kHz, the measured radiated sound power was 46.3 dB, SONAH recovered 39.6 dB, the WBH algorithm recovered 38.5 dB, l_1-norm minimization recovered 40.4 dB, and the hybrid algorithm recovered 40.9 dB.

So the sound power reconstructed by the different methods with 72 measurements are in general similar compared with the sound power reconstructed with 255 measurements, except for the SONAH method at 4 kHz. And similar conclusions can be drawn from the spatial sound field reconstruction results: e.g., SONAH and WBH failed to separate the two loudspeakers, WBH under-estimated the total sound power, etc. But at 4000 Hz, as described in the one loudspeaker experiment, spatial aliasing appeared due to low spatial sampling rate.

Then the number of microphones was further reduced to 20 by increasing the spacing between microphones to 0.12 m in both x and y directions, and the measurement still covers the same region. With the same equivalent plane set up and same parameters used in the previous experiments, the sound intensity reconstruction results are shown in Figures (6.32), (6.33) and (6.34). At 0.8 kHz, the measured radiated sound power was 46.7 dB, SONAH recovered 41.2 dB, the WBH algorithm recovered 26.9

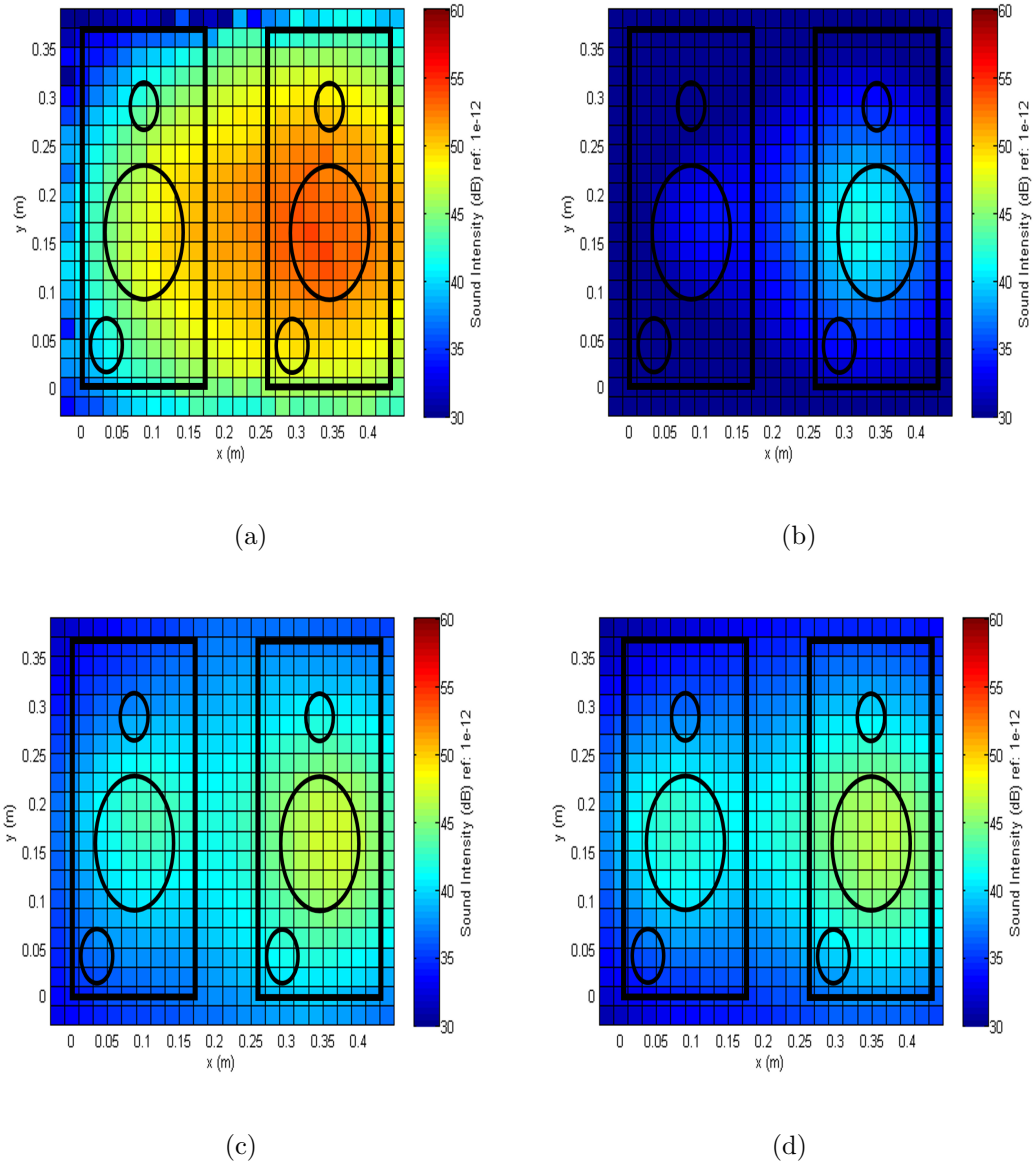

Figure 6.29. 0.05 m from loudspeaker front face sound intensity field reconstruction results with different NAH methods at 0.8 kHz with 72 microphones near-field measurement: (a) SONAH method, (b) WBH method, (c) l_1-norm minimization method, and (d) hybrid method.

dB, l_1-norm minimization recovered 37.2 dB, and the hybrid algorithm recovered 37.2 dB. At 2.4 kHz, the measured radiated sound power was 46.3 dB, SONAH recovered 38.7 dB, the WBH algorithm recovered 34.6 dB, l_1-norm minimization recovered 42.7

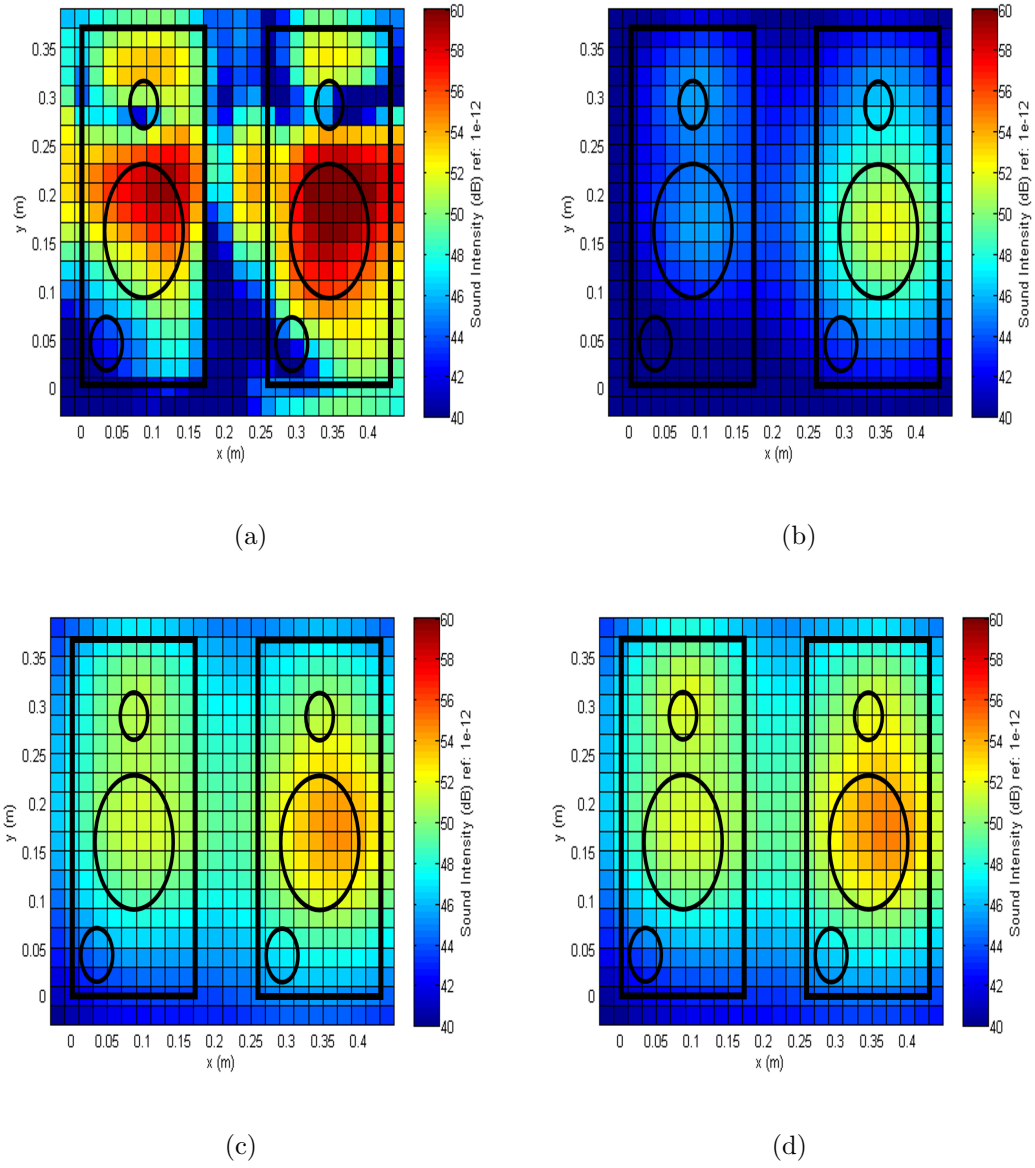

Figure 6.30. 0.05 m from loudspeaker front face sound intensity field reconstruction results with different NAH methods at 2.4 kHz with 72 microphones near-field measurement: (a) SONAH method, (b) WBH method, (c) l_1-norm minimization method, and (d) hybrid method.

dB, and the hybrid algorithm recovered 42.8 dB. At 4 kHz, the measured radiated sound power was 49.5 dB, SONAH recovered 33.3 dB, the WBH algorithm recovered

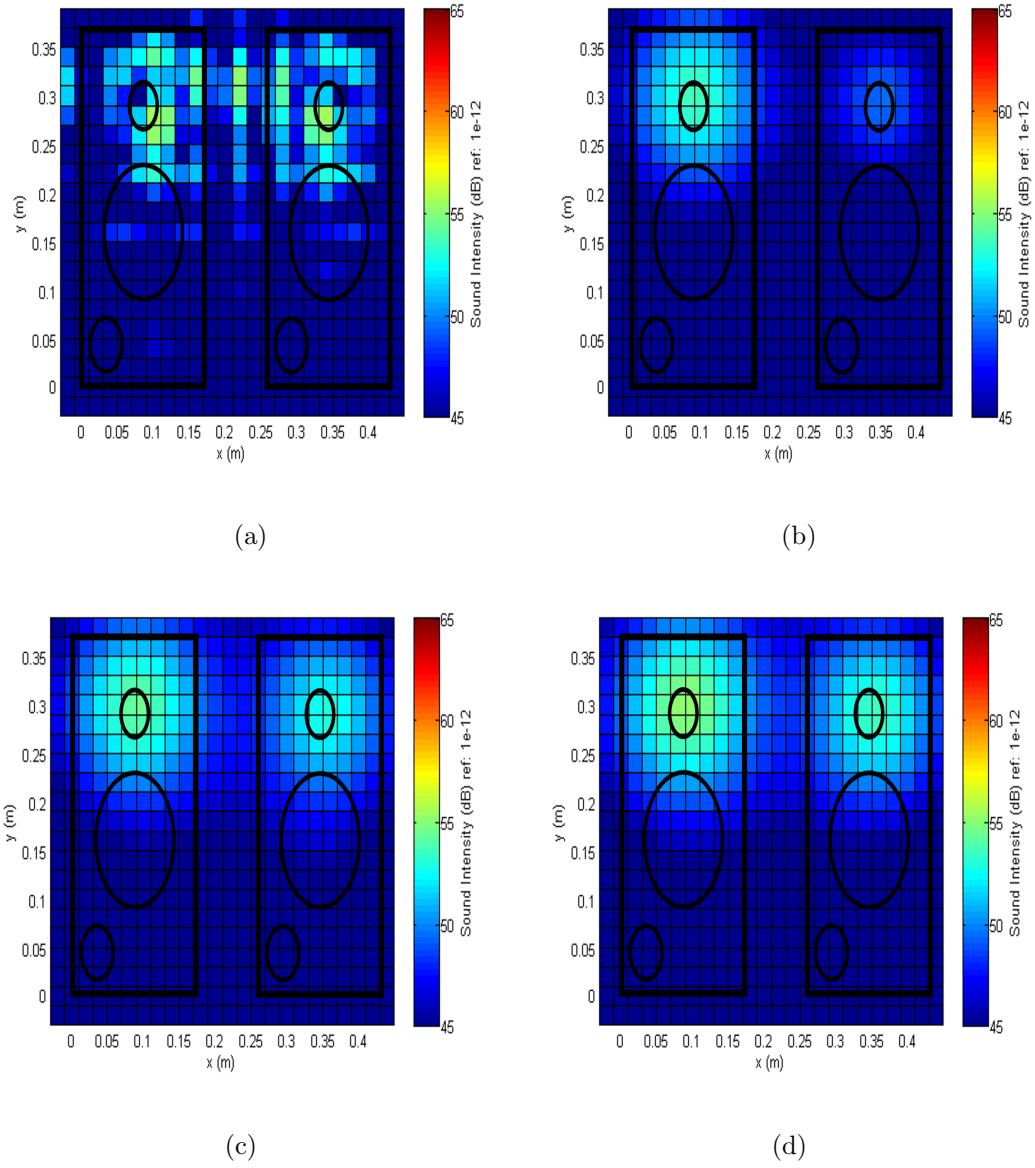

Figure 6.31. 0.05 m from loudspeaker front face sound intensity field reconstruction results with different NAH methods at 4 kHz with 72 microphones near-field measurement: (a) SONAH method, (b) WBH method, (c) l_1-norm minimization method, and (d) hybrid method.

35.2 dB, l_1-norm minimization recovered 39.9 dB, and the hybrid algorithm recovered 40.9 dB.

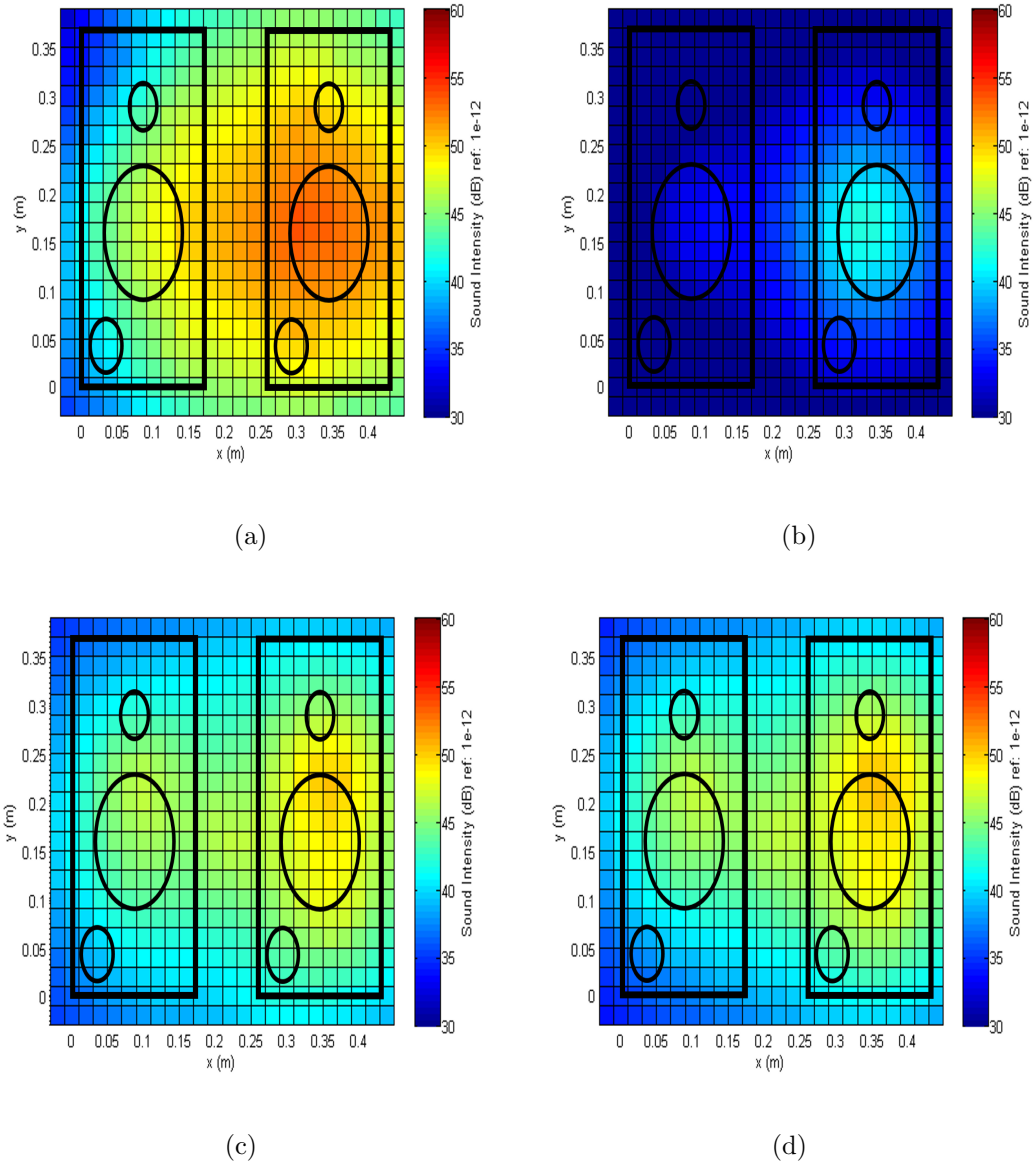

Figure 6.32. 0.05 m from loudspeaker front face sound intensity field reconstruction results with different NAH methods at 0.8 kHz with 20 microphones near-field measurement: (a) SONAH method, (b) WBH method, (c) l_1-norm minimization method, and (d) hybrid method.

Then with the microphone spacing increasing to 0.12 m, aliasing is observed not only at 4 kHz but also at 2.4 kHz with the SONAH method, as also found in the one loudspeaker experiment. And as in the one loudspeaker experiment: for the

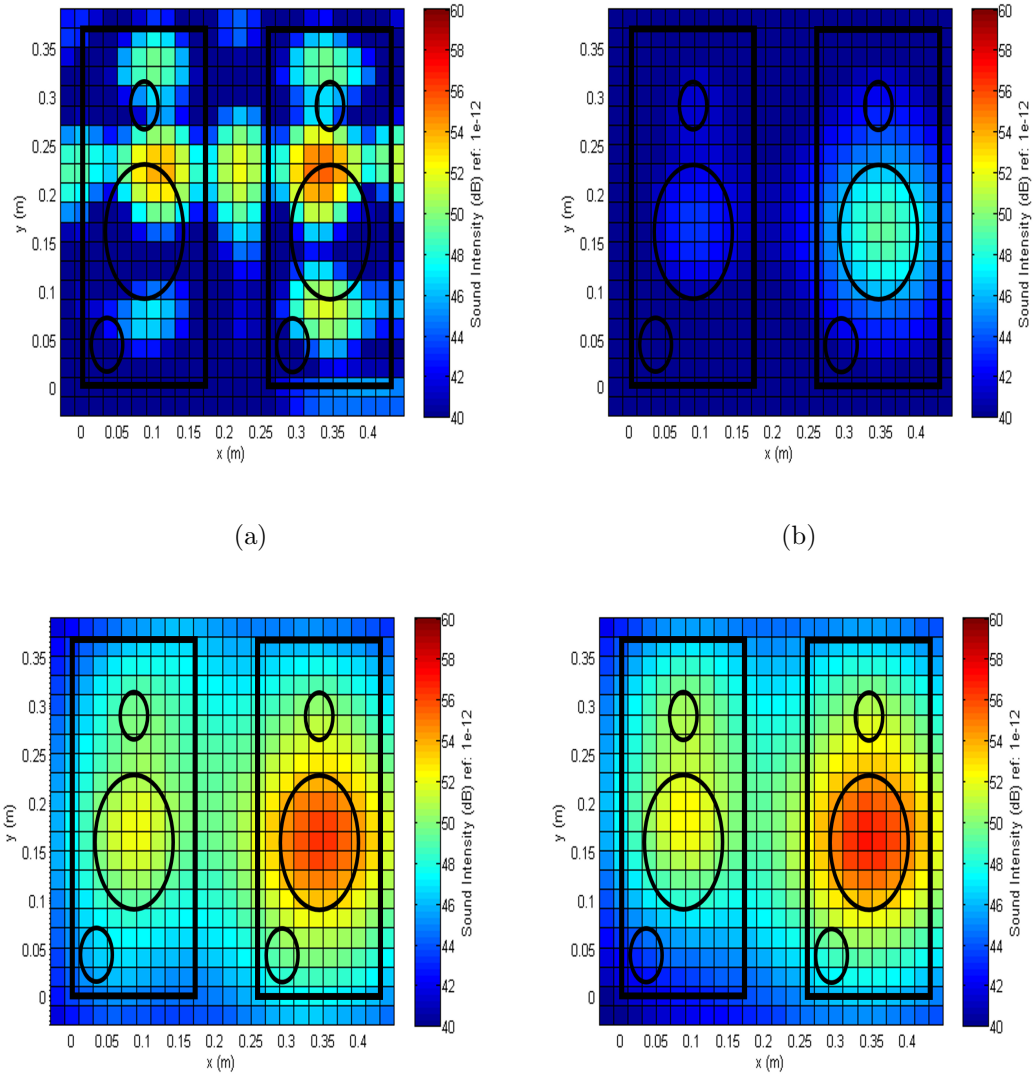

Figure 6.33. 0.05 m from loudspeaker front face sound intensity field reconstruction results with different NAH methods at 2.4 kHz with 20 microphones near-field measurement: (a) SONAH method, (b) WBH method, (c) l_1-norm minimization method, and (d) hybrid method.

sparse ESM algorithms, even when the spatial sample spacing is much larger than the wavelength at the frequency of interest, the major sound source location can still

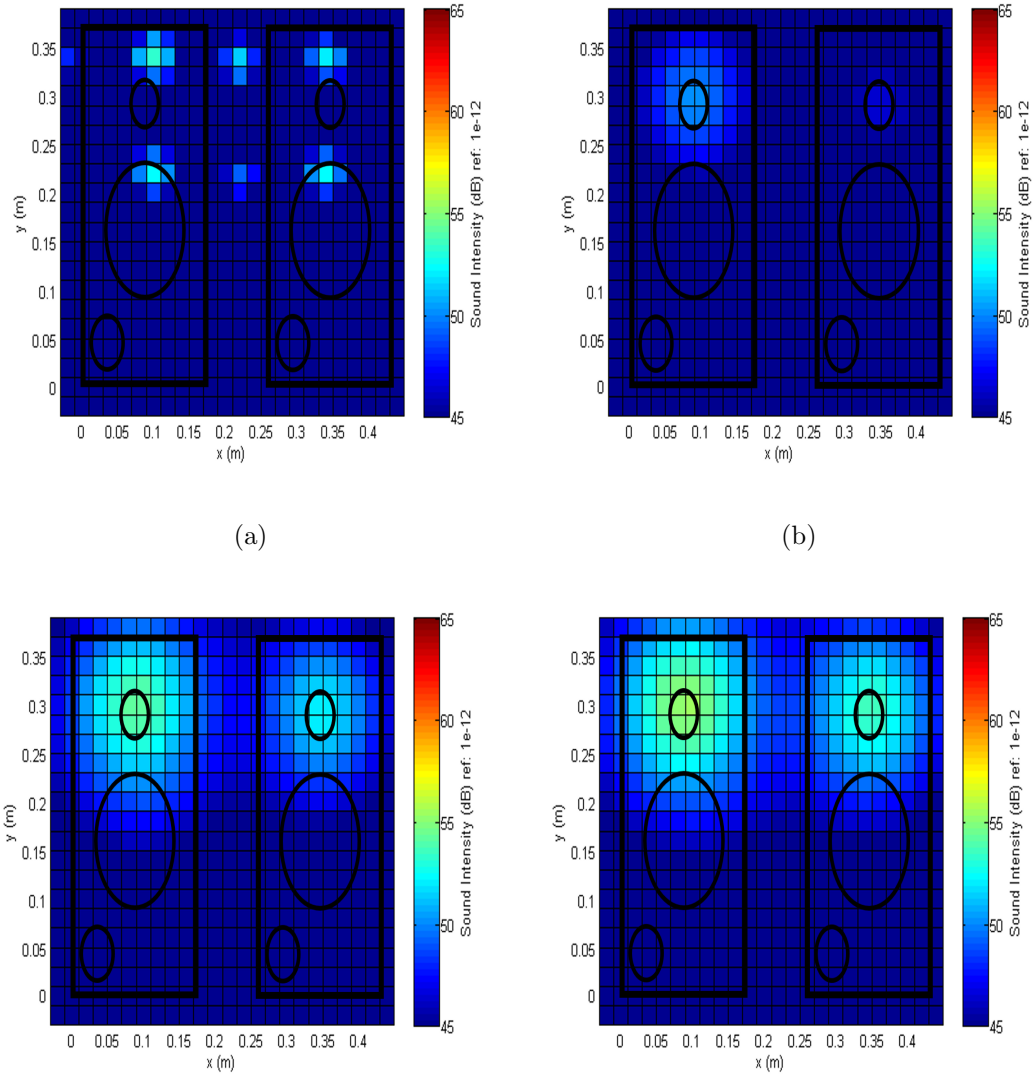

Figure 6.34. 0.05 m from loudspeaker front face sound intensity field reconstruction results with different NAH methods at 4 kHz with 20 microphones near-field measurement: (a) SONAH method, (b) WBH method, (c) l_1-norm minimization method, and (d) hybrid method.

be identified without aliasing in the loudspeaker test, and a similar sound power was recovered compare with the 72 and 255 measurements.

6.3.2 Reconstruction with Far-field Measurement

In this section, the sound source was the same two loudspeakers set up, but the intensity measurement was taken 0.485 m from the loudspeaker front face as in the far-field measurement described in the one loudspeaker experiment.

The measurement covered an area of 0.48 m by 0.42 m, and the intensity measurement spacing between points was 0.03 m, in both the x and y directions, and there were 255 sound pressure measurements as described in the previous near-field measurement. The input signal to the loudspeaker was Gaussian white noise of 25.6 kHz bandwidth generated by PULSE software through the computer. The time history data was processed with exactly the same parameter set up as described in previous sections. The monopoles were located on the equivalent source plane which was 0.02 m behind the loudspeaker front face. The monopole source mesh with a 0.01 m spacing in both directions covered an area of 0.48 m by 0.42 m area, which was the same as the measurement area. Figure (6.35) shows the relative position of the equivalent source plane, the reconstruction plane, the measurement plane and the loudspeaker position.

SONAH, WBH, l_1-norm minimization and the hybrid method were used to reconstruct the sound pressure and intensity field generated by the loudspeakers on the reconstruction plane, and the reconstruction results were compared with the intensity probe measurement. All the parameters used in different methods were exactly the same as described in the near-field measurement. The equations for the sound pressure, P, and velocity, $\vec{V}$, for the different methods at the reconstruction positions have been presented in previous chapters, and the sound intensity was calculated with equation (4.1). Then the total sound power over measurement plane was calculated with equation (4.2).

It is noted that as described in the one loudspeaker experiment, the far-field measurement data was used to reconstruct the sound field at 0.055 m from the loudspeaker front face, where the near-field intensity scan measurement was conducted. Then the

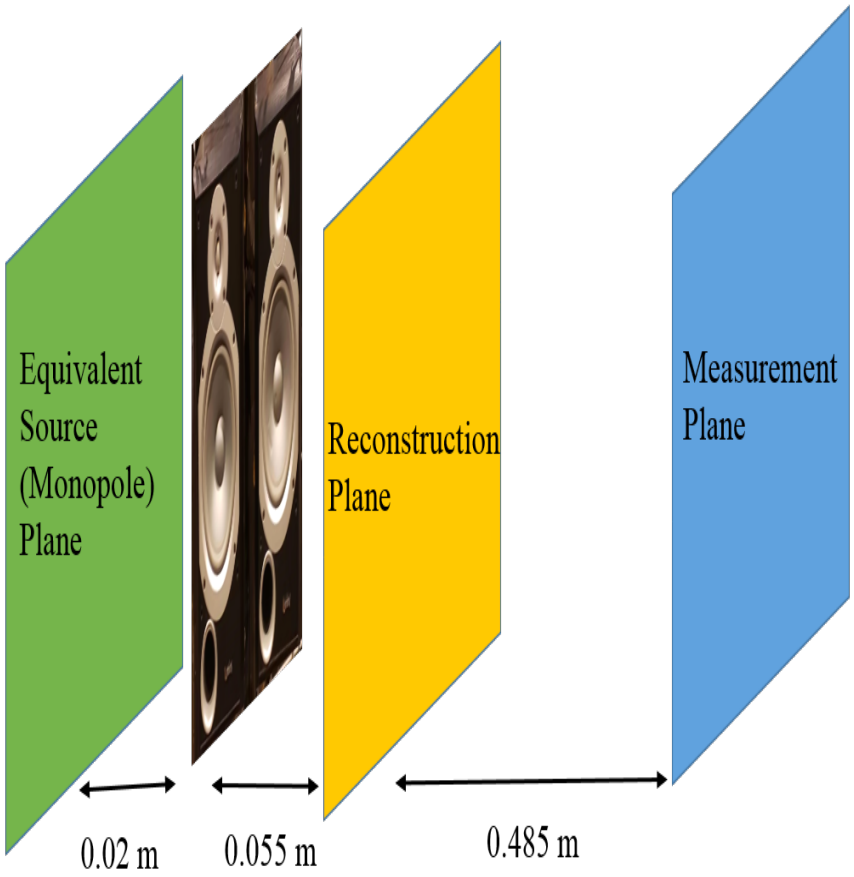

Figure 6.35. Relative position for far-field measurement set up.

reconstruction result will be compared with the direct measurement result presented in previous sections. Figures (6.36) (6.37) and (6.38) show the contour plots of the reconstructed sound intensity distributions 0.055 m from the loudspeaker front face, where the intensity measurement was conducted, at 0.8, 2.4 and 4 kHz, respectively.

From the spatial sound intensity reconstruction result, like the observation in the one loudspeaker experiment, the SONAH method failed to reconstruct the sound field with the far-field measurement at the different frequencies. The WBH algorithm identified one sound source in between the two loudspeakers at 0.8 kHz. At 2.4 kHz the algorithm found the loudspeaker on the right hand side and ignored the loudspeaker at the left hand side. Further, the algorithm separated the two tweeters

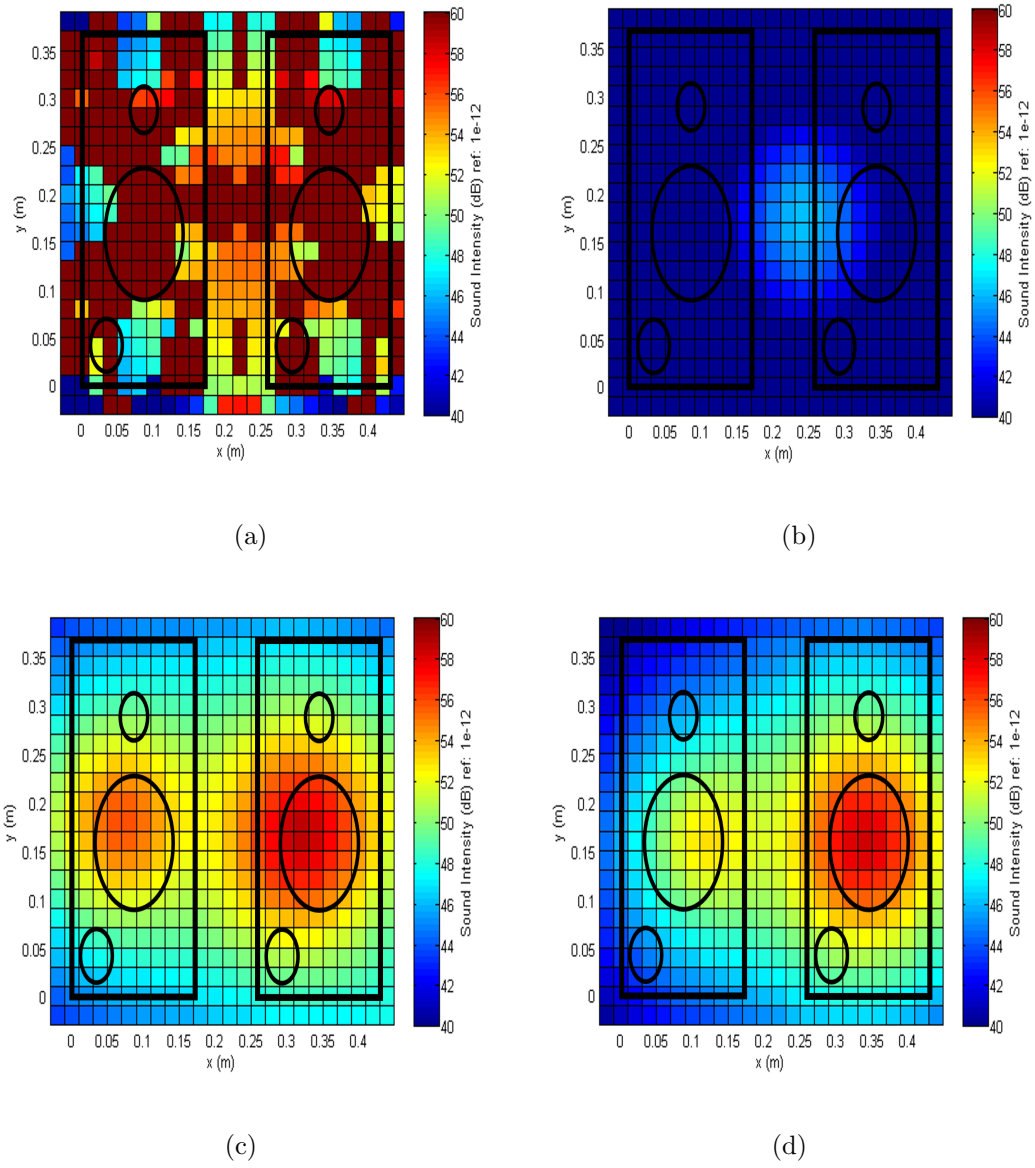

Figure 6.36. 0.05 m from loudspeaker front face sound intensity field reconstruction results with different NAH methods at 0.8 kHz with 255 microphones far-field measurement: (a) SONAH method, (b) WBH method, (c) l_1-norm minimization method, and (d) hybrid method.

at 4 kHz, which corresponded to the spacing-to-wavelength ratio observation in the simulation experiment. The l_1-norm minimization and the hybrid process was able to separate the two loudspeakers and identified the sound source locations correctly

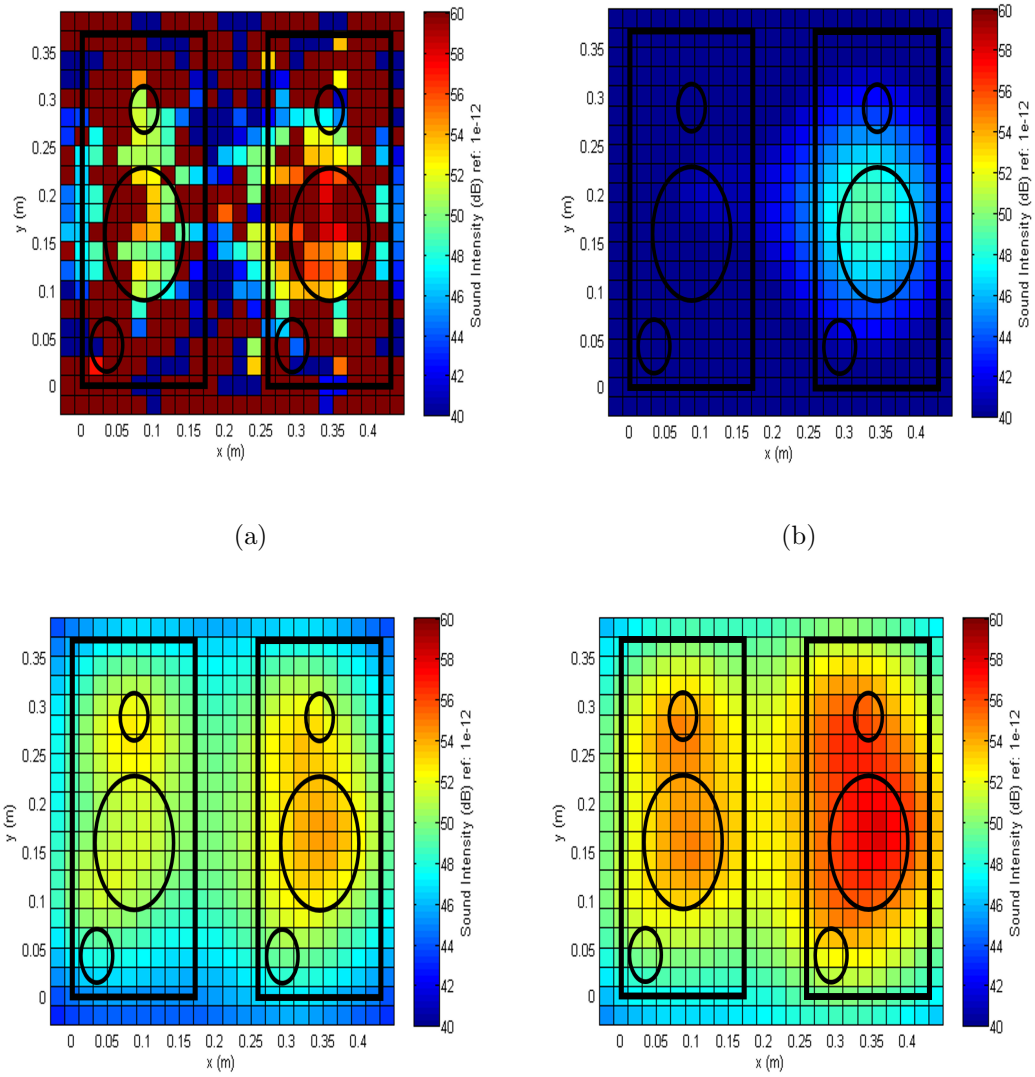

Figure 6.37. 0.05 m from loudspeaker front face sound intensity field reconstruction results with different NAH methods at 2.4 kHz with 255 microphones far-field measurement: (a) SONAH method, (b) WBH method, (c) l_1-norm minimization method, and (d) hybrid method.

at all three frequencies, but at 2400 Hz the separation between the tweeter and membrane was not clear. At 0.8 kHz, the WBH algorithm recovered 31.5 dB, l_1-norm minimization recovered 44.8 dB, the hybrid algorithm recovered 43.5 dB, and the near-

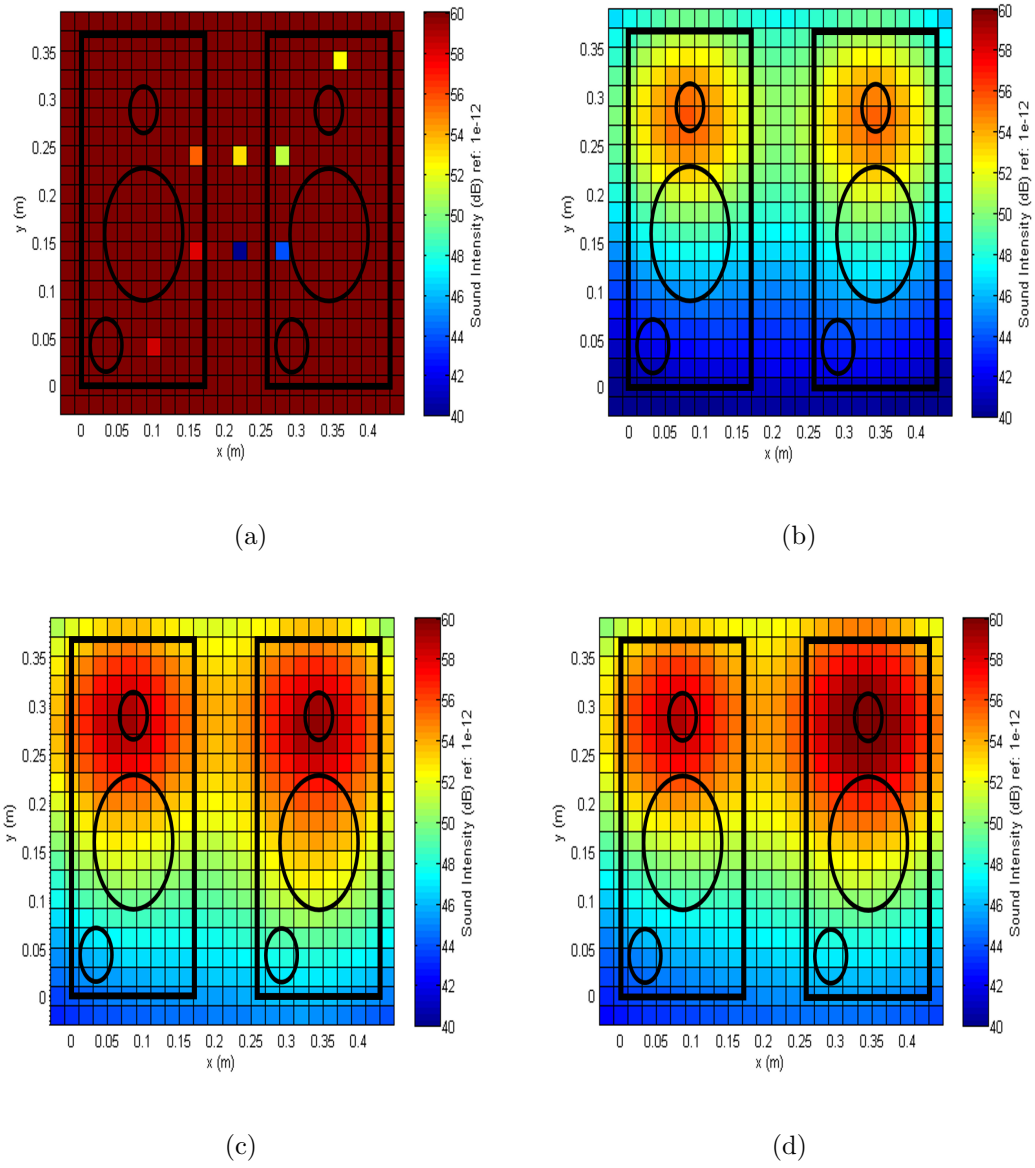

Figure 6.38. 0.05 m from loudspeaker front face sound intensity field reconstruction results with different NAH methods at 4 kHz with 255 microphones far-field measurement: (a) SONAH method, (b) WBH method, (c) l_1-norm minimization method, and (d) hybrid method.

field measured radiated sound power was 46.7 dB. At 2.4 kHz, the WBH algorithm recovered 34.4 dB, l_1-norm minimization recovered 42.9 dB, the hybrid algorithm recovered 45.8 dB, and the near-field measured radiated sound power was 44.0 dB.

The reconstructed sound power at 4 kHz, by the WBH algorithm was 42.6 dB, l_1-norm minimization recovered 46.5 dB, the hybrid algorithm recovered 46.9 dB, the near-field measured radiated sound power was 46.3 dB. Since SONAH cannot correctly identify the sound source locations, the reconstructed sound power with SONAH was not compared with the other algorithms. The sound power reconstructed by different algorithms were in general a litte bit larger then the reconstruction result with near-field measurement, and very close to the near-field intensity scan measurement.

Then as in the near-field measurement section, the spacing between microphones was doubled in both x and y directions and the 255 measurements was reduced to 72 measurements with the same patched measurement data. The set up of the equivalent source plane was kept the same: i.e., 2107 monopoles placed 0.02 m behind the loudspeaker front face. The parameters in SONAH, WBH, l_1-norm minimization and hybrid algorithm were kept the same as described in previous experiments. The sound field reconstruction results 0.055 m away from loudspeaker front face at 0.8 kHz, 2.4 kHz and 4 kHz are shown in Figures (6.39), (6.40) and (6.41).

It is interesting to find that the reconstruction result is similar to the experiment with one loudspeaker for the SONAH method: it failed to reconstruct the sound field at 0.8 kHz while arguably working at 2.4 and 4 kHz. At 2.4 kHz, the algorithm identified two large sound source regions but without the detail of the near-field measurement. And at 4 kHz SONAH identified the tweeter positions with a side lobe in between them. The sound power reconstructed by SONAH method was also small, 40.5 dB at 2.4 kHz and 36.3 at 4kHz. For the other algorithms the conclusions are similar to the reconstruction results with 255 measurements. At 0.8 kHz, the WBH algorithm recovered 31.7 dB, l_1-norm minimization recovered 45.4 dB, the hybrid algorithm recovered 43.4 dB, and the measured near-field radiated sound power was 46.7 dB, At 2.4 kHz, the WBH algorithm recovered 34.6 dB, l_1-norm minimization recovered 43.3 dB, and the hybrid algorithm recovered 44.1 dB, and the measured near-field radiated sound power was 44.0 dB. At 4 kHz, the WBH algorithm recovered 41.7 dB, l_1-norm minimization recovered 47.2 dB, and the hybrid algorithm recovered

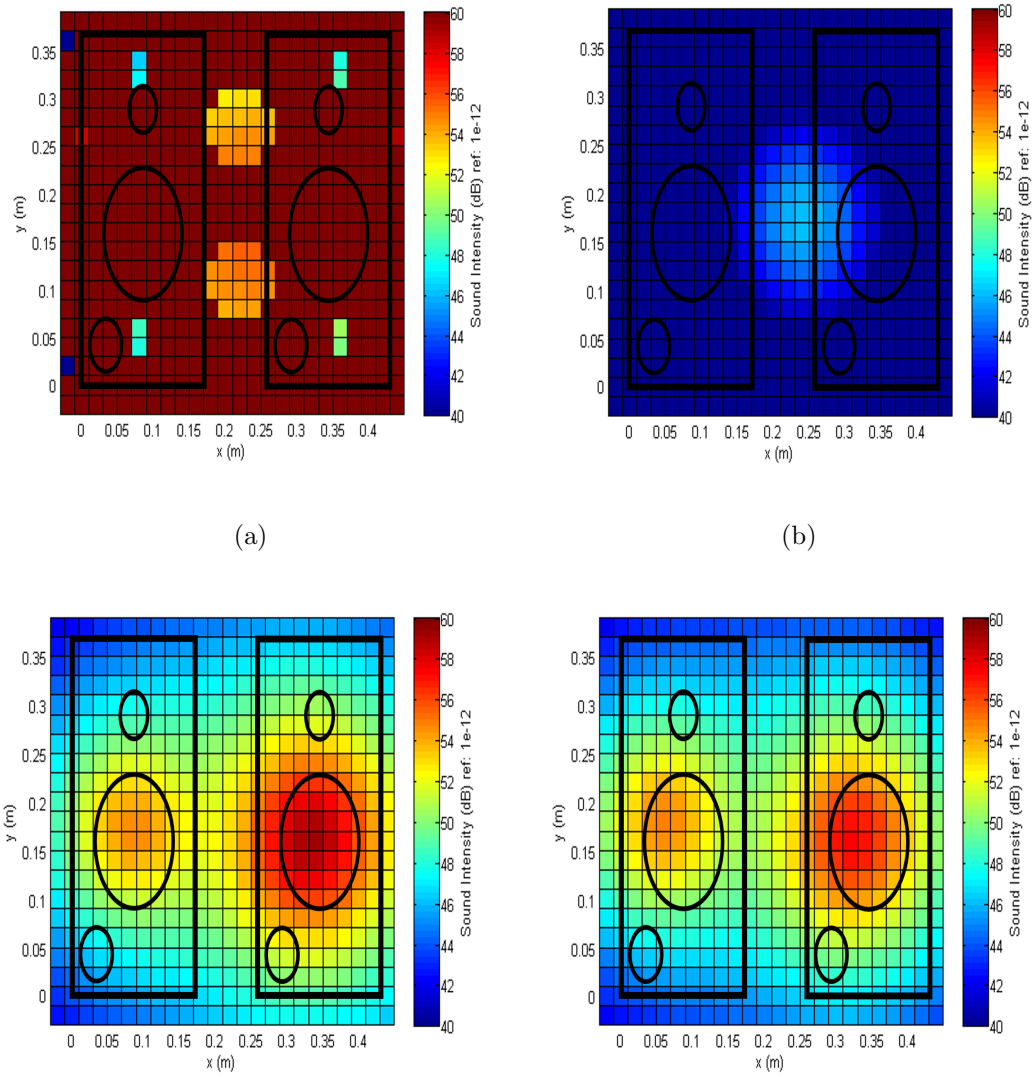

Figure 6.39. 0.05 m from loudspeaker front face sound intensity field reconstruction results with different NAH methods at 0.8 kHz with 72 microphones far-field measurement: (a) SONAH method, (b) WBH method, (c) l_1-norm minimization method, and (d) hybrid method.

48.0 dB, the measured near-field radiated sound power was 46.3 dB. The sound power reconstructed by the different methods with the 72 far-field measurements are in general similar to sound powers reconstructed with the 255 far-field measurements.

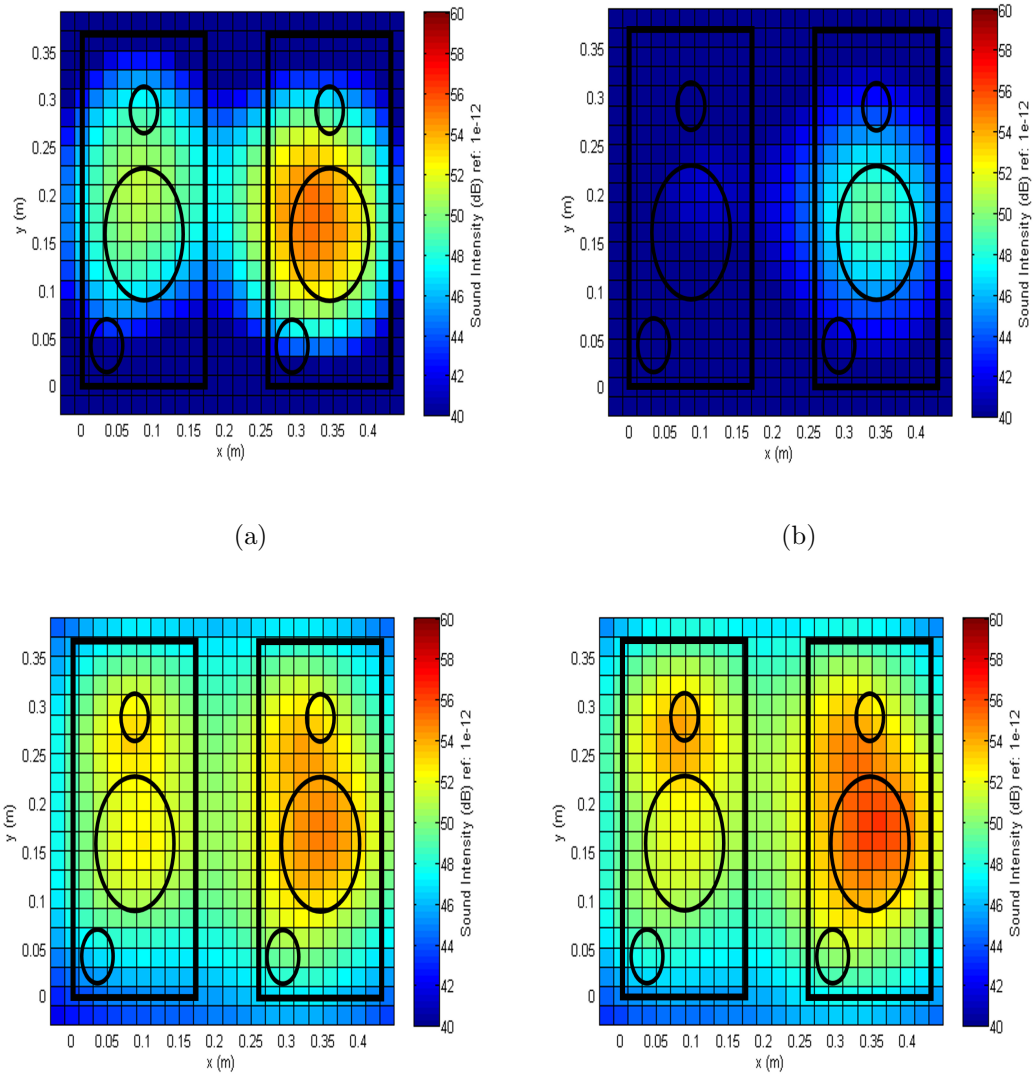

Figure 6.40. 0.05 m from loudspeaker front face sound intensity field reconstruction results with different NAH methods at 2.4 kHz with 72 microphones far-field measurement: (a) SONAH method, (b) WBH method, (c) l_1-norm minimization method, and (d) hybrid method.

To be consistent with near-field measurement experiment and to study the sound field reconstruction with a small number of microphone measurements, the spacing between the microphones was increased to 0.12 m in both the x and y direction. In this

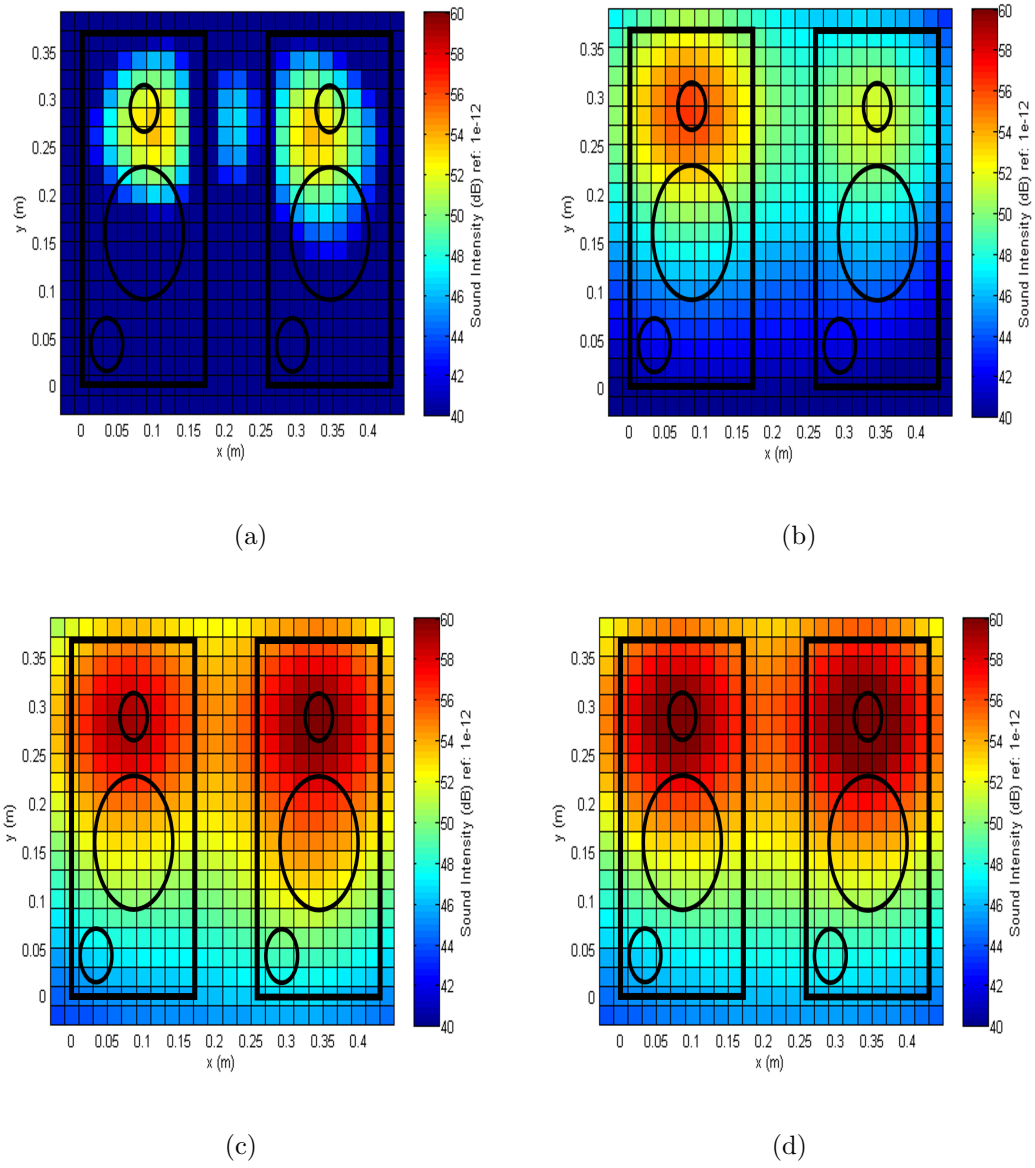

Figure 6.41. 0.05 m from loudspeaker front face sound intensity field reconstruction results with different NAH methods at 4 kHz with 72 microphones far-field measurement: (a) SONAH method, (b) WBH method, (c) l_1-norm minimization method, and (d) hybrid method.

case, there were only 20 microphone measurements for the sound field reconstruction. With the same equivalent plane set up and same parameters as used in previous

experiment, the sound intensity reconstruction results are shown in Figures (6.42), (6.43) and (6.44).

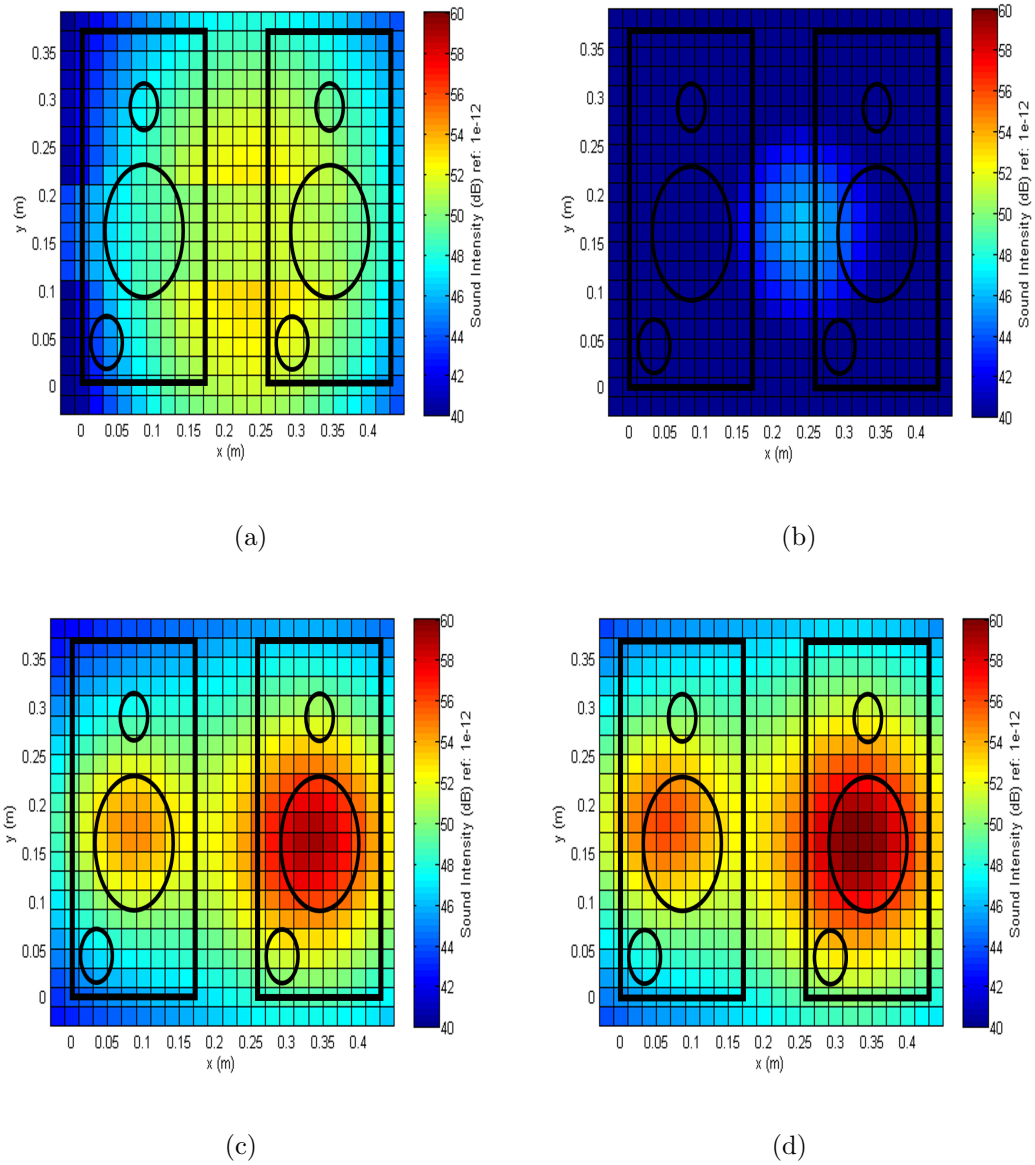

Figure 6.42. 0.05 m from loudspeaker front face sound intensity field reconstruction results with different NAH methods at 0.8 kHz with 20 microphones far-field measurement: (a) SONAH method, (b) WBH method, (c) l_1-norm minimization method, and (d) hybrid method.

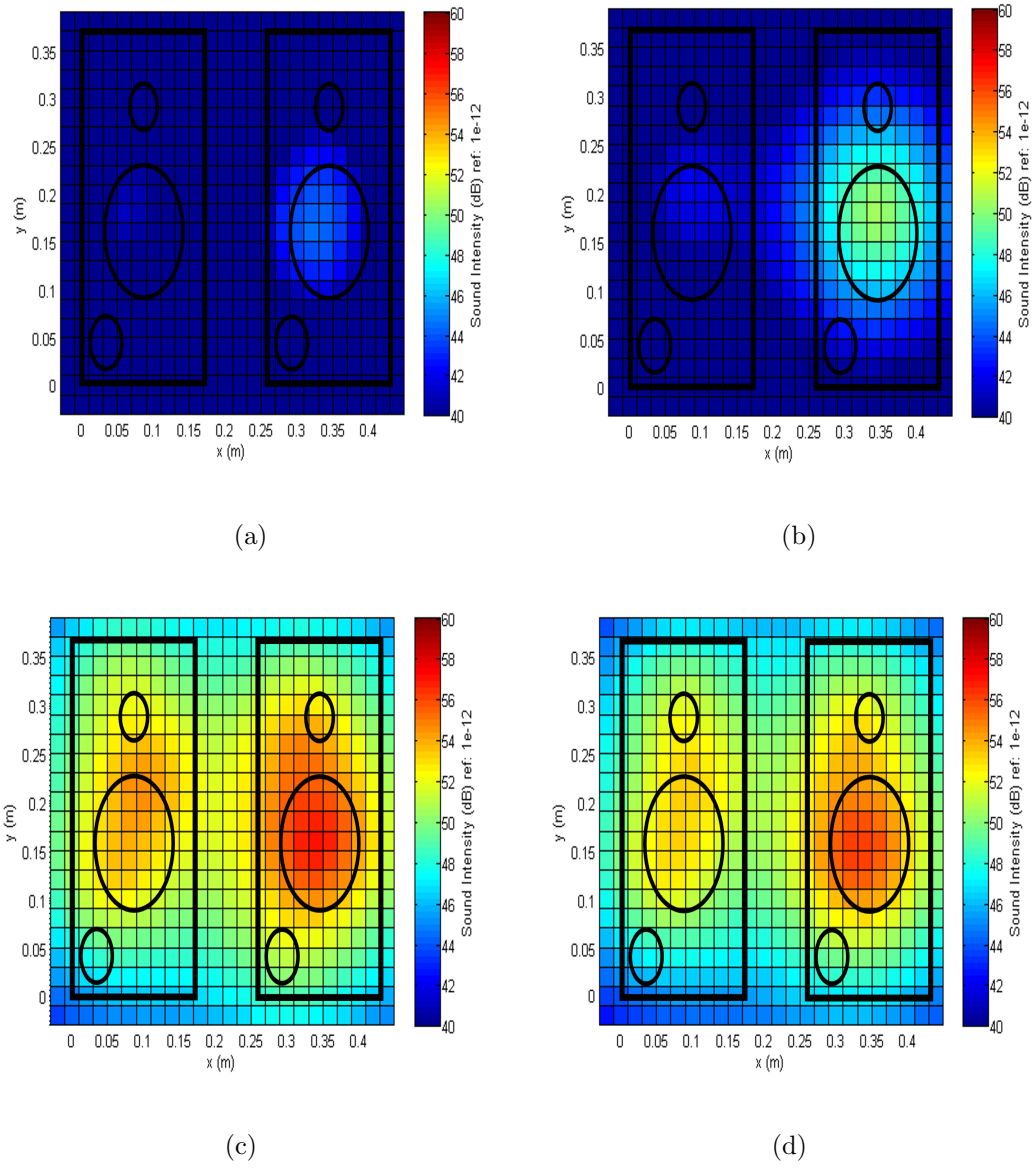

Figure 6.43. 0.05 m from loudspeaker front face sound intensity field reconstruction results with different NAH methods at 2.4 kHz with 20 microphones far-field measurement: (a) SONAH method, (b) WBH method, (c) l_1-norm minimization method, and (d) hybrid method.

With only 20 measurements, the SONAH method cannot reconstruct the sound field at any of the frequencies. For the sparse ESM algorithms, the major sound source location can still be identified but the closely-positioned sound sources become

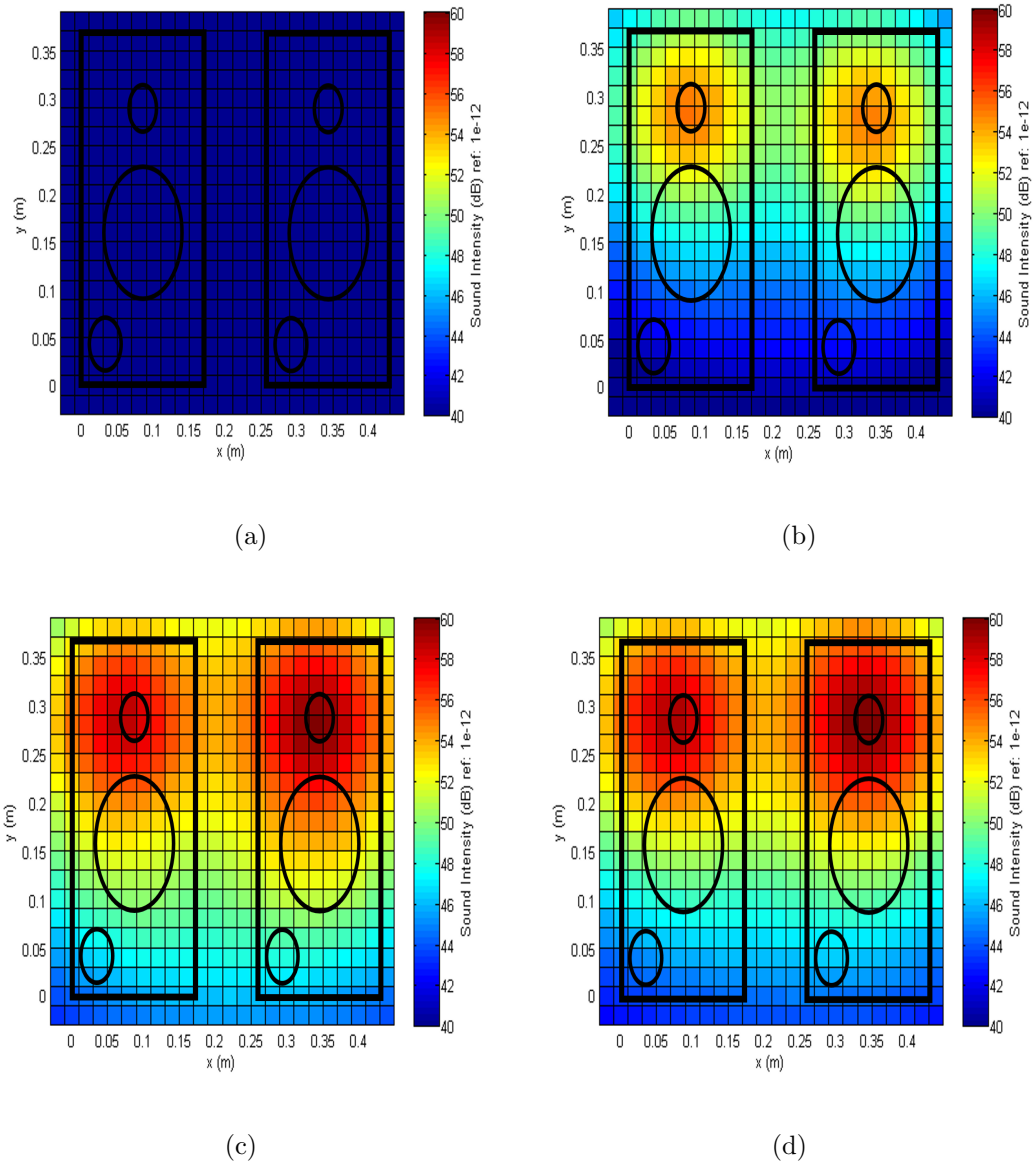

Figure 6.44. 0.05 m from loudspeaker front face sound intensity field reconstruction results with different NAH methods at 4 kHz with 20 microphones far-field measurement: (a) SONAH method, (b) WBH method, (c) l_1-norm minimization method, and (d) hybrid method.

harder to separate as the number of microphone decreases: e.g., at 2.4 kHz, the tweeter and membrane for two loudspeakers were identified as a large, single sound source instead of two separate sound sources, and the WBH algorithm ignored the

loudspeaker on the left hand side. At 0.8 kHz, the WBH algorithm recovered 31.4 dB, l_1-norm minimization recovered 44.7 dB, the hybrid algorithm recovered 45.1 dB, and the measured near-field radiated sound power was 46.69 dB. At 2.4 kHz, the WBH algorithm recovered 35.4 dB, l_1-norm minimization recovered 44.6 dB, and the hybrid algorithm recovered 43.6 dB, while the measured near-field radiated sound power was 44.0 dB. At 4 kHz, the WBH algorithm recovered 42.0 dB, l_1-norm minimization recovered 46.6 dB, and the hybrid algorithm recovered 46.5 dB, and the measured near-field radiated sound power was 46.3 dB. It is noted that the estimated sound power by the same method is consistent as the number of measurement decreased, as are the identified similar sound source locations, though the closely-positioned sources cannot be clearly separated.

The computation time for the SONAH method was longer than the sparse ESM algorithms: e.g., with 255 measurements and 550 reconstruction points, SONAH took 14 hours to finish the reconstruction, while as a comparison, with the same 255 measurements and 2107 monopoles, WBH took less than 3 minute, and the l_1-norm minimization and hybrid process took about 8 minutes.

6.4 Diesel Engine Noise Source Identification

In the previous section, based on the experimental results with simple sound sources, i.e., loudspeakers, it was shown that the sparse ESM algorithms were able to identify major sound sources when the number of measurements were limited and the measurement was token far from the sound source. In this section, a more complex sound source, i.e., diesel engine, was used as a sound source. Compared with a loudspeaker, a diesel engine is a more complex sound source: i.e., combustion noise, mechanical noise, etc. To visualize such a complex and large sound source with NAH, usually a large number of measurements with high spatial resolution is required to ensure avoiding measurement errors: i.e., spatial aliasing, windowing error, etc. Such measurement is usually costly and hard to perform which limits the use of NAH

in industry. Thus in this chapter, it is desired to prove that with the proposed sparse ESM algorithms, with a relatively small number of measurements relative accurate sound source locations can still be identified, even when the sound source is complex. In this chapter, due to the complexity of the sound source, the Partial Field Decomposition (PFD) is proposed to separate uncorrelated sound sources. Then with the sparse ESM algorithms the sound sources on diesel engine front face were reconstructed. The reconstruction results from different algorithm were comment upon.

6.4.1 Partial Field Decomposition (PFD)

As mentioned in the previous section, due to the complexity of the diesel engine, it is necessary to first separate the uncorrelated sound sources. In this section, the basis of PFD and the reconstruction of each partial field will be reviewed briefly. The sound field measured by the field microphones on the measurement surface can be expressed as a product of the data measured by a set of reference signals multiplied by appropriate transfer functions: that is, one can express this relation in matrix form [60],

$$\mathbf{p} = \mathbf{H}_{rp}^{\mathrm{T}}\mathbf{r}, \tag{6.2}$$

where $\mathbf{H}_{rp}$ is the acoustic transfer matrix that relates the measurement surface microphone signals, $\mathbf{P} = [p_1, ...p_m]^{\mathrm{T}}$, and the reference signals $\mathbf{r} = [r_1, ..., r_m]^{\mathrm{T}}$, in the frequency domain. Here N is the number of references, M is the total number of measurement microphones in the measurement array, and the superscript T denotes the transpose operator. When considering statistically random sources, equation (6.2) can be expressed in terms of cross-spectral matrices: i.e.,

$$\mathbf{C}_{pp} = \mathbf{C}_{rp}^{\mathrm{H}}\mathbf{C}_{rr}^{-1}\mathbf{C}_{rp} = \mathbf{H}_{rp}^{H}\mathbf{C}_{rr}\mathbf{H}_{r}p, \tag{6.3}$$

where $\mathbf{H}_{rp} = \mathbf{C}_{rr}^{-1}\mathbf{C}_{rp}$, the superscript H denotes the Hermitian operator, and the cross-spectral matrices $\mathbf{C}_{rr}$, $\mathbf{C}_{rp}$, and $\mathbf{C}_{pp}$, are defined as,

$$\mathbf{C}_{rr} = \mathrm{E}[r^{*}r^{\mathrm{T}}], \tag{6.4}$$

$$\mathbf{C}_{rp} = \mathrm{E}[r^* p^{\mathrm{T}}], \tag{6.5}$$

$$\mathbf{C}_{pp} = \mathrm{E}[p^* p^{\mathrm{T}}], \tag{6.6}$$

where the superscript * denotes the complex conjugate and E[...] represents the expectation operator.

In order to decompose the total sound field into a set of uncorrelated sound fields, a Singular Value Decomposition (SVD) is performed on the composite sound field,

$$\mathbf{C}_{rr} = \mathbf{U}\Sigma\mathbf{V}^H = \mathbf{U}\Sigma\mathbf{U}^H, \tag{6.7}$$

where Σ is a diagonal matrix composed of singular values, λ_i, $\mathbf{U}$ and $\mathbf{V}$ are unitary matrices that comprise the left and right singular vectors, and $\mathbf{U}$ and $\mathbf{V}$ are identical here since $\mathbf{C}_{rr}$ is a positive, semi-definite Hermitian matrix. The decomposed partial fields are then expressed as:

$$\tilde{\mathbf{p}} = \mathbf{C}_{rp}^{\mathrm{T}}\mathbf{U}^*\Sigma^{-\frac{1}{2}} = \mathbf{H}_{rp}^{\mathrm{T}}\mathbf{U}\Sigma^{-\frac{1}{2}}, \tag{6.8}$$

where the ith column vector of $\tilde{\mathbf{p}}$ represents the ith partial field.

6.4.2 Diesel Engine Experiment

The experimental was conducted in the Cummins Walesboro Noise & Vibration Lab. The test engine was an ISF-3.8, which is a four cylinder 3.8 liter diesel engine. The 36 element microphone array was placed parallel to the diesel engine front face, 0.58 m from the diesel engine. The measurement distance was far from engine because there was an intake pipe in front of the engine, so a closer measurement was not possible. The setup of the experiment is shown in Figure (6.45). During the test, it was noted that one microphone was not working properly, so measurements were made with the remaining 35 microphones. In the measurement, the sampling frequency was 25.6 kHz, in the time domain the measurement duration on each channel was 10 seconds for each test, then the measured data was A-weighted. In order

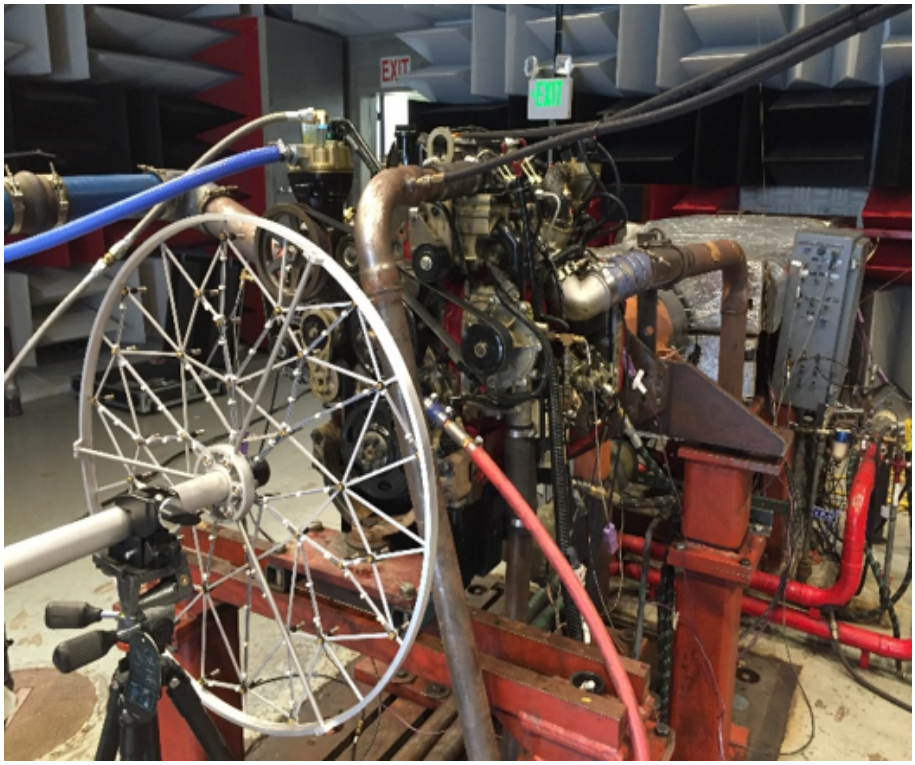

Figure 6.45. Diesel engine test experiment set up at Walesboro Noise & Vibration Lab.

to determine the number of major independent noise sources that contributed to the total sound field, the partial field decomposition process was performed before the sound field reconstruction. In the partial field decomposition process, first the data was transformed from the time domain to the frequency domain with 3200 Fourier Transform points with 8 Hz frequency resolution, corresponding to a segment length that was 1/50 of the total time length (i.e., 0.2 s). A Hann window was used, and the overlaps were half a segment length, so the data could be averaged 100 times. Then Welch s averaged periodogram method was used to calculate the cross-power spectral density matrix. Then, the PFD process was performed to separate the different partial fields. Next, the sound field were reconstructed with the sparse ESM algorithms, i.e., WBH, l_1-norm minimization and the hybrid process. The SONAH method was not considered in this experiment because the long measurement distance make the

method not suitable. The equivalent source plane with monopoles was placed 0.6 m from the measurement microphone array: i.e., 0.02 m behind the diesel engine front face. The reconstruction plane was 0.58 m from the measurement array: i.e., at the position of the diesel engine front face. The plane of monopole was 0.68 m by 0.48 m, and the monopole spacing was 0.01 m in both directions, so there were 3381 monopoles in the equivalent source model. The parameters in the WBH method were the same as presented in equation (3.13). And for the l_1-norm minimization procedure, the weighting parameter, λ_w, was chosen to be 20 after multiple trials. For the hybrid method, the weighting parameter in the l_1-norm minimization procedure was chosen to be 50, which is larger than than only apply l_1-norm minimization in order achieve a more accurate initial solution. And the parameters in the WBH method were kept same as in equation (3.13), except $D_0 = 5.1$ in order to keep secondary source in the first iteration. Since the noise sources that radiate energy to the far field are of interest, the holography results will be shown in terms of intensity. The sound pressure, P, and velocity, $\vec{V}$, were calculated with the same equations as in the loudspeaker experiment. Finally the intensity reconstruction result can be calculated by using equation (4.1). The microphone array measurement were conducted under two diesel engine operation condition on the test day: 750 rpm, idle and 1000 rpm, idle. Figure (6.46) shows the PFD result at 750 rpm, idle operation condition. The first and second sources are contributing most of the energy to the total sound field, so the first two uncorrelated sound sources will be reconstruct and added together to reconstruct the total sound field. Based on the spectrum, the sound field was reconstructed to identify the sound source locations at several peak frequencies: i.e., 160 Hz, 744 Hz, and 1040 Hz.

The reconstructed intensity distribution results with different sparse ESM algorithms are shown in Figures (6.47), (6.48) and (6.49). At 160 Hz, all the algorithms identified similar noise source locations: i.e., the crank pulley and the pipe in front of the engine. The WBH algorithm cannot correctly reconstruct the sound field, the reconstructed sound intensity value was very low, which is not realistic when the

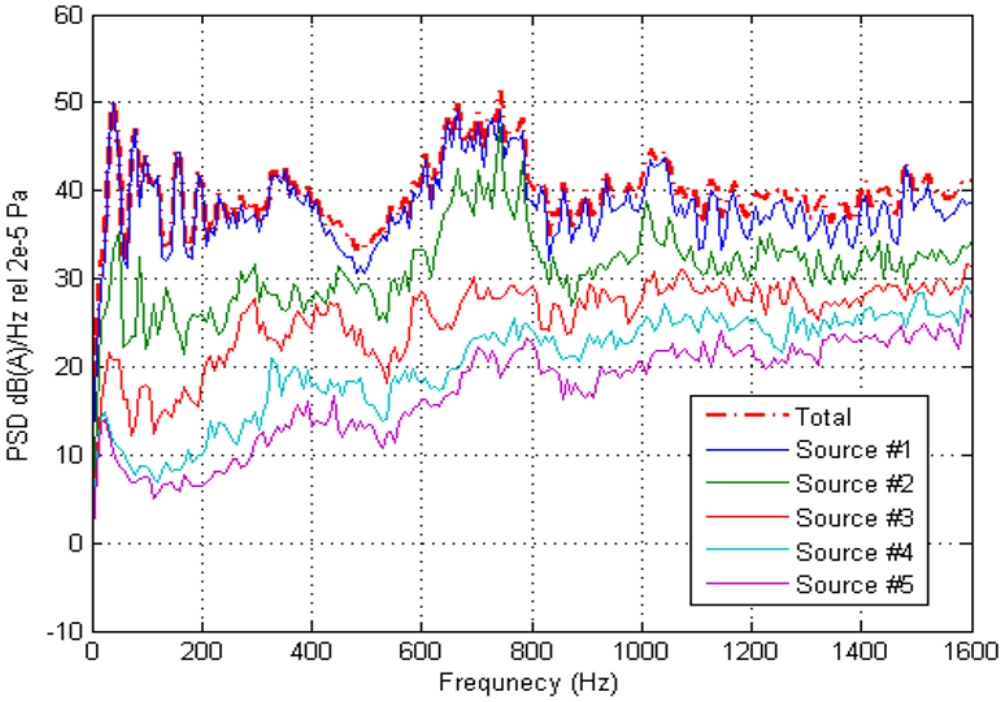

Figure 6.46. Partial field decomposition result for diesel engine operating at 750 rpm idle.

diesel engine is operating. The l_1-norm minimization and the hybrid method reconstructed more reasonable sound intensity level, and indicated similar sound source locations. When comparing the hybrid process reconstructed result with the $l_!$-norm minimization result, the hybrid process eliminated small sources, e.g., the hot spot at the corners, and assigned more weighting to the pipe position. It is noted that 160 Hz is a very low frequency which is difficult to identify accurate sound source location, since the wavelength is 2.14 m, which is larger than the engine dimension, so the reconstruction result can only be used as a reference even though the reconstruction result indicates reasonable source locations. At 160 Hz, the WBH algorithm recovered 30.7 dB, l_1-norm minimization recovered 47.0 dB, the hybrid algorithm recovered 53.7 dB. At 744 Hz, the WBH algorithm reconstructed the hot spot region at the left hand side and the sound intensity level is lower compared with the l_1-norm and the hybrid

process reconstruction results, which corresponds to the similar observations in the loudspeaker experiment at 800 Hz. The l_1-norm minimization and the hybrid process identified similar sound source locations, which also indicated the front pulleys, pipe and a sound source on the left hand side which was half out of the picture. The hot spot on the left hand side probably indicates sound coming from left side of the engine. At 744 Hz, the WBH algorithm recovered 35.2 dB, l_1-norm minimization recovered 52.2 dB, and the hybrid algorithm recovered 53.9 dB. At 1040 Hz, all three algorithms found the front pulleies as the sound sources; l_1-norm minimization and the hybrid process also identified the sound source close to the fun hub pulley. At this frequency, the WBH algorithm recovered 33.3 dB, l_1-norm minimization recovered 44.1 dB, and the hybrid algorithm recovered 47.4 dB.

The second test condition was the engine running at 1000 rpm, idle. The PFD result is shown in Figure (6.50), and based on the spectrum, the sound field was reconstructed at peak frequencies 104 Hz, 728 Hz, and 1720 Hz. These intensity reconstruction results are shown in Figures (6.51), (6.52) and (6.53).

At 104 Hz, all three algorithms identified the crank pulley as the noise source, l_1-norm minimization and the hybrid process also identified the pipe and the pulley at the upper right corner as noise sources. And the noise source at the top of the engine found by the l_1-norm minimization was eliminated as a ghost source in the hybrid process. Again, the sound intensity level reconstructed by the WBH method was not reasonable for an engine operating condition, which the l_1-norm minimization and the hybrid process reconstructed more reasonable sound intensity levels. At 104 Hz, the WBH algorithm recovered 29.3 dB, l_1-norm minimization recovered 46.4 dB, the hybrid algorithm recovered 52.3 dB. At 728 Hz, all three algorithms identified a noise source at lower left corner, which could be sound from left side of the engine. The l_1-norm minimization and the hybrid process identified the front crank pulley and the pipe as secondary noise sources. At 728 Hz, the WBH algorithm recovered 33.8 dB, l_1-norm minimization recovered 49.1 dB, the hybrid algorithm recovered 49.8 dB. At 1720 Hz, all three algorithms found the major noise source to be the

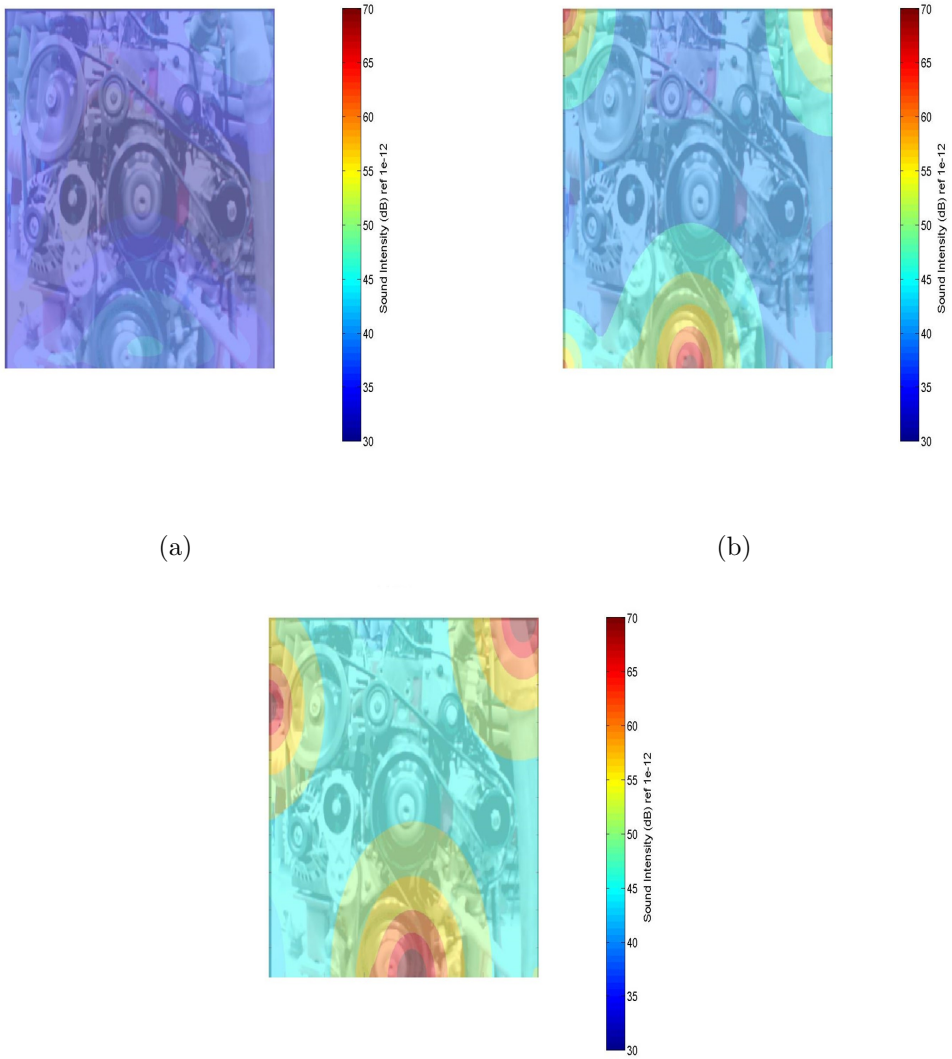

(a) (b)

(c)

Figure 6.47. Diesel engine front face sound intensity field reconstruction results with different spares ESM methods at 160 Hz engine operating at 750 rpm: (a) WBH method, (b) l_1-norm minimization method, and (c) hybrid method.

crank pulley at the center of the engine, and l_1-norm minimization and the hybrid process also identified the upper left pulley as a secondary noise source. Then the hybrid method also identified the pulley on the right hand side as noise source which

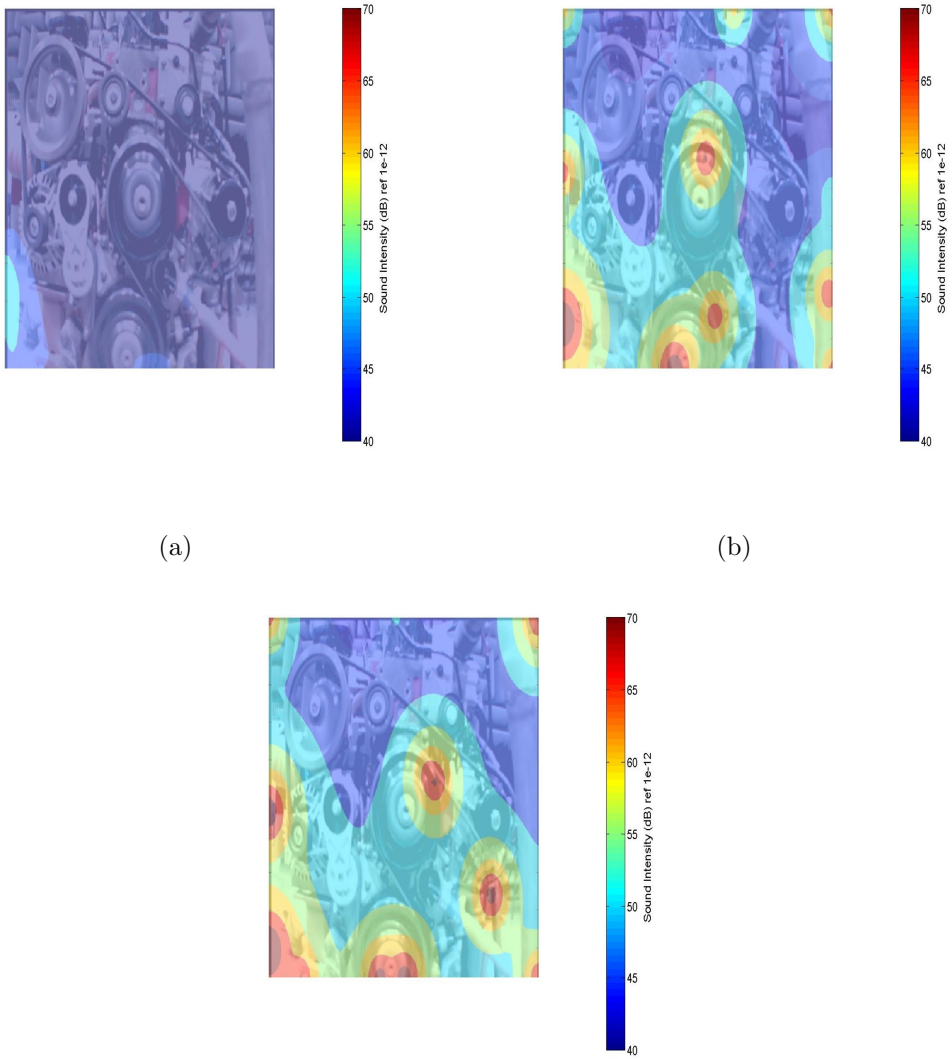

Figure 6.48. Diesel engine front face sound intensity field reconstruction results with different spares ESM methods at 744 Hz engine operating at 750 rpm: (a) WBH method, (b) l_1-norm minimization method, and (c) hybrid method.

was not found with l_1-norm minimization method. And when comparing with the reconstruction result obtained with the l_1-norm minimization, the result obtained with the hybrid process did eliminate the small ghost sources. At 1720 Hz, the WBH

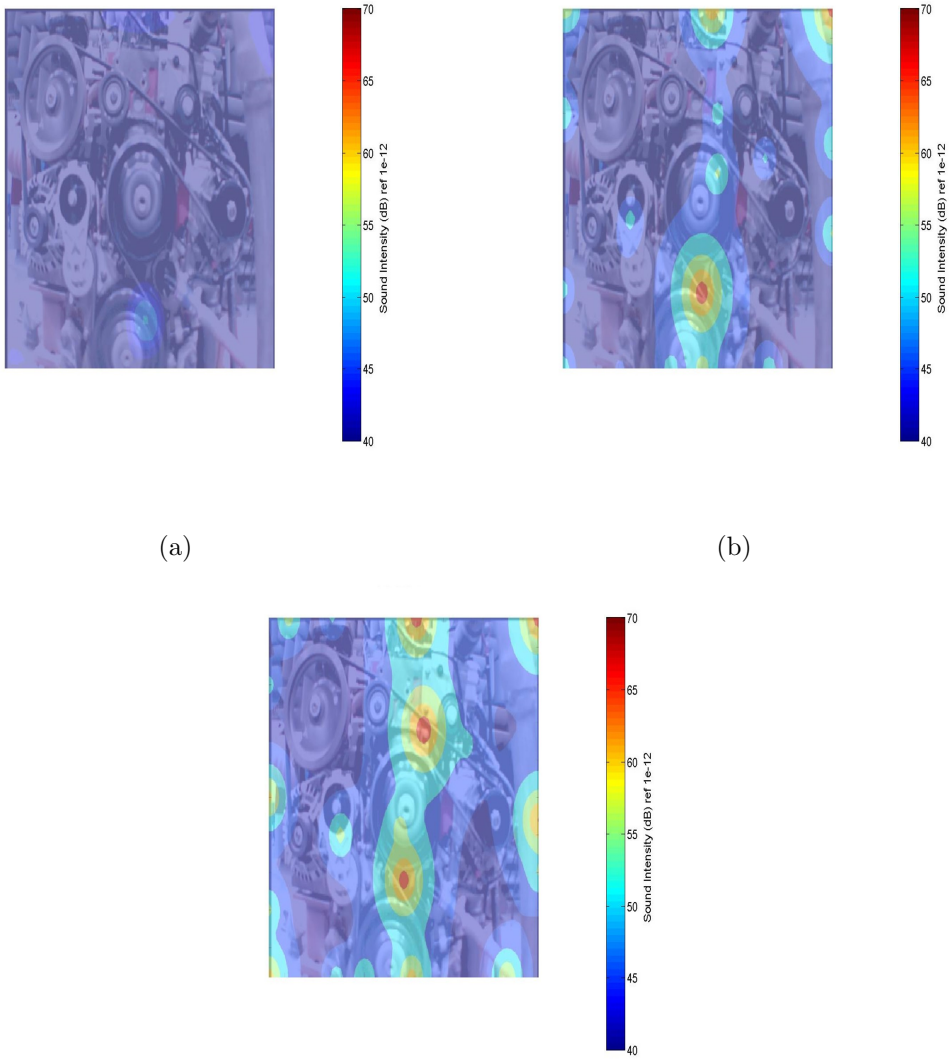

Figure 6.49. Diesel engine front face sound intensity field reconstruction results with different spares ESM methods at 1040 Hz engine operating at 750 rpm: (a) WBH method, (b) l_1-norm minimization method, (c) hybrid method.

algorithm recovered 31.2 dB, l_1-norm minimization recovered 39.8 dB, the hybrid algorithm recovered 41.8 dB. It is noted that since the diesel engine is a complex noise source and the number of measurements was relatively small, so the reconstruction

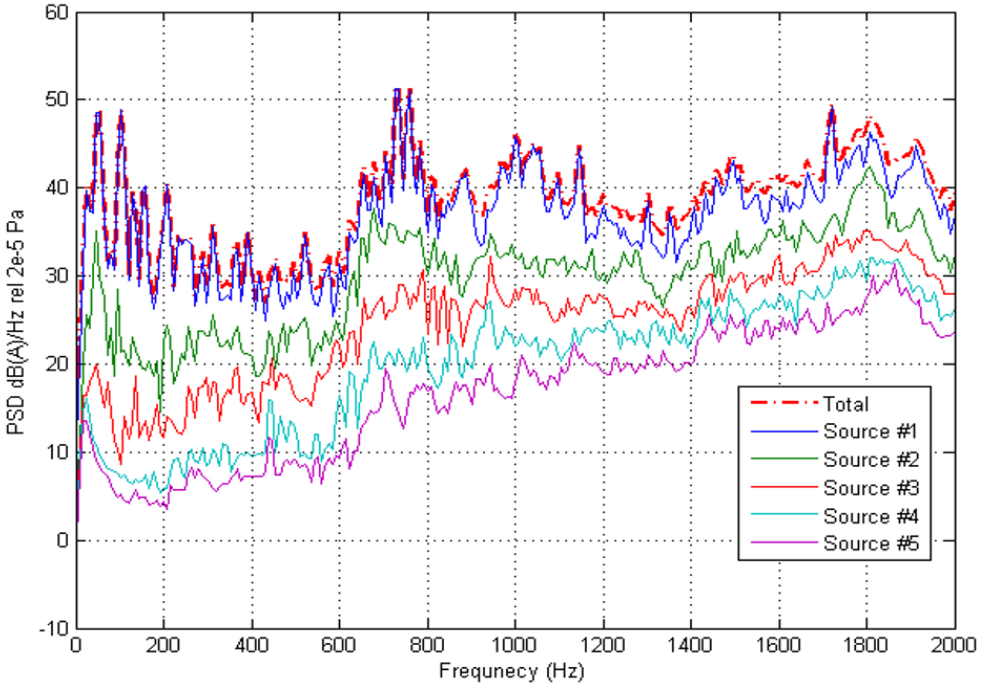

Figure 6.50. Partial field decomposition result for diesel engine operating at 1000 rpm idle.

results can only be used as reference, since there is still a need for further near-field measurements to confirm the results.

6.5 Summary

In this chapter, based on the experience with simulation experiments, the sparse ESM algorithms were applied to reconstruct the sound fields generated by different sound sources. The experiment began with a simple sound source: i.e., a loudspeaker. Based on the patched measurement principle, an equivalent simultaneous sound pressure measurement was constructed based on the intensity probe scan. The measurement was conducted in both near and far field, then based on the measured data, the number of measurements used for the sound field reconstruction was systematically decreased by doubling the spacing between adjacent measurements. It was found

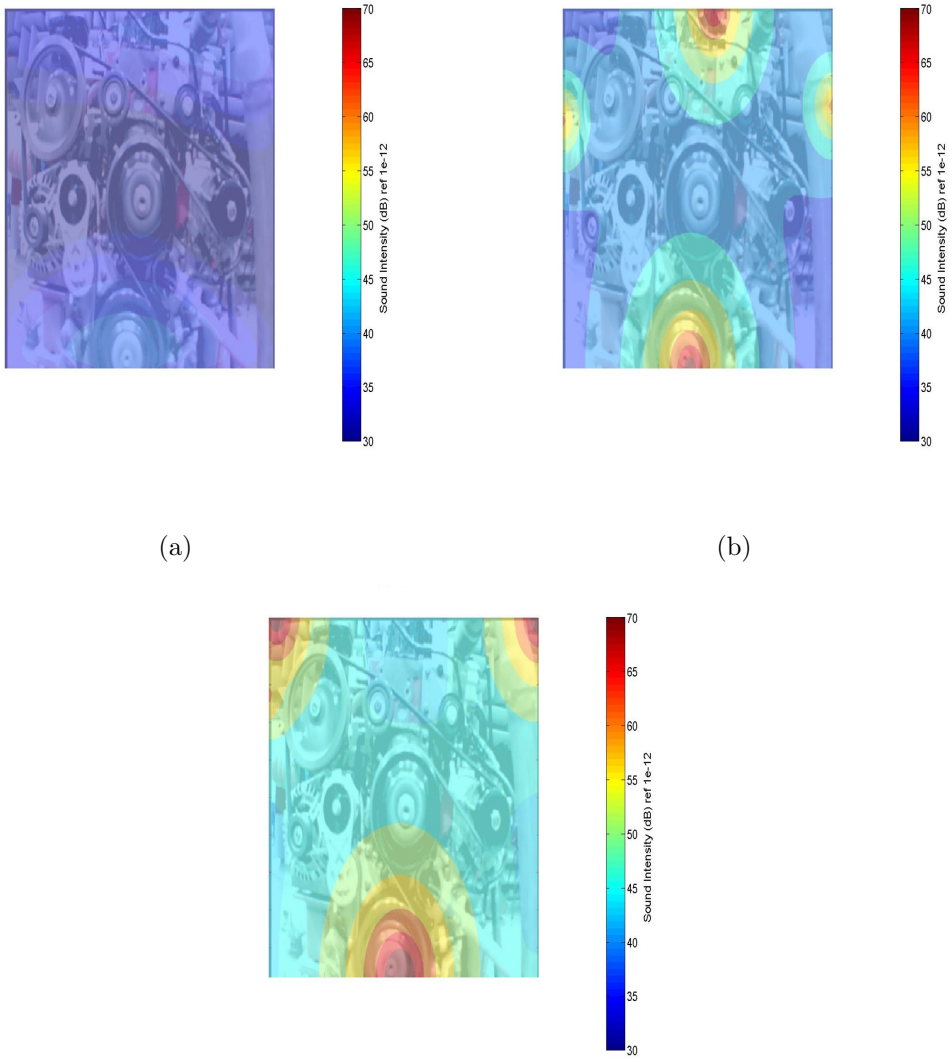

(a) (b)

(c)

Figure 6.51. Diesel engine front face sound intensity field reconstruction results with different spares ESM methods at 104 Hz engine operating at 1000 rpm: (a) WBH method, (b) l_1-norm minimization method, and (c) hybrid method.

that, with a close measurement that satisfied the spatial sampling rule, the SONAH method can reconstruct the most accurate sound field. The sparse ESM algorithms cannot reconstruct the sound field as accurately as the SONAH method, especially at

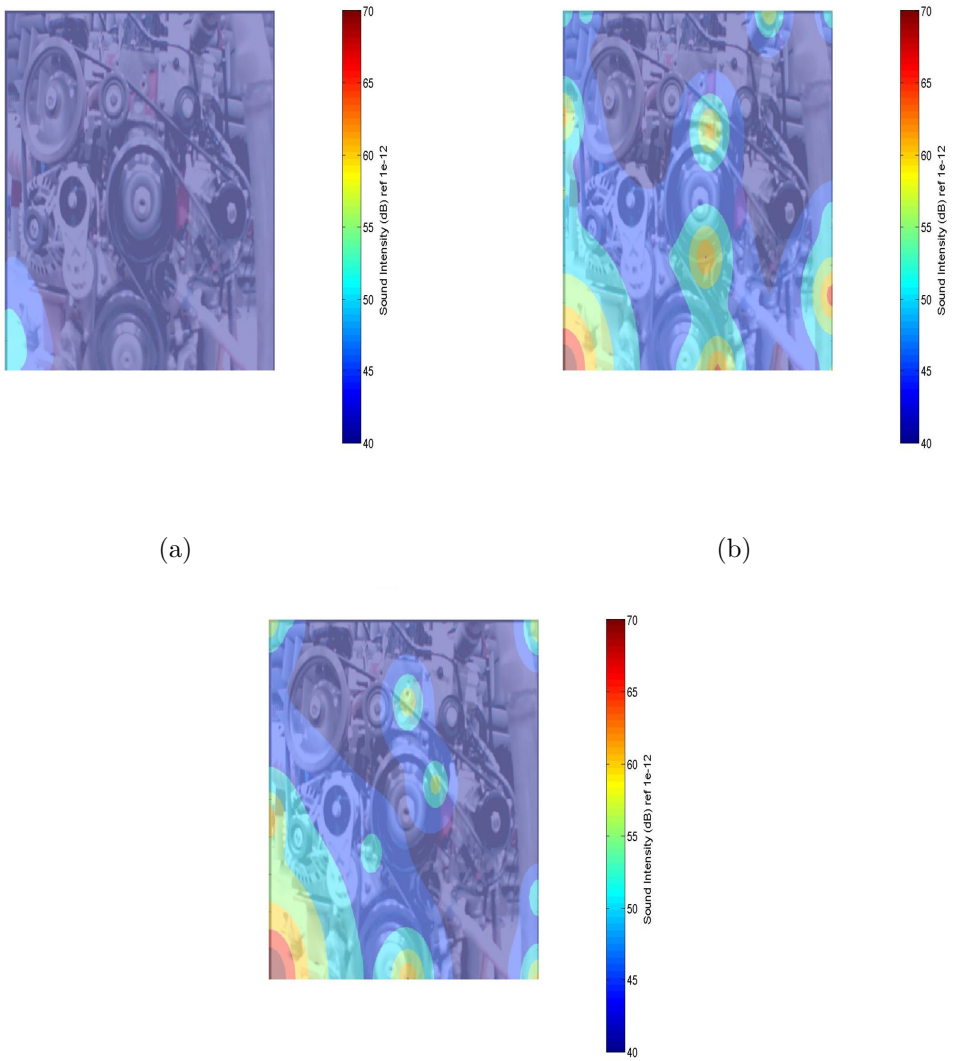

Figure 6.52. Diesel engine front face sound intensity field reconstruction results with different spares ESM methods at 728 Hz engine operating at 1000 rpm: (a) WBH method, (b) l_1-norm minimization method, and (c) hybrid method.

low frequency, but when the number of measurement is small and the measurement distance is far, the sparse ESM algorithms can still reconstruct accurate sound source location. When the measurement spacing was more than half of the wave length,

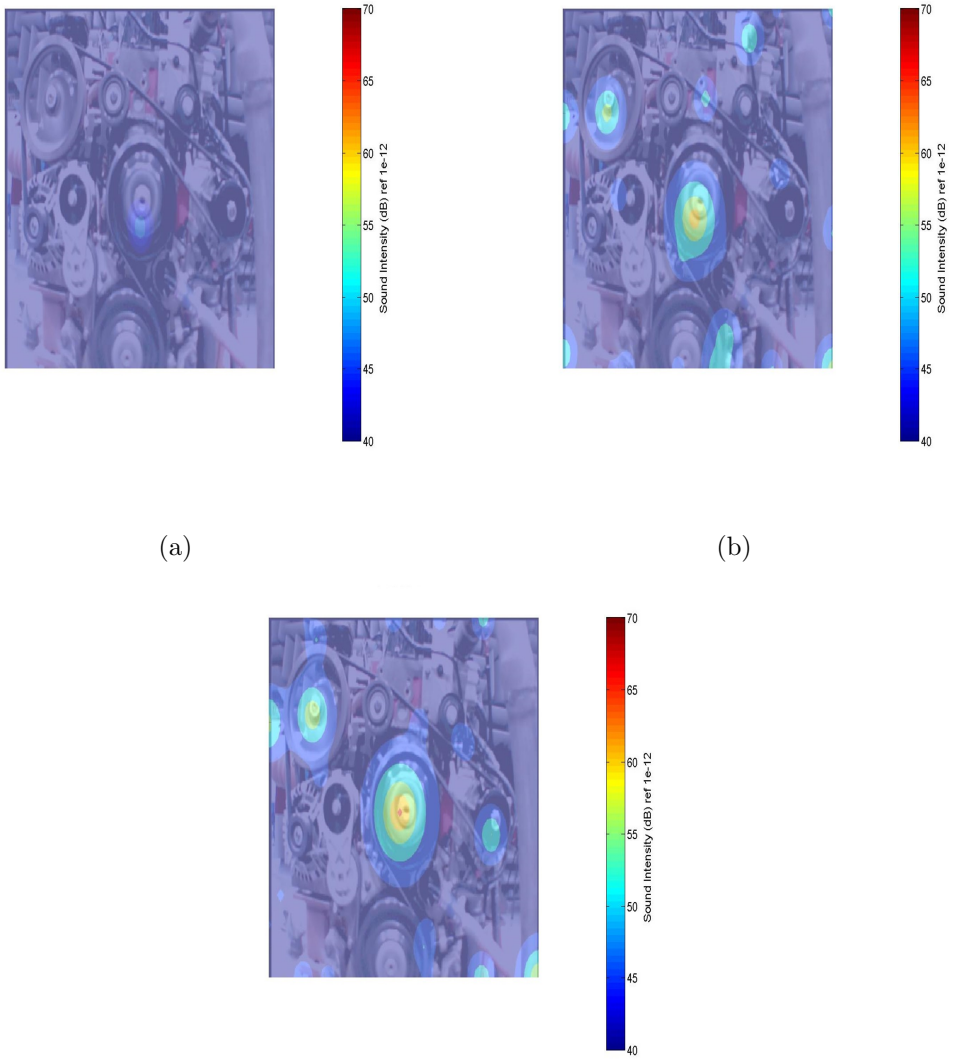

Figure 6.53. Diesel engine front face sound intensity field reconstruction results with different spares ESM methods at 1720 Hz engine operating at 1000 rpm: (a) WBH method, (b) l_1-norm minimization method, and (c) hybrid method.

aliasing appeared in the SONAH reconstruction results, and when the measurement distance was far, then SONAH cannot reconstruct the sound field. Then a 35 channel measurements were conducted on a diesel engine which is a complex sound source. It

was found that the sparse ESM algorithms basically identified similar major sound source locations, i.e., the front crank pulley position and the pipe when the engine was operating at 750 RPM and 1000 RPM. The l_1-norm minimization and the hybrid process reconstructed more detail and more accurate sound intensity level than the WBH algorithm.

7. SUMMARY AND FUTURE WORKS

7.1 Summary

Being able to identify sound sources helps engineers improve acoustical performance during the product design phase. NAH is a powerful tool that allows one to identify sound source locations with a measurement conducted away from the sound source, but the use of NAH is always limited by the measurement requirements. In the present work, motivated by the desire to accurately reconstruct sound fields with NAH methods that use a relatively small number of measurements, three sparse ESM algorithms were proposed. These three sparse ESM algorithms are all based on monopole equivalent source model: a large number of monopoles will cover the whole sound source region, thus creating an under-determined system. Since for an under-determined system, there are large number of possible solutions that mathematically satisfy the equations, it is desired to select the solution that indicates the true sound source position. Based on the principle of compressive sensing, it is desired that the solution be sparse so as to indicate the true sound source and avoid ghost sources, and at the same time that it br accurate enough to well represent the sound field. The first algorithm studied was Wideband Holography (WBH), a method which was originally proposed by Hald. This algorithm is an iterative process; at each iteration the system is solved by a steepest descent method, then a cardinality condition is applied to the solution to eliminate the ghost sources, and then with this truncated solution, the residual between the model predication and the measurements is calculated to check the solution accuracy. The iteration will stop if the solution satisfies one of the threshold condition: accuracy or cardinality. The second sparse ESM algorithm is l_1-norm minimization. In that algorithm, the objective function is the sum of the solution first norm and the second norm residual between the solution predic-

tion and the measurements. By minimizing this objective function, the solution first norm controls solution sparsity and the second norm residue guarantees the solution accuracy. The minimization problem was solved with an open source Matlab code CVX. Based on the simulation experiment, it was found that the initial solution that is used to begin the iteration in WBH has a strong influence on the final solution, and if there are sound sources closely-positioned, WBH cannot correctly separate them. For the l_1-norm minimization algorithm, the correct sound source position can be identified when the weighting parameter in the objective function is chosen appropriately as based on multiple trails in the present work. However, if the weighting parameter is chosen to be smaller than the appropriate value, the solution may not well-present the sound field, while if the weighting parameter is chosen to be larger than the appropriate value, the solution may contain ghost sources. Based on the experience with the WBH and l_1-norm minimization, a hybrid method was proposed in the present work. It is proposed to use the l_1-norm minimization with a relatively large weighting parameter to solve the system, then this solution is used as the initial solution to begin the WBH algorithm. In this way, the ghost sources created in the l_1-norm minimization solution are eliminated in the WBH process.

Experiments were then conducted to test the sparse ESM algorithms. The experiment was first conducted with a simple noise source: i.e., loudspeakers. In order to compare the reconstruction result with the true sound field, an intensity scan measurement was conducted close to the loudspeaker front face, then based on the same measurement, the sound field was reconstructed with different NAH algorithms. It was found that the sparse ESM algorithms are able to identify major sound source locations even when the number of measurements is small and the measurement was taken far from the sound source. Then an experiment wa conducted with a complex sound source: i.e., a diesel engine. In the experiment one set of 35 microphones array measurement was taken in front of the engine, and with this measurement the sound field on the diesel engine front face was reconstructed with sparse ESM algorithms.

It was found that the algorithms identified similar major noise sources at different frequencies and the major noise source for this engine is the crank pulley.

7.2 Future Works

For the future work, it is necessary to develop an automatic parameter selection strategy in the hybrid process to avoid having to select the parameters based on multiple trails. One possible approach is to use the L-curve method to select the weighting parameter, or chose the threshold condition based on background noise measurement. And an intensity probe scan measurement on the diesel engine front face should be conducted to compare with the reconstruction result and verify the reconstruction results.

REFERENCES

REFERENCES

[1] Don H Johnson and Dan E Dudgeon. *Array Signal Processing: Concepts and Techniques*. PTR Prentice Hall Englewood Cliffs, 1993.

[2] Earl G. Williams and J. D. Maynard. Holographic imaging without the wavelength resolution limit. *Physical Review Letters*, 45(7):554, 1980.

[3] Seong-Ho Yoon and Philip A Nelson. Estimation of acoustic source strength by inverse methods: Part ii, experimental investigation of methods for choosing regularization parameters. *Journal of Sound and Vibration*, 233(4):665–701, 2000.

[4] Philip A Nelson and Seong-Ho Yoon. Estimation of acoustic source strength by inverse methods: Part i, conditioning of the inverse problem. *Journal of Sound and Vibration*, 233(4):639–664, 2000.

[5] Earl G Williams and J. D. Maynard. Numerical evaluation of the Rayleigh integral for planar radiators using the FFT. *Journal of the Acoustical Society of America*, 72(6):2020–2030, 1982.

[6] Williams Earl G Maynard, Julian D and Lee Y. Nearfield acoustic holography: I. theory of generalized holography and the development of NAH. *Journal of the Acoustical Society of America*, 78(4):1395–1413, 1985.

[7] Martin Ochmann. The full-field equations for acoustic radiation and scattering. *Journal of the Acoustical Society of America*, 105(5):2574–2584, 1999.

[8] Sean F Wu. Methods for reconstructing acoustic quantities based on acoustic pressure measurements. *Journal of the Acoustical Society of America*, 124(5):2680–2697, 2008.

[9] Milton Abramowitz and Irene A Stegun. *Handbook of Mathematical Functions: with Formulas, Graphs, and Mathematical Tables*, volume 55. Courier Corporation, 1965.

[10] MA Rowell and DJ Oldham. Determination of the directivity of a planar noise source by means of near field acoustical holography, 1: theoretical background. *Journal of Sound and Vibration*, 180(1):99–118, 1995.

[11] Mingsian R Bai. Acoustical source characterization by using recursive wiener filtering. *Journal of the Acoustical Society of America*, 97(5):2657–2663, 1995.

[12] Earl G Williams, Brian H Houston, and Joseph A Bucaro. Broadband nearfield acoustical holography for vibrating cylinders. *Journal of the Acoustical Society of America*, 86(2):674–679, 1989.

[13] Moohyung Lee and J Stuart Bolton. Patch near-field acoustical holography in cylindrical geometry. *Journal of the Acoustical Society of America*, 118(6):3721–3732, 2005.

[14] Rolf Steiner and Jorgen Hald. Near-field acoustical holography without the errors and limitations caused by the use of spatial dft. *International Journal of Acoustics and Vibration*, 6(2):83–89, 2001.

[15] Yong Thung Cho, J Stuart Bolton, and Jørgen Hald. Source visualization by using statistically optimized near-field acoustical holography in cylindrical coordinates. *Journal of the Acoustical Society of America*, 118(4):2355–2364, 2005.

[16] Jørgen Hald. Patch near-field acoustical holography using a new statistically optimal method. *Bruel and Kjaer Technical Review*, page 40, 2003.

[17] Jørgen Hald. Basic theory and properties of statistically optimized near-field acoustical holography. *The Journal of the Acoustical Society of America*, 125(4):2105–2120, 2009.

[18] Andreas P Schumacher and Per Christian Hansen. Sound source resonstruction using inverse bem. In *INTER-NOISE and NOISE-CON Congress and Conference Proceedings*, volume 2001, pages 1870–1875. Institute of Noise Control Engineering, 2001.

[19] Earl G Williams. *Fourier Acoustics: Sound Radiation and Nearfield Acoustical Holography*. Academic press, 1999.

[20] AF Seybert, B Soenarko, FJ Rizzo, and DJ Shippy. An advanced computational method for radiation and scattering of acoustic waves in three dimensions. *Journal of the Acoustical Society of America*, 77(2):362–368, 1985.

[21] LH Chen and DG Schweikert. Sound radiation from an arbitrary body. *Journal of the Acoustical Society of America*, 35(10):1626–1632, 1963.

[22] Lawrence G Copley. Fundamental results concerning integral representations in acoustic radiation. *The journal of the acoustical society of America*, 44(1):28–32, 1968.

[23] PJT Filippi. Layer potentials and acoustic diffraction. *Journal of Sound and Vibration*, 54(4):473–500, 1977.

[24] Fish Jacob and Belytschko Ted. *A first course in finite elements*. Wiley, 2007.

[25] Gary H Koopmann, Limin Song, and John B Fahnline. A method for computing acoustic fields based on the principle of wave superposition. *Journal of the Acoustical Society of America*, 86(6):2433–2438, 1989.

[26] John B Fahnline and Gary H Koopmann. A numerical solution for the general radiation problem based on the combined methods of superposition and singular-value decomposition. *Journal of the Acoustical Society of America*, 90(5):2808–2819, 1991.

[27] R Jeans and IC Mathews. The wave superposition method as a robust technique for computing acoustic fields. *Journal of the Acoustical Society of America*, 92(2):1156–1166, 1992.

[28] Yangfan Liu and J Stuart Bolton. The use of non-collocated higher order sources in the equivalent source method. In *INTER-NOISE and NOISE-CON Congress and Conference Proceedings*, volume 2012, pages 7326–7337. Institute of Noise Control Engineering, 2012.

[29] Yangfan Liu. *Sound Field Reconstruction and its Application in Loudspeaker Sound Radiation Prediction*. Master's thesis, Purdue University, 2011.

[30] Yangfan Liu. *Efficient modeling of sound source radiation in free-space and room environments*. PhD thesis, Purdue University, 2016.

[31] Thomas F Coleman and Yuying Li. An interior trust region approach for nonlinear minimization subject to bounds. *SIAM Journal on optimization*, 6(2):418–445, 1996.

[32] Jiawei Liu, Yangfan Liu, and J Stuart Bolton. Noise source identification based on an inverse radiation mode procedure. In *INTER-NOISE and NOISE-CON Congress and Conference Proceedings*, volume 252, pages 495–502. Institute of Noise Control Engineering, 2016.

[33] Jiawei Liu, Yangfan Liu, and J Stuart Bolton. The application of acoustic radiation modes to engine oil pan design. *SAE Technical Paper*, 2017. 2017-01-1844.

[34] PC Hansen. Rank-Deficientand Discrete Ill-posed Problems. *Philadelphia, USA: SIAM*, 1997.

[35] Per Christian Hansen. Truncated singular value decomposition solutions to discrete ill-posed problems with ill-determined numerical rank. *SIAM Journal on Scientific and Statistical Computing*, 11(3):503–518, 1990.

[36] Andrey Tikhonov. Solution of incorrectly formulated problems and the regularization method. *Soviet Meth. Dokl.*, 4:1035–1038, 1963.

[37] Gene H Golub, Michael Heath, and Grace Wahba. Generalized cross-validation as a method for choosing a good ridge parameter. *Technometrics*, 21(2):215–223, 1979.

[38] Per Christian Hansen. Analysis of discrete ill-posed problems by means of the l-curve. *SIAM review*, 34(4):561–580, 1992.

[39] Per Christian Hansen. Numerical tools for analysis and solution of fredholm integral equations of the first kind. *Inverse problems*, 8(6):849, 1992.

[40] Earl G Williams. Regularization methods for near-field acoustical holography. *Journal of the Acoustical Society of America*, 110(4):1976–1988, 2001.

[41] Jørgen Hald. Fast wideband acoustical holography. *Journal of the Acoustical Society of America*, 139(4):1508–1517, 2016.

[42] Tongyang Shi, Yangfan Liu, and J Stuart Bolton. The use of wideband acoustical holography for noise source visualization. In *INTER-NOISE and NOISE-CON Congress and Conference Proceedings*, volume 252, pages 479–490. Institute of Noise Control Engineering, 2016.

[43] Tongyang Shi, Yangfan Liu, and J Stuart Bolton. A comparison of two equivalent source methods for noise source visualization. In *INTER-NOISE and NOISE-CON Congress and Conference Proceedings*, volume 254, pages 1058–1068. Institute of Noise Control Engineering, 2017.

[44] Tongyang Shi, Yangfan Liu, J Stuart Bolton, Frank Eberhardt, and Warner Frazer. Diesel engine noise source visualization with wideband acoustical holography. *SAE Technical Paper*, 2017. 2017-01-1874.

[45] Gilles Chardon, Laurent Daudet, Antoine Peillot, François Ollivier, Nancy Bertin, and Rémi Gribonval. Near-field acoustic holography using sparse regularization and compressive sampling principles. *Journal of the Acoustical Society of America*, 132(3):1521–1534, 2012.

[46] Takao Suzuki. L1 generalized inverse beam-forming algorithm resolving coherent/incoherent, distributed and multipole sources. *Journal of Sound and Vibration*, 330(24):5835–5851, 2011.

[47] Tongyang Shi, Yangfan Liu, and J Stuart Bolton. Noise source identification in an under-determined system by convex optimization. In *INTER-NOISE and NOISE-CON Congress and Conference Proceedings*, volume 274, pages 1308–1318. Institute of Noise Control Engineering, 2018.

[48] Jørgen Hald. A comparison of iterative sparse equivalent source methods for near-field acoustical holography. *Journal of the Acoustical Society of America*, 143(6):3758–3769, 2018.

[49] Michael Grant and Stephen Boyd. Cvx: Matlab software for disciplined convex programming, version 2.1, 2014. http://cvxr.com.

[50] Stephen Boyd and Lieven Vandenberghe. *Convex optimization*. Cambridge university press, 2004.

[51] Jon Dattorro. *Convex optimization & Euclidean distance geometry*. Lulu. com, 2010.

[52] John Wright, Arvind Ganesh, Shankar Rao, Yigang Peng, and Yi Ma. Robust principal component analysis: Exact recovery of corrupted low-rank matrices via convex optimization. In *Advances in neural information processing systems*, pages 2080–2088, 2009.

[53] Zhi-Quan Luo and Wei Yu. An introduction to convex optimization for communications and signal processing. *IEEE Journal on selected areas in communications*, 24(8):1426–1438, 2006.

[54] Frank R Eberhardt. *Study of the Feasibility of Estimating Combustion Noise Radiation in Reverberant Environments*. Master's thesis, Purdue University, 2011.

[55] Michael D Hayward. *Identification and Modification of Dominant Noise Sources in Diesel Engines*. Master's thesis, Purdue University, 2013.

[56] ME Wang and Malcolm J Crocker. On the application of coherence techniques for source identification in a multiple noise source environment. *Journal of the Acoustical Society of America*, 74(3):861–872, 1983.

[57] Darren L Hallman and J Stuart Bolton. A comparison of multi-reference nearfield acoustical holography procedures. In *INTER-NOISE and NOISE-CON Congress and Conference Proceedings*, volume 1994, pages 929–934. Institute of Noise Control Engineering, 1994.

[58] Hyu-Sang Kwon, Yong-Joe Kim, and J Stuart Bolton. Compensation for source nonstationarity in multireference, scan-based near-field acoustical holography. *Journal of the Acoustical Society of America*, 113(1):360–368, 2003.

[59] Peter Welch. The use of fast fourier transform for the estimation of power spectra: a method based on time averaging over short, modified periodograms. *IEEE Transactions on Audio and Electroacoustics*, 15(2):70–73, 1967.

[60] Moohyung Lee and J Stuart Bolton. Scan-based near-field acoustical holography and partial field decomposition in the presence of noise and source level variation. *Journal of the Acoustical Society of America*, 119(1):382–393, 2006.

VITA

VITA

Tongyang Shi was born in Harbin, Heilongjiang, China. He began his undergraduate education in Harbin Engineering University, where he studied underwater acoustics. During his freshman year, he join a collaboration program and went to Universite du Maine in France in his sophomore year, where he began study physical acoustics. He received dual bachelor degrees in digital signal processing and acoustics from Harbin Engineering University and Universite du Maine, respectively. After graduation in 2013, he continued one year of graduate study in Universite du Maine. The next year, he was accepted by Purdue University as a master's student in the Mechanical Engineering program, and began working on acoustical holography. In the 2015 fall semester, Tongyang obtained his master's degree, and decided to pursue a Ph.D degree in acoustics. In the spring semester of 2019, Tongyang finished his Ph.D degree.